Advanced Techniques for Continuous and Big Seismic Data Analysis: Empowered by AI and Unconventional Seismic Sources

アハマド, バハア オマル アハマド

Advanced Techniques for Continuous and Big Seismic Data Analysis:

Empowered by AI and Unconventional Seismic Sources

Ahmad Bahaa Omar Ahmad

Department of Earth Resource Engineering
Graduate School of Engineering
Kyushu University, Japan

This dissertation is submitted for the degree of

Doctor of Philosophy

January 2024

Abstract

This thesis presents novel processing approaches in seismic technology and neural network applications for processing big data to enhance environmental monitoring, such as stored CO2 monitoring. It revolves around 3 main significant potentials of advanced sources, continuous monitoring, and machine learning in geophysics that can integrate to analyze and interpret continuous monitoring data. The first chapter provides the background and objectives of the thesis, detailing its overall structure. Chapter two provides a comprehensive introduction to acquisition technologies, underlining their vital significance in the realm of geophysical exploration across various sectors, including oil, gas, and renewable energy. The chapter also presents a glimpse into the future of seismic acquisition, along with an exploration of other specialized techniques like passive seismic and the application of artificial intelligence (AI).

Chapter three delves into advancements in the Portable Active Seismic Source (PASS) design, both on the surface and in boreholes. It introduces the processing of two specialized designs: the High Energy-PASS (HE-PASS) for reflection and refraction seismic survey and the Borehole-PASS (B-PASS) for uphole and cross-hole surveys. The chapter outlines the setup of PASS and discusses the significant improvements made to PASS. The advanced PASS systems' results of field experiments are presented with a distributed acoustic sensing network and other dense vertical sensors. This chapter also explores techniques to enhance the signal-to-noise ratio (SNR), such as weighted stacking and spiking deconvolution. The HE-PASS signal was capable of propagating up to a 1 km offset distance even in rainy weather conditions, and the reflected wave could be imaged using distributed acoustic sensing. The chapter also discusses the relationship between the number of stacked sweeps needed and vertical depth through a heat map. It notes that as few as 60 shots are required for the HE-PASS to achieve a clear signal propagation in a 300-meter open borehole.

On the other hand, The B-PASS successfully covered a 450-meter diameter circle with enhanced signal propagation utilizing 500 sweeps. The chapter shows the negative impact of environmental noise on the source’s signal clearance. Additionally, the chapter includes tests conducted on the stability over durations of 10 hours for the original PASS and 19 hours for the B-PASS. These tests proved that both PASS models are stable and reliable active sources with no significant source signal variation.

Chapter four evaluates the effectiveness of Convolutional Neural Networks (CNN) in interpreting slump, fault systems, and gas chimneys in offshore 3D seismic data. I propose a method to increase the size of training data by applying slight deformation for the data to get data augmented. The study found that CNN is efficient and promising for seismic interpretation, providing faster and more accurate results compared to traditional methods. In this chapter, I made a qualitative comparison of my CNN results with a conventional approach (i.e., ant-track and coherency-attribute methods) to detect fault systems. CNN could deliver a human-like and more natural interpretation of the fault systems. The CNN successfully interpreted large 3D seismic volumes, accurately identifying a slump unit in the Kumano forearc basin in the Nankai Trough off the Kii peninsula, Japan. The CNN could detect new complex slump units that were not known before. I trained the CNN using 2D seismic data sourced from the Nankai Trough, conducting 10,000 iterations in the process. The outcome was a notable achievement, as the CNN attained a commendable 95% classification accuracy, specifically for slumping units. Then, I applied the trained model to seismic data from Sanriku-Oki, northeast Japan, to get an 85% matched result with human interpretation for the slump units. Furthermore, CNN was used to map the gas chimneys in the West Delta Deep Marine in Egypt accurately using only a single 2D seismic section.

In chapter five, I present a method based on AI to use the seismometer records of vehicles to create a traffic monitoring system. In this chapter, I investigated the efficiency of six machine-learning techniques (3 architectures of Neural Networks, Logistic Regression, Support Vector, Machine, and Naïve Bayes) to classify vehicles based on their size. I proposed a method to increase the size of training data by 500% using synthetic random noise. I used parameters like classification accuracy, recall, precision, and F1-score to evaluate each AI method. CNN, in particular, achieved state-of-the-art performance in analyzing new data compared to all other methods. The proposed CNN architecture could not only achieve 96% classification accuracy for vehicle size and analyze month-long (720 hours) records in 70 minutes of competitional time but also distinguish different types of vehicle overcrossing at the same time. This CNN architecture can be useful in identifying PASS signals and enhancing SNR.

The final chapter is a general conclusion with an overview of this thesis, highlighting the most important outcome of each chapter and the future direction for upcoming studies to optimize techniques for continuous seismic data analysis.

Acknowledgments

I am lucky to have been surrounded by remarkable, supportive, and enthusiastic people on my Ph.D. journey. I want to extend my heartfelt gratitude to all who have supported me, particularly my academic advisor, Takeshi Tsuji. Your guidance in science has been invaluable, and your dedication and enthusiasm have been truly inspiring. I am also deeply thankful to my Ph.D. supervisor, Tatsunori Ikeda, for the insightful discussions and non-stop support in this challenging journey. Thank you for everything you have taught me all these years.

Special thanks to all my lab mates, especially Tarek Imam, Chanmaly, and Fernando, for the enriching conversations and the impactful meetings during my Ph.D., which significantly influenced me. I also appreciate Ito san from the Earth Resource Engineering Department and OIWA san from the Graduate School of Engineering office for caring for me for five years at Ksyuhu University; thank you so much. A special acknowledgment to Professor Hakim Saibi from UAEU for his mentorship and brotherly support. I appreciate the financial support of the Japan Society for the Promotion of Science (JSPS) Fellowship and the Japanese Ministry of Education, Culture, Sports, Science and Technology (MEXT) scholarship.

Most importantly, I want to express my deepest gratitude to my mother, Eman Sultan, whose unconditional love and support have been my pillars. Your sacrifices and faith in me are beyond words, and I aspire to make you proud. Thank you.

This list of acknowledgments can only capture a small fraction of the people who supported my work. I send my deepest gratitude to all.

" I can only see a short distance ahead, but I can see plenty there that needs to be done."

- Alan Turing

Table of Contents

List of Figures

Chapter 1

Chapter 2

Chapter 3

Chapter 4

Chapter 5

List of Tables

Chapter 1

Chapter 3

Chapter 5

Chapter 1

General Introduction

1.1. Background

From the 1970s to 2020, seismic data acquisition underwent a remarkable evolution. In the 1970s, the technology was predominantly 2D with relatively low resolution, capturing data across tens to hundreds of kilometers of seismic lines, stored and processed using analog methods, limiting the data volume. The 1980s and 1990s marked a significant shift with the introduction and adoption of 3D seismic surveys, particularly in the oil and gas industry (Yilmaz, 2001a). These surveys covered larger areas, several square kilometers, with the transition to digital data storage during this period enabling the handling of larger data volumes, now measured in gigabytes. The 2000s saw further advancements in 3D seismic technology, with improved resolution and data acquisition rates reaching several tens to hundreds of square kilometers per survey, resulting in terabytes of data, thanks to enhanced computational capabilities (Krischer et al., 2016). A surge in high-resolution and 4D seismic data acquisition characterized the period from the 2010s to 2020. This era witnessed an exponential growth in data volumes, with modern surveys capable of generating petabytes of data, particularly with the incorporation of time-lapse (4D) seismic monitoring (Arrowsmith et al., 2022). This tremendous growth in data acquisition and processing capabilities reflects the technological innovations over these decades, including the development of more sensitive sensors and sophisticated processing techniques (Dugda et al., 2022). The historical growth in the acquisition rate of seismic data, particularly high-resolution data, is a story of technological evolution and increasing demand across several decades. Initially, in the oil and gas industry, seismic exploration was rudimentary, using basic methods like dynamite as a source and capturing data in analog format with low resolution (Liner et al., 2019). These early methods were constrained by the technology of the time and the logistical efforts required; however, over the years, seismic technology evolved significantly.

Recently, there has been a marked shift towards high-resolution and 4D seismic data acquisition, driven by the need for detailed subsurface imaging and dynamic monitoring, particularly in complex geological settings and projects like carbon capture and storage (Jenkins et al., 2015). The last two decades have witnessed exponential growth in data acquisition rates, pushed by technological advancements such as improved seismic sources and receivers, as is the case with new fiber-optic sensors (Daley et al., 2013). The digital revolution facilitated the transition from analog to digital data recording, allowing for the collection and processing of vast data volumes. High-performance computing has further revolutionized data processing, enabling the efficient handling of large amounts of high-resolution data. Industry trends, such as the move to more challenging offshore environments in oil exploration and stricter environmental and safety regulations, have also driven the demand for high-resolution surveys (Cordes et al., 2016). Today's rate of seismic data acquisition is not only faster but also involves much larger datasets with finer details compared to the past, as in Figure 1.1 (Arrowsmith et al., 2022). The challenges are managing and interpreting the enormous volumes of high-resolution data. However, this increase in data acquisition brings significant challenges. Processing and analyzing vast amounts of data efficiently is a major hurdle, as traditional methods can be time and resources consuming.

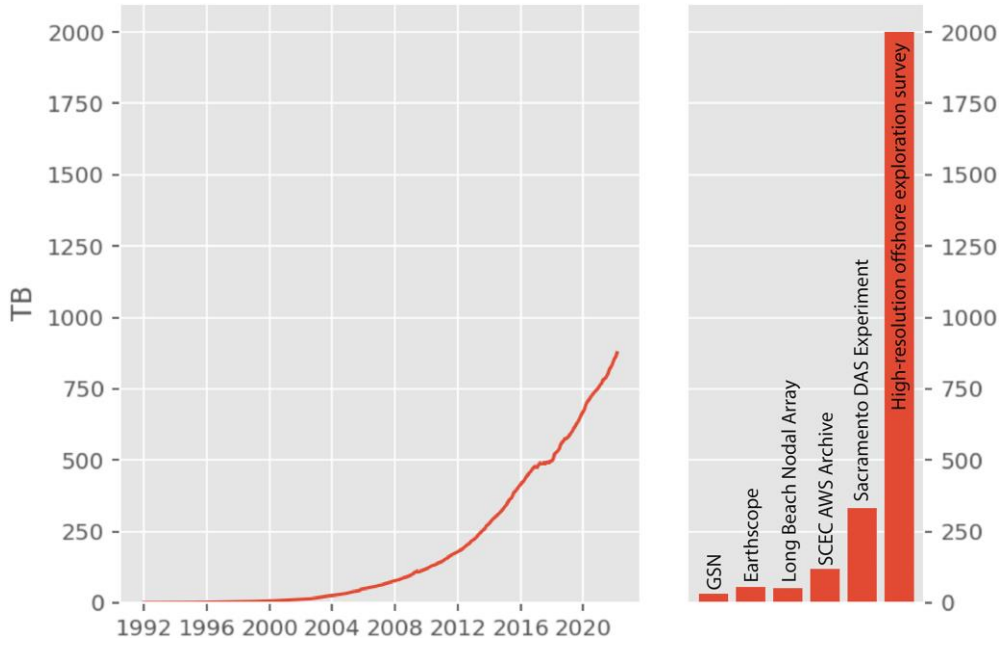

Figure 1.1 Data volume of the IRIS-DMC Archive as a function of time (left) and the corresponding data volumes of benchmark data sets without High-resolution offshore exploration survey (right) (Arrowsmith et al., 2022).

The management of large amounts of physical seismic data is paramount for CCS as it not only enables comprehensive monitoring but also facilitates more accurate modeling and assessment, ultimately enhancing the effectiveness of carbon capture and storage strategies. The significance of CCS in climate change mitigation arises from its ability to tackle the significant carbon dioxide (CO2) emissions produced by industries and power generation heavily reliant on fossil fuels, major contributors to global warming. By substantially reducing greenhouse gas emissions, CCS proves to be a crucial technology, especially in sectors like steel and cement production, where achieving direct emission reductions poses significant challenges. Moreover, in combination with bioenergy (known as BECCS), CCS can achieve negative emissions, actively removing CO2 from the atmosphere. As the world strives to meet ambitious climate targets set by the Paris Agreement, CCS stands out as an essential tool in the diverse portfolio of solutions needed to transition to a low-carbon economy. Its role in mitigating climate change is underscored in various scenarios presented by climate experts, including those from the Intergovernmental Panel on Climate Change (IPCC), highlighting its significance in global efforts to combat climate change (CHANGE, 2007).

CCS is an advanced technology aimed at mitigating climate change by capturing CO2 emissions from industrial processes and power generation and subsequently storing them underground to prevent their release into the atmosphere. The technology encompasses three primary stages: capturing CO2 using techniques like chemical solvents, transporting it typically via pipelines, and securely storing it in geological formations such as depleted oil fields or saline aquifers. Despite its potential, CCS faces challenges, including high operational costs, increased energy requirements, and concerns about the long-term stability of storage sites (Budinis et al., 2018). CCS technology is a focal point in climate change discussions due to its significance in reducing emissions, particularly from industries where alternative energy sources are limited. The deployment of CCS is contingent on overcoming these technological, economic, and regulatory hurdles. Governments and international bodies are increasingly incorporating CCS into climate policies, exploring incentives and regulatory frameworks to promote its application. The interest of countries and governments in CCS stems from the growing urgency to address climate change and the realization that reducing CO2 emissions is crucial to this effort. Here's a historical perspective on why CCS has gained importance:

1. **Early Awareness and Climate Science**: In the late 20th century, scientific consensus grew around the role of CO2 and other greenhouse gases in global warming and climate change. The Intergovernmental Panel on Climate Change (IPCC), established in 1988, played a pivotal role in assessing and communicating this impact (Fleming, 1998).

2. **Kyoto Protocol and International Agreements**: The Kyoto Protocol, adopted in 1997, was one of the first significant international agreements focusing on reducing greenhouse gas emissions, such as investing in emission reduction projects in developing countries (CDM) through trading emission credits (Miyamoto and Takeuchi, 2019).

3. **Technological Evolution**: In the early 2000s, CCS began to be recognized as a potential technology for reducing emissions from fossil fuel use, especially in sectors where alternatives were limited or non-existent.

4. **Policy and Economic Drivers**: The development of carbon pricing and trading schemes, such as the European Union Emissions Trading System (EU ETS), provided economic incentives for emission reduction technologies, including CCS (Groenenberg and de Coninck, 2008).

5. **Paris Agreement and Enhanced Climate Goals**: The Paris Agreement in 2015 marked a global commitment to limit global warming to well below 2 degrees Celsius (Meinshausen et al., 2022). Achieving this ambitious goal required a broad range of strategies, including CCS, to reduce emissions from key sectors like power generation industrial processes and even to achieve negative emissions through bioenergy with CCS (BECCS).

The current state of CCS showcases several operational projects globally, but widespread deployment at a scale that significantly impacts global emissions is still in the nascent stages. Future advancements depend on research aimed at enhancing efficiency and reducing costs, including novel materials for CO2 capture and innovative storage monitoring methods. CCS's role in climate change mitigation strategies is underscored in various scenarios by the Intergovernmental Panel on Climate Change (IPCC), highlighting its critical position in global efforts to address climate concerns. Continuous research and development, policy support,

and technological advancements are essential for CCS to realize its full potential in contributing to global climate change mitigation efforts.

1.2. CCS Future in Japan

Japan has been actively advancing its plans for CCS as part of its broader strategy to achieve carbon neutrality by 2050. Japan's plans for CCS are a multifaceted approach involving the selection of strategic projects, governmental financial support, a detailed roadmap with specific targets, and the creation of a legal framework to support these initiatives(Hibino et al., 2022). These efforts are integral to Japan's strategy to reduce CO2 emissions and achieve its long-term climate goals. Here are the key elements of Japan's CCS initiatives:

Selection of Advanced CCS Projects: On June 13, 2023, the Japan Organization for Metals and Energy Security (JOGMEC) selected seven role model projects, designated as Japanese Advanced CCS Projects, with the objective of scaling up business operations and reducing costs by 2030 (Ozawa et al., 2022). These projects are a critical step towards full-scale implementation of CCS in Japan, aiming to significantly contribute to the country's carbon neutrality goals by 2050.

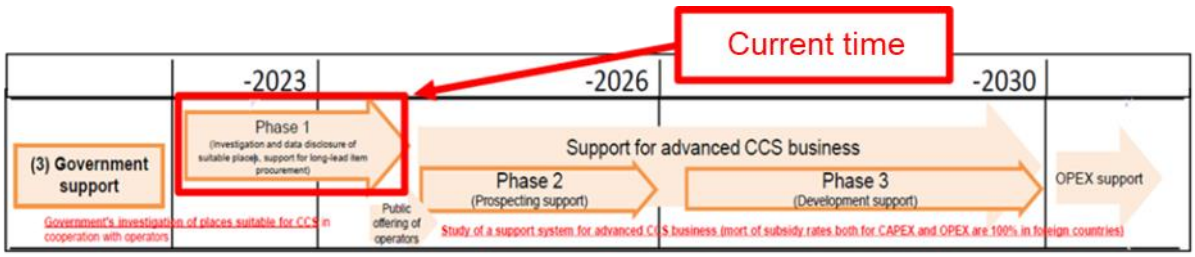

Figure 1.2 Roadmap of Government Support for the CCS Project in Japan (Jogmec report, 2023).

Government Financial Support and Project Locations: The Japanese government has provided financial support for these seven CCS projects. By 2030, these initiatives are expected to add a combined annual CO2 capture capacity of 13 million tonnes. Notably, five of these projects are planned to store CO2 within Japan in locations such as Hokkaido, the Sea of Japan, the Greater Tokyo area, and Kyushu.

Long-term CCS Roadmap Plan: Japan's long-term CCS roadmap, approved on January 26, outlines the country's plan to launch CCS businesses by 2030. This plan includes increasing

CO2 storage volumes to between 6 million and 12 million metric tons per year, a crucial step towards achieving the 2050 carbon neutrality target, as in Figure 1.2. (Jogmec report, 2023).

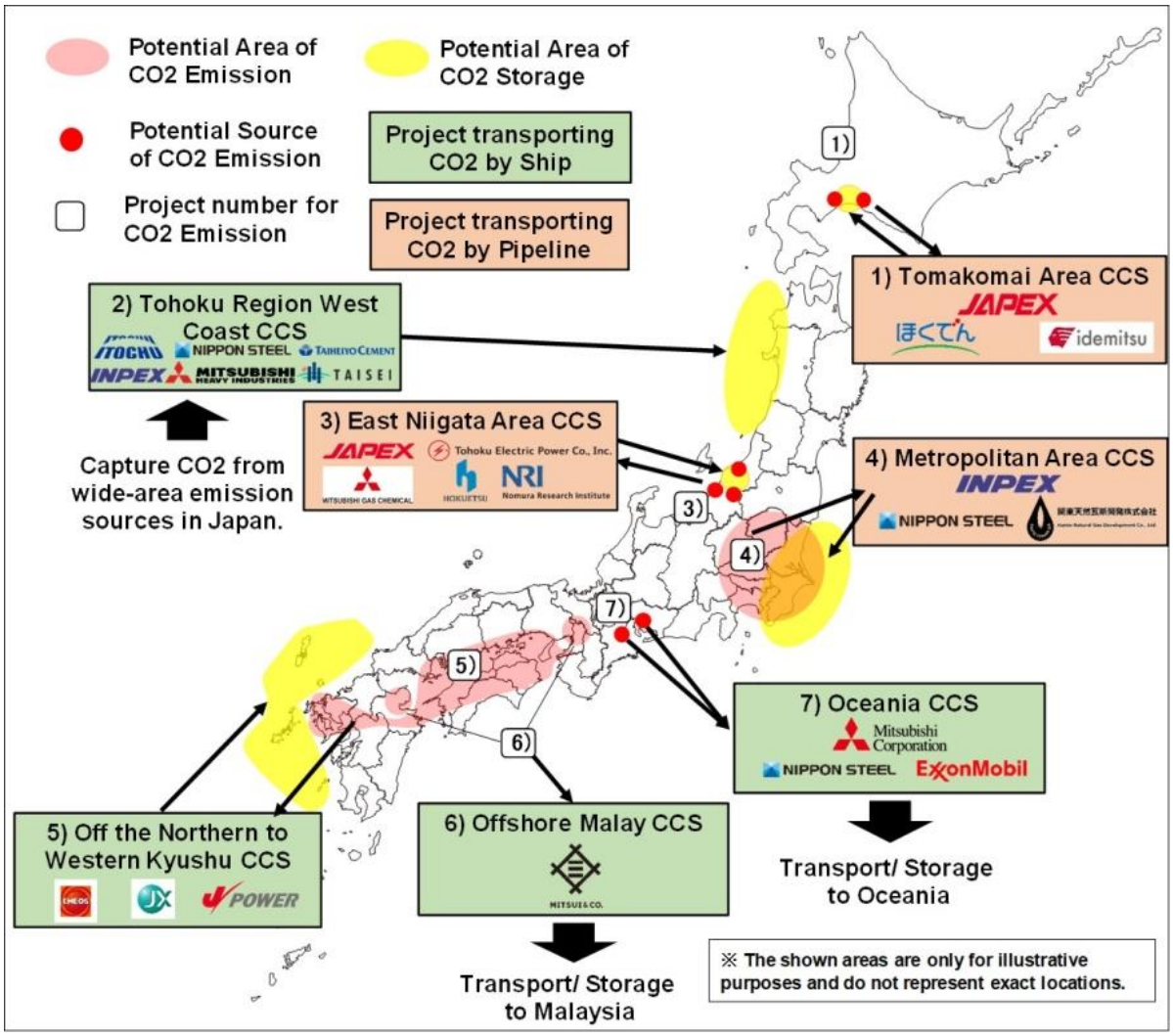

Figure 1.3 Location of 7 Japanese Advanced CCS Projects and companies proposed for each project. These projects will store approximately 13 Mtpa of CO2 in total (Jogmec report, 2023).

Overview of Selected Projects: The selected projects span various regions, including the Tomakomai Area, Tohoku Region West Coast, East Niigata Area, Metropolitan Area, and Northern to Western Kyushu (Tanaka et al., 2017; Ma et al., 2022). Additionally, there is an offshore project in the Malay region. These projects represent a diverse geographical spread, indicating Japan's commitment to exploring a variety of potential CCS sites, as in Table 1.1.

Table 1.1 Overview of Selected Projects (Listed from North to South)

Project	Company	Area of CO2 Storage	CO2 Storage Volume	CO2 Emission Source
Tomakomai Area CCS	JAPEX, Idemitsu Kosan Co.,Ltd., Hokkaido Electric Power Co.	Tomakomai Area	~1.5 Mtpa	Oil refinery, Electric power plant in Tomakomai Area
Tohoku Region West Coast CCS	ITOCHU Corporation, Nippon Steel Corporation, Taiheiyo Cement Corporation, Mitsubishi Heavy Industries, ITOCHU Oil Exploration Co., Ltd., INPEX Corporation, Taisei Corporation.	Tohoku Region West Coast.	~2 Mtpa	Wide-area of CO2 emission in Japan Steel plant, Cement plant, and Local emitter near CO2 storage
East Niigata Area CCS	JAPEX, Tohoku Electric Power Co., Mitsubishi Gas Chemical Company, Hokuetsu Corporation, Nomura Research Institute, Ltd.	Niigata Prefecture	~1.5 Mtpa	Chemical plant, Pulp mill, Electric power plant in Niigata prefecture
Metropolitan Area CCS	INPEX Corporation, Nippon Steel Corporation, Kanto Natural Gas Development.	Metropolitan Area.	~1 Mtpa	Multiple industries, including Steel plants in the Metropolitan Area
Off the Northern to Western Kyushu CCS	ENEOS Corporation, JX Nippon Oil & Gas Corporation, Electric Power Development, Ltd.	Off the Northern to Western in Kyushu	~3 Mtpa	CO2 emission in Setouchi / Kyushu region Oil refinery, Electric power plant in West Japan
Offshore Malay CCS	Mitsui & Co., Ltd.	The offshore east coast of the Malay peninsula in Malaysia	~2 Mtpa	Multiple industries, including Chemical/ Oil refinery in Kinki/ Kyushu.
Oceania CCS	Mitsubishi Corporation, Nippon Steel Corporation, ExxonMobil Asia Pacific Pte. Ltd.	Oceania	~ 2 Mtpa	Multiple industries, including steel plants, are in the Chubu region.

Legal Framework for CCS: Recognizing the importance of a supportive regulatory environment, Japan's industry ministry is working on establishing a legal framework for carbon capture and storage. This framework is essential for enabling companies to commence the underground storage of carbon dioxide, ensuring that CCS projects operate within a clear and stable regulatory context (Yanagi and Nakamura, 2020).

National Strategy for CCS: Japan's commitment to CCS is embedded in its broader national strategy to address climate change. The country, highly dependent on fossil fuels for energy production, recognizes CCS as a pivotal technology to reduce emissions while maintaining economic stability. Japan's strategy reflects a pragmatic approach to balancing its industrial needs with environmental commitments.

Research and Development (R&D) Investments: Japan has invested substantially in R&D for advancing CCS technologies. This includes developing more efficient and cost-effective methods of CO2 capture, improving the safety and reliability of CO2 transport and storage, and exploring new materials and technologies that could revolutionize the CCS process. These efforts are critical in reducing the overall costs of CCS, making it a more viable option for widespread adoption.

In addition, JOGMEC will develop not only domestic CCS projects but also CCS projects with overseas storage, mainly in Asia and Oceania, which might lead to decarbonization throughout the region. In this way, Japan will seek to achieve approximately 120 to 240 Mtpa of CO2 storage by 2050, eventually contributing to the stable supply of energy resources and carbon neutrality in Japan (Page et al., 2020; Al Ghafri et al., 2023).

1.3. Geophysical Techniques for CCS

In the context of CCS, the significance of geophysics is paramount and extends across the entire spectrum of a CCS project, from the initial stages of site selection to the final stages of post-closure monitoring. Geophysical surveys, primarily seismic methods, initiate the process by identifying and delineating suitable storage sites for CO2 containment. These surveys provide detailed information on the geological structures, including the depth, size, and structural integrity of potential storage reservoirs, as well as the properties of the overlying caprock. This information is critical for ensuring the safe and effective containment of CO2. As a CCS site becomes operational, geophysical methodologies, especially 4D seismic monitoring, become central to the monitoring process. This advanced technology provides dynamic, high-resolution subsurface images, enabling the tracking of the CO2 plume over time to ensure its expected behavior and confinement within predetermined boundaries, thereby preventing any leakage or unintended migration.

In addition to seismic methods, the application of electrical and electromagnetic techniques, including Electrical Resistivity Tomography (ERT) and Induced Polarization (IP), augment the monitoring efforts by identifying changes in subsurface electrical properties indicative of CO2 presence (Caesary et al., 2020). These findings are further enhanced by microseismic monitoring, which is capable of detecting subtle seismic activities suggesting rock movements or fractures, and gravity surveys, which are instrumental in monitoring density variations associated with CO2 injection. The role of acoustic monitoring, both downhole and at the surface, is also noteworthy, providing continuous, real-time data on the physical state of the storage site, crucial for early detection of potential issues such as caprock integrity breaches or leakage.

Furthermore, the integration of well-logging into the monitoring framework is invaluable. Well, logging involves deploying tools into boreholes to measure a variety of properties surrounding geological formations, thereby facilitating a thorough characterization of potential storage sites and continual monitoring of the CO2 within the storage reservoir.

The incorporation of satellite remote sensing into the monitoring strategy offers a broader perspective, enabling the observation of surface conditions that might reflect subsurface changes or leakages. In this array of technologies, InSAR (Interferometric Synthetic Aperture Radar) stands out for its ability to detect minute changes in the Earth's surface, providing indirect yet valuable insights into the behavior of the subsurface CO2 plume (Sweatman et al., 2010; Yang et al., 2015).

In conclusion, the array of geophysical techniques utilized in CCS is comprehensive and indispensable throughout the entire lifecycle of a CCS project. From the initial assessments and site selection to the operational monitoring and final verification stages, these methods collectively ensure the effectiveness, safety, and environmental compliance of CO2 storage. The synergistic application of these techniques offers a thorough approach to CCS monitoring, underlining their critical role in global climate change mitigation efforts.

Among the array of geophysical techniques for CCS monitoring, 4D seismic monitoring often stands out as one of the most effective (Jenkins et al., 2015; Grandi et al., 2017). Its high-resolution, subsurface imaging capability allows for precise mapping of the CO2 plume within the storage reservoir, which is crucial for understanding the behavior of the injected CO2. The temporal dimension of 4D seismic monitoring is essential for tracking changes during the CO2 injection and storage process, aiding in the early detection of potential issues like leakage or unexpected migration. This technology also ensures the safety and integrity of the storage site by providing detailed information on the CO2 plume and surrounding geological formations. Its comprehensive coverage is particularly beneficial for large-scale CCS projects, and its ability to be integrated with other monitoring techniques, such as logging, microseismic monitoring, and satellite remote sensing, enhances the overall monitoring solution. However, it's important to note that the suitability and feasibility of 4D seismic technology for a specific CCS project depend on various factors, including the project's scale, the characteristics of the storage site, and budgetary considerations.

1.4. Challenges and Innovations

Seismic acquisition must contend with environmental issues, the cost of data acquisition, and the need for high-resolution data. Innovations continue to focus on reducing the environmental impact and improving the quality and efficiency of seismic data acquisition. This includes the development of low-impact seismic sources, more sensitive and broadband sensors, advanced data analytics, and integrating seismic data with other geophysical and geological data. The seismic industry is also increasingly focused on developing methods to monitor reservoirs over time (4D seismic) and to image complex subsurface features, such as in areas with salt diapirs or subsalt formations(Lumley, 2010).

In summary, while 4D seismic monitoring is a powerful tool for monitoring Carbon Capture and Storage (CCS) projects, it does come with several challenges:

1. **High Costs**: One of the primary challenges of 4D seismic monitoring is the cost. Conducting seismic surveys, particularly 3D and 4D, is expensive due to the need for specialized equipment and skilled personnel. The cost can be especially prohibitive for smaller projects or in the early stages of site exploration and assessment.

2. **Complex Data Analysis**: The data obtained from 4D seismic surveys is complex and requires sophisticated analysis. Interpreting seismic data to track the movement and distribution of CO2 accurately requires advanced computational tools and expertise in geophysics and geology. This complexity can pose a challenge in terms of both the resources needed for analysis and the potential for misinterpretation of data.

3. **Temporal Resolution**: While 4D seismic monitoring provides an excellent spatial resolution, its temporal resolution can be limited. The time interval between successive seismic surveys is often governed by budgetary and logistical constraints, which might result in less frequent data and potentially miss rapid changes in the subsurface.

4. **Environmental and Regulatory Concerns**: Seismic surveys, especially those involving air guns or other loud sources, can have environmental impacts, such as disturbing marine life. These concerns can lead to regulatory challenges and the need for environmental impact assessments, which can add to the complexity and cost of the projects.

Additionally, there is a push to use seismic data not only for hydrocarbon exploration but also for carbon capture and storage (CCS) projects, geothermal energy exploration, and understanding the mechanics of earthquakes. As the demand for energy changes and environmental concerns become more pressing, seismic acquisition technologies and methods will continue to evolve, shaped by the need for more precise imaging with a reduced ecological footprint.

The Accurately Controlled Routinely Operated Signal System (ACROSS), first set up in 1996 in Japan, is a method for monitoring the Earth's subsurface (Yamaoka et al., 2001). It uses a motor to create controlled rotations timed with a GPS clock, ensuring it stays in sync with seismic stations that also use GPS for timing (Figure 1.4). This synchronization allows for coordinated monitoring over large distances. Starting in January 2000, the system was used on Awaji Island to monitor the ground for over a year. It successfully detected changes in the ground's seismic velocity, likely due to groundwater movement, especially after the area experienced strong earthquakes. These changes were observed as a temporary slowing down and then a gradual return to average speeds of seismic waves traveling through the ground (Yamaoka et al., 2001). The study showed that signals from this monitoring system could travel about 80 kilometers (as shown in Figure 1.5) to land-based seismometers and over 10 kilometers to sensors on the sea floor. Data from the sea floor sensors can be analyzed in real-time, which is particularly useful for detecting sudden changes, like potential CO2 leaks from reservoirs (Tsuji et al., 2021).

Figure 1.4 ACROSS source used in a previous study. Eccentric weights rotate around a horizontal axis to produce a sinusoidal signal (Suzuki et al., 2021; Yamaoka et al., 2014).

Using large active-source seismic systems like the ACROSS system in mountainous regions poses significant challenges. The rugged terrain restricts where you can place the equipment and limits the coverage for collecting seismic data. This often results in images of the subsurface lacking detail because we can't get as many data points as needed for high-resolution mapping. A compact and easily transportable system, the Portable Active Seismic Source (PASS) (Tsuji et al., 2022)., has been developed to overcome the challenges.

This system can be set up in various locations, even in rugged terrain, generating consistent and repetitive seismic signals across a broad spectrum of frequencies. This allows for increased source points, enhancing the ability to collect high-resolution seismic data in challenging environments.

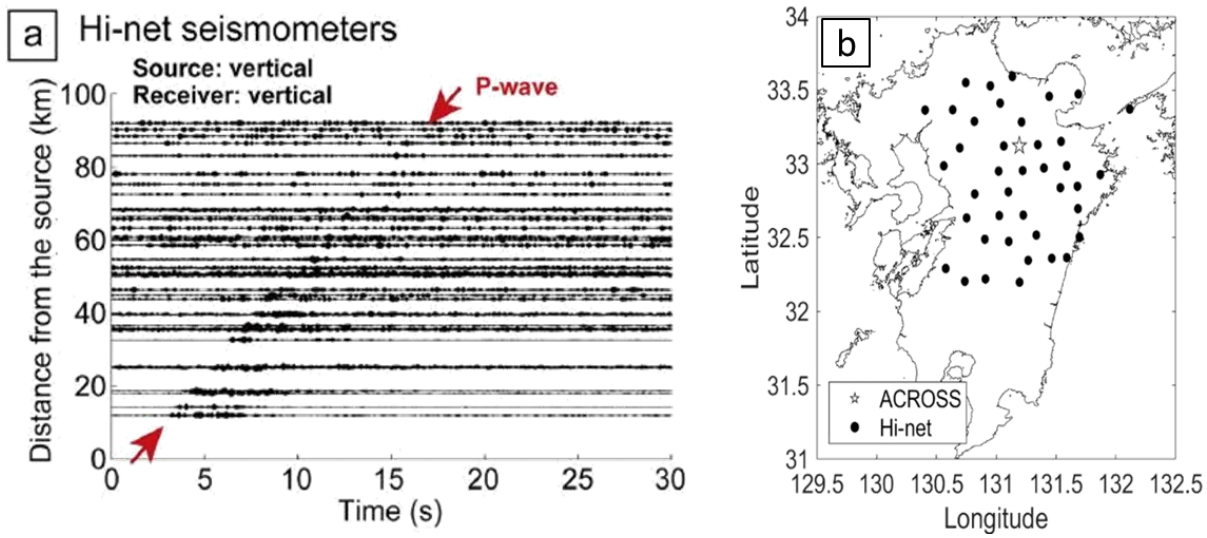

Figure 1. 5 Signal propagation from the continuous source system. (a) Transfer functions from the vertical source motion and the vertical component of Hi-net seismometers with two months of stacking. (b) Locations of the ACROSS source system and Hi-net seismometers in the Kuju geothermal field of Kyushu, southwest Japan (Tsuji et al., 2021).

Continuous monitoring systems in seismic exploration generate big amounts of data, which can be pretty challenging to manage and understand compared to data from traditional methods. This data is not just significant in quantity; it also keeps flowing, needing ongoing analysis, which can be time-consuming and expensive. To manage this flood of data, companies might need to use better data storage and management systems, like cloud services, that can grow with their needs while keeping data safe and sound. To process and analyze all this information, they'll need powerful computers and ways to process data in parallel to work through the data quickly, which would take time with regular computers.

Also, machine learning and artificial intelligence can make interpreting this data faster and possibly more accurate. These technologies can sort through the data automatically to find essential patterns, doing a job in moments that would take people much longer. These systems can quickly spot changes and give instant updates, necessary for keeping an eye on natural hazards, managing resources, or watching over the environment.

1.5. Objective and Approach

The objective of this dissertation is to develop a practical solution to the challenges encountered in processing continuous and big seismic data acquired through the monitoring and interpretation phases, particularly in the context of CCS future processing tools. The challenges identified and addressed in this study are twofold: firstly, those related to acquisition, such as cost, temporal resolution, and surface accessibility, and secondly, issues concerning data analysis, including the complexity of interpretation of large datasets.

This thesis, therefore, explores the processing of an innovative seismic source: a portable, active seismic system that addresses the acquisition challenges but simultaneously yields continuous and voluminous seismic data. In response to this, the dissertation also delves into pioneering techniques for managing and analyzing this big data, employing advanced artificial intelligence (AI) tools. This study contrasts the results derived from AI analysis with those from traditional analytical methods, emphasizing the efficiency and accuracy of AI in handling complex seismic datasets.

The focus on processing for unconventional seismic sources is a crucial aspect of this research. These low-impact sources, including non-explosive and low-energy options, significantly reduce environmental impacts and are viable in ecologically sensitive areas where traditional methods are not feasible. The ability of these sources to enable continuous or semi-continuous seismic monitoring is invaluable for real-time or near-real-time data acquisition. Such a feature is essential for CCS, as it facilitates precise tracking of CO2 movement and ensures the integrity of the storage site. However, the resulting large data volumes pose a new set of analytical challenges.

In addressing these challenges, the dissertation evaluates AI techniques applied to similar seismic data scenarios. While many researchers have utilized numerical attributes for AI predictions in petrophysical studies, this dissertation identifies a gap in the existing literature (Bugge et al., 2018; Zhao, 2018; Puzyrev and Elders, 2020; Wu et al., 2020; Zhang et al., 2020, 2021); however, the computational time involved in preparing seismic attributes, which is a critical factor for continuous and extensive seismic data in long-term CCS project monitoring with high temporal resolution.

The dissertation thus introduces a novel approach to Advanced Techniques for Continuous and Big Seismic Data Analysis, empowered by AI and Unconventional Seismic Sources. For the unconventional sources, a Low-Impact Continuous Source is employed, particularly suited to CCS monitoring. These sources underwent extensive field testing to evaluate their efficacy. An advanced AI technique was developed, utilizing a neural network for the analysis of continuous passive seismic sources and the interpretation of extensive 3D seismic data cubes. Through these methodologies, the research posits a promising pathway to safely and accurately monitor CCS projects using AI and unconventional seismic sources, offering significant improvements over traditional seismic monitoring approaches.

1.6. Thesis Structure

The research flow of this dissertation is summarized in Figure 1.6. This dissertation consists of five chapters as follows.

Chapter 2: This chapter describes the general background of the dissertation, with a brief review of acquisition technologies, emphasizing their pivotal role in geophysical exploration across various sectors, including oil, gas, and renewable energy.

Chapter 3: This chapter introduces the Portable Active Seismic Source systems, a breakthrough in continuous seismic survey methods optimized for carbon capture and storage (CCS) projects. It highlights PASS's superiority in addressing everyday challenges in seismic monitoring and its field-tested effectiveness in detecting subsurface waves.

Chapter 4: This chapter discusses the application of CNN in interpreting seismic data for slump fault systems in plate subduction zones in Japan and predicting chimneys in the Mediterranean Sea, Egypt. This approach demonstrates improved accuracy and efficiency in seismic interpretation, with potential applications in identifying various geological features, including gas reservoirs.

Chapter 5: This chapter explores the application of neural networks, particularly CNNs, in traffic monitoring using seismic data. This method showcases significant advantages in data efficiency and operational simplicity, overcoming the limitations of traditional traffic monitoring systems.

Chapter 6: This chapter presents the conclusions of the dissertation, which includes a summary of the conclusions made in preceding chapters and future directions.

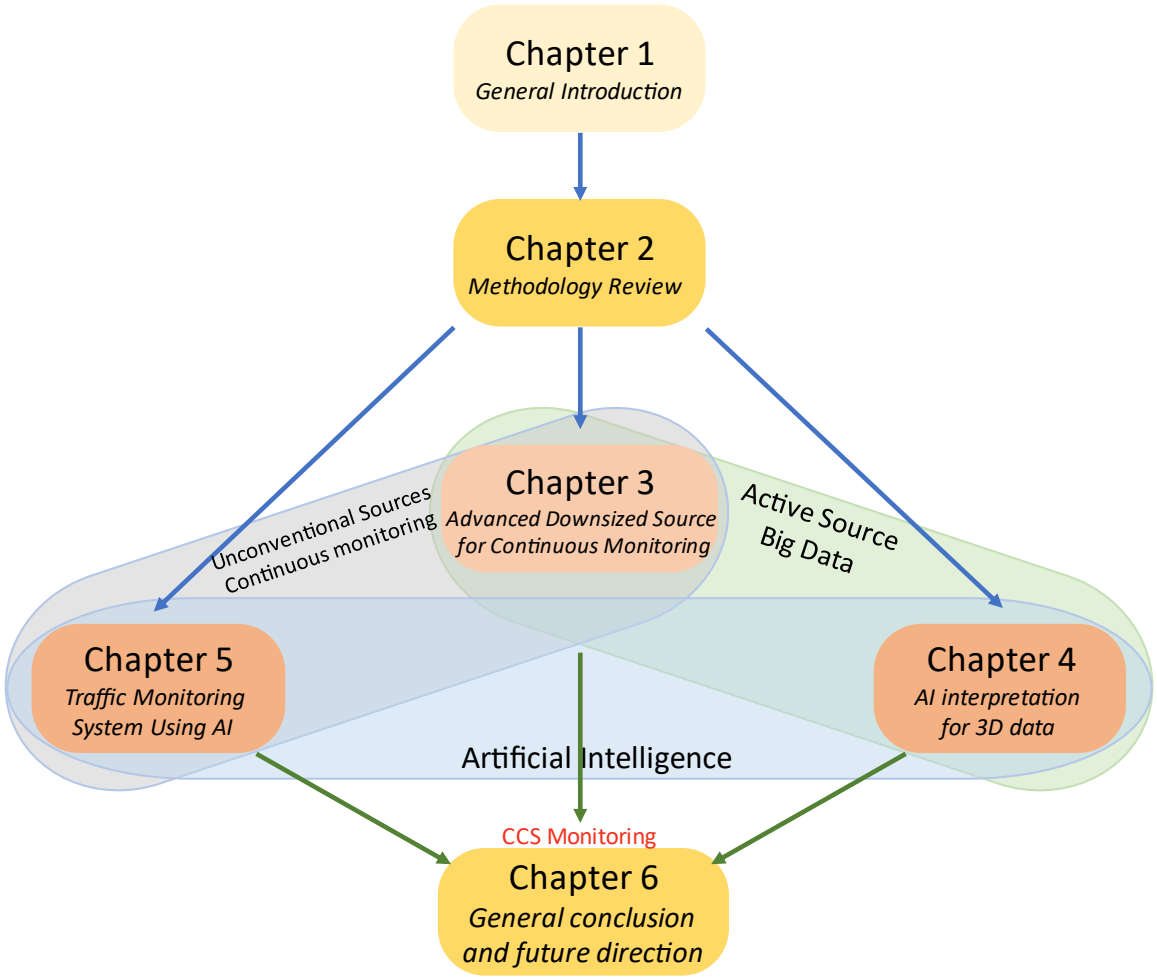

Figure 1. 6 Research flow of this dissertation.

Chapter 2

Methodology Review

2.1. Seismic acquisition

Seismic acquisition stands as a fundamental technique in the realm of geophysical exploration. It is particularly prominent within the oil and gas sector, but its importance extends to various disciplines, including geotechnical investigations and exploring geothermal energy sources. The method involves generating seismic waves that travel through the Earth's subsurface, which are then captured upon reflection by a series of sensors. These sensors record the nuances of the waves' journey—how they've been altered by the rock, fluid, and gas layers they've encountered. This recorded data is a sonic blueprint of the Earth's subsurface architecture, revealing the hidden stratigraphy, structure, and material properties beneath our feet. This information is invaluable in the hunt for oil and gas, as it directs explorers to the most promising reservoirs while helping to sidestep geological hazards that could complicate or endanger drilling operations. Beyond the energy sector, seismic acquisition plays a pivotal role in constructing the Earth's subsurface models for infrastructure projects, helping to predict the ground conditions for tunnels, foundations, and other civil engineering works. Similarly, in the search for geothermal energy—a growing field as the world seeks sustainable energy sources—seismology guides us to the hotspots where the Earth's heat is accessible and can be harnessed for power (Dziewonski and Anderson, 1984).

The art and science of seismic acquisition have evolved dramatically over the decades. The process now encompasses sophisticated technology to produce ever-clearer images of the subsurface. From the seismic sources that provide the energy pulse, whether controlled explosions or the more environmentally friendly Vibroseis, to the geophones and hydrophones that detect the faintest echoes from below, the equipment is continually refined for better precision and lower environmental impact (Gadallah and Fisher, 2008).

Data processing and interpretation have kept pace with these technological strides, employing complex algorithms and supercomputing power to translate raw data into three-dimensional visualizations of the subsurface.

These interpretations can then inform critical decisions, whether it's where to place a well, how to build a tunnel, or where to locate a geothermal plant. The seismic acquisition process sheds light on the immediate practicalities of industrial projects and feeds into the broader scientific understanding of geology and tectonics, offering snapshots of Earth's interior that are otherwise inaccessible (Council, 2001). The field's dynamism ensures that it will continue to adapt and innovate, embracing new technologies and computational methods to meet the dual demands of resource discovery and environmental stewardship.

The seismic acquisition process is a comprehensive and carefully coordinated set of procedures designed to map and interpret the Earth's subsurface structures. The entire process is outlined in a sequence of steps that ensure the acquisition of seismic data (Yilmaz, 2001b):

Planning: Before carrying out seismic surveys, extensive planning is required. This includes selecting the appropriate survey design that considers the target depth, resolution required, the geological complexity of the area, and the acquisition budget.

Surveying: Accurate positioning of the source points and receivers is critical. Land surveys involve physical surveys, while marine surveys use GPS and other navigational tools.

Data Acquisition: In this phase, seismic sources are activated at specific locations, and the response is recorded across a spread of receivers. This is controlled to ensure that the resulting data is high quality and spatially accurate.

Data Processing: The raw data is then processed to remove noise, enhance signal quality, and correctly position the subsurface reflectors. This step can be computationally intensive and requires sophisticated algorithms and software.

Interpretation: The final processed data is interpreted by geophysicists and geologists to understand the subsurface structure and composition.

Seismic sources are devices that generate controlled seismic energy. There are different types of land and marine environments(Parkes and Hatton, 1986).

Land Sources (onshore):

- **Dynamite**: One of the oldest methods involves detonating small charges in shallow holes. This provides a high-energy source capable of penetrating deep geological formations.
- **Vibroseis**: This source uses a large truck-mounted plate that vibrates on the ground to generate seismic waves over various frequencies, as appears in Figure 2.1a. It is safer and more environmentally friendly than dynamite.

Marine Sources (offshore):

- **Air Guns**: These are the most common marine sources and work by releasing high-pressure air into the water (Figure 2.1b). The rapid expansion of air bubbles creates acoustic energy.
- **Water Guns**: Like air guns, water is used instead of air to create a seismic pulse.

Other Sources: There are also non-explosive sources like weight dropping, electromechanical, and plasma sound sources with specific applications and characteristics.

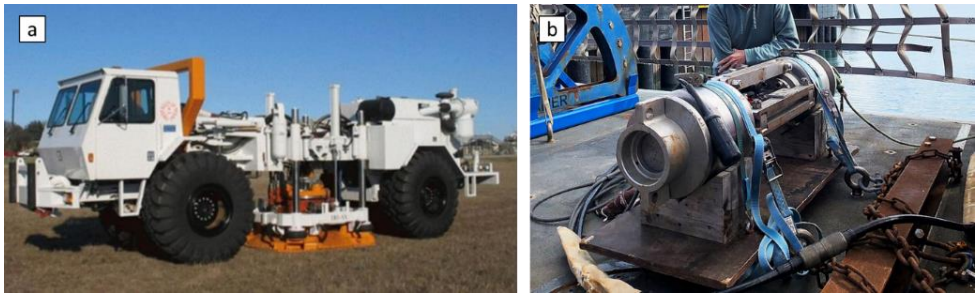

Figure 2.1 Shows some seismic sources, where (a) is a vibroseis while (b) is an 18-liter air gun seismic source.

Conventional seismic sources, especially those involving explosives, can have significant environmental impacts, including disturbance to wildlife and ecosystems. Consequently, there is an ongoing effort to develop sources that minimize these impacts while providing the necessary subsurface imaging capability (Binley et al., 2015; Zhang et al., 2019). Seismic acquisition is a field that is continually evolving with advancements in technology and data processing capabilities, leading to more efficient, accurate, and environmentally responsible methods to explore the Earth's subsurface.

2.1.1. Advanced Seismic Acquisition Techniques

The ultimate goal of seismic acquisition is to get the most precise possible picture of the subsurface geology. To achieve this, various advanced techniques and methodologies have been developed(Biondi, 2006; Gao, 2011):

- **3D Seismic**: Unlike traditional 2D seismic that provides a slice through the Earth, 3D seismic acquisition covers a grid of lines to produce a three-dimensional cube of data, offering a much more detailed view of the subsurface.
- **4D Seismic**: Also known as time-lapse seismic, 4D seismic involves repeating 3D seismic surveys over time to understand how a reservoir changes during oil and gas production. It was used in the Sleipner CCS project in Norway, as shown in Figure 2.2.
- **Multi-component Seismic**: Traditional seismic records only the vertical component of the wavefield. Multi-component seismic uses geophones that can also record horizontal wave movements, providing additional data that can be used to differentiate between fluid types and to characterize fractures and anisotropy in the rocks better.
- **High-Resolution Seismic**: This technique uses higher frequency seismic waves to provide a more detailed subsurface image, particularly useful for shallow-depth applications such as environmental studies and archaeology.

The quest for more precise and less intrusive seismic data collection has led to a significant evolution in seismic source technology. With the introduction of more advanced acquisition techniques, the innovation in seismic sources has aimed to enhance the quality of subsurface imaging while also striving to minimize environmental impacts. One of the notable advancements is the Vibroseis Sweep Optimization. Vibroseis trucks, which use large vibrating plates to send low-impact seismic waves into the Earth, have been refined to customize the frequency content of the vibrational sweep(Bouska, 2010). This customization means that the seismic waves can be fine-tuned to resonate with specific geological formations, enhancing the resolution of the seismic imaging and improving the penetration depth. Such targeted frequency sweeps are particularly beneficial when probing complex subsurface structures or seeking to improve the imaging for subtle geological features.

Array techniques represent another significant advancement in seismic source technology. Geophysicists can control the energy pattern emitted into the subsurface by employing multiple seismic sources and managing their firing sequence—simultaneously or with meticulously planned delays.

This approach results in a broader and more uniform energy distribution, leading to higher-quality data and more reliable imaging, as it mitigates the inconsistencies that single-source methods might produce (Mondol, 2010). Marine vibrator sources are at the forefront of current research and development, envisioned as the environmentally responsible successors to air guns. Unlike an air gun's sharp, explosive energy release, these devices are designed to provide a continuous, controlled seismic energy source.

The promise of marine vibrators is twofold: they are likely to reduce the acoustic shock to marine wildlife, addressing the environmental and regulatory concerns associated with traditional marine seismic sources, and they are also expected to generate a more consistent seismic signal, which could further refine the clarity and reliability of the data collected.

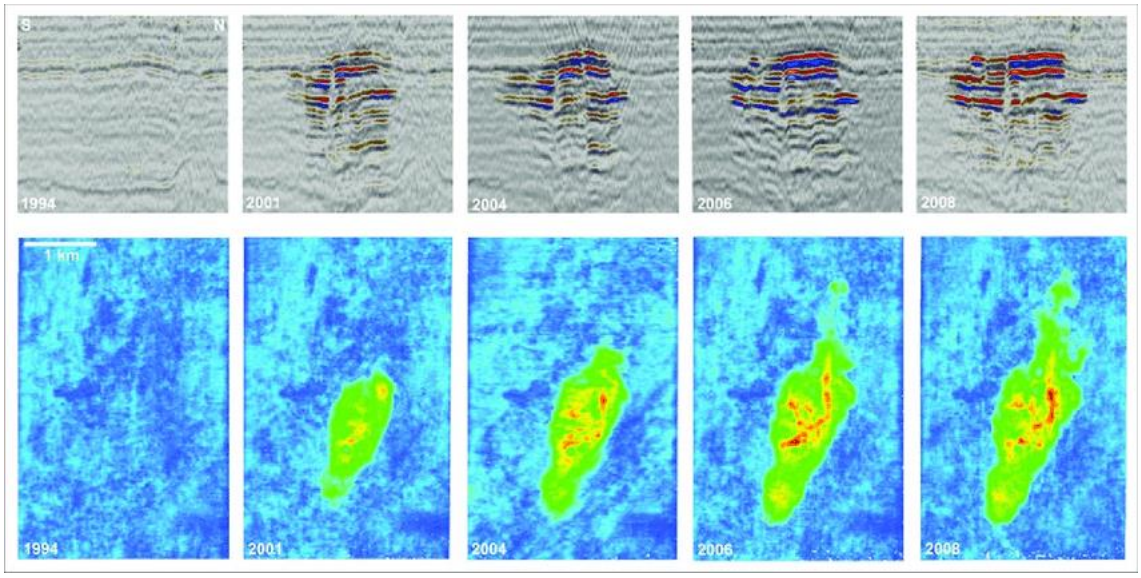

Figure 2.2 A selection of time-lapse seismic images of the Sleipner CO2 plume showing its evolution from 1994 (baseline) to 2008 (Jenkins et al., 2015).

2.1.2. Environmental Impact and Mitigation

The environmental footprint of seismic acquisition has come under increasing scrutiny as the world grows more conscious of the ecological impact of industrial activities. This heightened awareness has spurred the geophysical exploration industry to innovate and adopt practices that mitigate the impact on ecosystems (Jie et al., 2014; Naghizadeh et al., 2023).

Soft-start procedures exemplify one such mitigation practice, especially in marine seismic surveys. These procedures involve a gradual ramp-up of the seismic source's energy levels. The intent is to give oceanic fauna time to leave the vicinity before complete energy levels are reached, reducing the potential for harm or disruption to their natural behavior.

They complement operational adjustments like soft-starting a thorough environmental study. Before commencing seismic operations, companies are now more diligent in conducting extensive ecological impact assessments. These studies aim to understand the potential effects of seismic waves on the local ecosystems and to develop strategies that minimize ecological disturbances. The findings of these assessments can lead to adjustments in survey timings, locations, and techniques to lessen the environmental impact.

There's also a concerted effort in the industry to explore alternative energy sources for seismic acquisition. The goal is to find less intrusive methods that still provide the necessary subsurface images. One promising avenue is the development of marine vibrators, which promise a steadier and more controlled release of energy compared to traditional air guns. These devices could offer a less disruptive means of probing the subsurface, with the added benefit of producing a more consistent signal and improving data quality (Malehmir et al., 2012).

The seismic industry's response to environmental concerns involves procedural changes, extensive preparatory studies, and technological innovation. These efforts are vital for the sustainability of seismic exploration and maintaining the social license to operate in a world increasingly attentive to environmental stewardship.

2.1.3. The Future of Seismic Acquisition

The future of seismic acquisition lies in further reducing the environmental impact and increasing the resolution and efficiency of subsurface imaging. Innovations such as autonomous vehicles for deploying ocean-bottom nodes, machine learning algorithms for better data processing, and improvements in high-performance computing will continue to advance the field.

In essence, seismic acquisition and its associated technologies are in constant development, seeking to balance the need for resource exploration with the equally important requirement to protect our environment. Seismic acquisition, the backbone of subsurface geological exploration, has a rich history and a highly technical methodology that has evolved significantly over time. Here's a deeper look into its historical development and the intricacies of the acquisition process.

The genesis of seismic exploration can be traced back to the early 20th century, with Italian scientists probing into the enigmatic realm of earthquakes. These pioneers laid down the fundamental principles of seismology, which involved the generation of seismic waves and recording the time they took to reflect off subsurface geological layers. Initially, refraction methods dominated this exploration, well-suited to delineating large geological structures like sedimentary basins. But as the 1920s dawned, there was a paradigm shift towards reflection seismology, offering finer detail in subsurface imaging and proving particularly revelatory for oil and gas exploration. The mid-20th century saw seismic exploration breach the threshold into marine environments. The advent of air gun technology in the 1960s brought a seismic revolution, offering a reliable and controlled energy source that showed more consideration for marine life than the explosive methods of old. Yet, the '60s and '70s digital revolution truly transformed seismic acquisition.

The onset of digital recording brought unprecedented improvements in data quality and the interpretative prowess of geophysicists. This paved the way for three-dimensional seismic imaging in the 1980s, an innovation that soon became the linchpin of exploration efforts. As the 21st century approached, technological advances further refined seismic exploration.

Enhanced sensor technology, burgeoning computing power, and sophisticated signal processing algorithms have since propelled seismic imaging to new heights, delivering images of the subsurface with greater clarity and depth. These continual advancements promise to unravel the hidden geology beneath our feet and propel the industry toward safer and more efficient resource extraction, with seismic acquisition firmly at the helm of this ever-evolving journey (Freed, 2008; Hammond et al., 2019).

2.1.4. Detailed Seismic Acquisition Process

The seismic acquisition process is a meticulously crafted procedure that commences with an intricate design phase. In this stage, geophysicists meticulously plot out the survey, considering the extent of the area to be studied, the distribution of receivers across the terrain, the nature of the seismic source to be used, and the expected duration of the recording sessions. This planning may extend to creating sophisticated models to forecast the behavior of seismic waves within the geological context of the area. Once the plan is laid out, the seismic acquisition moves into its operational phase, strategically positioning sources and receivers—geophones on land or hydrophones in marine environments. On terra firm, geophones are arrayed in predetermined patterns, such as lines or grids, while seismic sources like Vibroseis trucks or controlled explosives are relocated as necessary to cover different survey points. In contrast, marine surveys involve streamers equipped with hydrophones, towed behind vessels, with air guns serving as the seismic source.

The core of the seismic acquisition is the data acquisition stage. The seismic source is triggered here, sending waves deep into the Earth's crust. The echoes of these waves, shaped and modulated by the geological strata they encounter, are captured by the array of receivers. The process is meticulously repeated to ensure comprehensive coverage and to establish data redundancy, which is critical for the reliability of the survey.

Next comes the pivotal phase of data processing. The initial raw data, often obscured by noise and complexity, transforms various filtering and signal enhancement processes. Techniques such as deconvolution, stacking, migration, and noise attenuation are applied to tease out a clearer picture from the gathered data.

Cutting-edge imaging methods like Full Waveform Inversion (FWI) and Reverse Time Migration (RTM) are harnessed to produce detailed visualizations of the subsurface(Qin et al., 2015). In the final interpretative phase, geoscientists step in to decipher the processed seismic data. They meticulously analyze the data to map subsurface structures and infer the composition of the Earth's layers, discerning the presence of different rock types and fluids.

In step with technological progress, modern seismic acquisition techniques have expanded the toolkit available to explorers and scientists. Ocean-bottom seismometers (OBS) offer a fresh perspective by resting on the seabed, thus enabling a unique vantage point to visualize complex geological formations. Wireless and node-based systems have introduced unprecedented flexibility, adapting to challenging land and marine terrains(Freed, 2008). Moreover, innovative survey strategies like multi-azimuth and wide-azimuth surveys capture seismic data from many angles, vastly improving the resolution of images in areas with intricate geological features. In sum, the seismic acquisition process has evolved into a sophisticated blend of science, technology, and strategy, all orchestrated to illuminate the enigmatic world beneath our feet, whether it's for extracting Earth's resources or understanding its hidden layers.

2.2. Passive seismic source

The seismic method can be divided into active seismic and passive seismic. Passive seismic uses background noise from natural events like earthquakes and oceanic microseism or artificial noise like urban traffic. Passive seismic usually focuses on low-frequency signals (0 – 20 Hz), sometimes called low-frequency seismology. Geophysicists record natural seismic energy from the Earth, such as microseisms (small, continuous vibrations), seismic noise, or the energy from distant earthquakes(Artman, 2006). Passive seismic monitoring is a non-intrusive method for studying the Earth's interior, harnessing naturally occurring seismic energy, as can be observed in the MS09 oil field (Figure 2.3).

This technique is primarily based on the continuous observation and analysis of seismic waves from various sources. Here are some detailed aspects of passive seismic sources and the monitoring process(Bohnhoff et al., 2010):

- **Seismic Noise and Ambient Vibrations:** Ambient seismic vibrations, often called seismic "noise," are generated by various natural and anthropogenic sources. This continuous vibration of the ground is typically low in amplitude but can be analyzed using sophisticated signal-processing techniques to infer subsurface properties.
- **Microseismic Events:** Microseismic events are minor seismic occurrences commonly associated with rock fracturing within the Earth's crust. These can be induced by natural processes or human activities, such as mining, reservoir injection, or withdrawal (e.g., water, oil, gas). Microseismic monitoring is crucial in tracking these events, which can inform us about changes in the subsurface stress field and potential geohazards.
- **Earthquakes:** Passive seismic methods include the analysis of waves generated by earthquakes, both local and distant. The waves generated by earthquakes can travel long distances and provide valuable data on the Earth's interior structure. Even the seismic waves from small, hardly felt earthquakes can be informative.
- **Seismic Interferometry:** One of the most exciting developments in passive seismic monitoring is seismic interferometry (Cheng et al., 2015). This technique uses the sensor's ambient noise to reconstruct the Earth's response to a virtual seismic source. It essentially turns random noise into a coherent signal that can be interpreted like active source data.
- **Array Deployments:** For effective passive seismic monitoring, seismic sensors (seismometers or geophones) are deployed over the area of interest. These arrays can cover anything from a small local area to a regional or continental scale. The array configuration and density affect the resolution and depth of the resulting seismic images.
- **Temporal Monitoring:** Because passive seismic can be conducted over extended periods, it is well-suited to temporal monitoring applications. By continuously recording the seismic noise over months or years, it is possible to detect and analyze changes in the subsurface over time. This is particularly valuable for monitoring geothermal reservoirs, supervising CO2 sequestration, or evaluating the health of hydrocarbon reservoirs.

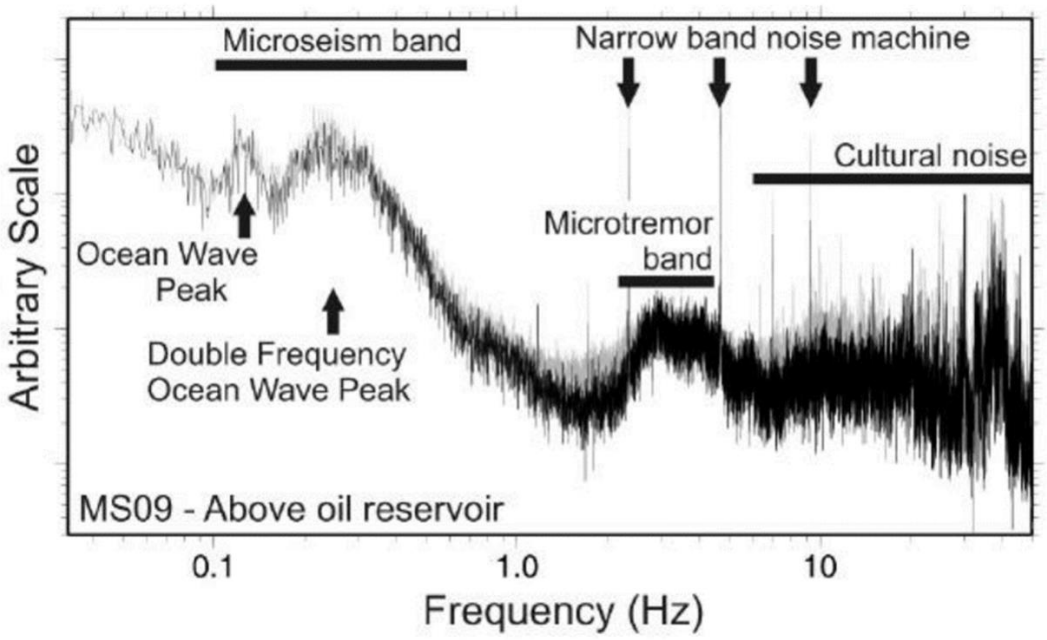

Figure 2.3 Typical spectra of ambient seismic vibrations recorded in a region with an oil reservoir in northeast Brazil (de Vasconcelos Lopes and Nunes, 2010).

However, one of the limitations is the reliance on sufficient natural seismic energy to penetrate and illuminate the subsurface structures of interest. In areas of low seismicity or for particular targets, the signal may not be strong enough to provide the desired information, necessitating active seismic methods to complement the data. Passive seismic monitoring continues to grow and evolve, with research focusing on improving data processing algorithms and sensor technology to maximize the information that can be gleaned from natural seismic vibrations.

2.3. AI for seismic

Deep learning is a subset of machine learning that relies on neural networks with many layers—hence the term "deep" (Figure 2.4). These deep neural networks engage in representation learning that can be guided by varying degrees of human supervision, from fully supervised to entirely unsupervised learning processes.

Architectures such as deep neural networks, deep belief networks, recurrent neural networks, and convolutional neural networks have significantly impacted various fields. In computer vision, speech recognition, natural language processing, and more, these deep learning models have achieved—and sometimes exceeded—human-level performance (Alam et al., 2020). The inspiration for artificial neural networks came from biological neural networks. However, artificial networks differ significantly; for instance, they are generally static and operate symbolically, while biological neural systems are dynamic and analog.

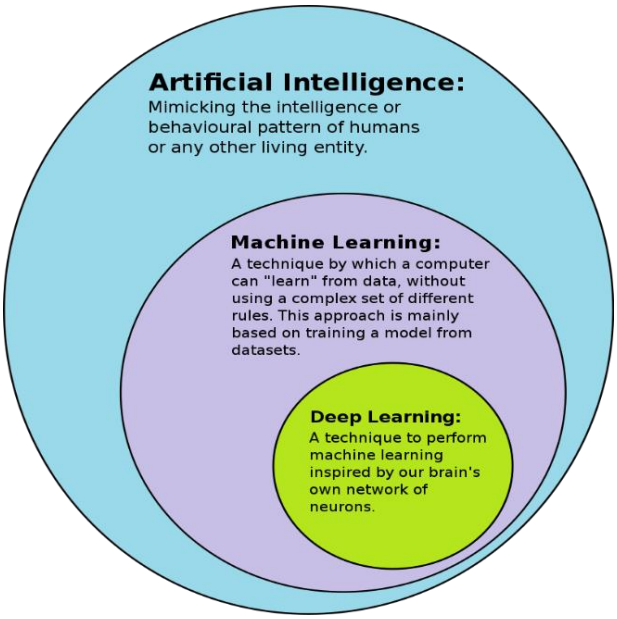

Figure 2.4 How deep learning is a subset of machine learning and how machine learning is a subset of AI.

The "deep" aspect of deep learning refers to the multiple processing layers that neural networks possess, which allows them to learn complex patterns. Early neural networks were limited by their inability to act as universal classifiers, but today's deep learning models overcome this with numerous layers that, while bounded in size, allow for practical application and effectiveness under certain conditions.

Deep learning models can also use layers that vary significantly from those in biological systems, enhancing efficiency, learnability, and clarity. Deep learning's impact on fields such as image recognition became particularly evident between 2011 and 2012, propelled by advances in GPU technology and neural network training methods like backpropagation.

Seismic signals are transient waves emitted by natural or artificial seismic events and can provide valuable information about the event source and the medium through which they travel. Seismic noise, on the other hand, refers to ground motion that doesn't match the desired seismic signal and is typically considered a nuisance. However, what constitutes "noise" can vary depending on the study's context, as sometimes these signals can offer valuable data for different seismic analysis applications (Bormann and Wielandt, 2013).

In an attempt to replicate human cognitive capabilities, artificial intelligence (AI) serves as a computational solution for addressing engineering challenges that prove challenging for conventional methods (Alavi and Gandomi, 2012). This fundamental aspect of AI has propelled advancements in seismology, particularly in dealing with extensive seismic data plagued by significant noise. The limitations of physics-based models, rooted in first principles, to define the intricate relationships within seismic data have sparked increased interest in AI in recent years (Li et al., 2018).

Applying an AI approach to data mining, processing, and analysis substantially enhances the precision and efficiency of earthquake detection, presenting exciting opportunities for the development of versatile seismic networks. These applications include detection and phase picking, early warning systems, ground-motion prediction, tomography, geodesy, and more.

AI offers an additional advantage over traditional methods by fostering increased computational efficiency in decision-making regarding earthquakes while reducing error rates (Azamathulla, 2013; Karbasi and Azamathulla, 2017). However, a limitation of AI methods lies in their sensitivity to parameters, especially when dealing with intricate experimental datasets. An effective strategy to address this challenge involves the use of robust optimization algorithms, such as genetic algorithms, particle swarm optimization, or Tabu search, for optimal control of AI method parameters.

Chapter 3

Advanced Downsized Active Seismic Source for Continuous Monitoring

3.1. Introduction

Reducing CO2 emissions using Carbon Capture and Storage (CCS) is becoming feasible and affordable (Haszeldine, 2009; Boot-Handford et al., 2014). The primary goal is to store the CO2 trapped deep beneath the geological formations securely. We require a vast global network of storage facilities to use CCS to reduce our carbon footprint (IEA, 2020). Most CCS projects are expected to decline around one million tons of CO2 annually. However, Managing scattered CO2 injection fields efficiently at low cost is challenging, so having a low-cost monitoring system is essential. The monitoring system should perform multiple vital tasks, including early detection of possible CO2 leaks, optimization of storage site operations through comprehension of CO2 movement and pressure, and—above all—minimization of the risk of any disruptions resulting from the CO2 injection-induced earthquakes (Chhun and Tsuji, 2020). Trustworthy monitoring data greatly influence public opinion and highlight how essential accurate and consistent field supervision is (Rock et al., 2017).

Monitoring subsurface formations is essential for general safety and controlling CO2 storage. This includes monitoring subterranean water sources, forecasting natural calamities like earthquakes, and assessing infrastructure stability. A common seismic approach for monitoring called "time-lapse" refers to the methodical tracking of changes over time within a particular area (Lumley, 2001; Furre et al., 2017). Typically, these surveys track spatiotemporal variations in seismic velocity to delineate temporal and spatial shifts in pore pressure or gas/fluid saturation (White, 2013). Consequently, temporal changes in seismic reflection characteristics permit assessing the spatial distribution of injected CO2 (Furre et al., 2017; Rock et al., 2017).

Time-lapse techniques have garnered significant attention in the Carbon Capture and Storage (CCS) realm. Noteworthy projects that have employed these techniques include the Weyburn-Midale and Quest endeavors in Canada, the In Salah project in Algeria, and the Sleipnir project off the coast of Norway (White, 2013; Furre et al., 2017; Rock et al., 2017). Additionally, smaller-scale CCS projects, such as Tomakomai in Japan, Ketzin in Germany, and Otway in Australia, also provide valuable lessons in this discussion (Whittaker et al., 2011; Steeper, 2013). Collectively, these objectives contribute to a comprehensive understanding of time-lapse phenomena under various circumstances. However, traditional time-lapse seismic monitoring, often constrained by budgetary considerations, tends to occur at overly extended intervals. This restriction affects the quick detection of significant changes in the reservoir, like CO2 leakage. To address this problem, I have developed a continuous monitoring approach that quickly identifies changes in seismic velocity, providing immediate information on reservoir changes (Lumley, 2001).

The Portable Active Seismic Source (PASS) system is a cost-effective, smaller-sized evolution of the Accurately Controlled Routinely Operated Signal System (ACROSS) shown in Figure 1.4 (Yamaoka et al., 2014). It maintains the core functions of ACROSS but is more accessible and versatile due to its reduced size and cost (Tsuji et al., 2020; Tsuji et al., 2021). A main feature of the PASS system is its ability to enhance the signal-to-noise ratio by stacking multiple signals. This systematic combination and processing allow for precise exploration and monitoring, even in remote locations. The PASS generates a signal by rotating an eccentric mass on a motor's axis. However, the PASS system's deployment on the surface poses challenges due to its sensitivity to various environmental factors such as rain, groundwater level fluctuation, and extreme temperature changes (Tsuji et al., 2022). A solution to this challenge is the sub-surface installation of the system, which has been shown to reduce its susceptibility to these disturbances.

Researchers are increasingly interested in using the attenuation of early seismic waves, known as first breaks, to analyze the density and thickness of underground layers. These waves are the initial ones that reflect the surface to determine the density of underground layers (Kim et al., 2004; Mok et al., 2016). For example, a study at Liso Field in Nigeria utilized an uphole seismic survey, where dynamite explosions within boreholes generated seismic signals (Adeoti et al., 2013). Such uphole surveys have become increasingly valuable for identifying the characteristics of the weathered surface layer and the deeper, consolidated geological strata. However, using dynamite as a seismic source in boreholes could significantly damage the borehole casing. While effective in generating seismic waves for subsurface exploration, this method carries the risk of harming the structure.

Conversely, cross-hole seismic surveying is a method that measures how fast seismic waves travel between boreholes to study underground layers. Seismic waves are created in one hole and picked up by sensors in nearby holes. Seismic velocity, calculated from the travel time of seismic waves, is essential for understanding Earth's subsurface geology (Wong et al., 1983). In this technique, one borehole acts as the seismic energy's origin point, while adjacent boreholes serve as detectors for the seismic waves. This differs from uphole processes, where surface geophones are employed, as illustrated in Figure 3.1. Cross-hole surveying is a potent modality for meticulous subsurface examination, especially when there's a demand for high-definition data (Mari et al., 2018).

In conjunction with other seismic methodologies like reflection and refraction surveys, this technique furnishes comprehensive perspectives on subsurface geology and its properties. If the vibration energy of the borehole PASS is high, the long distance between the two boreholes is possible.

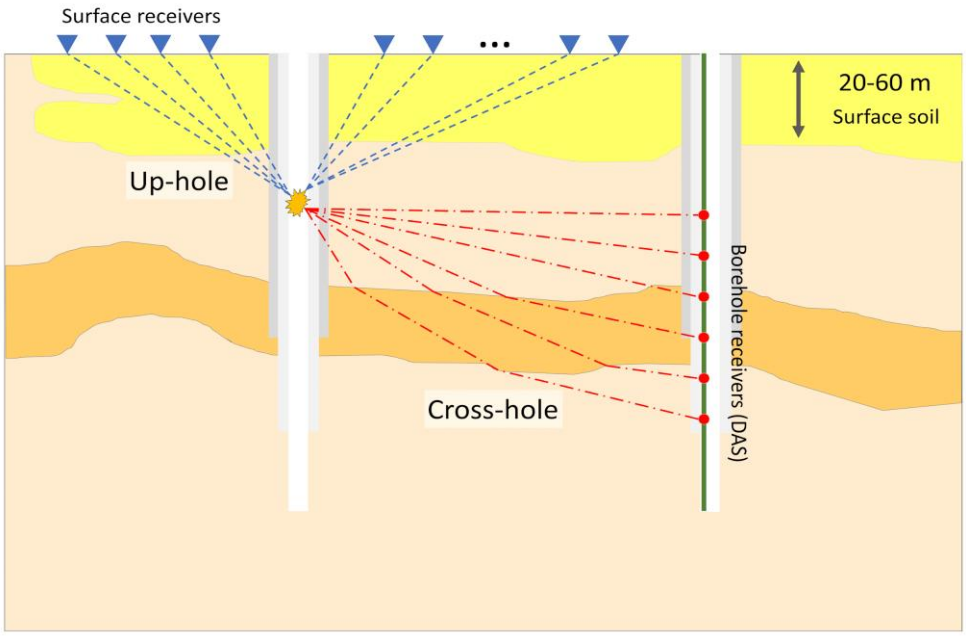

Figure 3.1 Schematic images of uphole and cross-hole seismic surveys depicting seismic sources at the surface and geophones positioned in boreholes. Seismic waves are generated in one borehole and detected in another (Ahmad et al., submitted).

Borehole surveys are becoming increasingly popular for understanding the subsurface geology in high spatial resolution. More than just determining structural properties, these surveys are also helpful at identifying fluid content within layers—a crucial insight for endeavors like water management and hydrocarbon exploration. However, Borehole surveys have some challenges, notably the high operational expenses and the need for seismic sources with a negative environmental impact. Most borehole sources use a well-anchored mechanical (like hammer-anvil), electromechanical source, or open-hole explosion (Cutler, 1998; Crane et al., 2013; Vergniault and Mari, 2020). Yet, the use of borehole seismic surveys remains sporadic, especially for monitoring tasks. Their ability to offer enhanced image clarity has boosted their reputation for time-lapse monitoring.

On the other hand, The generation of shear waves requires forceful mechanical movement, which can induce stresses that risk damaging the structural casing of the borehole. Implementing a strong shear wave (S-wave) source within a borehole while ensuring the casing remains undamaged presents a significant challenge for borehole surveys (Vergniault and Mari, 2020).

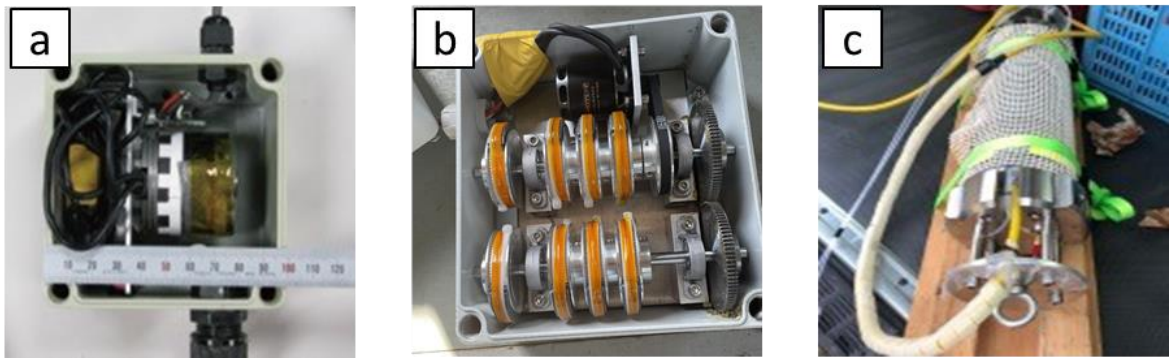

Figure 3.2 illustrates a comparison of the sizes of three continuous systems in this chapter. (a) A photograph showcases the PASS, which measures approximately 10 cm container (Tsuji et al., 2022). In (b), an image of the HE-PASS system with a compact size of 15 cm. (c), The borehole PASS design is displayed.

In this chapter, I have taken the foundational concepts of the Portable Active Seismic Source (PASS) system and reimagined it to create a specialized Active Seismic Source used for surface and borehole deployment. I will introduce results for 2 advanced designs of PASSs, as shown in Figure 3.2. The original PASS with a 4-cm motor (10-cm container), which was previously introduced by Tsuji in 2021, and the High Energy-PASS system is meant to be used on the surface, while the Borehole-PASS is designed to be used in the borehole. To simplify the PASS system, a geophone close to the PASS (Figure 3.3) is used to record the signal as the source function. The transfer function is calculated based on a cross-coherence approach (Nakata et al., 2011) for the chirp source and recorded waveforms to obtain the source signal.

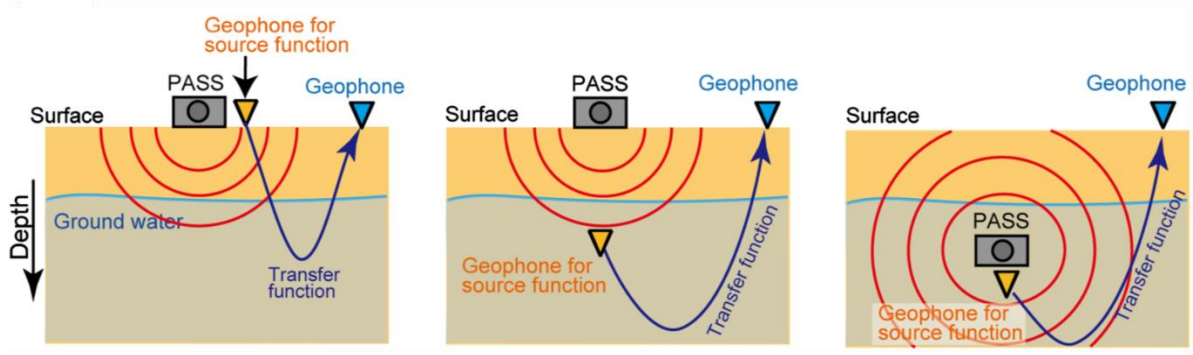

Figure 3.3 A conceptual image of the PASS and geophone deployments. Both yellow and blue triangles represent geophones; the yellow geophone is used to derive source functions and the transfer function (blue arrow) between the source wave and the data recorded by the blue geophone (Tsuji et al., 2022).

Here, I report the specifications of the advanced PASS system and the results of field experiments in a multi-field experiment. I coupled the PASS system with a distributed acoustic sensing (DAS) network based on fiber-optic cables that enabled us to acquire signals in a dense receiver array. On the other hand, the B-PASS system is engineered to address the challenges of surface noise. It is specifically designed to avoid damaging the borehole casing during the long term. I propose two multi-PASS configurations, each based on unique force orientations: vertical and horizontal. I aim to study how each setup influences signal spread and evaluate the B-PASS system's stability across different frequencies and depths in real-world conditions. Notably, the B-PASS system expertly navigates challenges posed by weathered layers, water level disturbances, and surface interferences—factors on the source function that have traditionally hindered the accuracy of seismic surveys. Beyond its current uses, the PASS system showcases adaptability, holding promise for varied applications like monitoring CO2 storage sites or geothermal reservoirs. It could also be used for imaging and monitoring embankments, dams, tunnels, and other built structures. Because the highly portable seismic source can be deployed on a drone, drone-based active-source seismic experiments are possible for such infrastructures. Permanent monitoring systems based on PASS may be valuable for public acceptance of geoengineering projects, such as CO2 storage and geothermal projects.

3.1.1. Portable Active Seismic Source (PASS) 4-cm model

Before the discussion of advanced models, we need to understand more about the original Portable Active Seismic Source, commonly called PASS, is an ingenious and compact piece of equipment for seismic exploration, and it was designed and proposed by Tsuji and Kinoshita in 2022. It uses a motor system to vibrate a mass at variable frequencies. The range of these vibrations can be finely tuned from a low hum at 20 Hz to a high-frequency buzz close to 1 kHz, accommodating the diverse requirements of subsurface exploration. Its versatility is further enhanced by its ability to produce 'chirp' signals, which are highly customizable sequences that can be adjusted for different frequency ranges and durations to suit the geological characteristics of the target area.

It's small enough to fit inside a cube measuring 10 centimeters on each side, making it convenient to transport to remote or inaccessible locations. Despite its modest size, the PASS is mighty. For instance, the model used in one study could generate a force of 19 newtons while rotating at 50 Hz. Its larger counterparts, which are meter-scale, can produce much greater forces by turning heavier weights but at the cost of increased size and the need for additional mechanisms like oil circulation to manage friction.

The PASS generates vibrations on both vertical and horizontal axes by rotating eccentric mass clock or anti-clockwise (Figure 3.4a-d). The eccentric mass (weight) is attached to a small motor (4 cm) (Figure 3.4g). This motion resulted in an angular force to both x and y, as shown in Figure 3.4e-f.

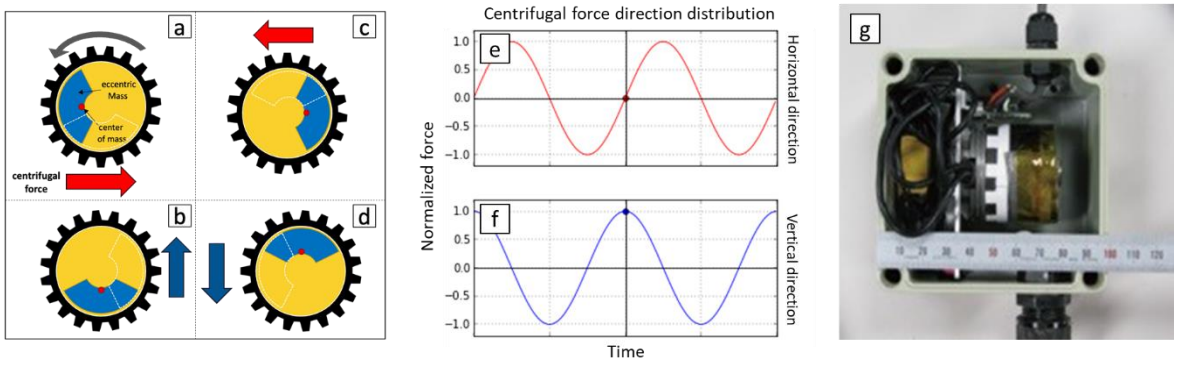

Figure 3.4 (a) to (d) shows the location of the rotational eccentrical mass while the centrifugal force direction at horizontal dictation at (e) and vertical direction at (f) for the 4-cm PASS (g).

A field experiment was conducted along a riverbank in Kyushu, southwest Japan, to assess the performance and reliability of the PASS. The experimental setup included an array of geophones spread across 900 meters, with the PASS positioned at one end. Over 112 minutes, the PASS was activated to emit chirp signals at half-minute intervals, resulting in 225 recorded shots. Vertical-component geophones were particularly important, as they are well-suited for capturing P-wave signals commonly used in reflection imaging and time-lapse (4D) seismic monitoring. Enhancing the ground coupling of the PASS was achieved by a simple yet effective method: positioning a car tire over the device, which was buried shallowly. This innovative approach to increasing coupling efficiency is a testament to the practical ingenuity behind the PASS system's design. The affordability of the PASS system is also noteworthy.

With a cost of approximately USD 1,000 per unit, it presents a cost-effective solution for seismic exploration. Moreover, burying the PASS helps to mitigate the impact of surface environmental fluctuations, such as those caused by rainfall or freeze-thaw cycles, which was evident from the collected field data. In essence, the PASS system represents a leap forward in seismic source technology, providing a low-cost, highly portable, and efficient tool for geophysical exploration due to its ability to be deployed quickly with minimal disturbance.

3.1.2. PASS (4-cm) signal propagation

To understand the behavior of seismic signals and their ability to traverse various distances with stability, a detailed field experiment was orchestrated along a riverbank near Kyushu University in the southwestern region of Japan. The integrity and conditions of riverbanks are paramount and routinely assessed to mitigate the risk of catastrophic flooding.

For this specific study, depicted in Figure 3.5, a comprehensive setup was established, featuring an extensive line of geophones arranged over 900 meters. This line included 19 geophones placed 50 meters apart, forming a strategic array to capture a wide range of subsurface responses (as indicated in Figure 3.5b). At the terminal point of this geophone array, the Portable Active Seismic Source, or PASS system, was strategically positioned alongside an additional geophone.

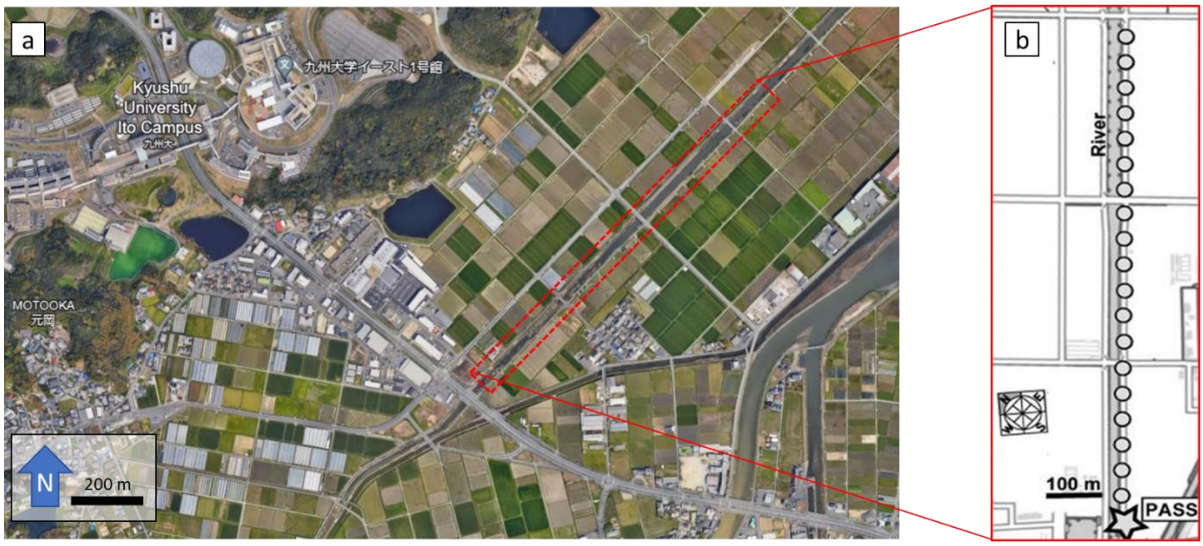

Figure 3.5 (a) the satellite image for the Riverbank field experiment near Kyushu University, (b) the profile of the survey area showing the locations of the PASS (star) and the 900 m array of geophones (Tsuji et al., 2022).

The collected data comprised signals recorded by vertical-component geophones, a choice motivated by the prevalent application of P-wave signals in reflection imaging and four-dimensional seismic monitoring. This selection was pivotal for capturing the necessary seismic information with clarity and precision.

A practical yet effective measure was employed to enhance the transmission of the seismic signals into the subsurface—termed the 'coupling' of the PASS to the ground—a vehicle was maneuvered so that one of its tires rested directly above the buried PASS unit. This simple action ensured that the PASS system was firmly anchored against the ground, optimizing the fidelity of the seismic signal generation. This methodology is a testament to the ingenuity of field engineering, where the tools are often utilized creatively to achieve scientific objectives.

In the field experiment conducted along a riverbank (Figure 3.5), Tsuji et al. (2022) investigated the propagation characteristics of P-wave monitoring signals. Initially, the signal clarity was limited, but a significant improvement was observed after a processing technique was applied by stacking 225 chirp signals, which amounted to approximately 112 minutes of data acquisition. This stacking process allowed for the clear detection of P-wave signals at distances exceeding 900 meters from the source, a finding that underscores the effectiveness of this signal enhancement technique (Tsuji et al., 2022). Prior to stacking, the single-shot signals emitted from the Portable Active Seismic Source (PASS) had a propagation reach of approximately 300 meters, with limited clarity. This experiment contrasts signal propagation and clarity before and after the stacking process.

Further analysis of the shot gathers indicated that the P-wave velocity (VP) was around 1600 meters per second. Given the proximity of the survey line to the river, the geological formation was primarily water-saturated, leading to a VP that was close to the speed of sound in water, as depicted in Figure 3.6. These results demonstrate the PASS system's potential in monitoring extensive areas, with the ability to detect P-wave signals over kilometer-scale distances after appropriate signal processing. However, it's noteworthy that surface waves, which generally travel at approximately 200 meters per second, were only observable near the PASS (within an approximate range of 100 meters).

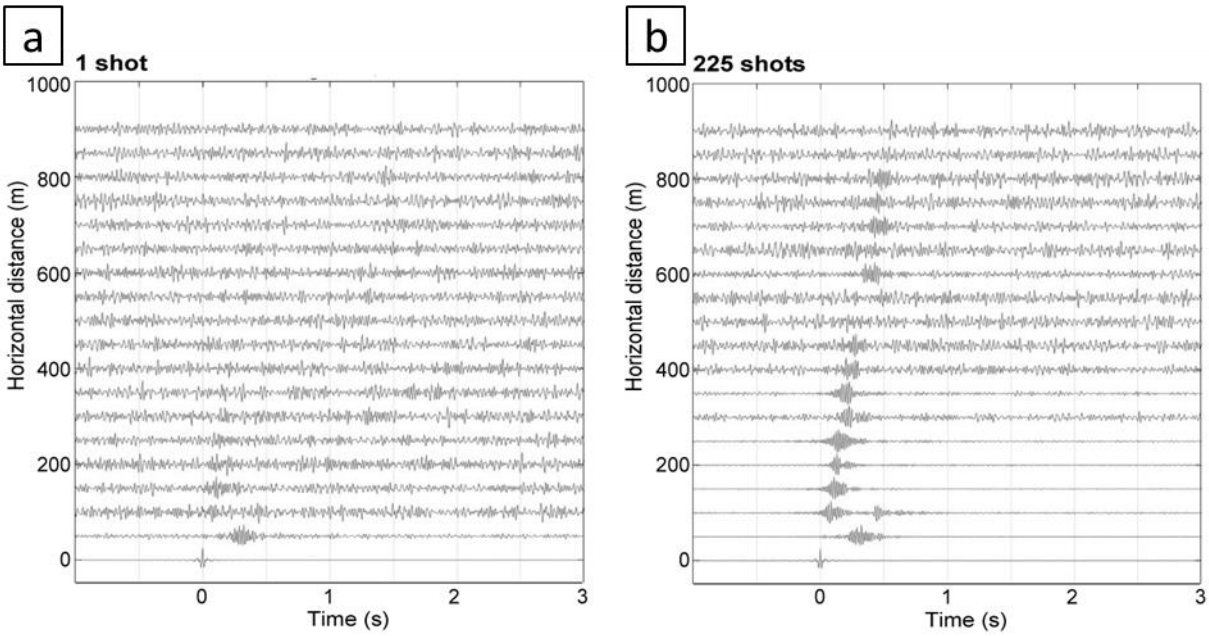

Figure 3.6 Experimental results from the riverbank site to evaluate propagation and stacking effect for shot gathers acquired along the geophone array clearly display the P wave. Waveform amplitudes are normalized by maximum amplitude where (a) it is shown with a single shot and (b) it is shown after stacking 225 shots (Tsuji et al., 2022).

3.2. Enhanced Portable Active Seismic Source

3.2.1. High energy Portable Active Seismic Source (HE-PASS)

Building upon the achievements of the PASS system, a new design has been developed for the Portable Active Seismic Source (PASS) system (Figure 3.4g). The axes design specifically focuses on improving the propagation of P waves and minimizing their susceptibility to surface variations. By addressing these aspects, the updated PASS system aims to optimize seismic data acquisition further and enhance the overall performance of seismic surveys in various environments. The PASS system utilizes a rotating symmetric configuration with two interconnected axes, employing gears to cancel out the individual horizontal motions generated by each axis of the mass. This design effectively enhances the vertical motion while minimizing any undesirable horizontal movements. I present an in-depth analysis of the PASS system, including its specifications and answering (DAS) network, to capture signals in a densely distributed receiver array.

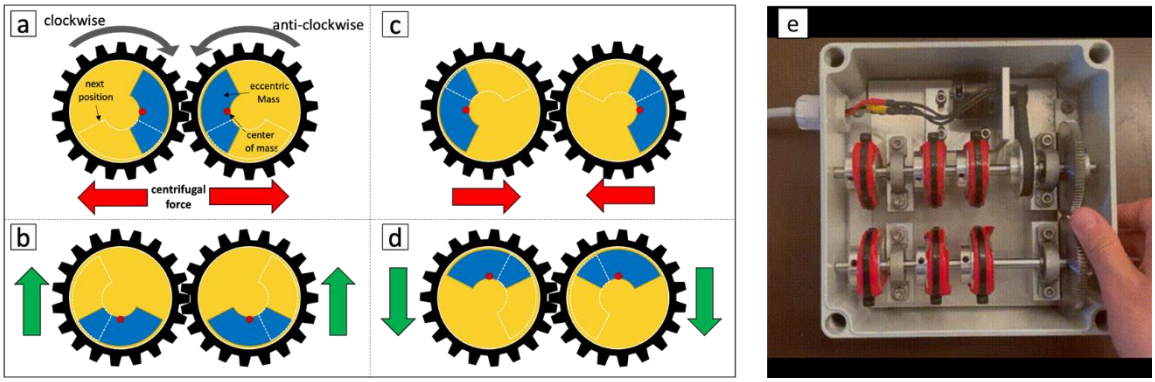

Figure 3.7 Demonstrates the sequence of vibration motion in a single cycle. The weight begins at position (a) and progresses to positions (b), (c), and (d) before returning to position (a) again during the transitions from (a) to (b) and from (c) to (d), the horizontal movements effectively cancel each other out. However, the vertical movement amplifies as the weight travels from (b) to (c) and from (d) back to (a) for HE-PASS in (e).

The PASS system employs a motor-driven mechanism to generate signals by oscillating a suitably weighted mass within controlled frequency ranges. Specifically, the system utilizes an eccentric rotating mass positioned slightly far off the rotational axis/axes to generate the desired signal. Pure vertical motions are achieved by rotating multiple masses in opposite directions around two axes, as depicted in Figure 3.7. Distributing the eccentric mass across several points on each axis to enhance system stability and maximize mass utilization, as shown in Figure 3.7e. Notably, these modifications have minimal impact on the overall system size, as the PASS system remains compact and power-efficient.

3.2.2. Borehole Portable Active Seismic Source (B-PASS)

The Borehole-PASS (B-PASS) system can generate continuous and repeatable signals, specifically chirps, within a 5 to 70 Hz frequency range. These chirps are produced through the rotation of an eccentric mass. The B-PASS configuration includes two distinct designs, each yielding a ground motion signal that is either predominantly vertical or horizontally oriented. Through the process of stacking these chirp signals, the signal-to-noise ratio of the seismic data is enhanced, thereby improving the transfer function's quality. The transfer functions, also known as Green's, are computed by cross-correlating the recorded signals at various seismic stations with the source function by the monitoring source system.

The orientation of the eccentric mass's rotation axis in the source system is crucial in controlling the force direction. Our group at Kyushu University and the University of Tokyo have developed two designs for the B-PASS system to make it easier to understand and use. In the first design for vertical motion, we used two axes connected by a gear mechanism. Essentially, it eliminates unwanted horizontal movement and enhances the up-and-down motion. On the other hand, for the second design that deals with horizontal motion, we use multiple masses that rotate around the vertical axis in the same direction. This design minimizes vertical motion and focuses mainly on horizontal movement. These unique designs allow the B-PASS system to be flexible and adapt to different monitoring needs. To couple the B-PASS system with the casing, we used a hydraulic mechanism This mechanism employs water-pressurized force to attach the B-PASS to the borehole wall firmly. Refer to Figure 3.8 for a visual representation of this attachment mechanism.

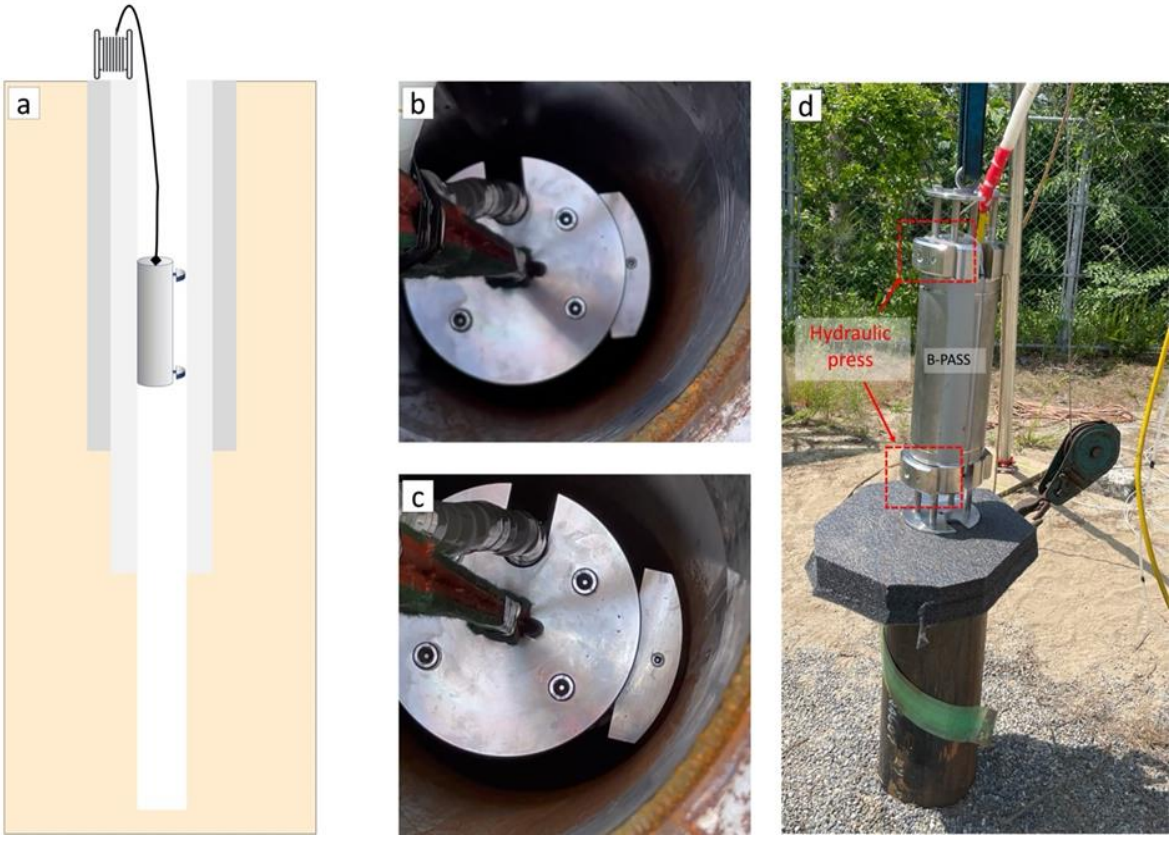

Figure 3.8 Hydraulic mechanism stabilizing B-PASS in a well. (b) Hydraulic press before locking in place. (c) Hydraulic mechanism locked inside the borehole. (d) Actual photo of B-PASS in a borehole with the highlighted hydraulic press for stability (Ahmad et al., submitted).

In the B-PASS study, I have successfully positioned the borehole-PASS source within an open borehole in northern Japan. The B-PASS system was configured to operate within a range of frequency bands, including 0.5-60 Hz, 0.5-70 Hz, 10-50 Hz, 10-60 Hz, 10-70 Hz, 20-50 Hz, and 20-60 Hz. These varied frequency settings were utilized at three distinct depths: 0.5 m, 25 m, and 50 m below the surface. I used 29 geophones Distributed on three profiles to examine how far B-PASS signals travel. These geophones were placed at intervals spanning up to 425 meters. The field experiment was conducted in two phases: the horizontal design in November 2022 and the vertical design in May 2023, by systematically evaluating the transfer functions of each stacked frequency band on each depth to understand the behavior of the signals produced by B-PASS.

3.3. Method

The PASS system utilizes a persistently low amplitude waveform but is exactingly repetitive. Stacking these recurrent waveforms, the system amplifies the signal-to-noise ratio (SNR) of the seismic signals, proficiently diminishing random noise. A sequence of steps is executed before stacking to enhance the quality of the received signal. The foremost step incorporates applying a bandpass filter congruent with the frequency range of the B-PASS operation. Following the framework depicted in Figure 3.10, this assists in reducing ambient noise. Subsequently, a transfer function is calculated using a cross-correlation method for the B-PASS source. This process entails utilizing a built-in B-PASS geophone (as in Figure 2) and recorded waveforms from the geophones as shown in the next function (Yilmaz, 2001b):

$$(x * y)(\tau) = \int_{-\infty}^{\infty} x(t)y(t+\tau)dt \qquad (3.1)$$

Where $(x * y)(\tau)$ represents the cross-correlation between two seismic traces *x* -the B-PASS- and *y* -the surface receiver- at a time t with lag τ, τ is the lag parameter, indicating how much *y(t)* is shifted concerning *x (t)*.

In the cross-correlation analysis, a time window equivalent to the duration of each chirp (30 seconds) is employed; an example of the source function *(x)* can be seen in Figure 3.9. In the following stage, the transfer function for each sweep is weighted based on the SNR.

This weighting process involves assessing the variance of both the silent and sweep windows, shown in red in Figure 3.9. These variance values are utilized to implement a weighted stacking technique, as expressed in the following function (3.2):

$$G_k = \frac{\sum_n \frac{g_{nk}}{var\,[Noise_n]}}{\sum_n \frac{1}{var\,[Noise_n]}} \qquad (3.2)$$

Where G_K is the stacking result of n sweeps number, while g_{nk} is the transfer function in the time domain, and *Noise* is the window of the noise at the end of each sweep of n, which is an index of operation, and k is an index of time series data.

This meticulous procedure involving filtering, transfer function calculation, and weighted stacking significantly contributes to elevating the quality of the received signals and bolstering the overall reliability of the B-PASS system's seismic data analysis. Adopting weighted stacking, as opposed to simple average stacking, is a critical factor in this process. By employing weighted stacking, I carefully consider each sweep's distinct quality.

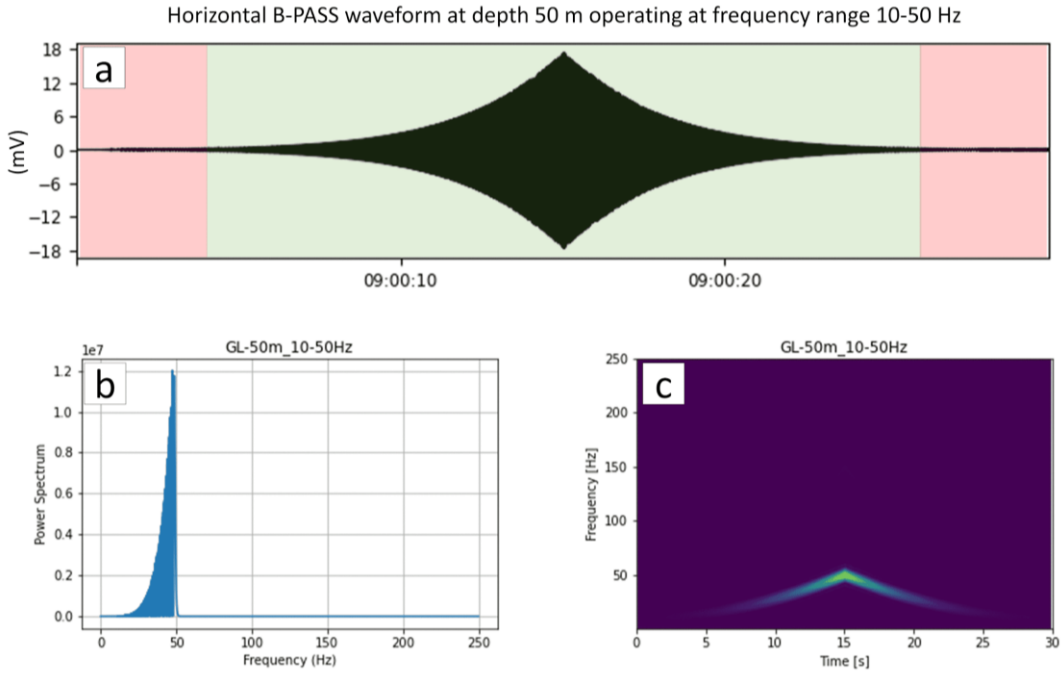

Figure 3.9 Vertical B-PASS Waveform at 50 meters depth with 10-50 Hz operating frequency and Spectra: (a) Individual 30-second sweep waveform with signal (green) and quiet window (red) for SNR calculation. (b) The power spectrum and (c) Spectrogram are related to the sweep in (a) (Ahmad et al., submitted).

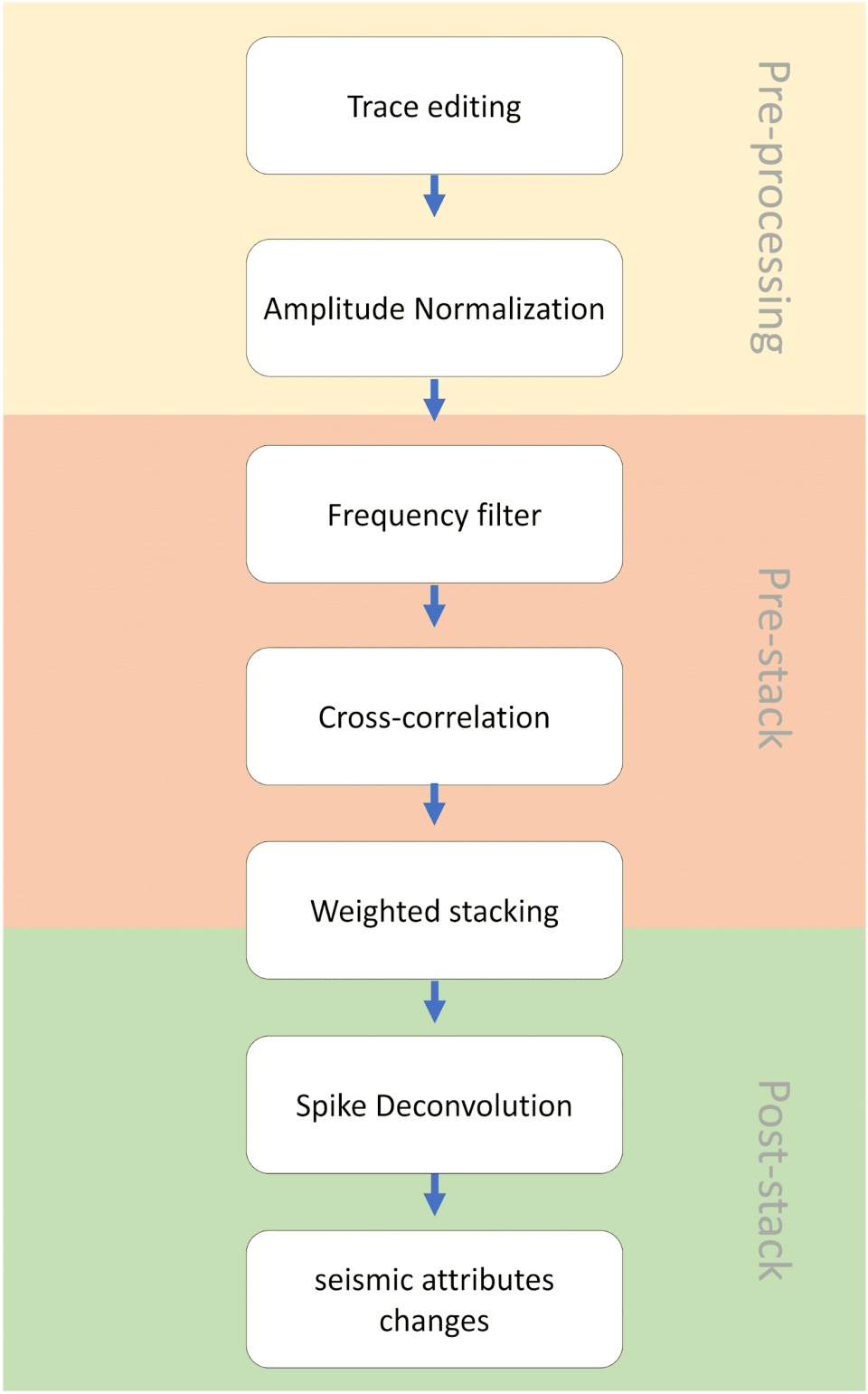

Figure 3.10 Three-stage workflow for processing PASS data in this study: pre-processing, pre-stacking, and post-stacking (Ahmad et al., submitted).

To complete the data processing, I incorporate spike deconvolution, a technique employed further to enhance the resolution and quality of seismic data. This step proves crucial in mitigating the distortions introduced by subsurface layers and improving the overall interpretability of the acquired data. I used time domain deconvolution, which is a signal processing technique used to remove or correct the effects of a convolution operation from a recorded signal(Ligorría and Ammon, 1999; Wang et al., 2016).

Spike deconvolution is a process that sharpens seismic data by stripping away the seismic wavelet, which obscures the underlying geological details. Spike deconvolution involves the estimation of the seismic wavelet embedded within the seismic trace, which is the record of reflected seismic energy received by geophones. An operator known as a deconvolution operator, is computed to counteract the wavelet's influence. This operator is designed to effectively 'collapse' the wavelet into a singular spike, thus enhancing the temporal resolution (Aki and Richards, 2002; Robinson and Treitel, 2012). Applying this operator across the seismic data suppresses the seismic wavelet, thereby sharpening the seismic reflections. These reflections are crucial as they represent interfaces between different geological strata. Sharper reflections improve the interpretability of the data, allowing geoscientists to delineate subsurface structures and stratigraphy with greater precision(Yilmaz, 2001b). Figure 3.11 shows the stacked signals before and after applying Spike deconvolution.

Additionally, spike deconvolution aids in reducing seismic noise and enhancing the signal-to-noise ratio, which is crucial for high-fidelity data analysis. This process also assists in identifying subtle geological features that might be overlooked without this refinement. The method's efficacy in deciphering complex geological formations, such as fault zones or layered sedimentary structures, is noteworthy. Moreover, advancements in computational algorithms have streamlined the spike deconvolution process, making it more efficient and accurate in extracting detailed geological information from seismic data. This advancement is vital for resource exploration, earthquake research, and environmental studies.

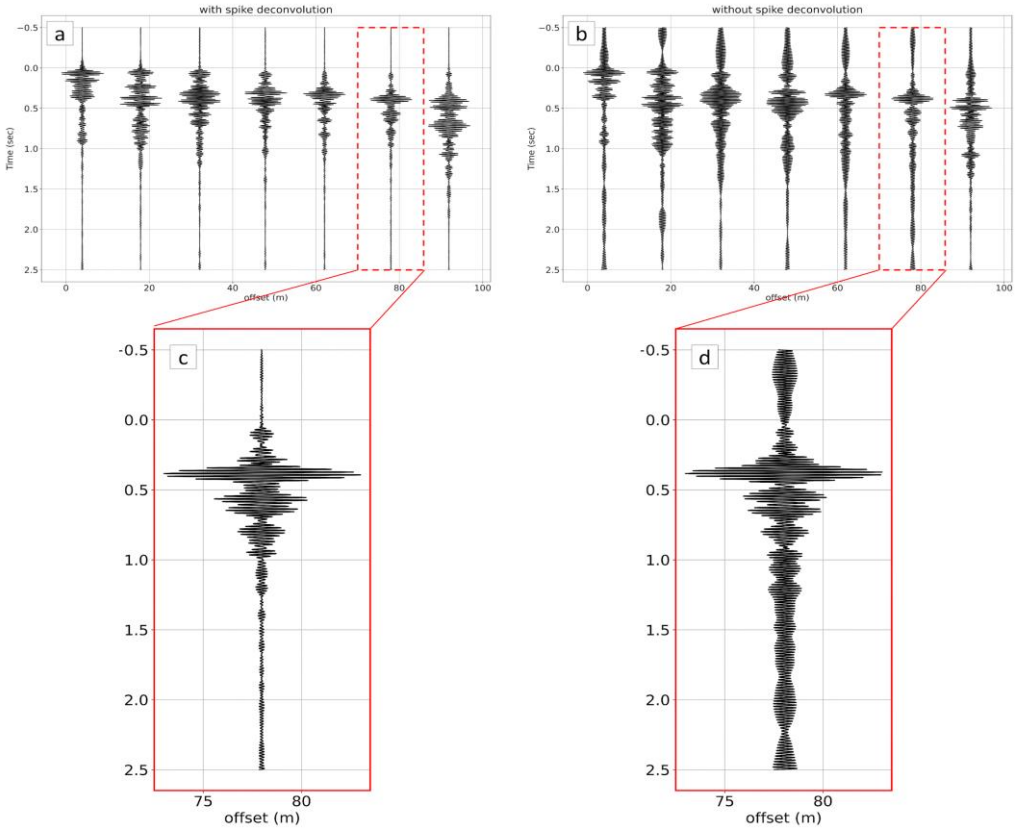

Figure 3.11 Impact of Deconvolution on the Received Signal: (a) After deconvolution. (b) Before deconvolution. Zoomed traces at 80 meters offset, (c) After deconvolution. (d) Before deconvolution (Ahmad et al., submitted).

3.4. Field Data

3.4.1. HE-PASS experiment in Kashiwazaki Field

In March 2022, a field test was conducted to evaluate the efficacy of the high-energy Portable Active Seismic Source (HE-PASS) in conjunction with Distributed Acoustic Sensing (DAS) technology. The DAS system employed in this test consisted of 900 channels arranged horizontally with an inter-channel spacing of 1.04 meters. Distributed Acoustic Sensing is a technique that transforms standard optical fiber cables into extensive arrays of sensitive microphones. These 'microphones' are capable of detecting sound and vibrations over vast distances. DAS operates by transmitting light pulses through the optical fiber and analyzing minute variations in the backscattered light, which seismic waves, temperature fluctuations, or physical disturbances can cause. This technology has diverse applications, including structural health monitoring of bridges and pipelines, earthquake detection, and security

surveillance of borders or critical infrastructure. Its expansive coverage, enabled by a single fiber cable, renders DAS both efficient and cost-effective.

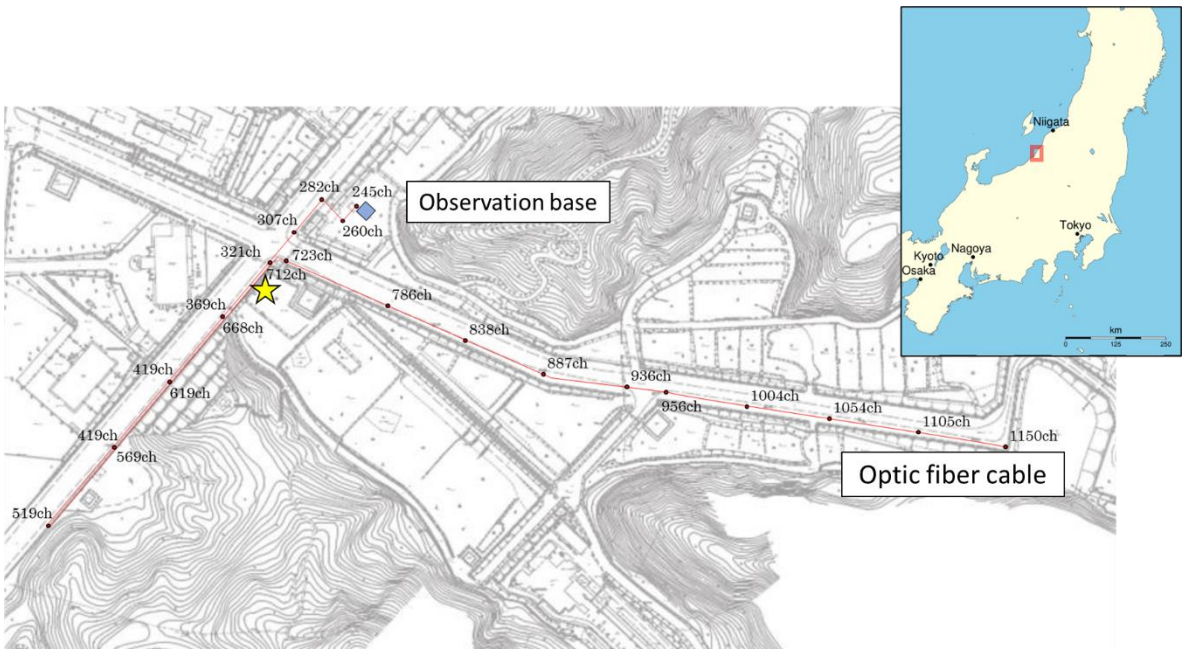

Figure 3.12 Map of the study area of Kashiwazaki Field (from the JGI) showing the layout of the fiber-optic cable (red colored line) and the HE-PASS location (yellow star). The study area is in northern Japan, south of Niigata.

The field test was carried out at the Kashiwazaki Test Field, located in Kashiwazaki City, Niigata Prefecture, Japan. JOGMEC's facility is designed to conduct research related to oil development technologies and train engineers in this sector. During the experiment, the HE-PASS was strategically positioned adjacent to the DAS channel (refer to Figure 3.12 for the setup). The operation of the HE-PASS spanned 150 minutes, encompassing a total of 295 sweeps. These sweeps were conducted across a frequency range of 10 to 50 Hz.

3.4.2. HE-PASS experiment in Nagaoka Testing facility (borehole)

In July 2022, the second field test of the High-Energy Portable Active Seismic Source (HE-PASS), integrated with Distributed Acoustic Sensing (DAS), was conducted in proximity to the Physical Measurement Consultant office at the Nagaoka branch facility, located in Nagaoka City, Niigata prefecture, Japan. This facility is equipped with a purpose-built open borehole designed specifically for seismic testing. For this experiment, a 300-meter DAS array was vertically installed in the borehole shown in Figure 3.13. The HE-PASS unit was positioned 25

meters from the observation hole to facilitate an accurate assessment of seismic wave propagation from a controlled source.

This field test was scheduled overnight to reduce environmental noise interference, thereby enhancing the precision of the data collected. A vehicle was placed over the HE-PASS unit to stabilize the seismic source. The weight of the vehicle served to maintain the positional integrity of the source during the testing period. A 1-C Atom geophone, with a sampling rate of 250 Hz, was situated near the seismic source. This high-resolution recording equipment was critical for capturing the source function and analyzing the signal propagation in the borehole environment. The objective of this test was to observe and quantify the signal propagation at real depth under controlled conditions.

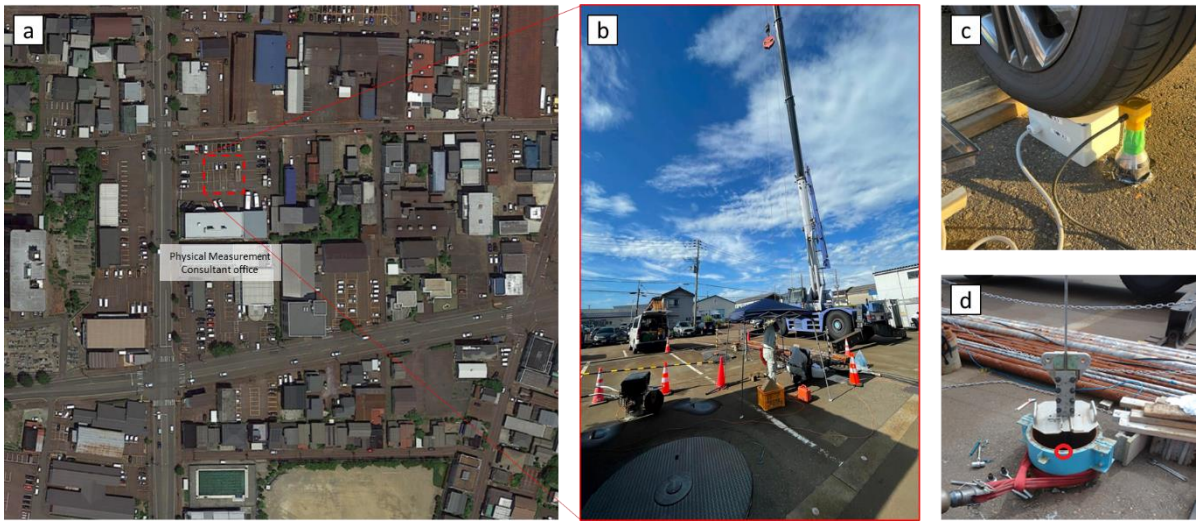

Figure 3.13 (a) satellite image of the facility and well. (b) is a view showing the crane to hold DAS in the borehole. (c) the HE-PASS under a vehicle and next to it a geophone for source function, (d) the borehole head.

3.4.3. HE-PASS experiment in North Shonai

In December 2022, the final experiment involving the High-Energy Portable Active Seismic Source (HE-PASS) was conducted in Northern Shonai town, located within Sakata City, Yamagata Prefecture, Japan. This experiment took place in an open field, which is part of the Japan Petroleum Exploration (JAPEX) facility, a location chosen for its geological relevance to the study. The experiment entailed deploying the HE-PASS at five locations to use multiple shooting locations for shoot gathering and imaging, as illustrated in Figure 3.14. Surface

sensors provided by the Japan Geoscience Institute (JGI), a private entity specializing in geophysical and geological survey services, were utilized for data acquisition. These sensors are part of an integrated approach to seismic data collection in the field.

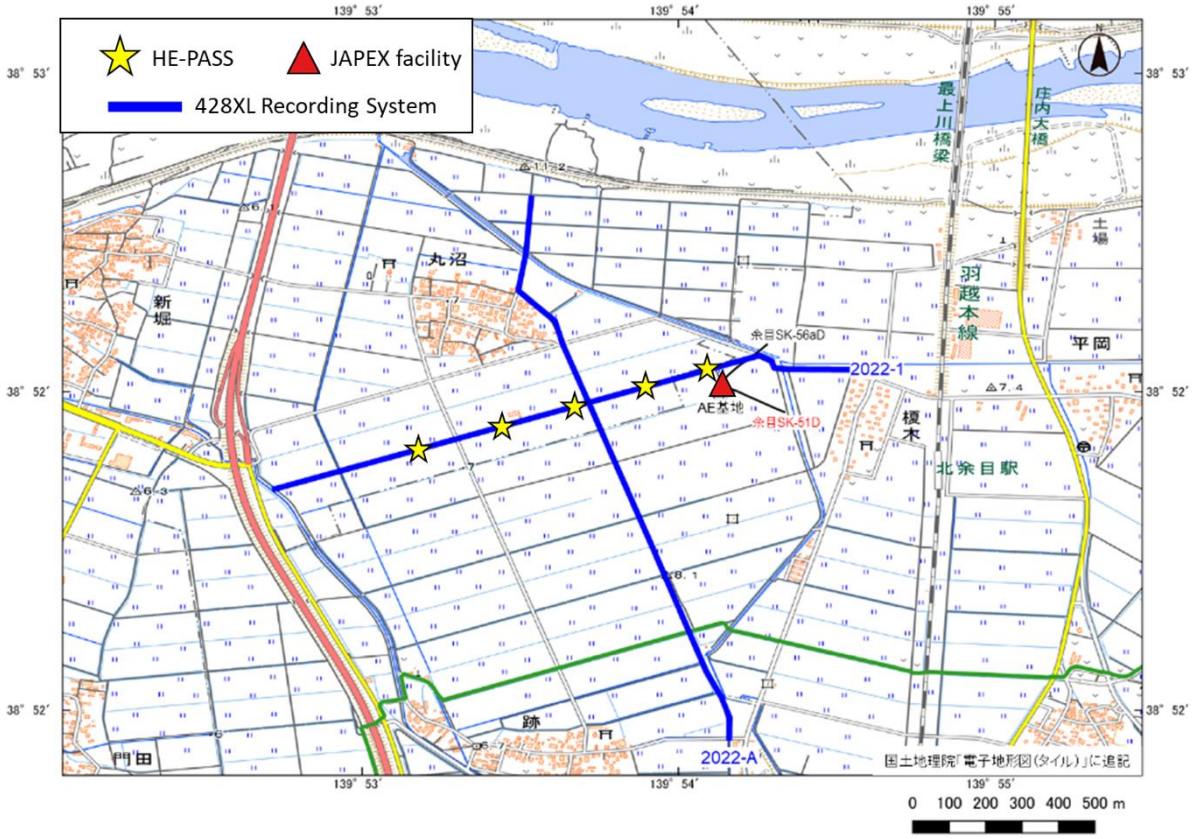

Figure 3.14 Map of the study area of North Shonai Field showing the layout of the 428XL Recording System (blue colored line) and the HE-PASS locations (yellow star). HE-PASS has moved to 5 locations, as shown in the map.

The data recording was executed using the Sercel 428XL Recording System, a high-precision seismic data acquisition system, as illustrated in Figure 3.15. This setup included three channels per station, arranged in the order of Vertical, North-South (NS), and East-West (EW). The total number of receiver channels employed was 1,149, with a spatial interval of 10 meters between each station. The experiment comprised two seismic profiles. The first profile, extending from east to west, utilized 420 channels (channel numbers 85-504), covering 140 locations and resulting in a total length of 1.4 kilometers. The second profile was oriented from north to south, encompassing 600 channels (channel numbers 508-1107) across 200 locations. Due to the non-linear arrangement of the second profile, its total length

was approximately 1.98 kilometers. Channels 505-507, reserved for vibroseis, were not utilized in this study.

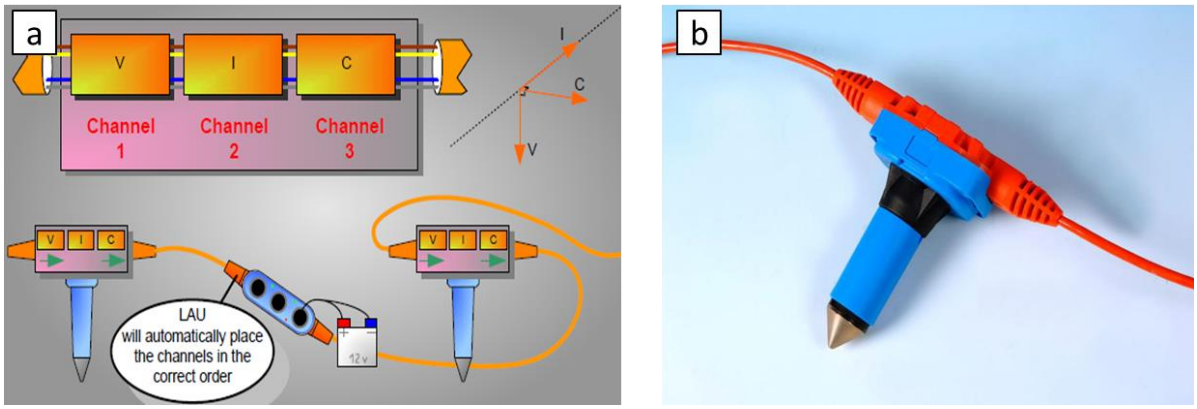

Figure 3.15 428XL Recording System has 3 channels per station as shown in (a) the order is Vertical, then Inline, then Crossline. (b) is a real photo of the station (geophone) at each location.

For this research, only the vertical channels (up-down component), with a total number of 1019 channels, were analyzed. This focus aligns with the primary objective of developing HE-PASS, which is to enhance vertical seismic motion detection. Meteorological conditions during the experiment included cloudy skies and wet soil conditions resulting from earlier scattered rainfall. The source system was secured under a vehicle during the experiment to ensure stability and protection.

3.4.4. B-PASS experiment in the Nakajou field

The B-PASS system testing occurred in an old field with an abandoned gas well in Nakajou, Niigata, north Japan. This site was chosen for its remote setting, away from urban areas, resembling potential future CCS project locations. The expansive layout, including the base operations, offered an environment conducive to the experimental needs. The site has access to the main roadway of Nakajou, facilitated seamless operations and movement during my study, and was used to study the influence of environmental noise. Instrumentally, two types of geophones, the Atom (both 1-component and 3-components) and the SmartSolo IGU-BD3C-5 with a 3-component sensor, are illustrated in Figure 3.16.

In November 2022, the B-PASS system, designed for horizontal motion, was deployed to conduct an uphole survey to evaluate both the distance and stability of signal propagation

within the borehole. This execution happened in an open borehole. The operational plan for the initial survey is detailed in Table 3.1. The B-PASS system emitted sweeping signals at 30-second intervals between each consecutive sweep. For this analysis, 34 geophones were strategically placed and arranged into four profiles with a maximum horizontal offset of 610 meters, illustrated in Figure 3.17a. The geophone deployment included SmartSolo, each featuring three components, and Atom-1C Seismographs, each with a single vertical component sensor, all set to record at a 500Hz (2 ms) sampling rate. Unlike the SmartSolo sensors with built-in batteries lasting a month, the Atom geophones required battery replacements every two days for recharging; the battery replacement took time from 8:00-9:00 every two days from starting the survey or if needed.

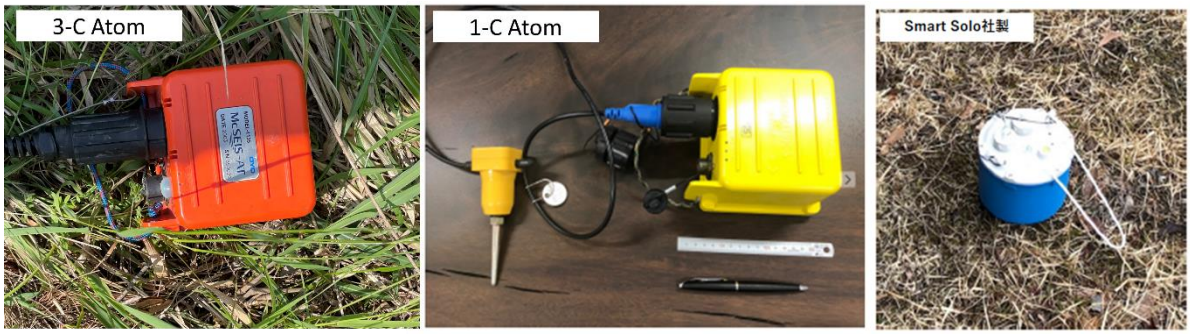

Figure 3.16 types of geophones were used in the Nakajou field experiment: the Atom (3-components, 1-components) and the SmartSolo IGU-BD3C-5 with a 3-components sensor shown respectively from left to right.

Table 3.1 Horizontal Motion B-PASS: Operations and Parameters.

Source depth	Sweeps	Frequency	Starting time (JST)	end time (JST)
50 cm	104	10～60Hz	2022-11-17 16:35	2022-11-17 18:21
	30	5～60Hz	2022-11-18 16:10	2022-11-18 16:39
	30	5～70Hz	2022-11-18 16:41	2022-11-18 17:10
	30	10～70Hz	2022-11-18 17:12	2022-11-18 17:41
	30	20～50Hz	2022-11-18 17:43 to	2022-11-18 18:12
	30	20～60Hz	2022-11-18 18:14	2022-11-18 18:43
	832	10～50Hz	2022-11-18 18:45	2022-11-19 8:36
25 m	231	10～60Hz	2022-11-19 10:22	2022-11-19 14:12
	1097	10～50Hz	2022-11-19 14:15	2022-11-20 8:31
50 m	231	10～60Hz	2022-11-20 10:11	2022-11-20 14:01
	9761	10～50Hz	2022-11-20 14:04	2022-11-27 8:43
	33	5～60Hz	2022-11-27 9:47	2022-11-27 10:19
	33	5～70Hz	2022-11-27 10:22	2022-11-27 10:54
	33	10～70Hz	2022-11-27 10:57	2022-11-27 11:29
	33	20～50Hz	2022-11-27 11:31	2022-11-27 12:03
	33	20～60Hz	2022-11-27 12:05	2022-11-27 12:37

Subsequently, another uphole survey using the vertical motion design of the B-PASS system was undertaken in the same field six months later, in May 2023. This survey, lasting three days, involved the deployment of 29 geophones, arranged differently than in the November 2022 survey. The operational timeline for this follow-up survey is provided in Table 3.2, maintaining 60-second intervals between sweeps.

This time, the 29 geophones were strategically arranged into three distinct profiles, as demonstrated in Figure 3.17b and recorded at a higher sampling rate of 1000Hz (1 ms). The maximum horizontal offset achieved in this survey reached up to 425 meters, disregarding any topographical elevation offset considerations.

Table 3.2 Vertical Motion B-PASS: Operations and Parameters.

Source depth	Sweeps	Frequency	Starting time (JST)	end time (JST)
50 cm	2250	10～50Hz	2023-05-17 13:52	2023-05-18 8:46
25 m	450	10～50Hz	2023-05-18 9:34	2023-05-18 14:00
50 m (night)	1000	10～50Hz	2023-05-18 14:35	2023-05-18 23:18
50 m (morning)	460	10～50Hz	2023-05-19 6:15	2023-05-19 10:00

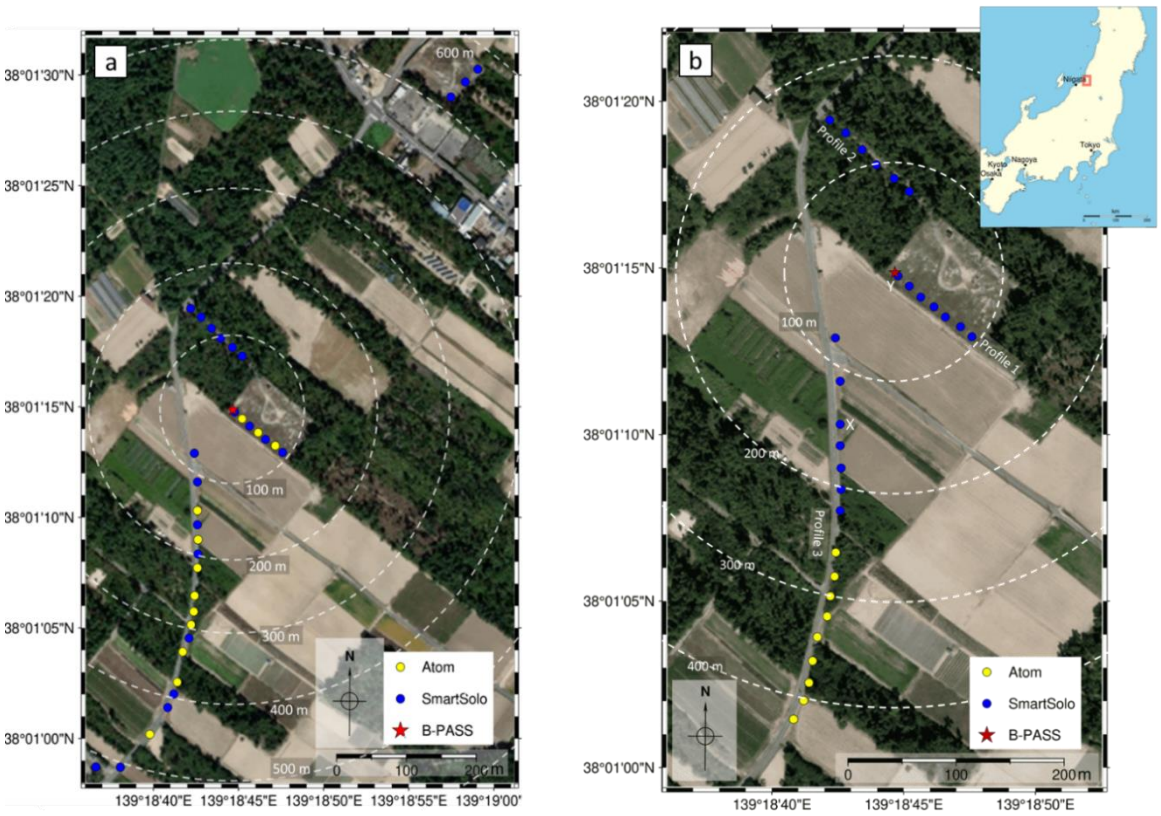

Figure 3.17 Map of the study area of the B-PASS experiment in the Nakajou field showing the layout of the distribution of geophones(blue and yellow colored circles) and the B-PASS location (red star). (a) shows sensor distribution for the horizontal B-PASS configuration, while (b) shows the distribution for the vertical configuration (Ahmad et al., submitted).

3.5. Results and Discussion

3.5.1. Signal enhancements by stacking

HE-PASS experiment in Nagaoka Testing facility (borehole)

I observed the enhancement of the signal while stacking and creating heatmaps using Spearman's rank correlation coefficient *(ρ),* which is a statistical measure to assess the monotonic relationship between two ranked variables (Daniel, 1990). In the context of Figure 3.18c, Spearman's rank correlation coefficient was calculated between each stacking step, and the best-stacked signal was obtained with 120 shots. The purpose was to evaluate the improvements and identify the optimal monitoring interval. The calculation of Spearman's rank correlation coefficient allows us to assess the effectiveness of the stacking process at different intervals and determine the optimal number of shots for achieving improved signal quality and clarity.

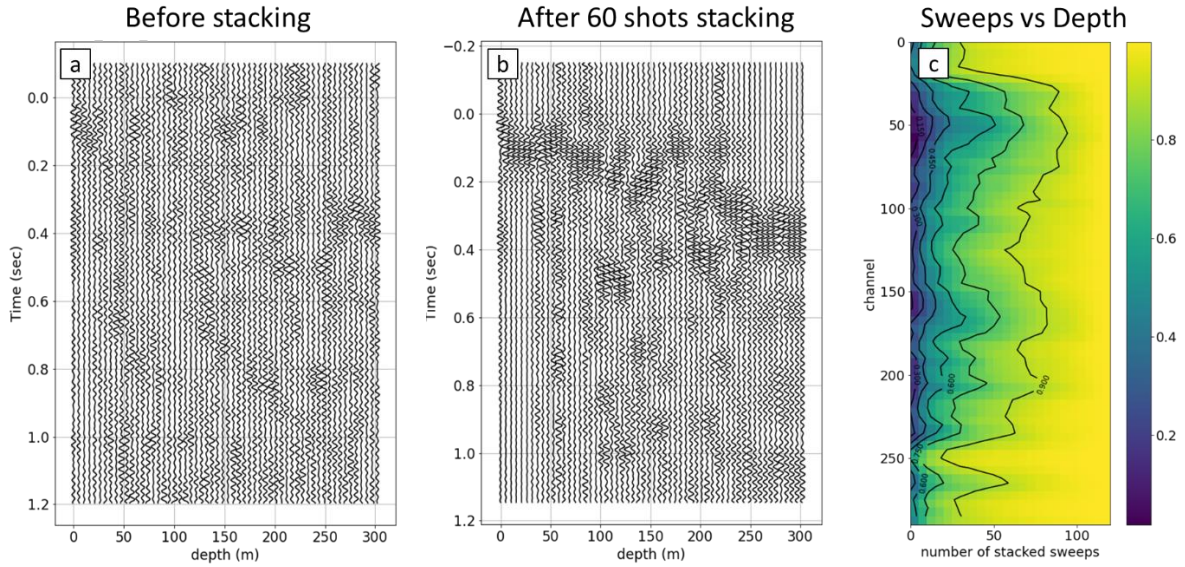

Figure 3.18 Illustrates the dramatic effect of stacking the PASS vibration on the received signals. (a) shows the received signal for a single sweep without any stacking, while (b) shows the clear enhanced after stacking 60 shots. (c) Heat map for the correlation between 120 stacked shots and every step stacking (Ahmad et al., 2023).

Figure 3.18 presents three panels illustrating the evolution of a seismic signal from a single sweep to multiple stacked sweeps and the relationship between the number of stacks and signal clarity at various depths. Figure 3.18a displays a single seismic sweep, which is a raw,

unprocessed signal from the High-Energy Portable Active Seismic Source (HE-PASS). The traces, or waveforms, appear relatively noisy and lack coherent signal patterns. This is typical of raw seismic data, where individual sweeps can be dominated by ambient noise and the complexities of subsurface geology. The seismic signal became clear after stacking 60 sweeps, equivalent to approximately 30 minutes of data collection. Key seismic events (HE-PASS signal) became more coherent, and continuous reflections can be tracked across multiple traces, allowing for a better interpretation of the subsurface structure.

The heatmap in Figure 3.18c represents the relationship between the number of stacking sweeps and the signal clarity at various depths. The color gradient likely represents Spearman's rank correlation coefficient. The heatmap shows that signal clarity at greater depths does not indeed require a larger number of stacks, as indicated by the transition from cooler to warmer colors with increased stacking. In the experiment, I found that 60 shots were enough to obtain a clear signal at a depth of 300 meters.

B-PASS experiment in the Nakajou field

The process of stacking continuous chirp signals obtained from the B-PASS system yields a notable enhancement of the signals while concurrently canceling out random noise. This stacking technique leads to an amplified and clearer representation of the desired signals. The transfer functions established between the source and a three-component seismometer, which is positioned 150 meters away from the source (marked as "X" in Figure 3.17b), illustrate that the signal quality is significantly improved through stacking (Figure 3.19). In particular, the stacked data successfully highlights the distinct monitoring signal (Figure 3.19). Consequently, this stacking process enables a temporal resolution of approximately 4 hours for the seismometer situated at a distance of 150 meters from the borehole. This outcome underscores the effectiveness of stacking in enhancing the signal quality and extending the temporal resolution of monitoring efforts for seismic observations.

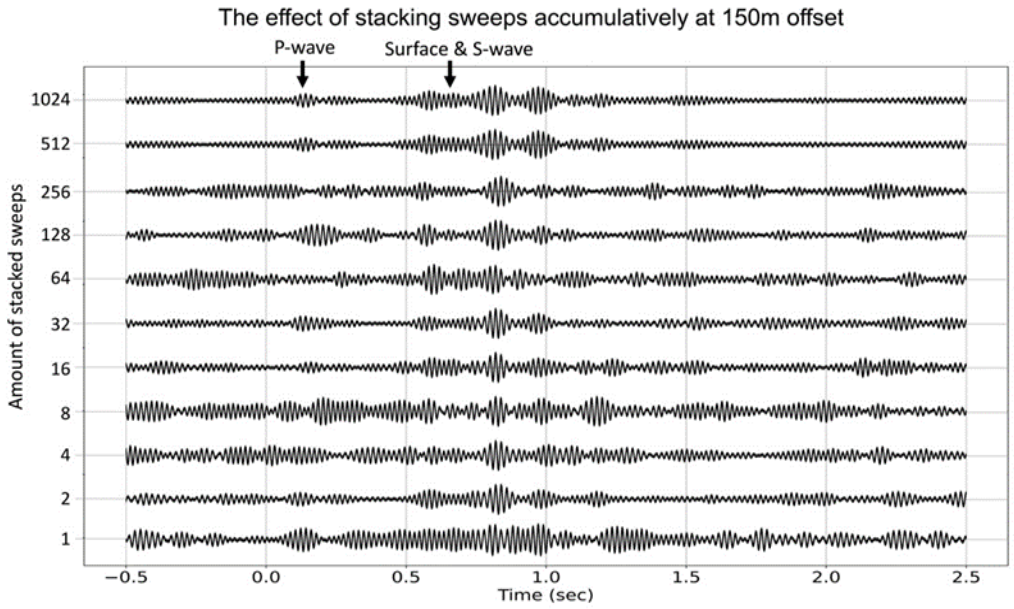

Figure 3.19 Stacked signal effect at 150-meter offset: Enhanced P-wave and S-wave with a black arrow visible after 512 cumulative stacked sweeps through cross-correlation (Ahmad et al., submitted).

3.5.2. Signal propagation distance

HE-PASS experiment in Kashiwazaki Field

This section presents the unfiltered seismic data recorded over a span of 150 minutes (or 2.5 hours) from the DAS channels ranging from 282 to 1150, as shown in Figure 3.20. The time scale on the vertical axis shows the travel time range in seconds, which is a proxy for the depth in the subsurface. Notable features in this section include distinct refracted waves, suggesting the presence of geological boundaries. Additionally, a reflected wave is visible at a depth of approximately 1.2 seconds in Figure 3.20d, providing information about subsurface layers.

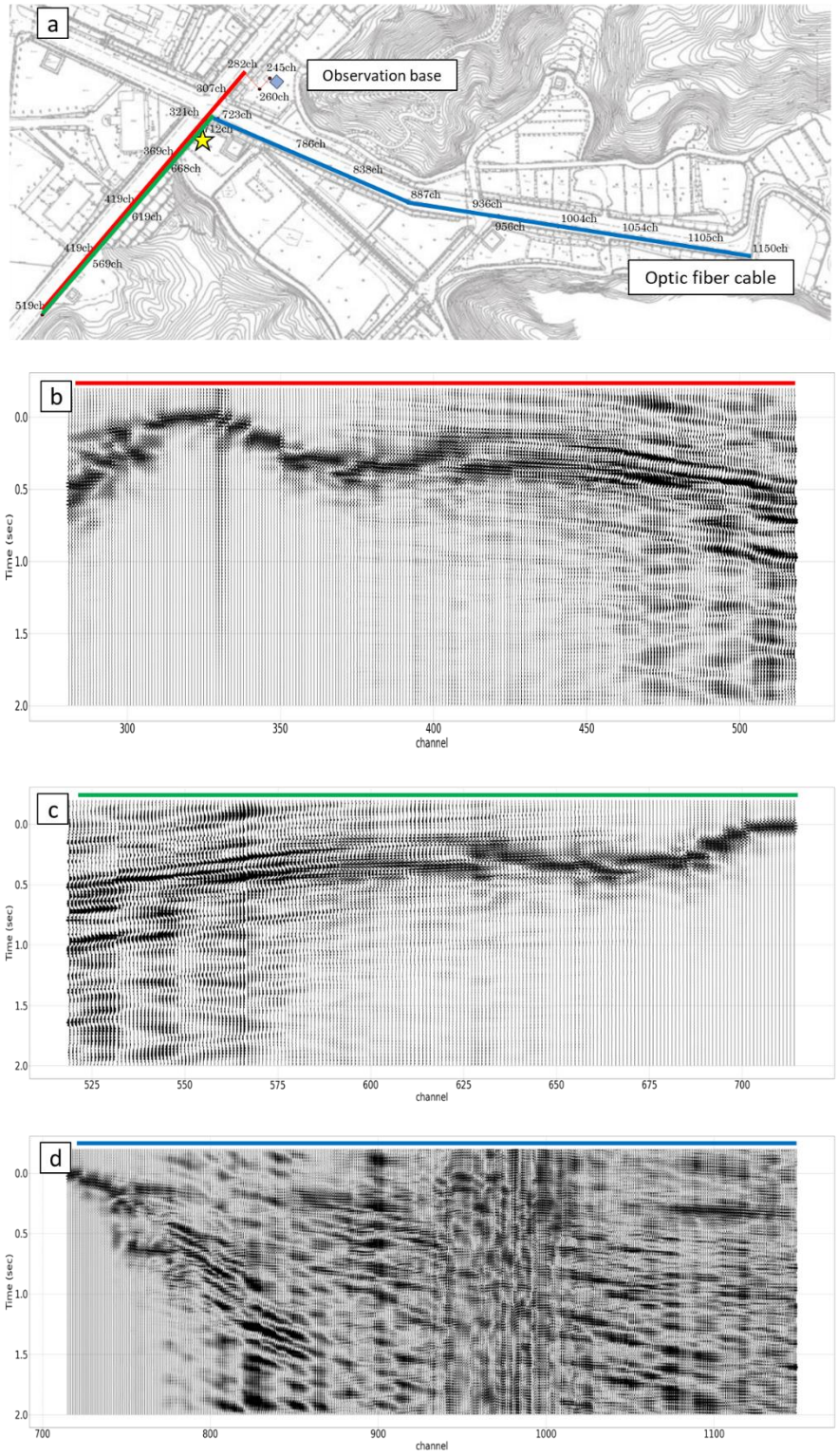

Figure 3.20 (a) Map of the study area of Kashiwazaki field showing the layout of the fiber-optic cable (3 colors line) and the HE-PASS location (yellow star). The results of the stacked signal are shown as follows: (b) from channel 282 to 519 (red color in the map), (c) from channel 520 to 720 (green color in the map), and (d) from channel 721 to 1150 (blue color in the map), without overlapping the channels based on the offset.

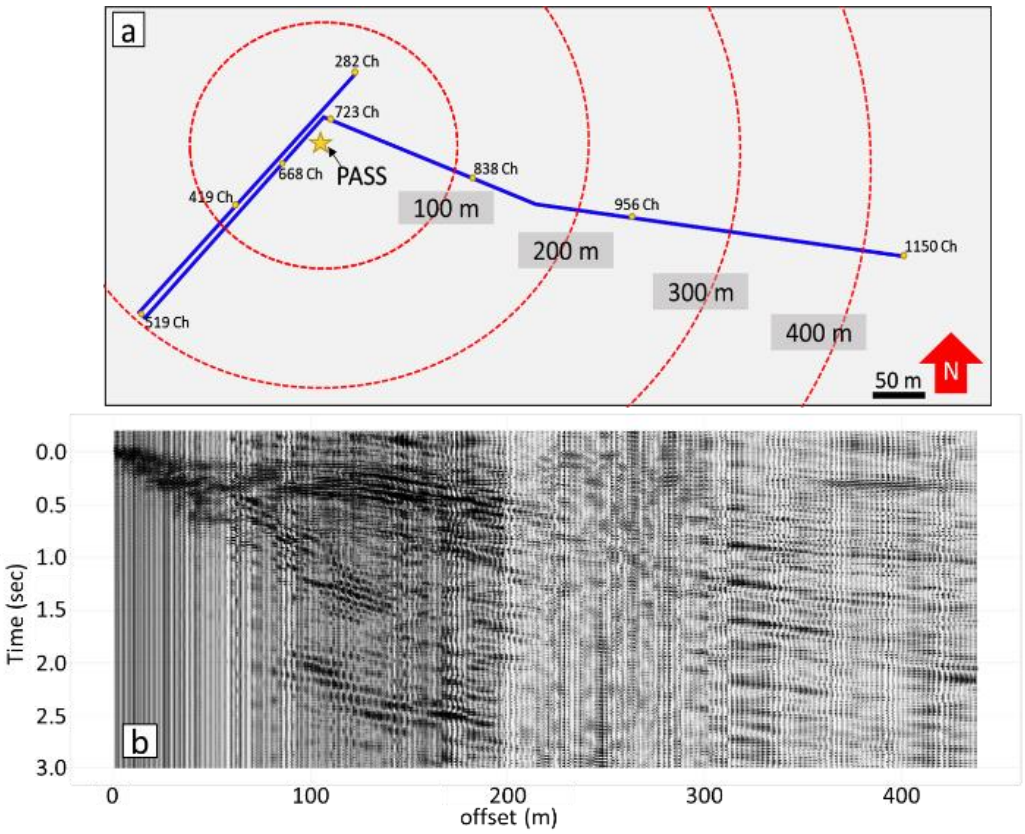

Figure 3.21 (a) Map of the Kashiwazaki field showing the layout of the DAS (blue line) and the pass location (yellow star). (b) Signals were recorded at channels (channels 282–1150) and overlapped based on the offset.

The clarity and continuity of the signals at offsets up to 400 meters are remarkable, particularly considering the unfiltered nature of the data. This suggests a high level of source energy from the HE-PASS and effective transmission through the subsurface, which is noteworthy given the topographical challenges often present in the Kashiwazaki area.

The results from Figure 3.21b indicate that the PASS system is capable of providing high-resolution subsurface images, which is essential for geological and geophysical studies in the field. The ability to detect both refracted and reflected waves at considerable depths and offsets without the need for signal enhancement through filtering demonstrates the PASS system's potential for detailed subsurface characterization in the Kashiwazaki Field.

HE-PASS experiment in North Shonai

The map in Figure 3.22a displays the layout of the FDU 428XL receivers (depicted by blue lines) around the Portable Active Seismic Source (HE-PASS, indicated by a yellow star) in field of North Shonai. The red concentric circles represent distance offsets from the PASS system, with channel numbers noted at key distances. This configuration was set up to capture the seismic waves generated by the PASS. The blue lines represent two profiles: the inline direction channels (85 to 505), extending east to west, and the crossline direction channels (508 to 1107), extending north to south. The longest inline offset is noted at 1.2 kilometers, and the farthest crossline offset reaches up to 900 meters, illustrating the substantial area in Figure 3.22. The seismic section shows the data recorded by the vertical channels, with the channels from 85 to 505 covering east to west and channels from 508 to 1107 covering north to south. The data visualization demonstrates signal propagation despite the HE-PASS system operating for only one hour. Body waves are discernible over a distance greater than one km.

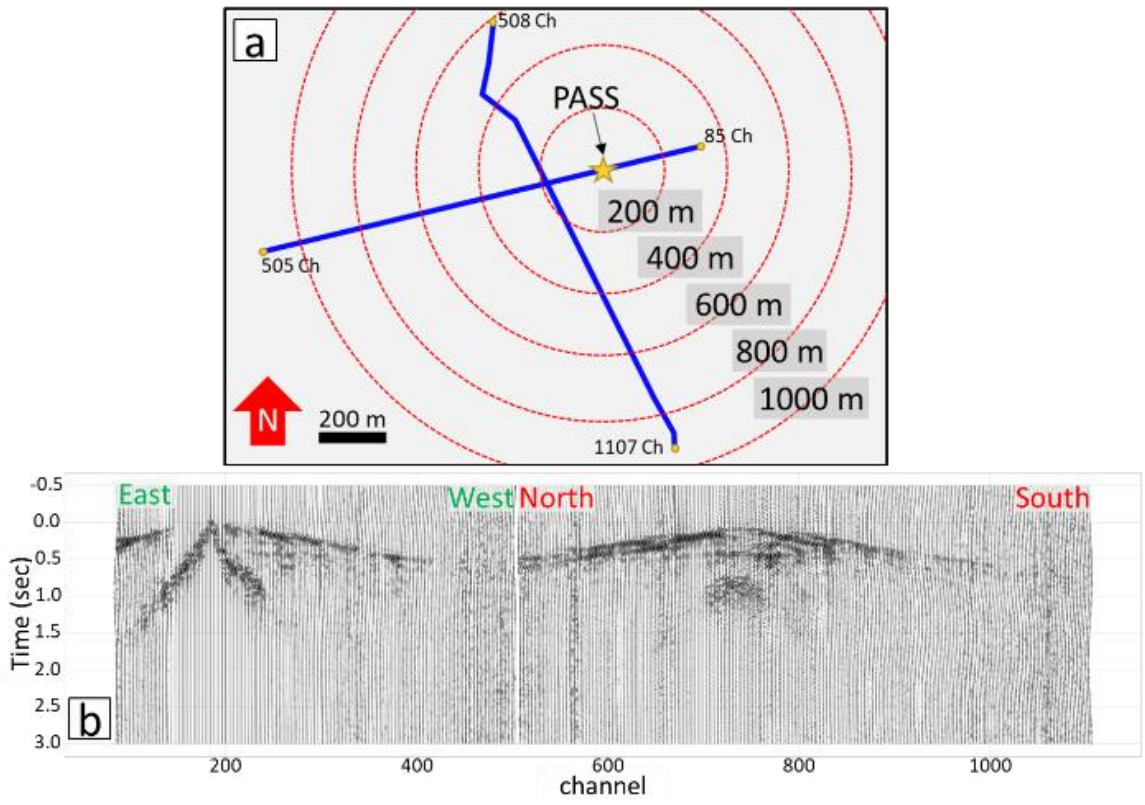

Figure 3.22 Map of the North Shonai showing the layout of the FDU 428XL receivers (blue lines) and the HE-PASS location (yellow star). (b) Signals were recorded at (428XL receivers) vertical channels (Ahmad B. Ahmad et al., 2023).

The clarity of the seismic signals across such distances is a notable achievement, considering the test's relatively short duration and the challenging conditions posed by the wet soil environment, as illustrated in Figure 3.23. The strategic placement of a vehicle further emphasizes the experiment's success in enhancing the coupling between the buried PASS system and the ground. This method, which improves the transmission of vibrations into the subsurface, has shown to be an effective technique in this context. Figure 3.24 shows each location after stacking each for 120 sweeps or 2 hours. I can see the variation in the signal due to the water saturation in the soil, which brings up the concern about the temporal variation of the monitoring signal. This result indicates that attenuation is reduced when ice forms in the shallow subsurface and water saturation decreases, probably owing to increased cementation between the soil grains and reduction of pore water, as can be seen in the field conditions.

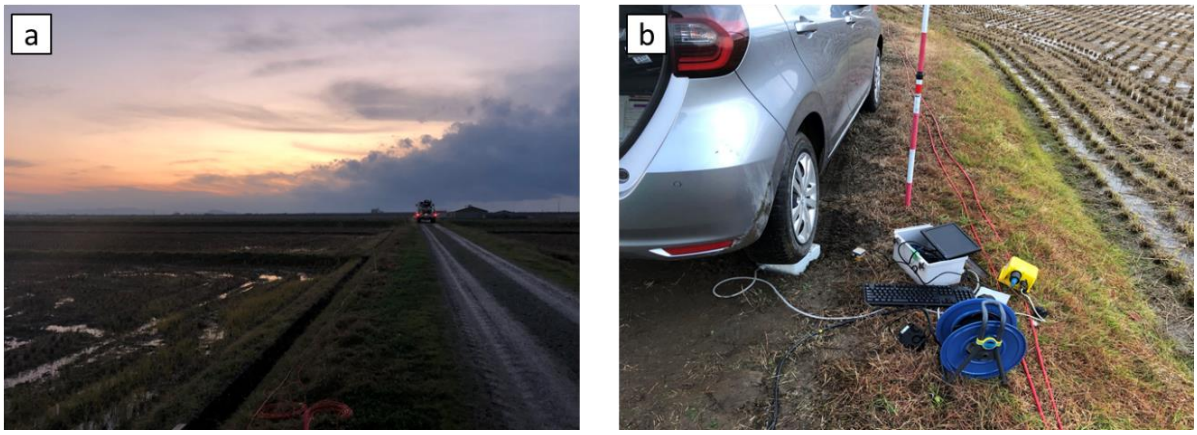

Figure 3.23 Photos from a field experiment in North Shonai. (a) shows the cloudy weather condition after rain at 16:30, while (b) shows the HE-PASS stabilized with a car in wet soil.

These results illustrate the PASS system's ability to effectively transmit distinct and detectable seismic signals over expansive areas, demonstrating its effectiveness for seismic exploration in suitable environmental conditions. The experiment in North Shonai, with its long profiles and substantial signal reach, demonstrates the potential of the PASS system for detailed subsurface imaging in geophysical surveys.

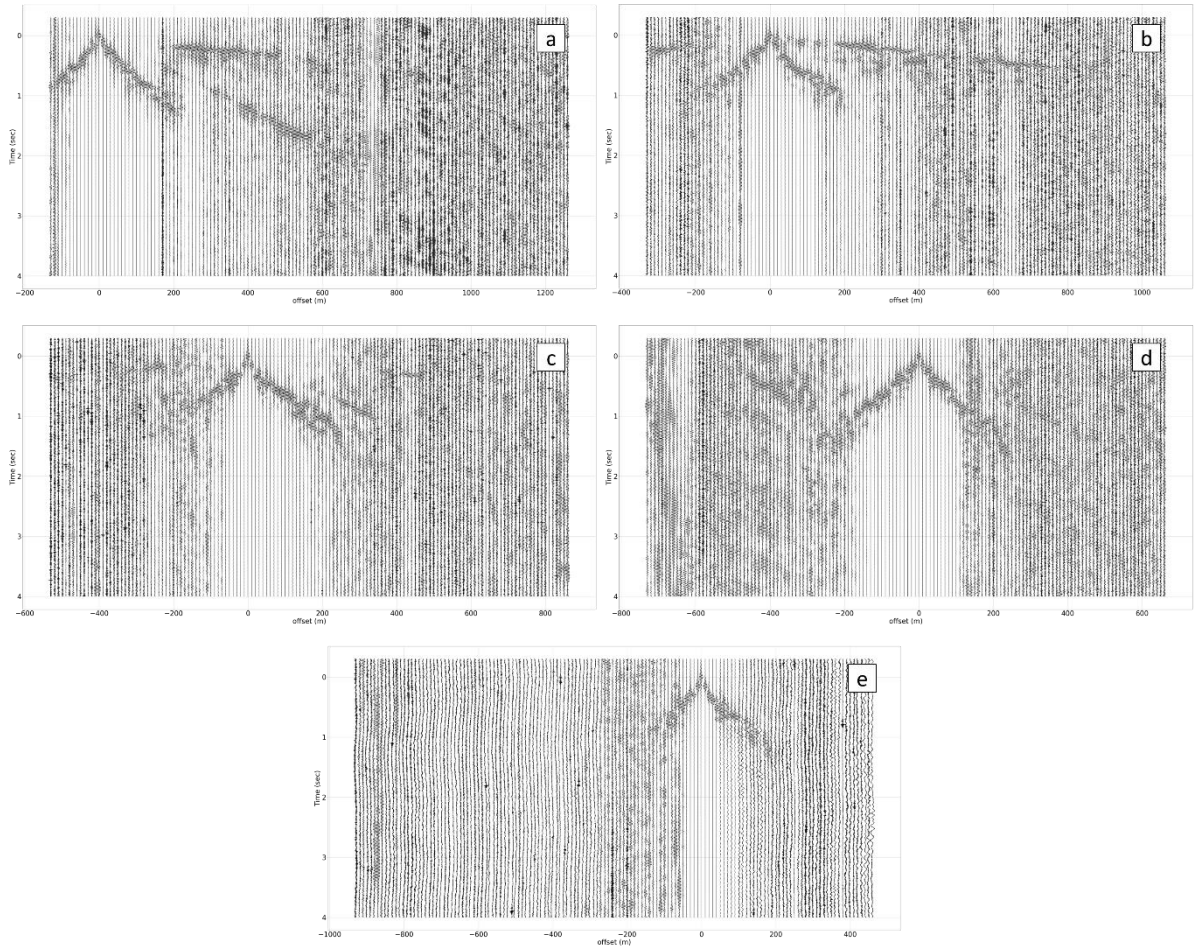

Figure 3.24 The results of the 120 stacked sweeps in the 5 locations a to e are located from east to west. (a) and (b) were conducted before the rain, while (c) and (d) were acquired while it was raining, finally (e) was acquired in the final stage of rains with very wet soil. All sections are shown with respect to offset using the HE-PASS from the inline 428XL receivers.

B-PASS experiment in the Nakajou field

To assess the extent of signal propagation facilitated by the B-PASS system, I conducted a comprehensive analysis of the signals recorded by all seismometers within the three profiles (as depicted in Figure 3.25). I could obtain A remarkable observation for the P-wave and S-wave using B-PASS at a depth of 50 meters by stacking 900 sweeps at a B-PASS depth of 50 meters, encompassing around 7.5 hours, utilizing source frequencies ranging from 20 - 60 Hz.

Despite the compact nature of the monitoring source system, I was able to discern that the monitoring signal propagated over a distance exceeding 425 meters (Figure 3.25). This impressive range of signal propagation can be attributed to the well-controlled and continuous nature of the signals generated by the source system. Figure 3.25 visually presents the transfer functions. The initial wavefield arrival within this context likely indicates the P wave. I also evaluated the signal propagation for the B-PASS system for horizontal components with multiple frequencies, shown in Figures 6S-10S (supplementary material).

The exceptional propagation distances observed for both P and S waves demonstrate the potential for monitoring an extensive geographical area using the compact and controlled source system. This outcome underscores the efficacy and versatility of the B-PASS system, particularly in its ability to enable widespread monitoring of seismic activity within the region.

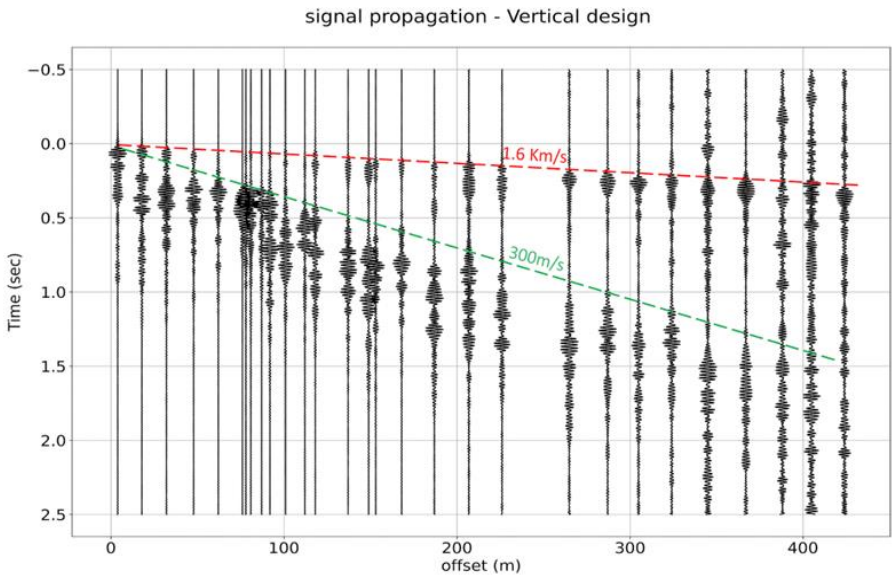

Figure 3.25 Clear Signal Propagation at 425 Meters Using Vertical Motion B-PASS: Body wave (red) and surface wave (green) (Ahmad et al., submitted).

3.5.3. Source repeatably

Original PASS (4-cm)

Recognizing the pivotal role of a stable source signal in ensuring accurate monitoring, my investigation delved into a comprehensive assessment of source signal stability over a 10-hour experiment. This rigorous examination aimed to minimize two significant sources of variation: temporal variations in the ground, encompassing the coupling between the source and the ground, and temporal variations in environmental noise.

To mitigate the impact of temporal variations in the ground, including coupling conditions, I strategically collected monitoring data in a parking area paved with asphalt, where such variations could be effectively ignored (Figure 3.26). Additionally, a pragmatic approach was employed by calculating the transfer function between two geophones positioned approximately 2 meters apart, thereby bypassing temporal variations in the ground. In the commitment to minimizing environmental noise, particularly from vehicular traffic, the evaluation was meticulously conducted during nighttime hours, spanning from 20:00 to 06:00.

The results of this comprehensive assessment, as illustrated in Figure 3.26, showcased remarkable consistency in both the phase and amplitude of the estimated transfer functions over the entire 10-hour duration. To further validate the stability of the PASS system, cross-correlations were conducted between these transfer functions and a reference (specifically, the transfer function derived from chirps 231 to 240, denoted by the black arrow in Figure 3.26a). The outcome, depicted in Figure 3.26b, underscored the striking similarity of the estimated transfer functions, providing unequivocal evidence that the PASS system consistently generates a stable monitoring signal.

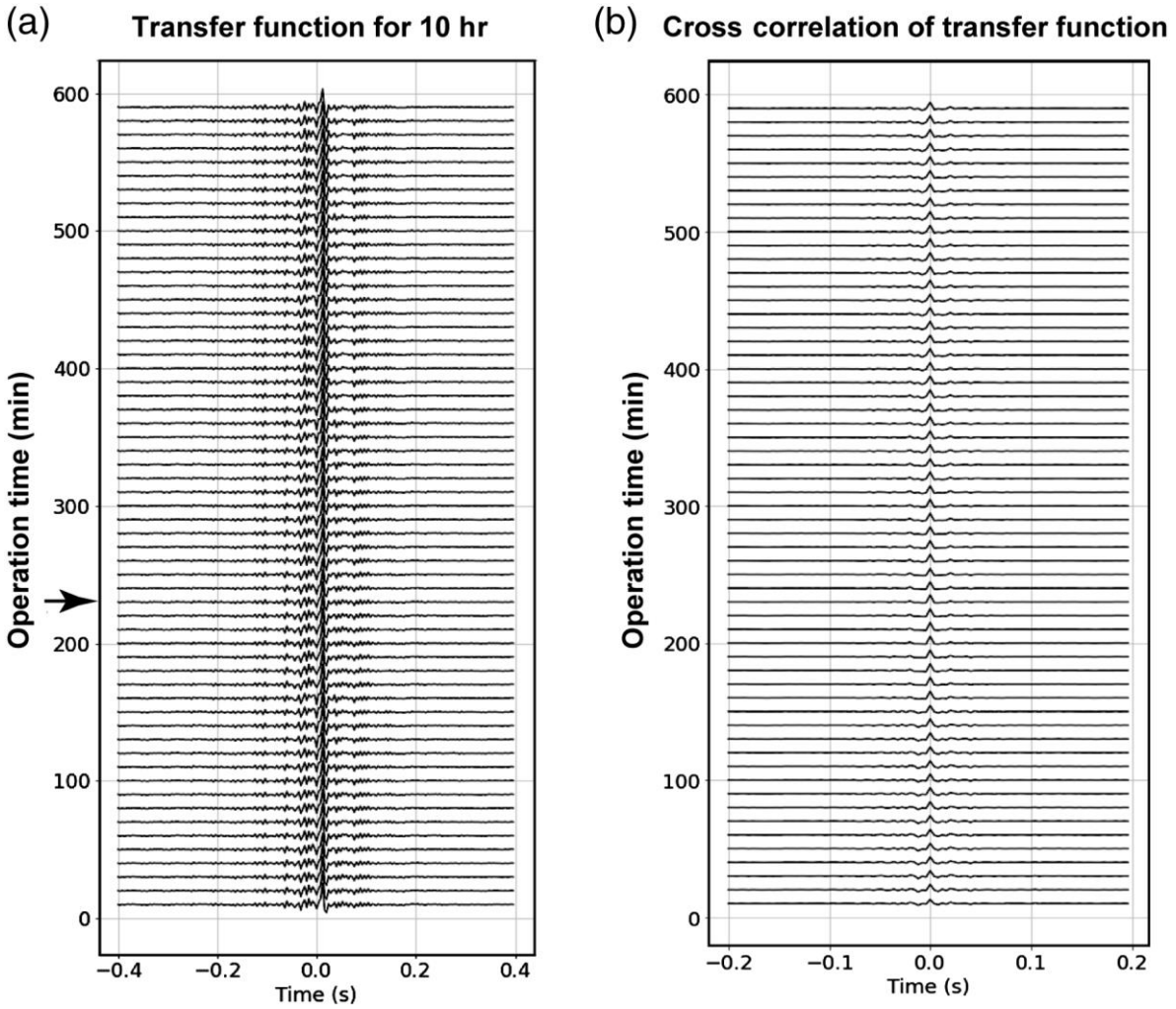

Figure 3.26 Evaluation of source stability. (a) Temporal variation of the transfer function in stable ground and minimal variation of environmental noise. Each trace is a stack of 10 transfer functions; traces are displayed every 10 shots. (b) The cross-correlation of the transfer function is shown in panel (a). The reference transfer function for the cross-correlation analysis is indicated by the black arrow in panel (a). The similarity of the cross-correlations indicates a stable source signal (Tsuji et al., 2022).

B-PASS

Seismic monitoring aims to provide consistent and reliable insights into subsurface conditions. The integrity of these insights directly depends on the source signals' stability and consistency. The stability of the source signal is a cornerstone for obtaining reliable seismic data. Variations in the signal can introduce errors, subsequently compromising the monitoring results' accuracy and reliability. Recognizing this, I undertook a rigorous approach to evaluate the consistency and stability of the source signals generated by the B-PASS system. A prolonged operation duration of 19 hours was chosen to provide a reliable dataset, ensuring that any anomalies or fluctuations in the signal could be readily identified. A stable source signal confirms that any variations detected in the recorded data indicate actual changes in the subsurface conditions, not artifacts introduced by defects in the source signal itself. So, I used the source function (sweep) to measure any change through time by comparing the source functions.

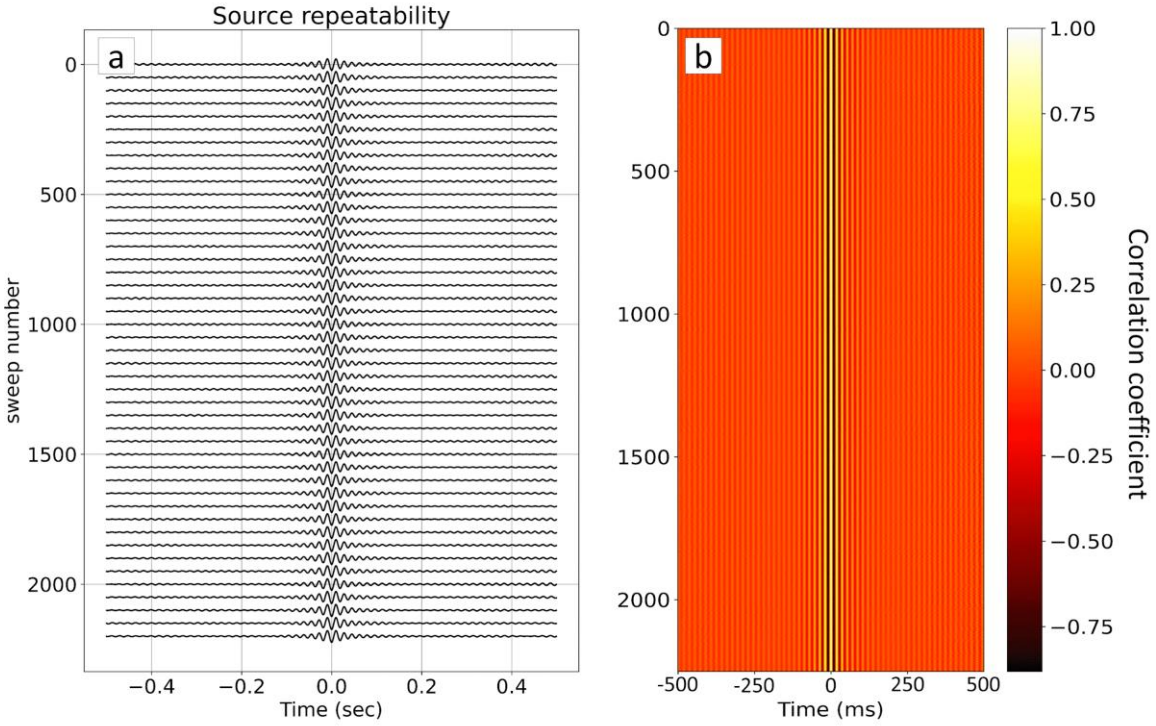

Figure 3.27 Stability Illustration: (A) Source averaged every 50 sweeps. (B) The correlation coefficient between the first sweep and all sweeps indicates consistent signal stability throughout.

The results (Figure 3.27) illustrate an experiment on the B-PASS system's stability. The phase and amplitude of the estimated transfer functions exhibited minimal variations over an extended period of 1126 minutes or approximately ~19 hours, covering 2,250 sweeps at deep 0.5 meters in the borehole. This consistency indicates the system's capability to generate a stable monitoring signal over prolonged durations, a pivotal feature for continuous monitoring applications. Further validation of the signal's stability was obtained through the cross-correlation analysis. I could quantify the signals' similarity over time by comparing the estimated transfer functions with a randomly chosen reference sweep. The high degree of similarity observed, as depicted in Figure 3.27b, reinforces the system's consistency in generating stable signals. In essence, the findings from this evaluation provide a robust endorsement of the B-PASS system's capabilities. With a reliable and consistent source signal, the B-PASS system ensures that the insights obtained from seismic monitoring are accurate and dependable, offering a valuable subsurface exploration and monitoring tool.

3.5.4. Vertical vs. Horizontal ground motions of B-PASS

The B-PASS system can generate both P and S waves, contingent upon the specific design being utilized. This encompasses vertical and horizontal motions, which are contingent upon the rotational axis configuration within the B-PASS system. To gauge the impact of each B-PASS system design, I conducted a comparison using three-component seismometers in profile 1, positioned in very close proximity (up to 100 meters away from the borehole). The objective was to observe how vertical and horizontal motions manifest at the same offset. To quantify the strength of motion in each component for seismometers at profile 1, I employed the root-mean-square (RMS) for a single sweep. The calculation is conducted using the following function(3.3):

$$RMS = \sqrt{\frac{1}{N}\sum_{i=1}^{N} x_i^2} \qquad (3.3)$$

Here, *N* represents the number of samples, and *Xi* denotes the amplitude of the motion in each component (Orfanidis, 1996) at each seismometer in profile 1 and shows the results after normalization in Figure 3.28.

By employing this approach, I can effectively assess and compare the intensity of motion for both vertical and horizontal components, shedding light on the specific effects of the B-PASS system design on seismic wave generation and propagation at the targeted seismometer location.

Consequently, records captured by the three-component seismometers at profile number 2 yield multiple wavefields. The transfer function derived from the vertical source and receiver records is indicative of P-wave propagation, while the transfer function originating from the horizontal source and receiver represents S-wave propagation.

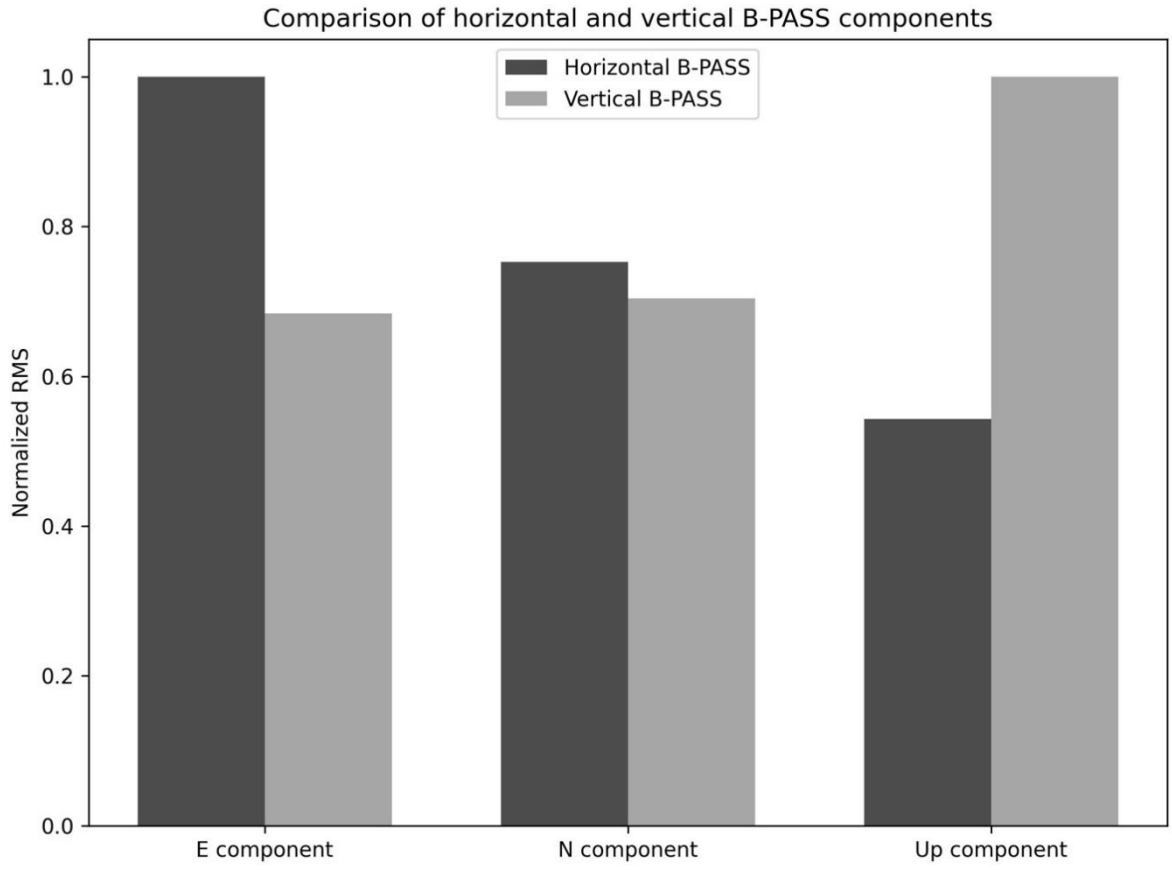

Figure 3.28 Comparison of RMS of each Motion Component (E, N, UP) between Vertical and Horizontal PASS Designs (Ahmad et al., submitted).

3.5.5. Effect of Urban Noise on B-PASS Signal

The influence of ambient noise resulting from human activities on the acquired signals is a significant consideration, especially given the relatively weak nature of the recorded signal. To assess this impact, I undertook an evaluation by implementing the B-PASS system during nighttime hours (18:40 to 20:00) as well as daytime hours (6:40 to 10:00). The objective was to discern the effect of minimizing environmental noise, particularly from vehicle traffic, during the stacking process. This assessment was conducted by comparing the outcomes of nighttime and daytime B-PASS operations. In this assessment, I concentrated on profile 3 and employed the B-PASS system at a depth of 50 meters, employing frequencies within the range of 10 to 50 Hz. The stacking process involved a total of 400 sweeps (equivalent to 3.3 hours) for both nighttime and daytime shifts. The intention was to discern any differential impact of human activities' noise on the stacking process, and the results are depicted in Figure 3.29.

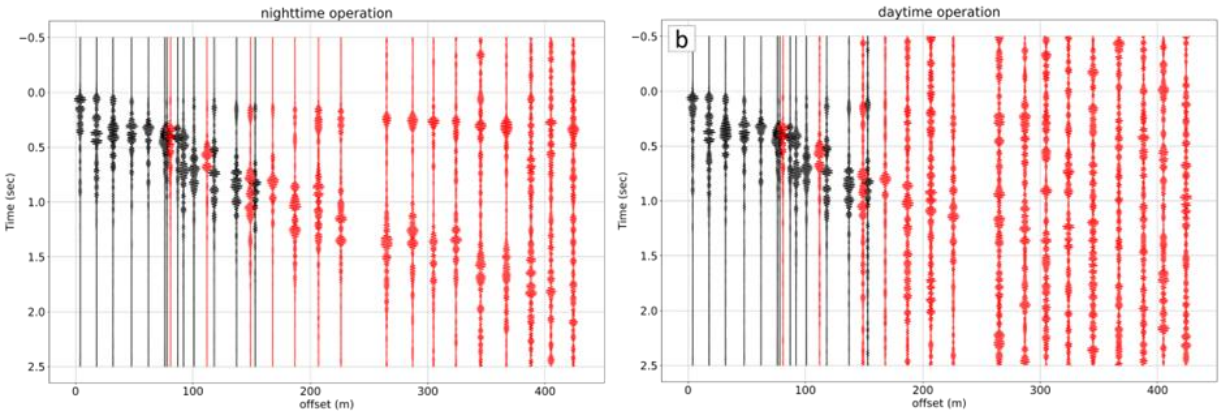

Figure 3.29 Signal Propagation with 400 Stacked Sweeps: (a) Nighttime sweeps (6 p.m. - 9:20 p.m.). (b) Daytime sweeps (6 am - 9:20 am). Red traces correspond to Profile 3 near the main road.

To delve further into the analysis, I also calculated the Probability Power Spectral Density (PPSD). This method allows us to evaluate the field noise while showcasing the distribution of power spectral density values across frequencies and time(Nimiya et al., 2021).

This graphical representation can be instrumental in identifying patterns, trends, and anomalies within seismic data. It's worth noting that a signal's power spectral density (PSD) is typically computed through the application of the Fourier transform(Shearer, 2019). The PPSD adds a probabilistic aspect to the PSD by calculating the probability density of the PSD values at each frequency. For continuous-time signals, the PSD can be mathematically defined as the following function (3.4) :

$$S(f) = \lim_{T\to\infty} \frac{1}{T} |X(f,T)|^2 \qquad (3.4)$$

where *S(f)* is the power spectral density at frequency *f*, *X(f, T)* represents the Fourier transform of the signal within a time window *T*. In this context, it serves as a crucial component of evaluating the effects of ambient noise on the acquired seismic data.

As depicted in Figure 3.30b of the Probability Power Spectral Density (PPSD) spectrogram, a discernible pattern emerges. Notably, a relatively elevated amplitude, measuring approximately -70 dB, consistently emerges each day between the hours of 5 a.m. and 8 p.m. This occurrence transpires across the frequency range of 10 to 100 Hz. Remarkably, this frequency range squarely aligns with the operational range of the B-PASS system (10-50 Hz). The recurring presence of this elevated amplitude signifies a significant observation. It unequivocally suggests that human activities contribute substantially to the ambient noise, exerting a notable interference on the comparatively delicate signals harnessed by the B-PASS system. The coherence between the detected noise pattern and the operational frequency range of the B-PASS system strongly indicates that this noise is indeed a considerable factor affecting the integrity of the B-PASS signals.

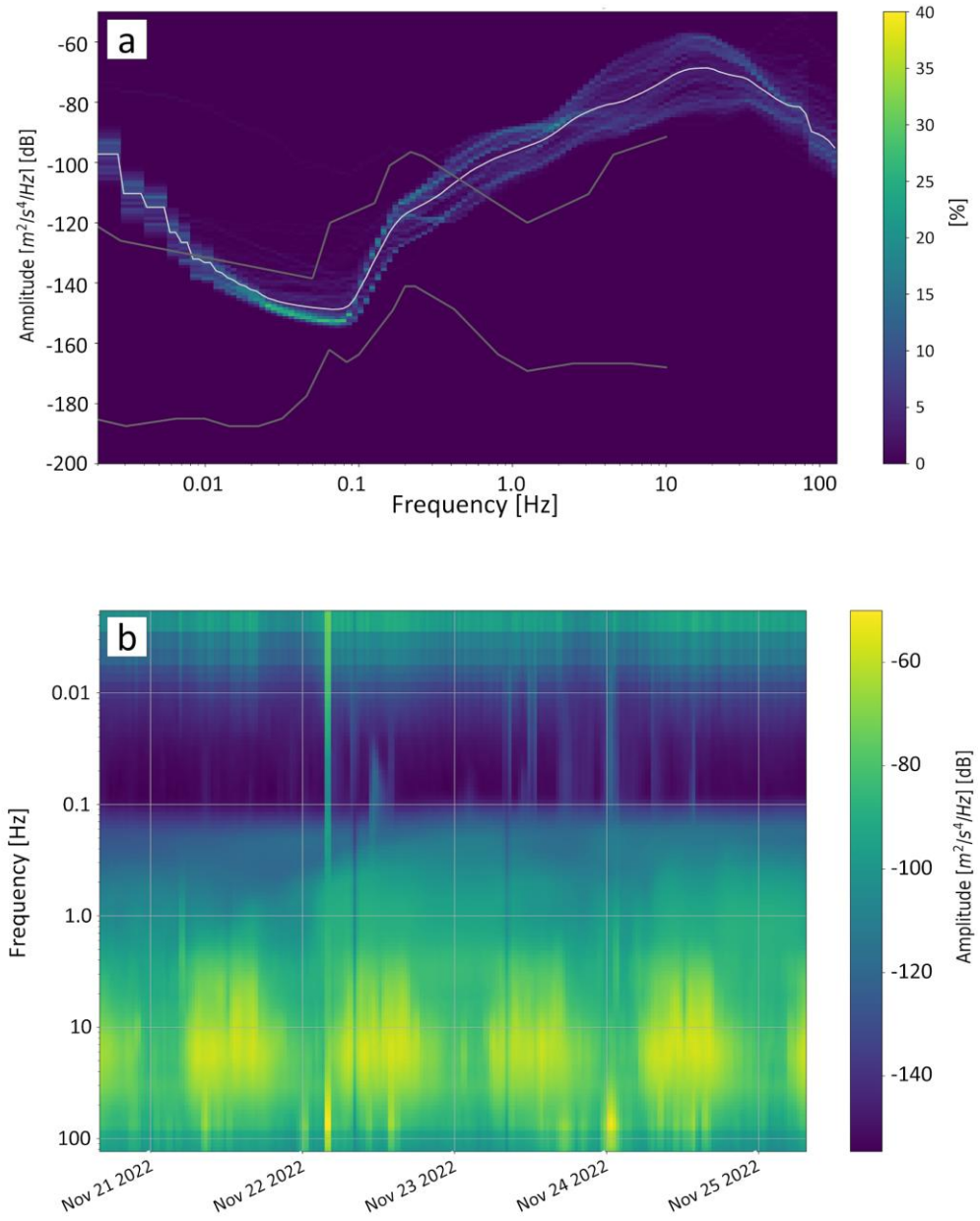

Figure 3.30 (a) PPSD for the geophone near the well with the mean represented by the white curve. (b) Spectrogram of PSD for the period 20-25 November (JST) (Ahmad et al., submitted).

This realization underscores the critical importance of accounting for and mitigating the impact of human-induced noise in seismic data acquisition and analysis. The harmonious alignment of the noise pattern with the B-PASS operational range necessitates thoughtful strategies for noise reduction and signal enhancement, further reinforcing the need for meticulous considerations in optimizing the effectiveness of the B-PASS system for accurate and reliable seismic data interpretation.

3.6. Conclusions

In conclusion, this comprehensive analysis underscores the significant advancements in borehole seismic survey techniques, primarily through developing and applying innovative systems like B-PASS and HE-PASS. Drawing inspiration from the original PASS design, these systems stand out for their specialized design tailored for borehole use, effectively addressing challenges like surface noise interference and preserving borehole casing integrity. The B-PASS, with its ability to generate stable, low-energy seismic signals through eccentrical mass rotation, has proven effective in monitoring large areas and detecting deep subsurface waves, with field tests verifying its effectiveness up to 425 meters horizontally from the borehole location.

The HE-PASS system further enhances this capability, achieving even greater signal propagation over 1 km with just 60 minutes of operation. Both systems' adaptability, demonstrated by their varied applications in monitoring CCS projects, landslides, volcanoes, earthquake faults, and built structures, and their environmental friendliness, underscore their potential to revolutionize seismic monitoring. The collaboration with research institutions and industry leaders is envisioned to refine these tools further, increasing their adoption and impact in diverse geological settings, including mountainous areas and extraterrestrial environments. With these advancements, I stand on the cusp of a new era in seismic monitoring, poised to enhance safety, efficiency, and environmental sustainability in geoscience and engineering applications.

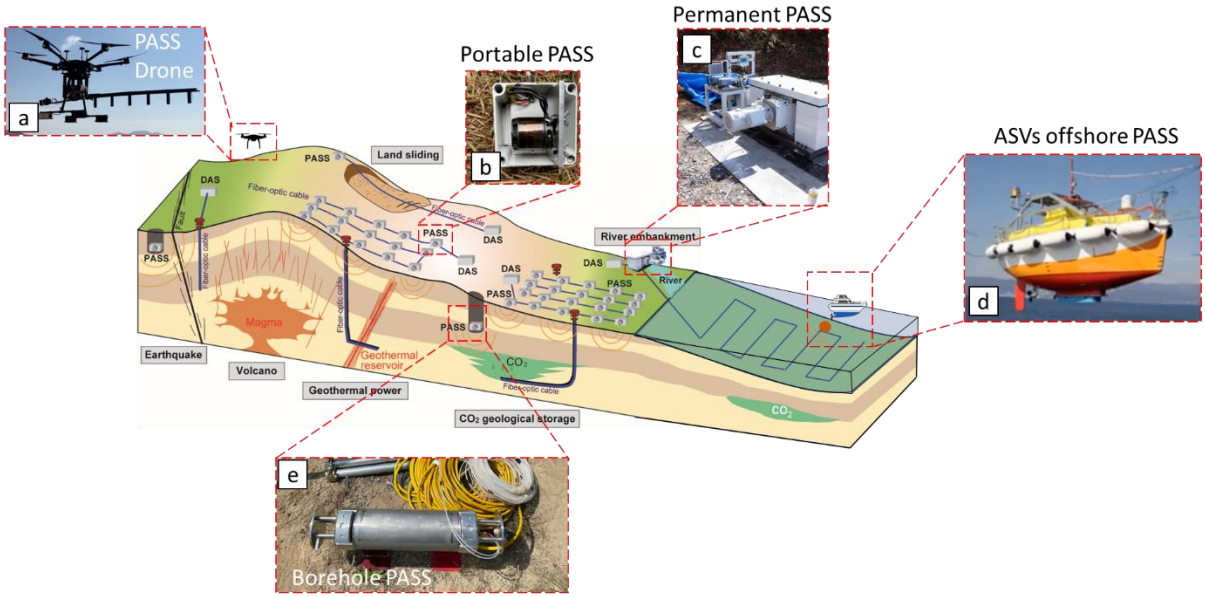

Figure 3.31 Schematic images of various PASS deployments for monitoring modified from(Tsuji et al., 2021). (a) shows the PASS on the Drone (Tsuji et al., 2021 SEGJ), (b) shows the 4-cm PASS(Tsuji et al., 2022; Ahmad B. Ahmad et al., 2023), (c) shows the ACROSS(Tsuji et al., 2021), (d) shows the offshore PASS speaker, and (e) shows the borehole PASS (Ahmad et al., submitted). The image was modified from (Tsuji et al., 2021).

These systems' capabilities in detailed imaging, long-range monitoring, and adaptability in challenging environments position them as pivotal tools in seismic research and environmental monitoring. Their potential in assisting CCS projects and other geoengineering initiatives reflects a promising step towards more effective and sustainable monitoring methods, contributing to the broader goal of environmental preservation and safety in various applications. The collaboration between research institutions and industry leaders and continued innovation in these systems are essential for their evolution and broader adoption, paving the way for a greener, safer future in seismic monitoring and geological research.

Chapter 4

Automatic interpretation Based on 3D offshore seismic data

4.1. Introduction

Slumping, the down-slope sliding of rock masses or unconsolidated material (Tarbuck and Lutgens, 1984), is commonly caused by seismic events (Perucca et al., 2014). Slump structures develop when land masses move along planar surfaces(Girty, 2009). Along continental margins, slumps mainly result from earthquakes and can cause disastrous tsunamis. In 1964, 124 people were killed in Alaska (USA) after a M_w 9.2 earthquake caused submarine slumps that produced destructive tsunamis along the Alaskan coast (Press and Jackson, 1965). In March 2011, a M_W 9.0 earthquake struck Tohoku (on the northeast coast of Honshu, Japan), and the resultant tsunami caused extensive damage. The tsunami was generated, at least in part, by seafloor slumping (Kawamura et al., 2012).

Slumps are related to hydrocarbon resources. They influence the hydrocarbon migration and accumulation processes (Kret et al., 2020). In the Sanriku-oki area (i.e., plate convergent margin in northeast Japan), many slump units identified from 3D seismic data control gas migration, creating gas pockets above slump edges (Eng and Tsuji, 2019). Under particular temperature and pressure conditions, these free gases develop into gas hydrates (Chhun et al., 2018). The slump units also influence the gas hydrate (Kret et al., 2020). Although gas hydrates are considered a potential energy resource, gas hydrate dissociation can cause submarine landslides, such as the Storegga slide off the east coast of Norway (Hühnerbach and Masson, 2004). Slumping processes have been studied using geophysical techniques based on 2D and 3D seismic data (Lee et al., 1999; Martinez et al., 2005). Slump units are generally classified as simple or complex slumps (Thierry and Pierre, 1996): simple slump deposits typically do not generate other failures, whereas complex slump deposits can destabilize neighboring areas.

Therefore, complex slumps are difficult to interpret manually, requiring extensive knowledge of local geological features and familiarity with their expression in seismic profiles. Listric normal faults are commonly associated with complex slumps in forearc basins (Martinez et al., 2005); tsunamis in these regions have been attributed to mass movements caused by extensional slumps on these faults (Tsuji et al., 2013). Thus, it is important to understand the distributions and geometries of listric faults to reveal the generation mechanisms of tsunamis and slumps. Such faults further work as hydrocarbon migration pathways and influence the gas and hydrate reservoirs (Chhun et al., 2018). The manual interpretation of such geological features (e.g., slump units and faults) from seismic profiles is difficult, time-consuming, and requires extensive geological knowledge. Also, such features are often overlooked within large 3D seismic volumes. However, machine learning (ML) offers techniques that can be applied to interpret slumps and faults from 3D or 4D (time-lapse) seismic data. The ML-based methods could identify the slumps and faults with many characteristics.

An effective and well-developed ML method employs convolutional neural networks (CNNs), is flexibly designed, and can solve many problems, even in the exploration of geophysics (e.g., Zhao and Mukhopadhyay, 2018). Deep learning techniques have been recently used to identify different kinds of seismic facies automatically based on manual labels (Bugge et al., 2018; Zhao, 2018; Puzyrev and Elders, 2020; Wu et al., 2020; Zhang et al., 2020, 2021). Originally inspired by biological processes in the brain (Fukushima, 1988), neural networks can classify multi-dimensional data (e.g. Tsuji et al., 2009). CNN consists of four components: (1) learnable filters, (2) activation functions, (3) pooling/downsampling layers, and (4) fully connected layers. The first layer acts as a features extractor, also known as the convolutional layer, that contains a trainable filter to extract low-level features, whereas the last component is a fully connected neural network that classifies the extracted features. Here, I investigated whether CNN can be used on real 3D seismic data.

The convolutional neural networks (CNNs) were used effectively to map the distribution of complicated geological formations (e.g., slump, fault) on Japan's eastern coast. CNN's convolutional filters produce multi-synthetic properties that are utilized for classification using shallow Multilayer Perceptron (MLP). I employ backpropagation methods to improve a

convolutional filter and two fully connected neural layers for 10,000 iterations using manually labeled 2D seismic sections to detect geological structures.

The 3D automated results were compared qualitatively to the manual interpretation by experts. The result includes a complete study of the distribution pattern of gas channels and precise information for imaging the gas chimneys. The technique used in the current work is advantageous for imaging gas chimneys, channels, and other conventional and unconventional hydrocarbon reservoir rocks in diverse basins in any part of the world.

4.2. Data

4.2.1. Nankai Trough Data

To train, validate, and test my CNN-based slump identification scheme, I used 3D multichannel seismic reflection data acquired in the Nankai Trough (Figure 4.1), a feature of the subduction zone between the Philippine Sea and Eurasia plates, which extends 900 km SW–NE offshore southwest Japan (Tsuji et al., 2005). Large earthquakes (M_W ~8) occur at intervals of 100–150 years (Ando, 1975). Slump units and normal faults are well developed in the Kumano forearc basin above the accretionary prism, and methane hydrate and free gas accumulations have been identified in the forearc basin sequences (Chhun et al., 2018).

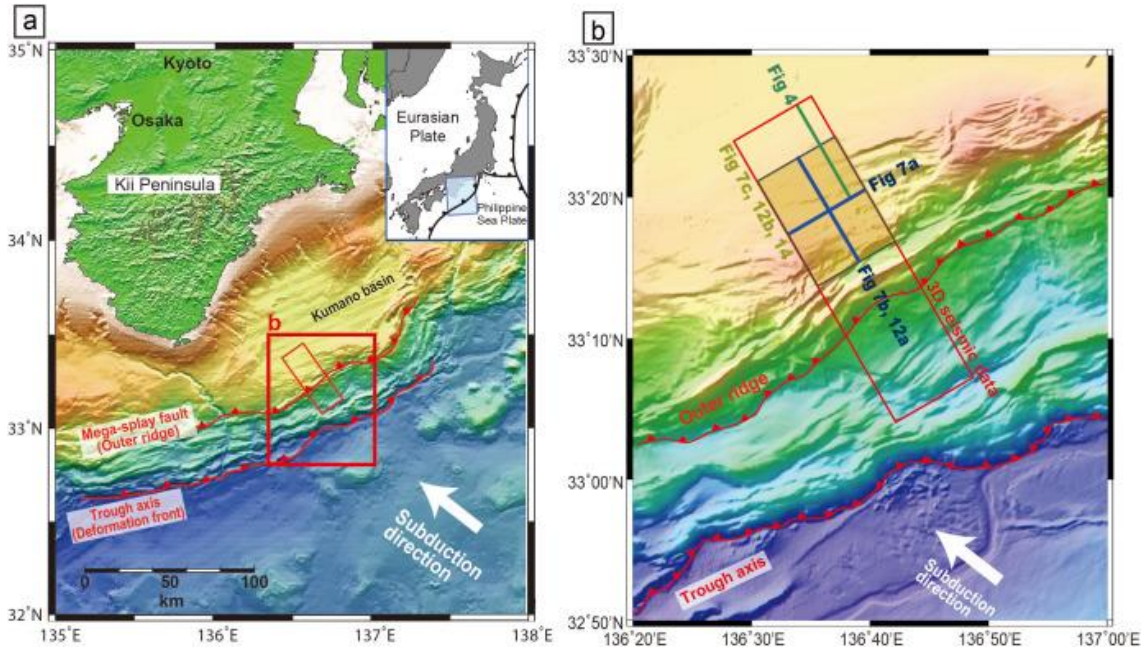

Figure 4.1 (a) Map of the study area and location of the 3D seismic dataset in the Nankai Trough. (b) Enlarged view showing individual lines used to visualize my results.

The seismic data processing included low-cut filtering at 5 Hz, frequency-wavenumber filtering, 3D radon filtering, velocity analysis, 3D pre-stack time migration, and 3D post-stack depth conversion (Moore et al., 2009). The 3D seismic data volume used in this study includes inlines 2,135–2,745 at intervals of 18.75 m and crosslines 3,000-7,990 at intervals of 12.50 m.

The seismic data were sampled at an interval of 4 ms, equivalent to 5 m vertical resolution in the interval of the Kumano basin sequence (Chhun et al., 2018; Pape et al., 2014). Although the seismic data show many complex structures that indicate slumping units and fault sets, interpreting the spatial distribution of these geological phenomena is difficult due to technical 3D imaging limitations and the complexities of the sub-bottom geological structures (Uraki et al., 2009). Therefore, I automatically applied CNN to interpret slumps and faults within the 3D seismic volume.

I used the northwest portion of the seismic survey area covering the forearc basin (Figure 4.1b). The data were manually interpreted based on known slump units (Lackey et al., 2018). These manual interpretations trained and validated the CNN model. I prepared 85 manually interpreted seismic sections and randomly divided them into a ratio of 3:1 for training and validation, respectively. The number of training sections was limited due to the difficulty of correctly interpreting a large volume of 3D seismic data and the limited trusted previous interpretations. In the Nankai data or many other cases, I have data for testing, but I have a few interpreted data to build the training data set. As detailed in the following sections, I addressed this problem by creating training data using different configurations.

To test the generality of my CNN model for slump identification, I used another 3D seismic data from far from the Nankai Trough area. The 3D seismic volume was acquired in the Sanriku-Oki forearc basin by the Ministry of Economy, Trade and Industry Japan in 2008 under the National Program for Oil and Gas Prospecting (Kret et al., 2020).

4.2.2. West Delta Deep Marine Data

The Nile Delta, situated in northeastern Africa, is considered a quintessential example of the world's deltas. It has evolved through various geological events influenced by the regional tectonics of the Mediterranean, which has sculpted its current physiographic features.

Today, the delta is recognized as a significant region for gas reserves, with promising prospects for future petroleum exploration. Located off the coast of Egypt, the West Delta Deep Marine (WDDM) concession spans an area of approximately 6,150 square kilometers along the northwestern boundary of the Nile cone, roughly 50 to 100 kilometers offshore. This concession is a key contributor to Egypt's energy sector, supplying about two-thirds of the nation's gas production. Despite its significance, there remains a gap in comprehensive geological knowledge of the Nile Delta due to the scarcity of detailed subsurface data. Gas reserves in the WDDM concession occur within a range of stratigraphic layers, extending from the Lower Miocene to the Lower Pliocene epochs. The area's potential was further evidenced by drilling thirteen consecutive exploratory and appraisal wells across nine different fields. As of the early 2000s, the Nile Delta's offshore regions have rapidly gained recognition as a significant gas-producing province, as reported by Samuel and colleagues in 2003(Ismail et al., 2021).

The investment landscape in Egypt's gas and oil sector, particularly in 2003, reflected robust international interest, with investments estimated at around $2 billion. The natural gas sector, in particular, was experiencing rapid growth, according to Bermúdez-Lugo in 2003. The WDDM concession, depicted in Figure 4.2, was acquired in 1995 by the BG Group.

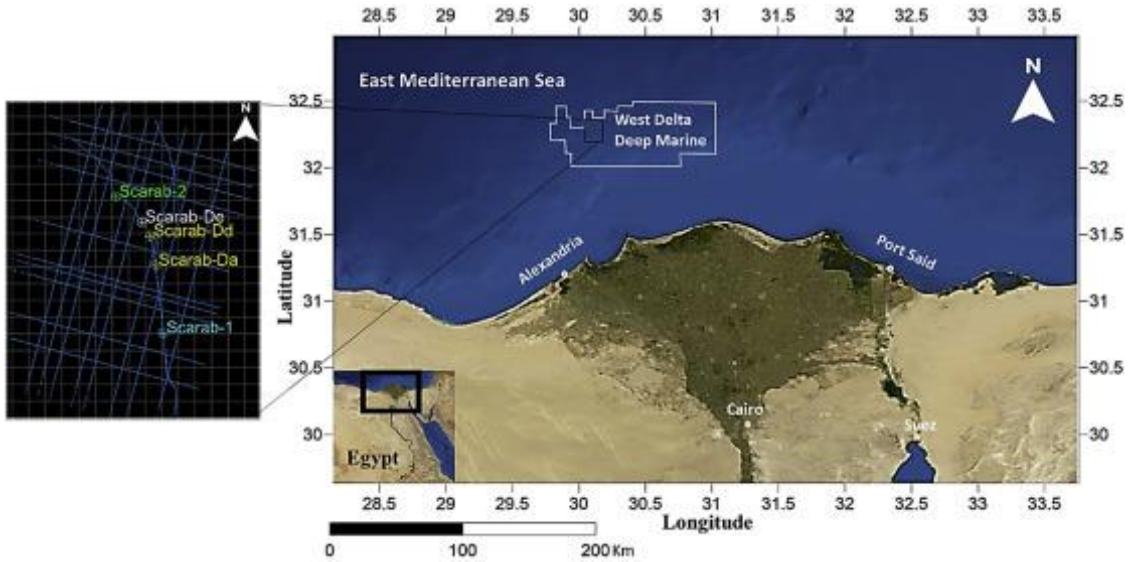

Figure 4.2 Map of north Egypt showing the location of West Delta Deep Marine concession with the locations of the wells and the 2D-seismic lines, modified from Google Earth.

4.3. Methods

4.3.1. CNN architecture

CNN breaks problems into smaller-scale tasks. In face recognition (e.g., mouth, nose, eyes), CNN breaks facial features: edges, curves, and circles. These objects are easily detected using an edge-detecting Gabor-like filter (Gabor, 1946). To detect higher-level features such as slump units and faults on seismic reflection profiles, CNN combines low-level features into higher-level features and finally builds detectors for each feature class.

All CNNs comprise two main layers: a convolutional layer and a fully connected layer (Figure 4.3). In the convolutional layer, nodes in the sublayer receive the input and apply muli-channels kernel filters tuned to extract specific characteristics; multi-filters are also applied to highlight combined or multiple features.

The output of the sublayer serves as an input for second convolutional sublayers, and this procedure repeats until high-level features are detected. Example feature maps from each convolutional sublayer in my seismic interpretation are shown in Figure 4.4. For any 2D input and filter, the output from a convolutional sublayer is described as:

$$Y_{i,j} = f(h \times X)_{i,j} = f\left[\sum_{m=-c}^{c} \sum_{m=-c}^{c} (h_{m,n})(X_{i-m,j-n})\right], \quad (4.1)$$

where *Y* is the output, *X* is the value of the input neurons, *h* is the value of filter weight for the learnable filter with *m* and *n* coordinates of the kernel filter (convolutional filter), *c* is the distance between the center of the filter and the edge of the filter, *i* and *j* are the indexes of rows and columns of the convoluted output *Y*, and *f* is the nonlinearity activation function. The activation function introduces nonlinearity into the multiplication result, determining whether the filter *h* has detected a given feature and ultimately indicating whether the feature is present in the image. Positive values in nodes represent the features that guide CNN to find the targeted geological structures.

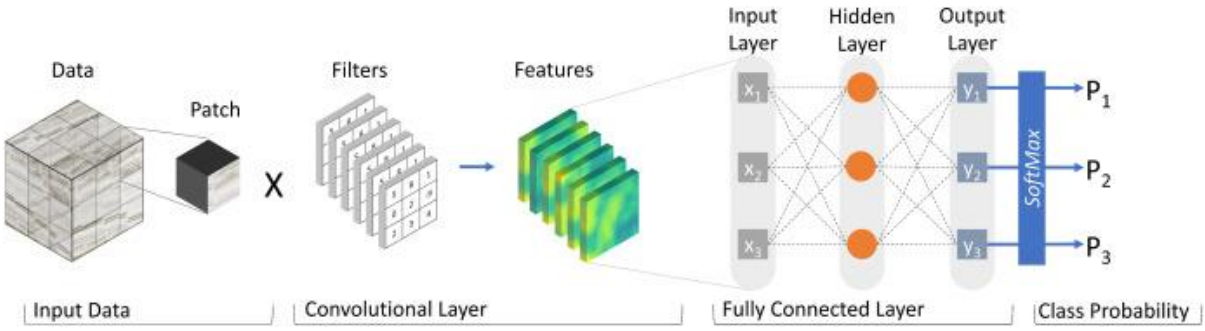

Figure 4.3 The architecture of the convolutional neural network used in this study. The input data is a 65 × 65 x 65 seismic patch, going through a 3D convolutional layer and fully connected layer.

Because the nonlinearity of the nodes is suitable for learning more complex structures, I used the nonlinear activation function. One of the most common and effective nonlinearity functions is the rectified linear unit (Nair and Hinton, forthcoming), which returns zeros for all negative values and retains all positive values as follows:

$$f(x) = \max(0, x). \tag{4.2}$$

To help the network transform information about the spatial arrangement of pixel values into features containing information relevant to the classification task (the feature domain), I down-sampled between subsequent convolutional sublayers to decrease the spatial resolution. I used zero padding on the border of input data to prevent washing away some information at the borders and reduce the volume of input data by a small amount after each convolution layer. After the last convolutional sublayer, CNN achieves high-level feature classifications to help the network identify and classify the desired objects.

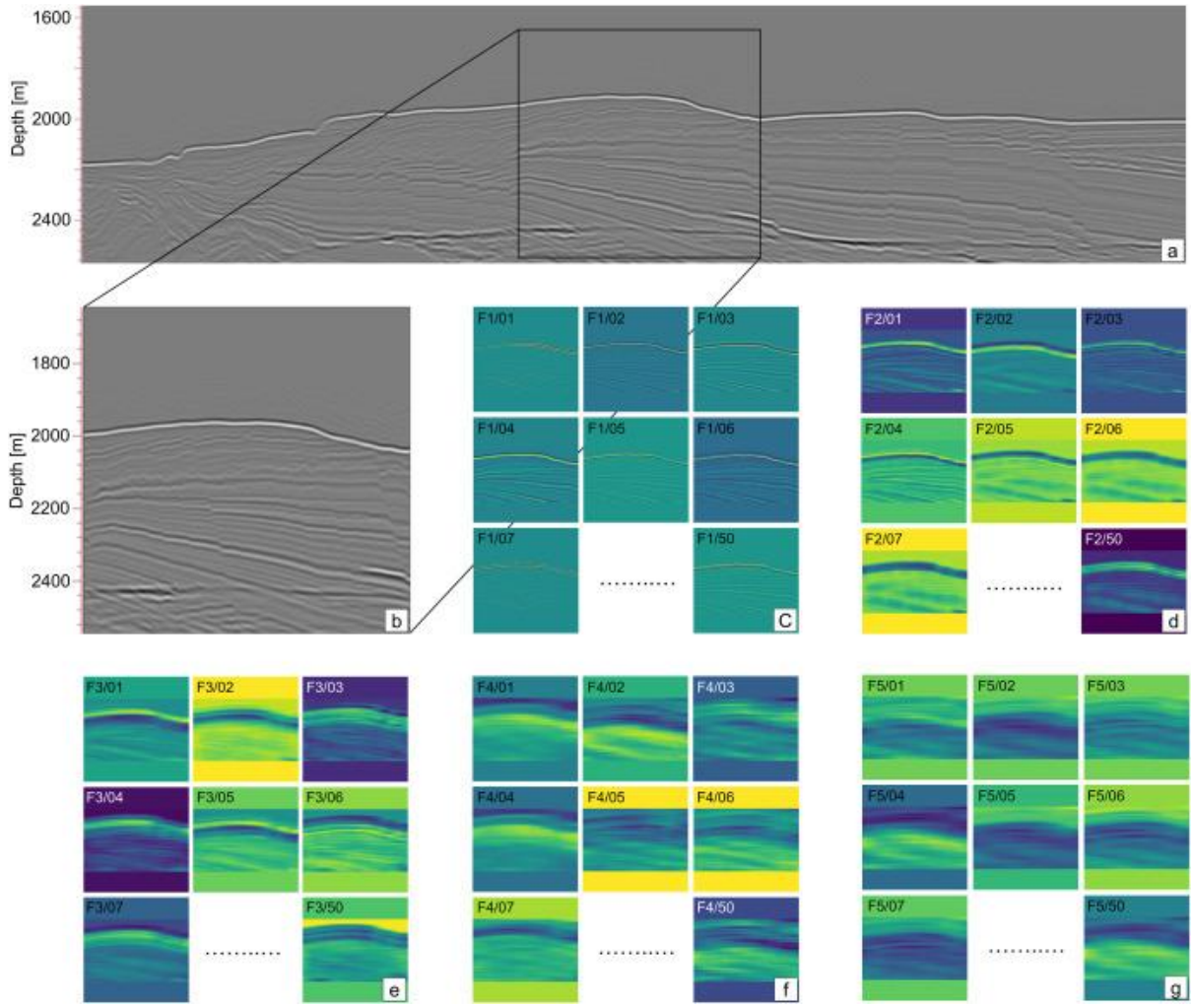

Figure 4.4 (a) Seismic profile from the 3D Nankai data, and (b) an example gray-scale seismic patch input into the convolutional layer. (c) The output of the first convolutional sublayer (50 low-level features), (d–f) the outputs of the second, third, and fourth sublayers, respectively, and (g) the output of the last convolutional sublayer (attributes)(Ahmad and Tsuji, 2021a).

Classification is then performed in the fully connected layer. The fully connected layer is a classifier and comprises input, hidden, and output sublayers. To reach the class (output) sublayer, I sent the input values to hidden sublayers by multiplying them by weights connected to the hidden sublayers as follows:

$$N_{hidden} = [X_1, X_2 \cdots X_n] \times \begin{bmatrix} W_{1-1} \\ W_{2-1} \\ \vdots \\ W_{n-1} \end{bmatrix} + b, \qquad (4.3)$$

where *N* is the value in a single neuron in the hidden sublayer, *X* is the list of input values in the input sublayer, *W* is the weights that start randomly and then determined after the training process to connect *N* and *X*, and *b* is a bias which allows shifting the activation function. Finally, each neuron is subjected to the SoftMax function (Shim et al., 2017) to normalize the probabilities of each class:

$$S(N) = \frac{e^N}{\sum_n e^{N_n}}. \quad (4.4)$$

The sum of S(N) across all feature classes for a given patch is 1.

After passing through the hidden sublayers, the fully connected layer should produce a true class for each seismic patch in the output sublayer. The architecture of the CNN model is similar to the architecture proposed for salt dome detection on seismic profiles (Wadeland et al., 2018).

4.3.2. Training and validation

To train the CNNs, I used the 3D seismic data in the Nankai Trough. The 85 sections were selected randomly to cover the entire portion of the 3D survey area (Figure 4.1b) and used in the training and validation process. Training sections were prepared manually by interpreting and labeling sections into two classes (the slumping area and the other in Figure 4.5). I used a small batch size of 32 with 16 samples from each class as hyperparameters (Claesen and de Moor, 2015). This amount of training data is relatively small and might not represent the entire study area; this is not due to a lack of data but to the difficulty in interpreting geological structures within 3D seismic volumes.

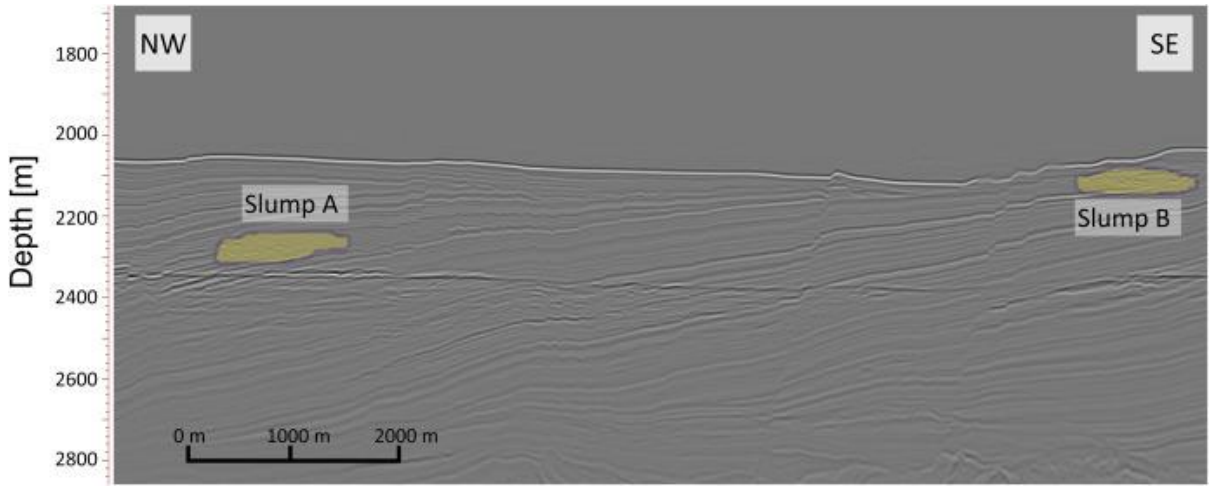

Figure 4.5 The seismic profile of inline 2,641 was used to train the CNN for slump identification. Two training classes were used, and slump units were highlighted on this profile. This profile contains two small slumps.

To solve the limited training data problem and increase the model accuracy, I applied random deformation of the original training patches as ±20% random stretching (Figure 4.7b), ±15° random rotation (Figure 4.7c), and random flipping (Figure 4.7d). The augmented data may include a single type of deformation, as shown in Figure 4.7b, c, d, or multiple deformations applied on the same data patch. I used the drop-out technique to prevent overfitting with a factor of 0.5 (Srivastava et al., 2014a). This augmentation approach simulates a larger training dataset (over 10,000 iterations) while avoiding overfitting (Waldeland et al., 2018), improving the accuracy of the model predictions (up to 90% in the validation process; Figure 4.8a). The error ratio of the training and validation process was evaluated using a cost function that indicates how much the network needs improvement (Figure 4.8b); a well-trained network minimizes the cost function. For the cost function, I used cross-entropy with the Adam optimizer. The Adam optimizer based on the Stochastic gradient descent technique to minimize the cost function (Kingma and Ba, 2015):

$$E = -\sum y'_k \log(y_k), \tag{4.5}$$

where y_k is the SoftMax (Eq. 4) output for class k and y'_k is either 1 if the prediction was correct or 0 if it was wrong. The training and validation processes were performed using a Tesla K80 GPU and lasted approximately 10 hours and 20 min for the entire training process.

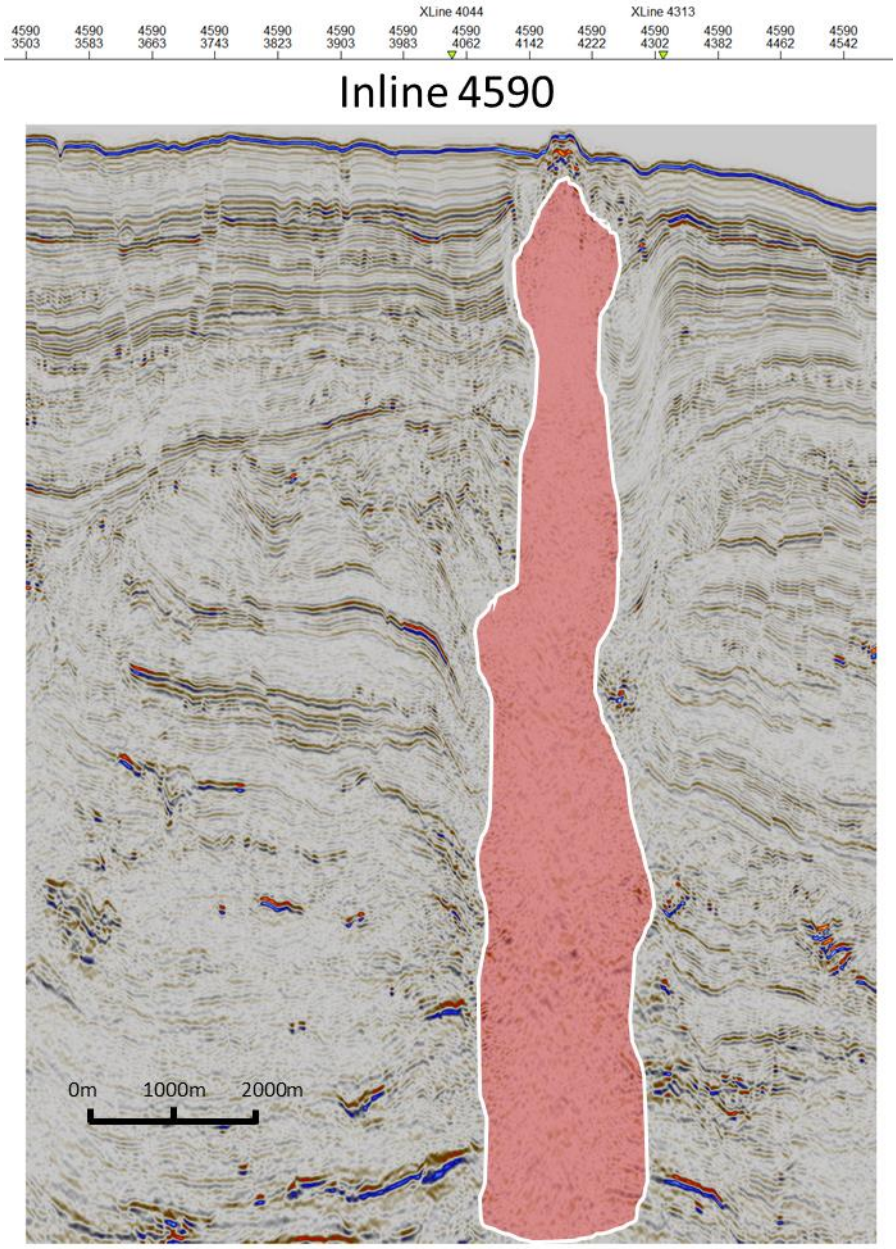

Figure 4.6 The seismic profile of inline 2,4590 was used to train the CNN for gas chimney identification. Two training classes were used, and slump units were highlighted on this profile.

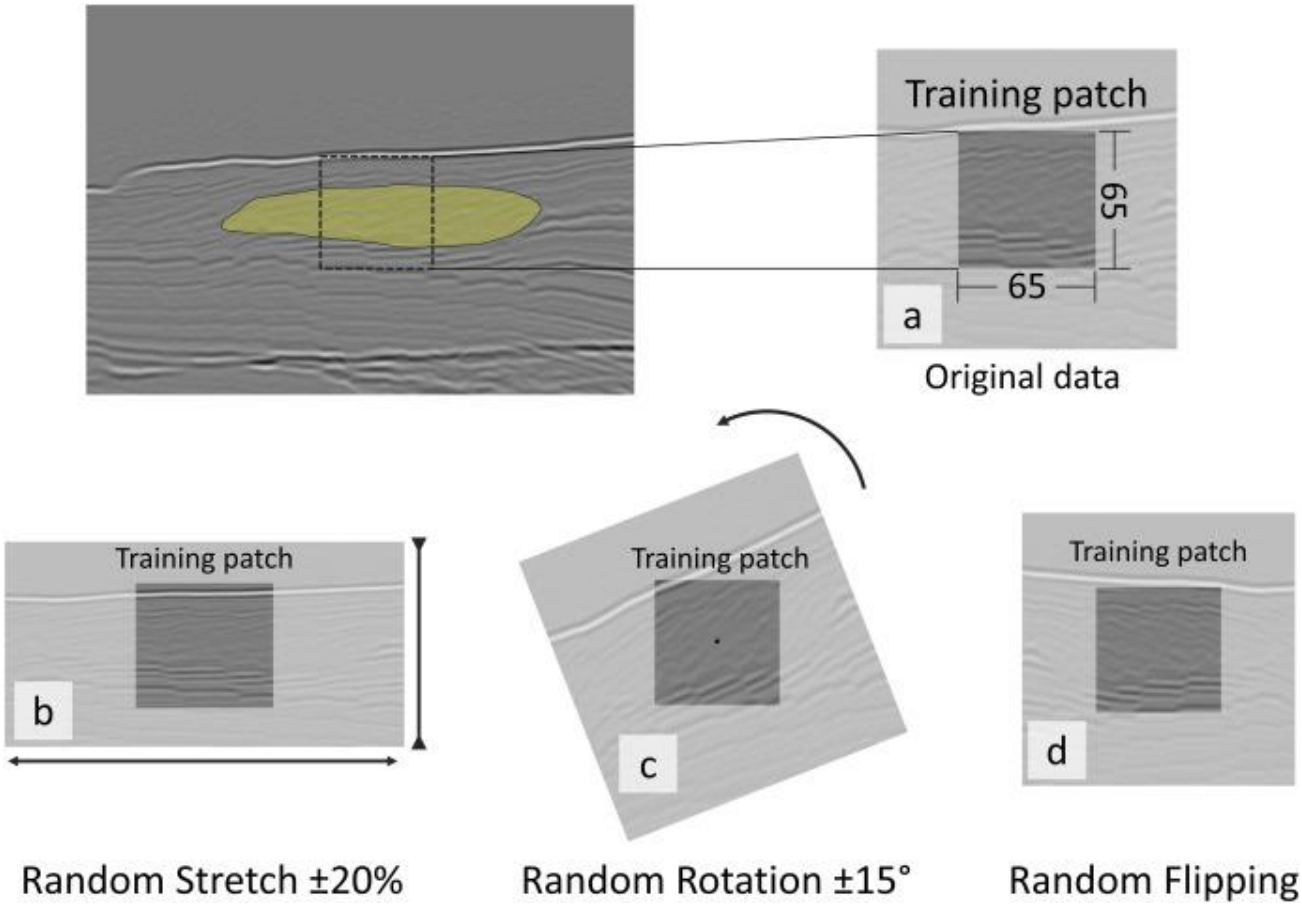

Figure 4.7 An example of the data augmentation process. (a) The original data patch before applying random deformations. (b) After applying random stretching with factor ±20 %, the data patch on the x- and y-axis. (c) The data patch after applying random rotation with factor ±15° around the z-axis. (d) The data patch after applying random flipping (Ahmad and Tsuji, 2021a).

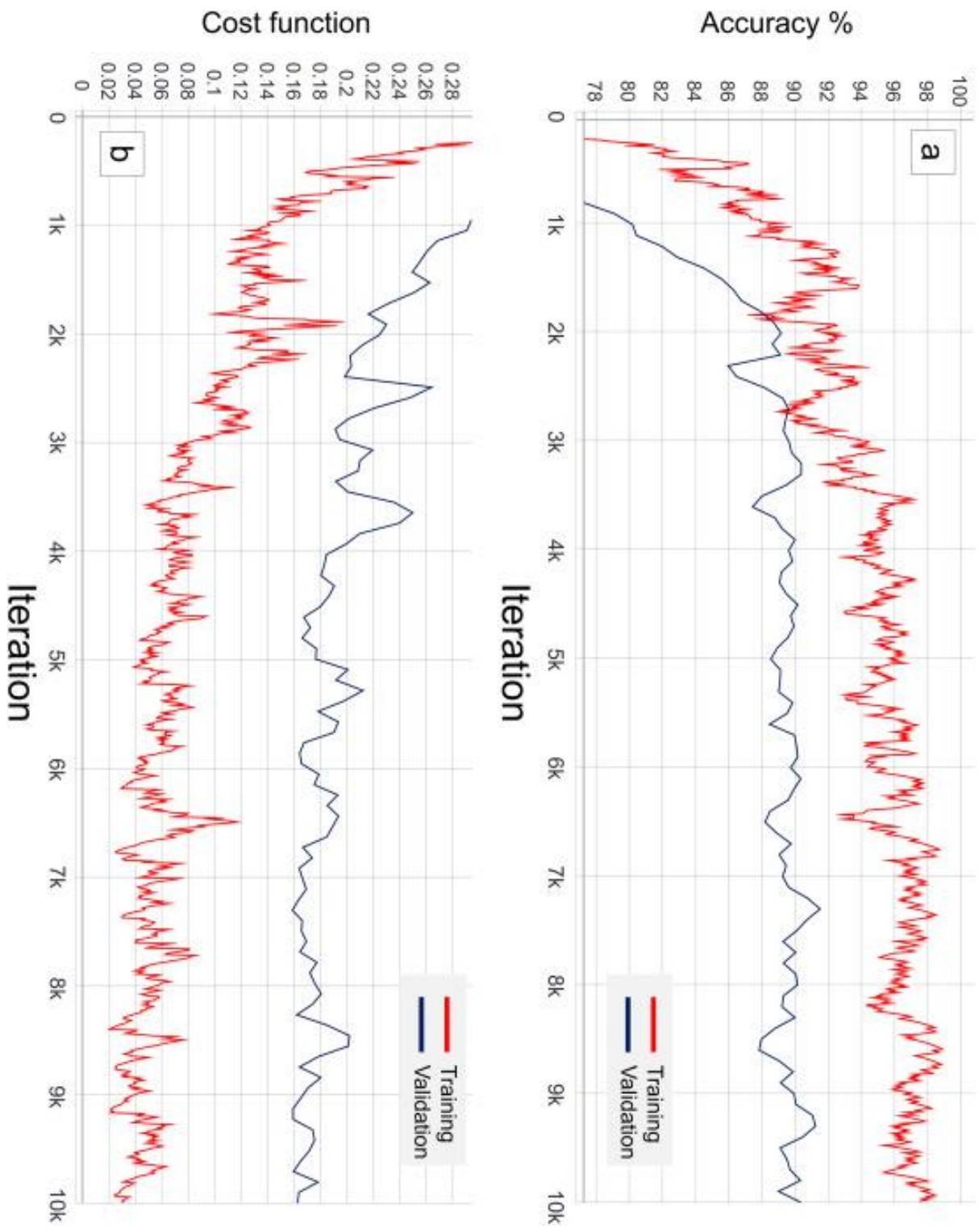

Figure 4.8 Improvement of the CNN over 10,000 iterations for training (red curve) and validation (blue curve) processes after smoothing by a factor (0.7). (a) The accuracy reached 98 % for the training process and reached 90 % for the validation process. (b) The cost function (cross-entropy) was reduced to 0.03 for the training process and reached 0.17 for the validation process (Ahmad and Tsuji, 2021a).

4.3.3. Analysis

The CNN analyzed small subsets (patches) of the 3D seismic dataset (with dimensions of 65 × 65 × 65 samples) and applied 50 multichannel 3 × 3 × 3 sample filters in each convolutional sublayer. I also tested patches of 32 × 32 × 32 samples and obtained the same result after a longer training. The filters in convolutional layers were applied every 4^{th} sample for the fault prediction model and every 16^{th} sample for the slumping prediction model.

I ran the algorithm using the Google Colaboratory Cloud platform with a Tesla K80 GPU with 25 GB RAM. Google Colaboratory is a research project based on the Jupyter Notebook for prototyping machine learning models on powerful GPUs (Bisong, 2019). The prediction process (class prediction and refitting of the results in the 3D seismic volume) for a 33-GB Nankai 3D seismic volume took ~24 min. For the Sanriku-Oki 3D seismic data, I used a GeForce RTX 2080ti GPU with 64 GB RAM to run the model. The prediction process for the 5.4GB Sanriku-Oki 3D seismic volume took 6 min without retraining.

4.4. Results and Interpretation

4.4.1. Slump prediction

To understand how the neural network identifies slumps, I must understand the input that the fully connected layer received (Figure 4.4g). These high-level feature maps represent attributes of the dataset, which the convolutional layer learned to identify during the training process for slump interpretation. I obtained 50 attributes, each highlighting specific geological features. These attributes might seem pointless individually, but their combined use led the neural network to identify slumps accurately. To identify the “slump” attribute, I selected small sections of the dataset in which slumps were present or absent.

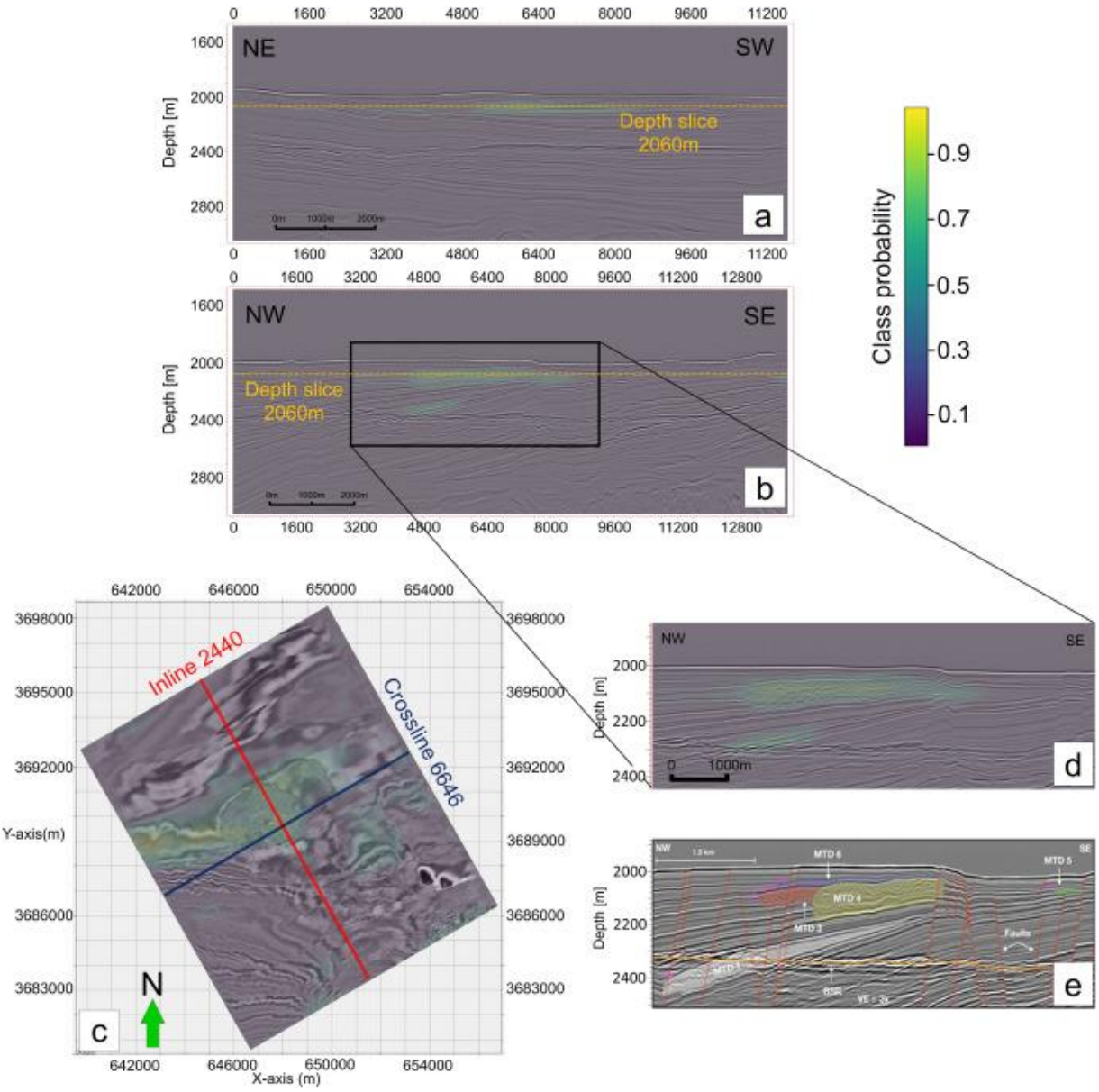

Figure 4.9 Results from the CNN highlighting a large slump in (a) crossline seismic profile 6,646, (b) inline seismic profile 2,440, (c) a depth slice at 2060 m below the sea surface, and (d) an enlarged view of the slump in (b) for comparison with (e) the slump (MTD 4) interpreted by Lackey et al. (2018).

The classification results of the full 3D dataset show that the network successfully delineated known slump units in the Kumano forearc basin (Figure 4.9). The CNN highlighted an area with a high probability of being a slump (warmer color in Figure 4.9). To assess the quality of the automatic interpretation, I compare it with a manual interpretation of an inline test section (Figure 4.9e). Slumps are commonly associated with sliding along landward dipping sedimentary sequences (5–7°; Lackey et al., 2018) and can be identified in seismic profiles

based on their chaotic reflections (Lackey et al., 2018; Eng and Tsuji, 2019). Based on the results shown in the depth slice (Figure 4.9c), I accurately mapped and delineated a huge slump across the Kumano forearc basin at 2,060 m below the sea surface (previously interpreted by Lackey et al., 2018) and other minor slumps that I have not interpreted by manual picking in the SE part of the seismic profile (Figure 4.9d).

Moreover, the ability to interpret slumps in a depth slice could discover an uninterpreted slump in the SE part of the seismic volume (Figure 4.9c). On the other hand, CNN has misinterpreted the SE part of MTD 4 Figure 4.9d) and the NW part of MTD1 (Figure 4.9e). The reasons for these misinterpretations are described in the discussion.

To clarify the 3D distribution of slump units, I applied a 0.5 threshold to the probability map and determined the boundaries of slumps detected by CNN. Figure 4.10 shows several large slumps detected by CNN. The youngest large slump (shown in Figs. 4.9a,c) is labeled with orange in Figure 4.10, covering an area of ~7 km^2 with ~1.3 km^3 volume, followed by an older slump labeled with blue (MTD1 in Figure 4.9e), covering an area of ~25 km^2 with 3.0 km^3 of volume. CNN detected other 12 smaller slumps with a volume between ~0.35 ~1.00 km^3, most of which are distributed in the south of the Kumano basin where normal faults are well developed due to uplifting of the outer ridge.

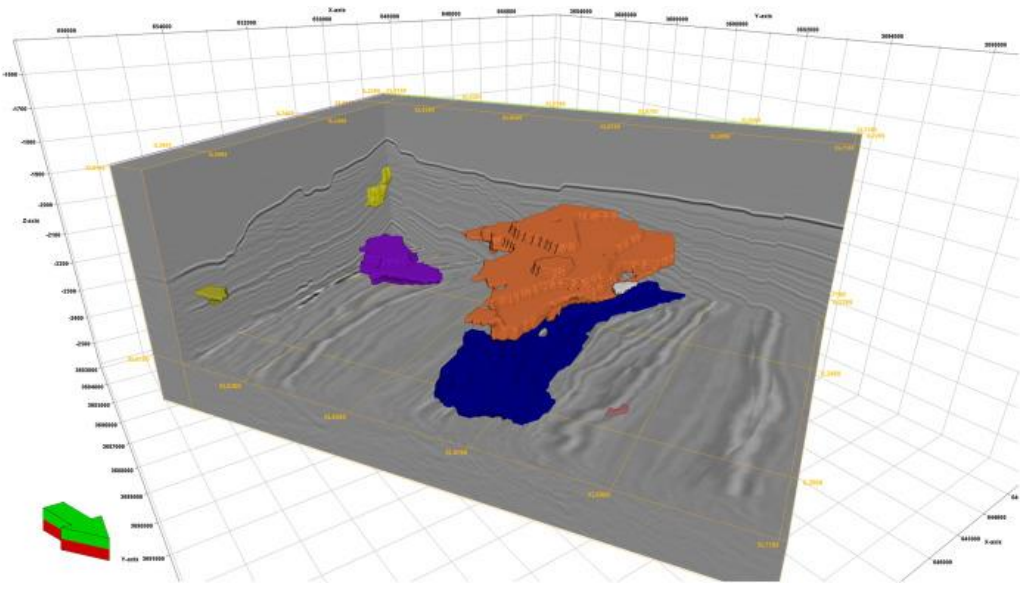

Figure 4.10 Three-dimensional view of the detected slumps by CNN in the Kumano basin. (orange slump is 1.3 km^3, a blue slump is 0.65 km^3, a red slump is 0.1 km^3, and yellow slump is 0.05 km3) (Ahmad and Tsuji, 2021).

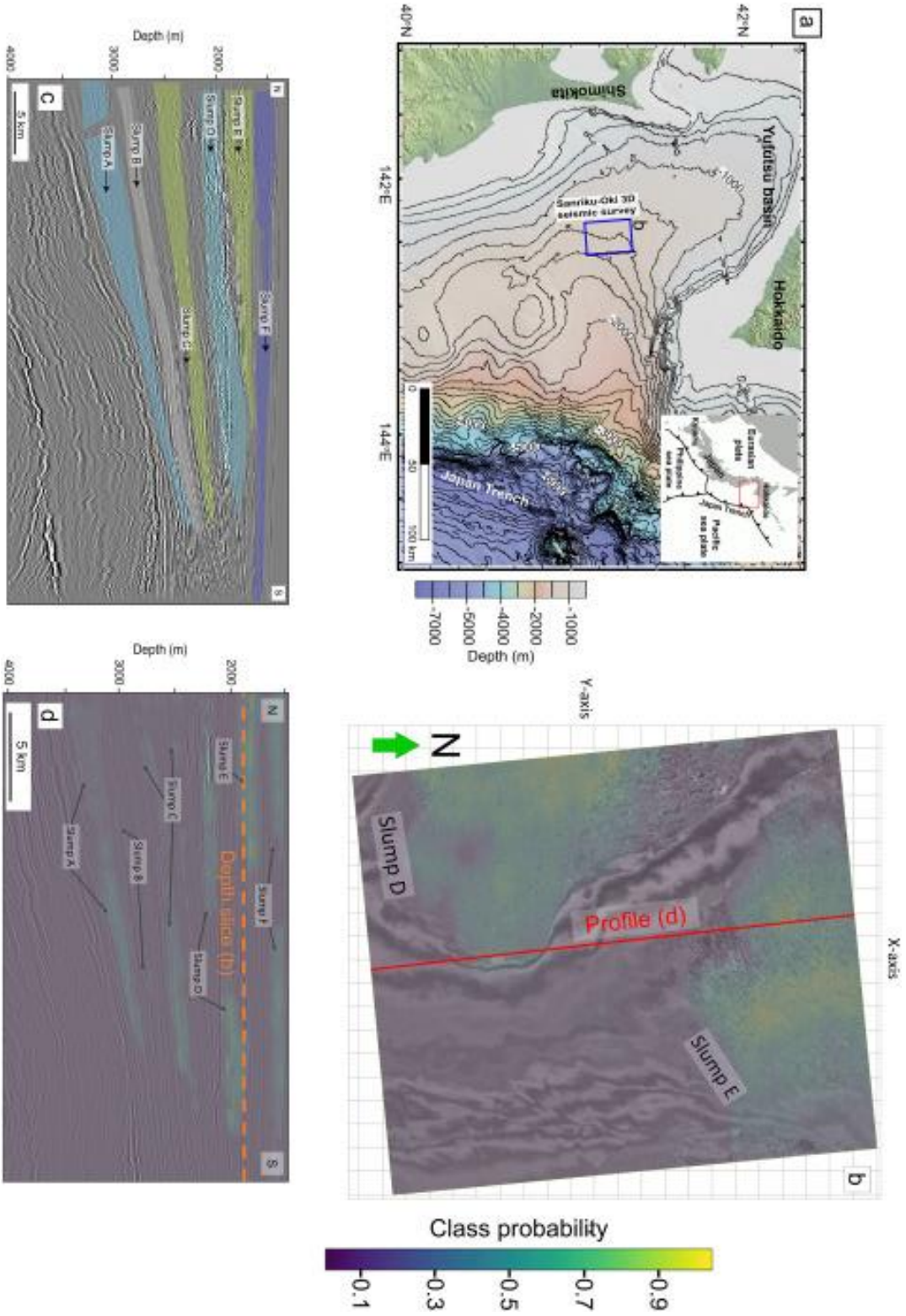

Figure 4.11 (a) Map of the Sanriku-Oki study area and location of the 3D seismic data (Kret et al., 2020). (b) The depth slice shows the distribution of slumping units identified by my CNN. (c) Manual slump interpretation by Kret et al. (2020) to compare with automatic interpretation (panel d). (d) Inline seismic profile showing the automatically interpreted slumping units (A–F) (Ahmad and Tsuji, 2021).

Based on previous studies (Moore et al., 2015; Moore and Strasser, 2016; Lackey et al., 2018), the two main slumps (orange and blue in Figure 4.10) were believed to be buried MTDs. The younger slump (orange in Figure 4.10) is aged ~0.35 Ma and formed a positive topographic feature on the seafloor. The older slump (blue in Figure 4.10) extends in a large area with a lense-shaped structure, and it is gradually getting thinner toward the south direction and aged <0.9 Ma. The other smaller slumps are rotational surficial landslides that occur at the seafloor, and their ages range between ~0.3-1.24 Ma. Those slumps were generated mainly due to the dynamic loading by earthquakes that accompanied slip events and steeper landward-dipping strata associated with the uplifting of the outer ridge area.

I applied the model trained by the Nankai 3D seismic data to the Sanriku-Oki 3D seismic data in northeast Japan (Figure 4.11a). The Sanriku-Oki area is ~1000 km away from the Nankai 3D seismic data. Although the training data is derived from the Nankai 3D data, CNN has shown promising results for the Sanriku-Oki 3D data (Figure 4.11b, d). The previous study (Kret et al., 2020) interpreted six slumping units in the Sanriku-oki 3D seismic volume (Figure 4.11c). My CNN model trained by the Nankai data has successfully detected the slumps in the same geologic formation (Figure 4.11d).

To evaluate the performance of the retrained CNN, I have retrained the CNN model with a single section from Sanriku-Oki 3D seismic data for 1000 iterations. The accuracy of the results has improved (Figure 4.12), and most false-negative results were covered. This improvement highlights the importance of retraining when applying CNN to new data (i.e., different types of slump).

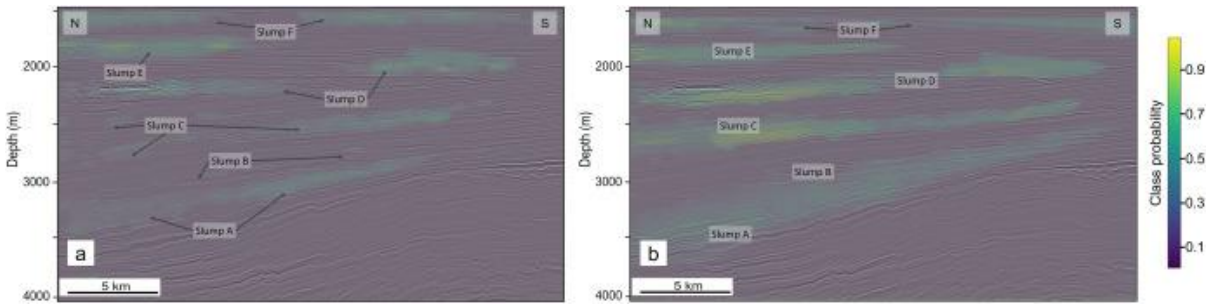

Figure 4.12 A comparison of slump prediction results with and without retraining the CNN model. (a) A probability map for predicted slumps without retraining the model in the testing area (i.e., Sanriku-Oki data). (b) A probability map for predicted slumps after retraining the model in the testing data (Ahmad and Tsuji, 2021).

4.4.2. Fault prediction

Many previous studies have demonstrated that CNN can be applied to identify faults (Cunha et al., 2020; Di et al., 2018a, 2018b; Guitton, 2018; Wu et al., 2019). To characterize the relationship between the faults and slumps, I extracted the faults in the 3D seismic volume in the convergent plate margin zone via CNN and evaluated its effectiveness. I used the pre-trained model (Wu et al., 2019). This model was trained on 2,000 synthetic 3D seismic cubes with dimensions 128 x 128 x 128 (Figure 4.13). The CNN learned 512 attributes (features) to describe and identify faults of all orientations. Figure 4.14 presents an automated interpretation of fault patterns within the Kumano forearc basin, executed by a convolutional neural network (CNN) model. This representation is particularly illuminating, as it successfully brings to light a series of normal faults consistently identified across various subsurface imaging perspectives, including depth slices and inline and crossline sectional views. The depicted fault locations exhibit a notable degree of match and continuity, underscoring the CNN model's adeptness at delineating fault structures.

The interpretative power of the CNN is on full display in these results, affirming the model's utility and accuracy in identifying geological discontinuities. Moreover, an intriguing observation from Figure 4.14 is the discernible relationship between the slump units and the detected normal faults in the basin. It becomes apparent that these slump units predominantly reside in zones exhibiting a sparser distribution of normal faults. This spatial correlation underscores CNN's capability in fault detection and highlights its potential to unravel complex geological relationships within the Forearc basin environment.

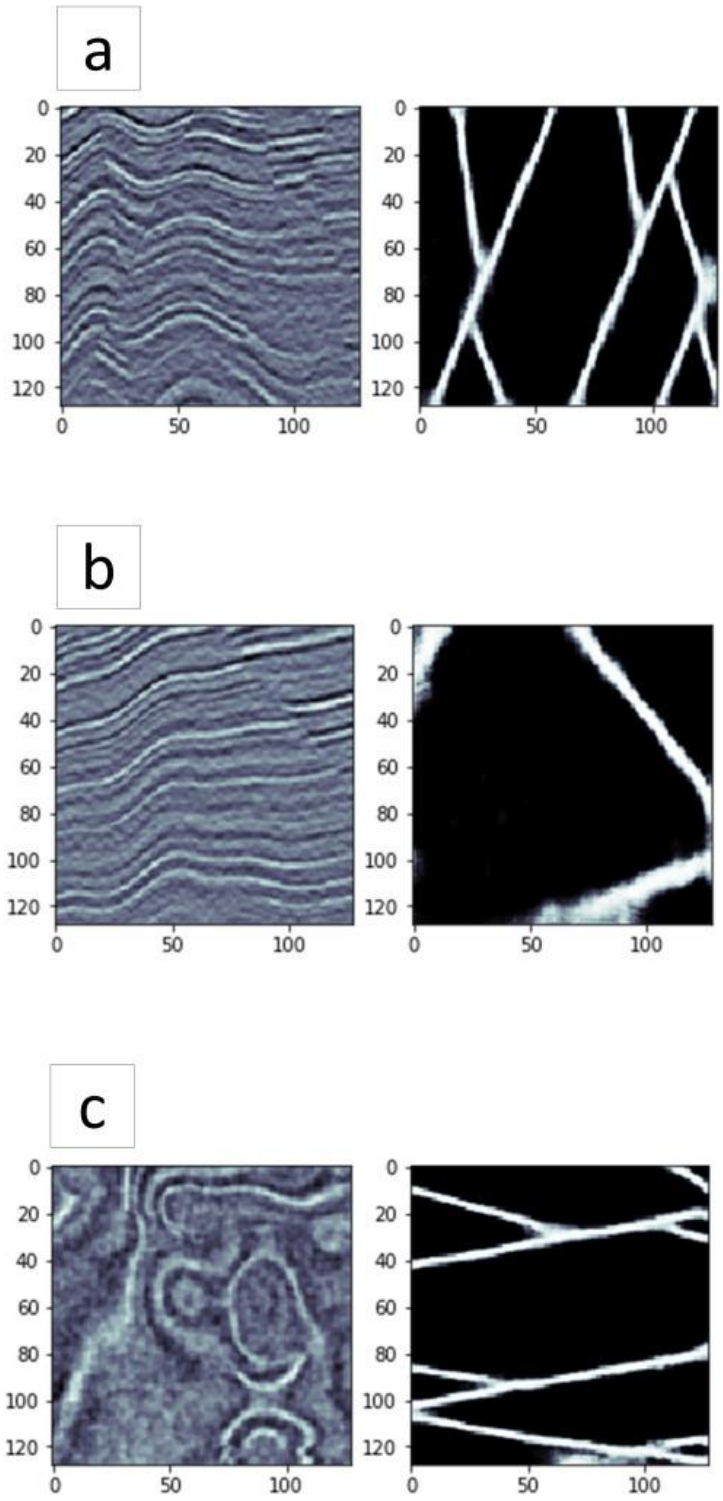

Figure 4.13 An example of the synthetic (128 × 128 x 128) 3D seismic cube used in CNN training. (a) The right panel is inline, and the left is the interpretation for the synthetic faults with white color. (b) The right panel is the crossline, and the left is the interpretation of the faults. (c) The right is the depth slice, and the left is the interpretation of the faults (Ahmad and Tsuji, 2021).

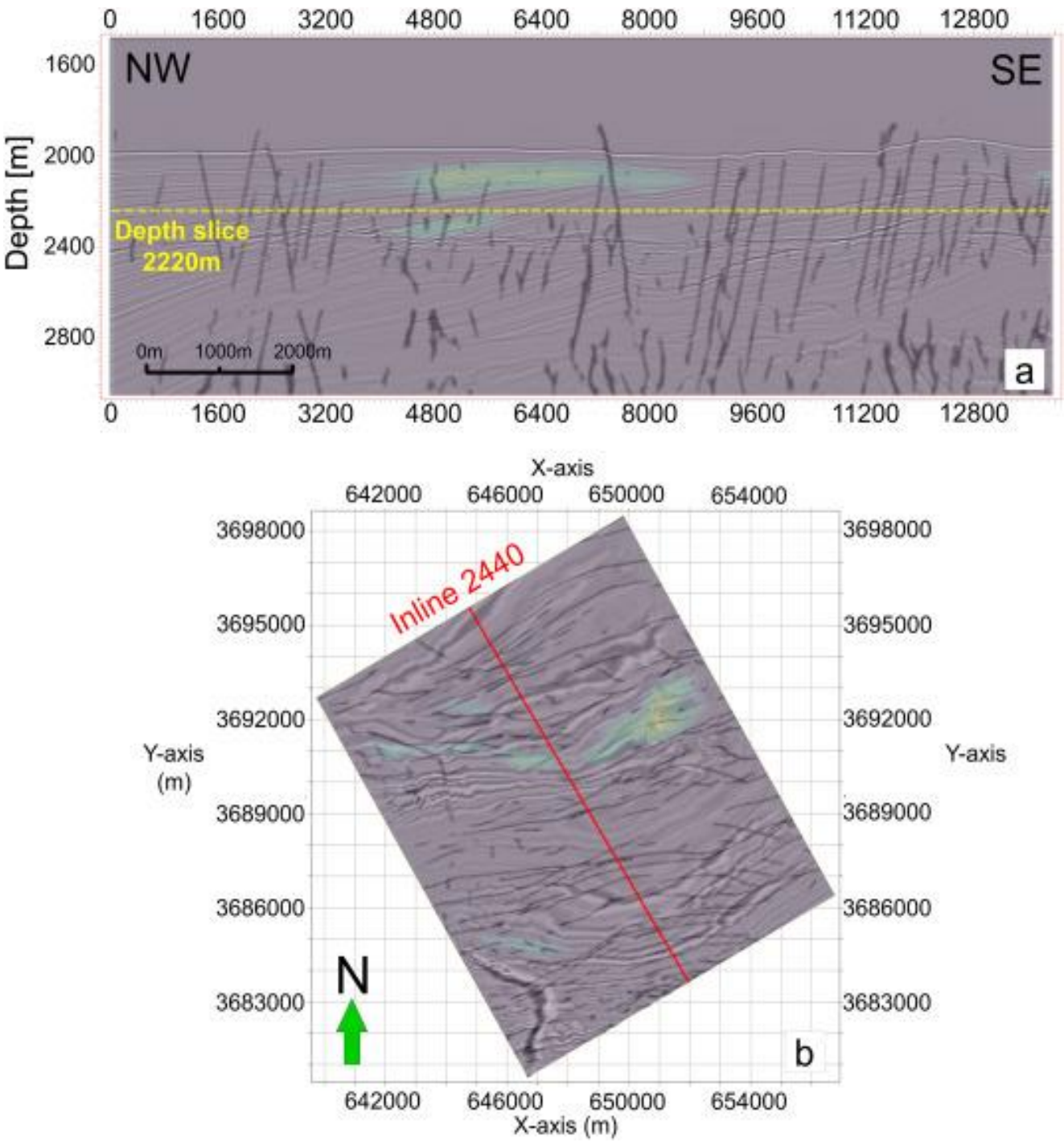

Figure 4.14 Result of CNN fault identification with probability for predicted slump unit (color). (a) Identified faults (dark gray linear features) on inline seismic profile 2440. (b) Identified faults in a depth slice at 2220 m below the sea surface (Ahmad and Tsuji, 2021).

4.4.3. Gas chimneys prediction

Convolutional Neural Networks (CNNs) have demonstrated remarkable accuracy in detecting rare geological structures such as gas chimneys, achieving success rates as high as 85%. Leveraging the power of artificial intelligence, these networks enable us to pinpoint gas channels, a previously challenging task through manual visual inspection. The promising model that achieved these feats was initially trained using data from the West Delta Deep Marine (WDDM) region, yet its application is not geographically constrained; it can be adapted for use in other areas, both within and beyond the borders of Egypt. The adoption of CNN in seismic interpretation represents a significant time-saving advancement, potentially revolutionizing the field by substituting manual analysis with the efficiency of artificial intelligence. This shift is underpinned by the neural network's ability to process complex input data. For instance, the network relies on high-level feature maps to identify slumps. While these attributes may seem abstract, their collective integration empowers the neural network to discern gas chimneys with high precision. To fine-tune the detection of the "gas chimney" attribute, researchers strategically selected data segments known to contain or lack these structures, thereby enhancing the model's interpretative accuracy. The CNN highlighted an area with a high probability of being a gas chimney warmer color (Figure 4.15).

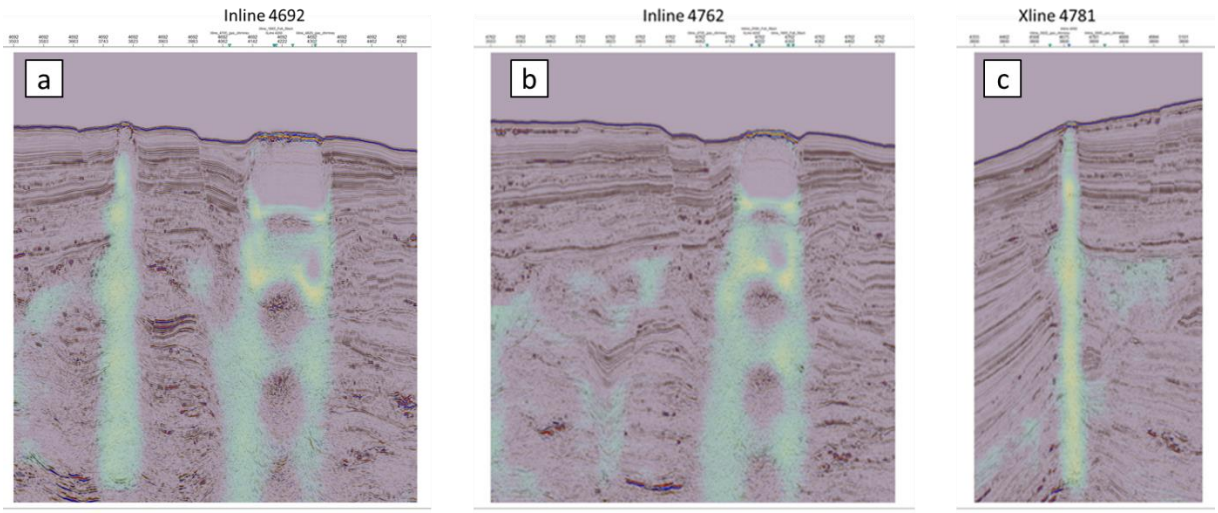

Figure 4.15 Results from the CNN highlighting gas chimneys in (a) inline seismic profile 4,692, (b) inline seismic profile 4,762, and (c) crossline seismic profile 4,781

I employed a technique that involves adjusting the probability map's threshold to enhance the understanding of the spatial arrangement of gas chimney units within a three-dimensional framework. By setting this threshold value to 0.5, I effectively established a criterion for distinguishing the gas chimneys within the dataset. This process enabled us to define the precise boundaries of the gas chimney structures that the Convolutional Neural Network (CNN) had successfully identified. The visual outcome of this method is displayed in Figure 4.16, which captures several prominent gas chimney formations. These formations, highlighted by CNN, testify to the network's capability to discern and outline such geological features from the complex subsurface data. The clear identification of these gas chimneys validates the CNN's analytical strength and provides a crucial step forward in the accurate geological mapping of the area under study.

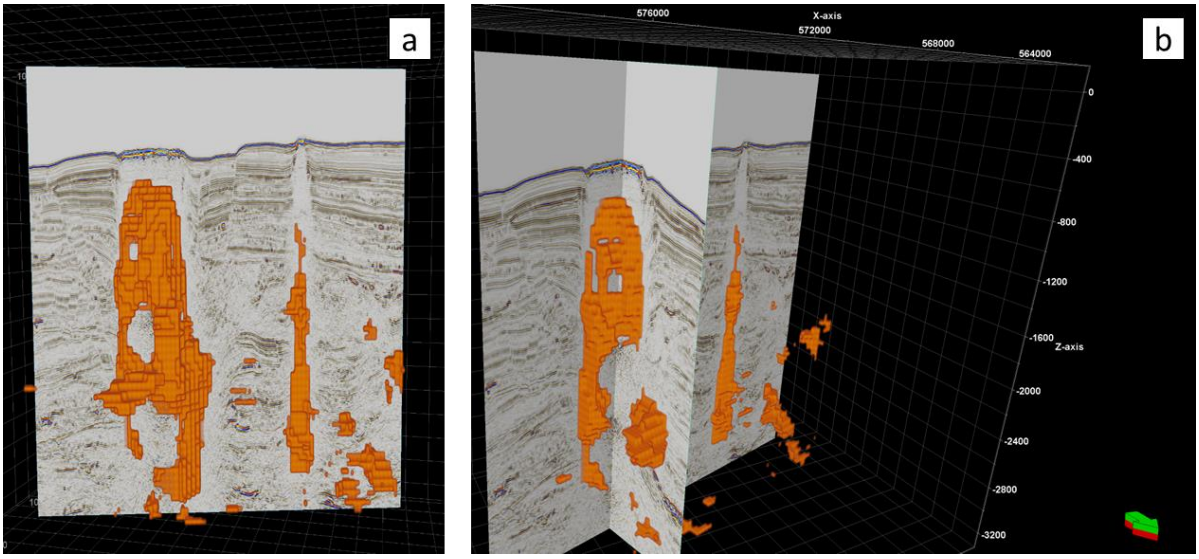

Figure 4.16 Three-dimensional view of the detected slumps by CNN in the West Delta Deep Marine (WDDM) basin. The orange shows two gas chimney units, whereas (a) shows only the crossline seismic profile 4,720, and (b) shows the crossline seismic profile 4,720 and the inline seismic profile 4,762.

4.5. Discussion

I aimed to test the effectiveness of CNN in identifying complex 3D slump units and fault distributions in plate subduction zones. My CNN model successfully detects the geological structures; the automatic slump interpretation is very close to the manual interpretation (Figs. 4.9d,e), although manual interpretations strongly depend on the interpreter. However, the spatial distribution of slump units identified in this study is larger than those identified manually. I could discover uninterpreted slump units in the 3D seismic volume. Furthermore, I evaluate slump distribution based on probability values and quantify the likelihood that my interpretations are accurate.

On the other hand, CNN has misinterpreted the SE part of MTD 4 (Figure 4.9d). This misinterpretation might result from the augmented training data or a less accurate manual interpretation of the training sections. Misleading training data might have led to an inaccurate CNN model regarding generalization. Another misinterpretation in the NW of MTD 1 (Figure 4.9e) is that the CNN has not located the extension on the slump unit under the bottom-simulating reflector (BSR). This misinterpretation is probably because of the limited number of training sessions. The slump units in the Kumano Forearc basin may represent most mass-transport deposits (MTD), but the features of some slump units are different, and CNN needs more training data to detect them correctly. Therefore, the misinterpretation could have been avoided by having better training quality with more training sections and less augmented data created by deforming the original data.

I further evaluated the effectiveness of applying the CNN model to a different geologic setting (i.e., Sanriku-Oki plate convergent margin). The CNN could detect some parts of slumping units in the Sanriku-Oki seismic data as high probability areas without retraining the model (Figure 4.12a), as the southern part of slump D and the eastern part of slump E have similar seismic facies to the slumping units that occurred in Kumano basin. However, CNN has failed to detect most of slumps B and C and correctly interpret slump A using the model trained only on Kumano basin data. Therefore, I retrained the CNN using the Sanriku-oki data (Figure 4.12). I recommend carefully preparing the training data to avoid false-positive predictions or misleading the model to avoid many false-negative predictions.

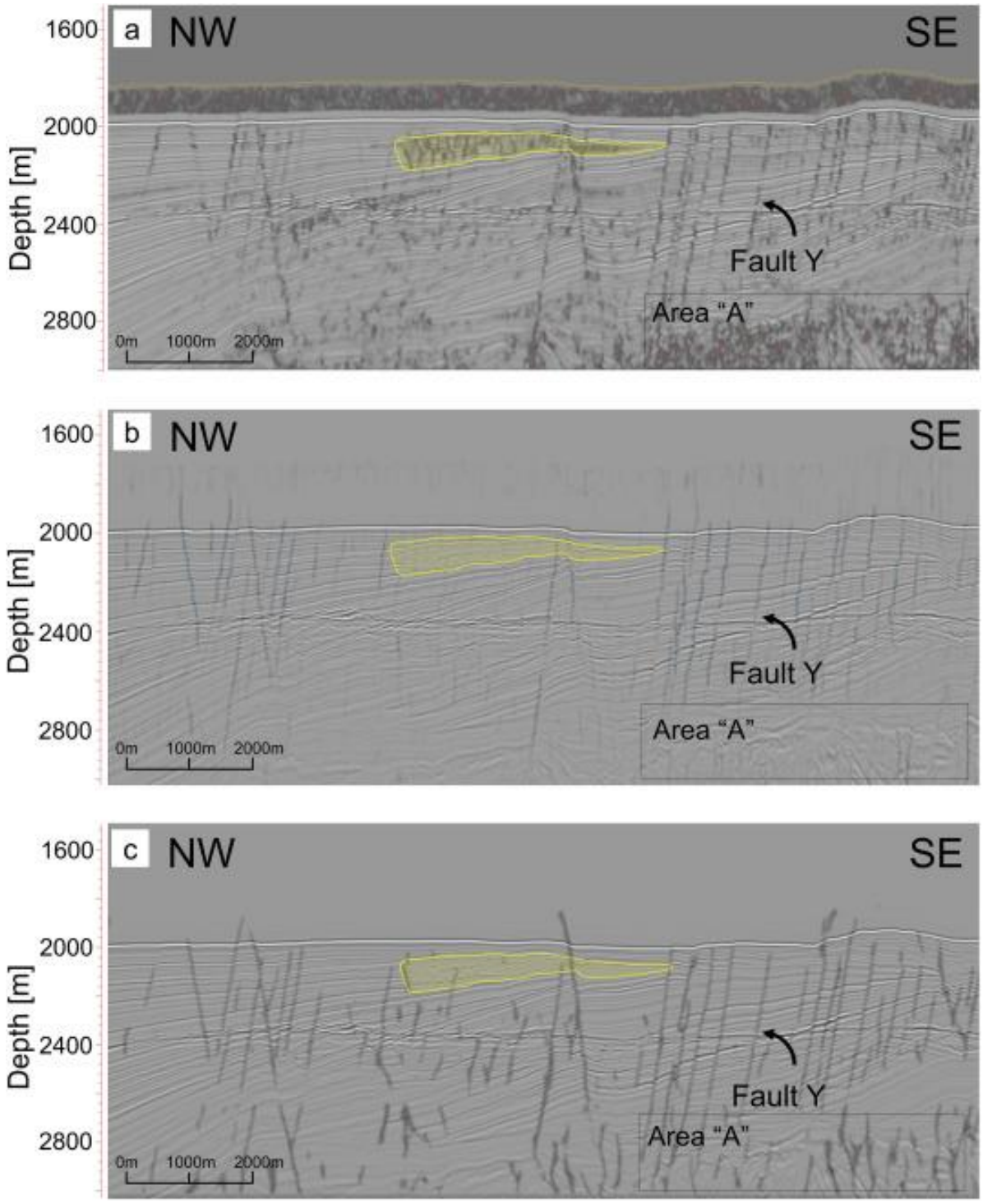

Figure 4.17 Comparison of automatic fault interpretations of inline seismic section 2,440, including fault 'Y' and a slump (marked in orange). Results are from (a) coherence attributes, (b) the ant-tracking method, and (c) by CNN (Ahmad and Tsuji, 2021a).

I cannot compare my results with other approaches because no previous works have employed CNN for slump interpretation. Nonetheless, previous studies have proposed several methods for automatic fault interpretation, such as the ant-tracking approach (e.g., Chopra and Marfurt, 2017). Here, I compared my CNN fault identifications with two other methods: the ant-tracking approach (Figure 4.17b) and the coherence attribute (Figure 4.17a). Ant-tracking and coherence attribute methods have been effective methods for automatic fault detection in the last decade. The ant-tracking approach is an efficient method of fault interpretation capable of identifying very small fracture occurrences (Chopra and Marfurt, 2017), although it requires smoothing or filtering the seismic data before fault identification. The coherence attribute is useful for imaging geologic features such as faults (Chhun et al., 2018; Kawabata et al., 2018) but focuses on interpreted horizons (reflectors) to find fault locations; therefore, calculation of this seismic attribute usually requires a high computational cost (Zhang et al., 2015).

Figure 4.17 compares faults identified by the coherence attribute, ant-tracking, and the present CNN methods. Area 'A' in Figure 4.17 specifically compares fault interpretations in the deeper parts of the Kumano forearc basin: the fault distribution in the reflection profile is poorly resolved by the ant-tracking method (Figure 4.17b) and noisy using the coherence attribute (Figure 4.17a), whereas my CNN interpreted the faults there (Figure 4.17c). Notably, these faults distributed deep in the basin contain gas accumulations (Provost et al., 1998), and some upward migration of gas through faults into the shallow section of the Kumano forearc basin has been reported, where hydrate and gas reservoirs have been identified (Chhun et al., 2018). Fault interpretations using CNN are continuous and smooth. Fault 'Y' is discontinuously interpreted using the coherence attribute (Figure 4.17a). The ant-tracking method results in a continuous but not smooth interpretation; fault 'Y' has offset at the boundaries of geological formations because this attribute is influenced by the reflection horizons with low frequency (~30Hz) (Figure 4.17b).

On the other hand, my CNN produced a continuous and smooth interpretation of fault 'Y' (Figure 4.17c). Although it is difficult to detect faults in areas of low reflection amplitude by using conventional methods, CNN is capable of identifying faults, even in low-amplitude

areas, because they rely on spatial features at multiple scales. Finally, an important advantage of using CNN for fault interpretation is their ability to distinguish between faults and discontinuities associated with other geological structures. For example, the coherence attribute misidentified the slump as a series of minor faults (Figure 4.17a), whereas my CNN distinguished between larger faults and the apparent minor faults within the slump (Figure 4.17c). Figure 4.18 shows the fault distribution using three methods on the depth slice at 2220 m below the sea surface. The ant-tracking and CNN are superior to coherence attributes in terms of quantity and quality of interpretation. However, the CNN could not detect the minor faults as ant-track because the training data only includes large displacement faults (Figure 4.13). I should use such faults in the training to classify the minor faults by CNN.

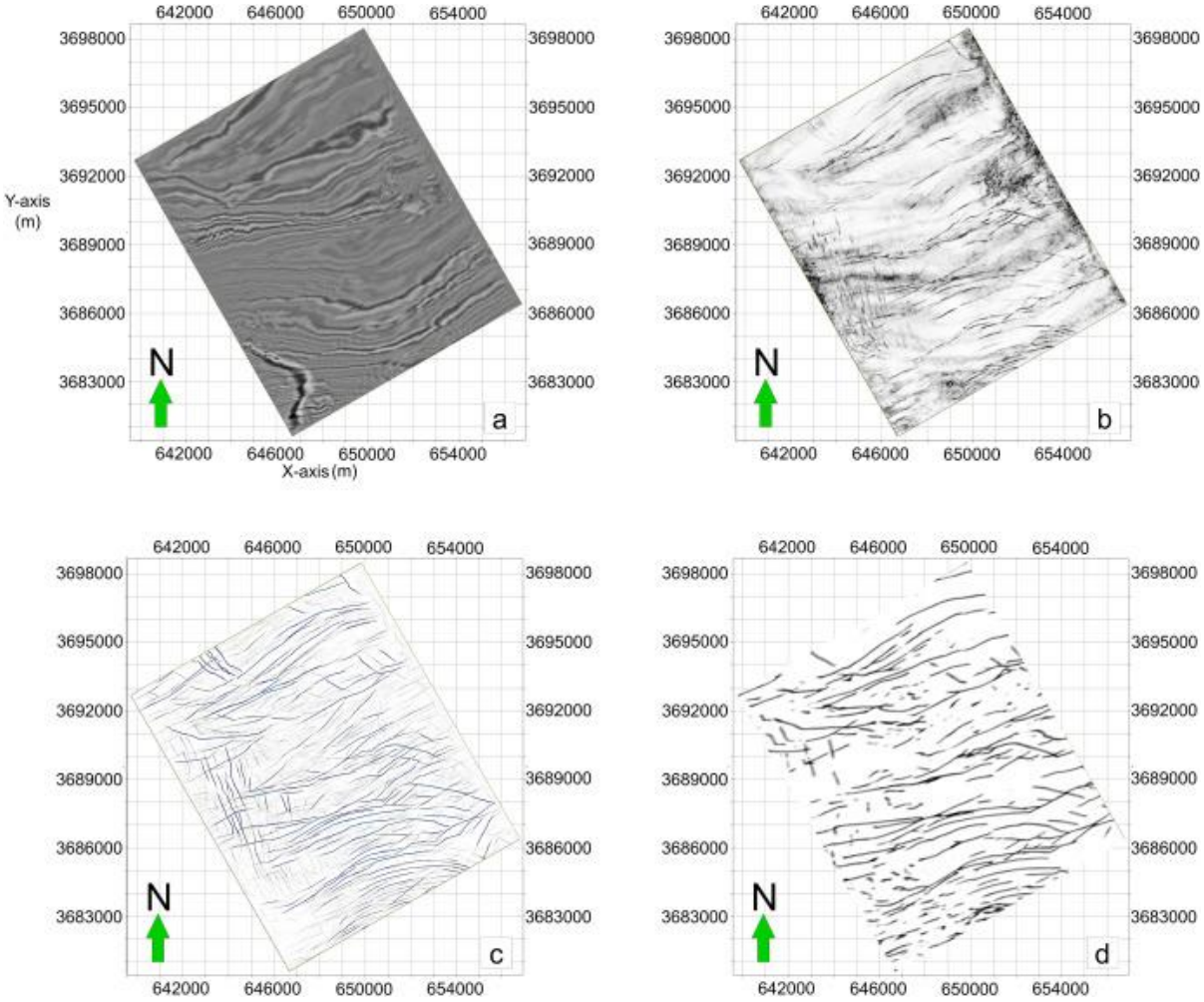

Figure 4.18 Depth slices for 2220 m below the sea surface in the Kumano basin to show fault distribution. (a) The original seismic depth slices. (b) The result of coherence attributes. (c) The result of the ant-track method. (d) The result of the CNN model is trained by synthetic data (i.e., larger displacement faults) (Ahmad and Tsuji, 2021a).

4.6. Conclusion

I tested the efficiency of CNN in interpreting slump and fault systems in plate subduction zones. The CNN proved to be an effective and promising method for seismic interpretation and may provide faster, more accurate interpretations. My CNN quickly interpreted large 3D seismic volumes and correctly identified a large slump unit in the Kumano forearc basin. Furthermore, as this approach calculates the probabilities of its predictions, I can quantify the accuracy of the identified slump unit. Automatic fault interpretation using CNN could be more accurate than traditional automated interpretation methods. As the filter weights are determined, more training with a large training data set results in better accuracy and better generalization. Nonetheless, I recommend CNN training with the seismic data of the target regions to improve the classification results.

My study demonstrates that the CNN approach can be used for slump and fault identification in seismic volume. Because the slump and fault have different characteristics on seismic profiles, I expect that this approach can be used for the identification of other geological targets, such as gas reservoirs. The proposed method could be improved by trying to find more optimum deep learning architectures, such as RCNN, U-net, and SegNet. Different hyper-parameters could further improve classification accuracy in different targets. For example, U-net is a developed CNN architecture and is widely used in fault-detecting works (Li et al., 2019a; Wu et al., 2019; Liu et al., 2020; Yang et al., 2020).

The CNN creates a map that estimates the likelihood of gas presence, which is then refined into a three-dimensional model of where gas is likely to be found. Additional steps are taken to make sure the model is smooth and accurate. When these automated 3D models are checked against expert geologists' manual interpretations, they match up very well. This method isn't just good for finding gas in Japan; it can be applied to different kinds of hydrocarbon reservoirs worldwide, as long as the geological conditions are similar.

Chapter 5

Traffic Monitoring System Using Machine Learning Algorithms

5.1. Introduction

Many countries invest heavily in traffic monitoring systems (Lee and Coifman, 2015), which collect and analyze traffic data to derive statistical information, such as the number of vehicles on the road and their temporal patterns. Governments use these statistics to forecast transportation needs, improve transportation safety, and schedule pavement maintenance work. Identifying the size of vehicles is a key task that helps to predict noise levels and road damage. The characteristic mix of vehicle types that use a roadway can determine the geometric design of the road based on the Traffic Monitoring Guide report published by the Federal Highway Administration in the United States (Administration, 2016). Vehicle classification systems make use of many recent advances in sensing and machine learning technologies (Abiodun et al., 2018). Although newer systems perform vehicle classification with higher accuracy, they differ in their characteristics and requirements, such as the types of sensors used, parameter settings, operating environment, and cost. Many traffic monitoring systems rely on vision-based vehicle classification techniques, usually based on cameras, that deliver high classification accuracy ranging between 90%~99% (Won, 2019), covering large areas compared with emerging alternatives. Although camera-based systems have high classification accuracy, their performance can be affected by weather and lighting conditions, as well as other factors. For instance, vehicles can be missed when they are obscured by large vehicles. Furthermore, the system requires huge investments in infrastructure to perform a complete coverage of the road network.

Another important problem is the privacy concerns of vehicle occupants, as many people do not feel comfortable being exposed to cameras. An inductive loop detector based on the magnetic characteristics of vehicles is one of the most commonly used traffic monitoring

systems for vehicle detection and classification(Coifman and Neelisetty, 2014). The loop detector system is based on a coil of wire placed under the roadway to capture the change in the magnetic profile signal's characteristics, such as amplitude, phase, and frequency when a vehicle passes over it (Jeng and Chu, 2014). Several studies on the loop detector technique have shown its high accuracy (99% accuracy) for large vehicle classification, such as cars, trucks, and vans (Wu and Coifman, 2014a, 2014b; Balid and Refai, 2018; Li et al., 2019b), it was also proven that loop detectors have no dependency on the vehicle speed (Lamas-Seco et al., 2015). Although the loop detector system is the most widely adopted in-roadway-based vehicle classification technique, it might not be the most suitable system for easy and low-cost implementation, as it requires coil installation under the roadway surface.

Various privacy-preserving solutions have been proposed, using different kinds of sensors in, over, or at the side of roadways (Won, 2019). A combination of infrared and ultrasonic sensors (up to 99% accuracy) (Odat et al., 2018) or magnetic sensors used in roadways and on the side of roadways with an accuracy of up to 96.4% in the case of using multiple sensor networks (Li and Lv, 2017; Dong et al., 2018; Mocholi Belenguer et al., 2019). In addition to previous methods, new methods for traffic congestion monitoring in urban areas were proposed based on GPS, social media data, and network data collected directly from vehicles (Litman, 2007; Carli et al., 2015, 2018; Ahmed et al., 2016; Wang et al., 2017). These methods have contributed to evolving intelligent transport systems (ITSs) and provide clear information on traffic flow and traffic destiny for urban areas. However, most proposed methods have not achieved a classification accuracy comparable to inductive loops and camera-based systems; moreover, they may require special installations, such as loop detectors in the road (Martin et al., 2003). Various vibration-based vehicle classification systems have been developed to avoid these shortcomings. Vehicles produce vibrations from two main sources: the engine system and the interaction between the tires and the road (Ketcham et al., 2005; Moran and Greenfield, 2008; William and Hoffman, 2011). These signals depend strongly on the size of the vehicle. However, these signals can be hard to identify owing to the complexities of the seismic waveform and the influence of the underlying geology on the propagation of the seismic wave. I have overcome these problems by using artificial intelligence (AI) techniques.

Moreover, seismic data are relatively smaller in size than videos recorded by a camera. One hour of a single-channel seismic record is 5 MB, while one hour of video can be 1 GB. For long-term monitoring, smaller data sizes have a large advantage in data management.

In practice, seismic signals generated by vehicles are hard to distinguish, as most civilian vehicles generate similar vibrations at frequencies below 20 Hz. However, because these signals travel through the ground, they are less sensitive to wind noise, which is an advantage for vehicle detection (Jin et al., 2019). Because AI has been instrumental in the dramatic improvement of voice recognition technology in the last decade, such as voice analysis (Zhao, 2018), I chose to test the application of similar techniques to recognize vehicles from seismic waves. Furthermore, AI has been widely applied for the classification of seismic events (Shimshoni and Intrator, 1998; Perol et al., 2018; Titos et al., 2018; Yuan et al., 2018). The application of AI to seismic information for monitoring traffic promises to offer the advantages of low power requirements, easy implementation, and low cost, in addition to its advantages in occupant privacy.

A study published in 2010 used a neural network to classify vehicles based on seismic data (Evans, 2010). The study used acoustic data recorded with a microphone to supplement the seismic data, and the best classification accuracy achieved was 92%. Another study published in 2019 relied exclusively on seismic signatures (Jin et al., 2019). That study proposed extracting spectral features of vehicle seismic signals using a log-scaled frequency cepstral coefficient (LFCC) matrix, a step that requires preprocessing the seismic data in the frequency domain. This method achieved classification accuracy as high as 91.39%. However, both studies concerned heavy military vehicles and cannot be generalized to civilian vehicles. Moreover, neither approach could use raw seismic data without preprocessing or supplementation by other data.

In this chapter, I include two studies. In the first study, I used three neural networks to classify the size of cars using seismic waves, while in the second study, I compared the best neural network from the first study with ML algorithms—Logistic Regression (LR), Support Vector Machine (SVM), and Naïve Bayes (NB). Previous studies by other researchers have captured and categorized waveform data from various sources to investigate how effectively ML approaches can extract information from seismic waves; thus, I also contrast the findings of

this investigation with the published CNN-based approach. Although the second study shares the same goal and data set as the first study of this chapter, it discusses the usage of more straightforward and linear methods, such as LR, to conclude if those methods are beneficial. Another difference between these methods (SVM, LR, and NB) and neural networks is that the idea of neural networks highly depends on optimized variables (weights/filters), making it relatively computationally consuming. The first study investigated only a specific branch of ML, neural networks, and focused on the well-known architectures for voice recognition, such as CNN and RNN. To my knowledge, this is the first study to use Logistic Regression, Support Vector Machine, and Naïve Bayes to predict and classify vehicles using their ground motions. This chapter describes my proposed traffic monitoring system for civilian applications. My purpose was to build and optimize a neural network that takes a window of waveform data as input, labels it as either seismic noise or a vehicle signal, and identifies the type of vehicle. The proposed approach relies on seismic data alone without preprocessing. In this study, I tested three different neural network architectures that are widely used for the analysis of time series data, including voice recognition. My approach was applied to civilian traffic, and I achieved 99% classification accuracy in the training process and 96% accuracy in the validation process.

5.2. Methods

Neural networks, the main backbone for machine learning, operate in a way that is analogous to biological processes in that the connectivity pattern between neurons resembles the organization of the animal visual cortex (Grossberg and Rudd, 1989). Neural networks use little preprocessing compared to other classification algorithms. This means that the network learns its optimal processing filters, which are manually prepared in traditional algorithms. This independence from prior knowledge and human effort in feature design is a major advantage. Consequently, neural networks can efficiently find relationships between a set of input raw data (in this case, seismic waveforms) and the desired output value (vehicle class probabilities).

Neural networks consist of three main components: neurons, weights, and bias. In a feedforward process, the neurons are determined by the values of the previous input and the weights variable that connects previous inputs to the neuron, as shown in Figure 5.1.

Bias is an independent variable that acts as a refresher that perturbs the function by adding a constant. The output Y of all neurons can be calculated as follows:

$$Y = f[\sum_1^n (X \times W) + b] \quad (5.1)$$

where *n* is the number of neurons in the previous layer, *X* is the value that the neuron holds, *W* is the weight that connects *Y* with *X*, and *b* is the bias. The nonlinearity activation function *f* can be changed depending on the application of the neural network. To ensure a fair comparison of the three neural network models I evaluated in this study, I adopted the rectified linear unit (ReLU) (Nair and Hinton, 2010) as an activation function after all layers. The ReLU equation returns all negative values to zero and keeps positive values:

$$f(Y) = max(0, Y) \quad (5.2)$$

Neurons are usually stacked in groups called hidden layers. The simplest neural network contains a single hidden layer and an output layer with a single neuron. In this study, I used three different models with complex architectures designed to classify data in the time domain. Each candidate architecture had its weights and biases optimized in a training process via back-propagation. In all three models, the output of the last layer was subjected to the *SoftMax* function (Shim et al., 2017) to normalize the probabilities by the following:

$$S(N) = \frac{e^N}{\sum_n e^N n}, \quad (5.3)$$

where *N* is the value of the output layer, and *n* is the number of neurons in the output layer. Table 5.1 lists the specifications of the three models.

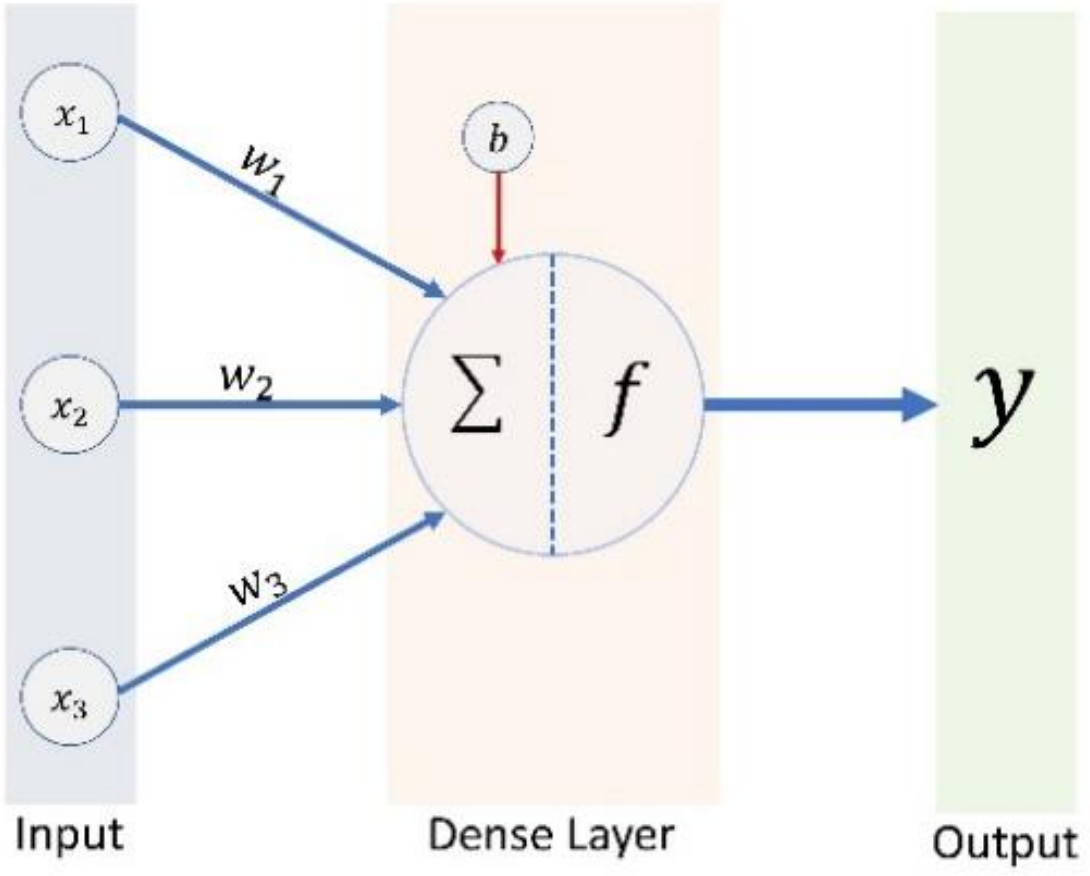

Figure 5.1 A simple neural network illustrating Equation (1). Inputs (x) multiplied by weights (w) are summed in the dense layer, adding bias (b), and then the activation function (f) is applied to get the output (Ahmad and Tsuji, 2021b).

Table 5. 1 Characteristics of the three neural network architectures used.

	DNN	**CNN**	**RNN**
Number of dense layers	11	4	2
Special layer	None	Convolutional layer	LSTM
Activation function after dense layers	ReLU	ReLU	ReLU
Activation function after the final layer	SoftMax	SoftMax	SoftMax
Trainable parameters	605,572	87,170	871,684

5.2.1. Deep Neural Network

A deep neural network (DNN) is a simple network with many hidden layers. A large number of hidden layers is advantageous for dealing with time-series data (Titos et al., 2018). my DNN model contains 11 hidden layers. The first four hidden layers contain 256 neurons, the middle three layers have 128 neurons, and the last four have 64 neurons. This decrease in neuron count helps DNN to compress the information into fewer neurons. The last layer, the output layer, contains four neurons representing the four classes in my model (Figure 5.2). Before each decrease in the size of the hidden layer, I apply batch normalization to avoid internal covariate shifts (Ioffe and Szegedy, 2015). The details of the DNN model architecture are given in Table 5.2.

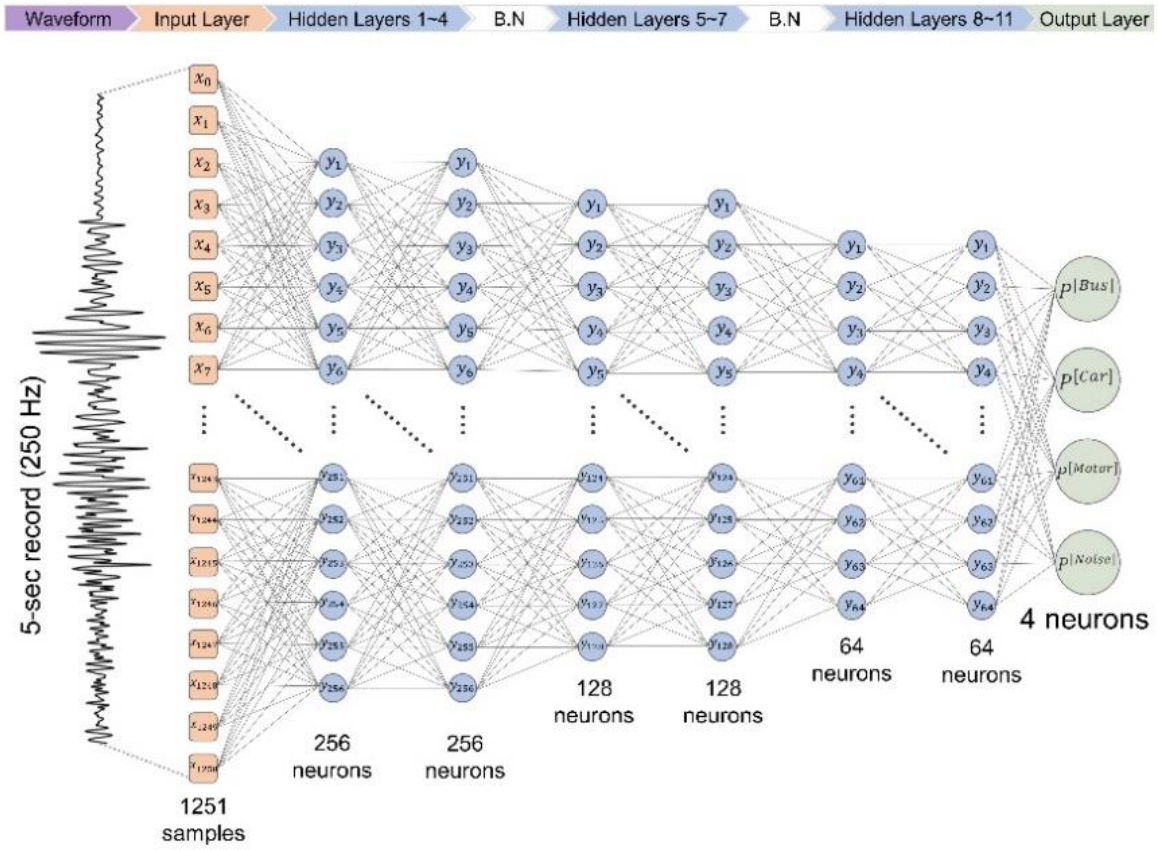

Figure 5.2 The DNN architecture used in this study. The 5 s waveform is discretized as 1251 samples and fed to 11 dense layers, including two batch normalization (B.N) operations between hidden layers 4 and 5 and hidden layers 7 and 8. The model produces four values indicating the probability of each vehicle class (Ahmad and Tsuji, 2021b).

Table 5. 2 The components of DNN's architecture, the output of each layer, and the parameters.

Layer (type)	Output Shape	Param #
Hidden_Layer_1 (Dense)	(1, 256)	320512
Hidden_Layer_2 (Dense)	(1, 256)	65792
Hidden_Layer_3 (Dense)	(1, 256)	65792
Hidden_Layer_4 (Dense)	(1, 256)	65792
Hidden_Layer_5 (Dense)	(1, 128)	32896
Batch Normalization	(1, 256)	1024
Hidden_Layer_6 (Dense)	(1, 128)	16512
Hidden_Layer_7 (Dense)	(1, 128)	16512
Batch Normalization	(1, 128)	512
Hidden_Layer_8 (Dense)	(1, 64)	8256
Hidden_Layer_9 (Dense)	(1, 64)	4160
Hidden_Layer_10 (Dense)	(1, 64)	4160
Hidden_Layer_11 (Dense)	(64)	4160
Output Layer (Dense)	(4)	260

Total params: 606,340
Trainable params: 605,572
Non-trainable params: 768

5.2.2. Convolutional Neural Network

The convolutional neural network (CNN) has become popular for solving problems that contain features such as image recognition and is considered the best algorithm for visual recognition problems (Waldeland et al., 2018). CNN contains a convolutional layer before the main neural network that is made up of multi-channel filters that extract unique features of each class. CNN thus breaks problems into smaller tasks, making the classification task for the next layers much easier (Zhao, 2018). The convolutional layer functions as a feature extractor, and the neural network (also called the fully connected layer) is classified based on features instead of the raw data. The CNN I used for this study contained four convolutional layers with 50 filters (sized 1 × 5) in each layer. I used MaxPool as a downsampling layer with a dimension of (1 × 3) to keep the maximum value of each of the 3 samples. So, the output of the MaxPool layer is one-third of the original data (1247/3 = 415 samples). There are 4 convolutional layers, each followed by a MaxPool layer. The final output of the convolutional layer is 50 channels signal, and each channel contains 13 features. In other words, the output is (13 × 50) the features map. I used a flatten layer to convert this map to a list with 650 variables to introduce it into the fully connected layer.

The fully connected layer contains four hidden layers and a final output layer (Figure 5.3). The details of the CNN model architecture used in this study are listed in Table 5.3. I chose four convolutional layers after testing different numbers of layers and considering the trade-offs between accuracy and computational time.

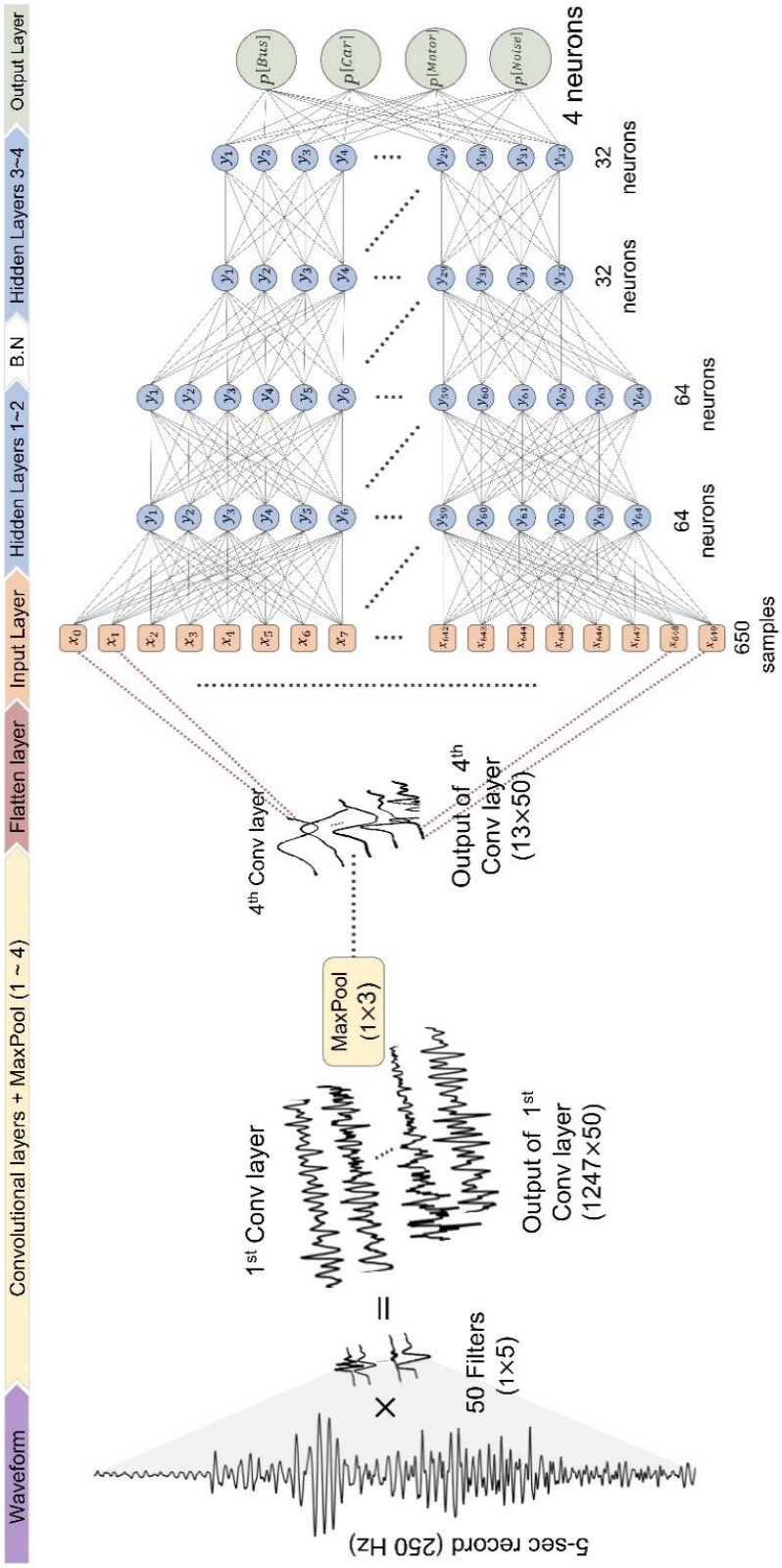

Figure 5.3 The CNN architecture was used in this study. Five convolutional layers each contain 50 filters and a MaxPool layer to downsample the amount of contained data. The convolutional and flattening layers condense the original 1251 samples to 650 samples containing filtered features (Ahmad and Tsuji, 2021b).

Table 5. 3 The components of CNN's architecture, the output of each layer, and the parameters.

Layer (type)	Output Shape	Param #
Conv_Layer_1	(1, 1247, 50)	300
MaxPooling2D	(1, 415, 50)	0
Conv_Layer_2	(1, 411, 50)	12550
MaxPooling2	(1, 137, 50)	0
Conv_Layer_3	(1, 133, 50)	12550
MaxPooling2	(1, 44, 50)	0
Conv_Layer_4	(1, 40, 50)	12550
MaxPooling2	(1, 13, 50)	0
Flatten	(650)	0
Hidden_Layer_1 (Dense)	(64)	41664
Hidden_Layer_2 (Dense)	(64)	4160
Batch Normalization	(64)	256
Hidden_Layer_3 (Dense)	(32)	2080
Hidden_Layer_4 (Dense)	(32)	1056
Output Layer (Dense)	(4)	132

Total params: 87,298
Trainable params: 87,170
Non-trainable params: 128

5.2.3. Recurrent Neural Network

The recurrent neural network (RNN) is a recently developed architecture in which connections between nodes form a directed graph along a temporal sequence, which allows it to exhibit temporal dynamic behavior (Abiodun et al., 2018). RNN is similar to DNN but also includes a memory of previous results. My RNN model used two layers of long short-term memory (LSTM), as shown in Figure 5.4 and Table 5.4 in the supplementary material. I anticipated a similar performance gain in seismic recognition because LSTM was responsible for the dramatic advancement in speech recognition (Hochreiter and Schmidhuber, 1997).

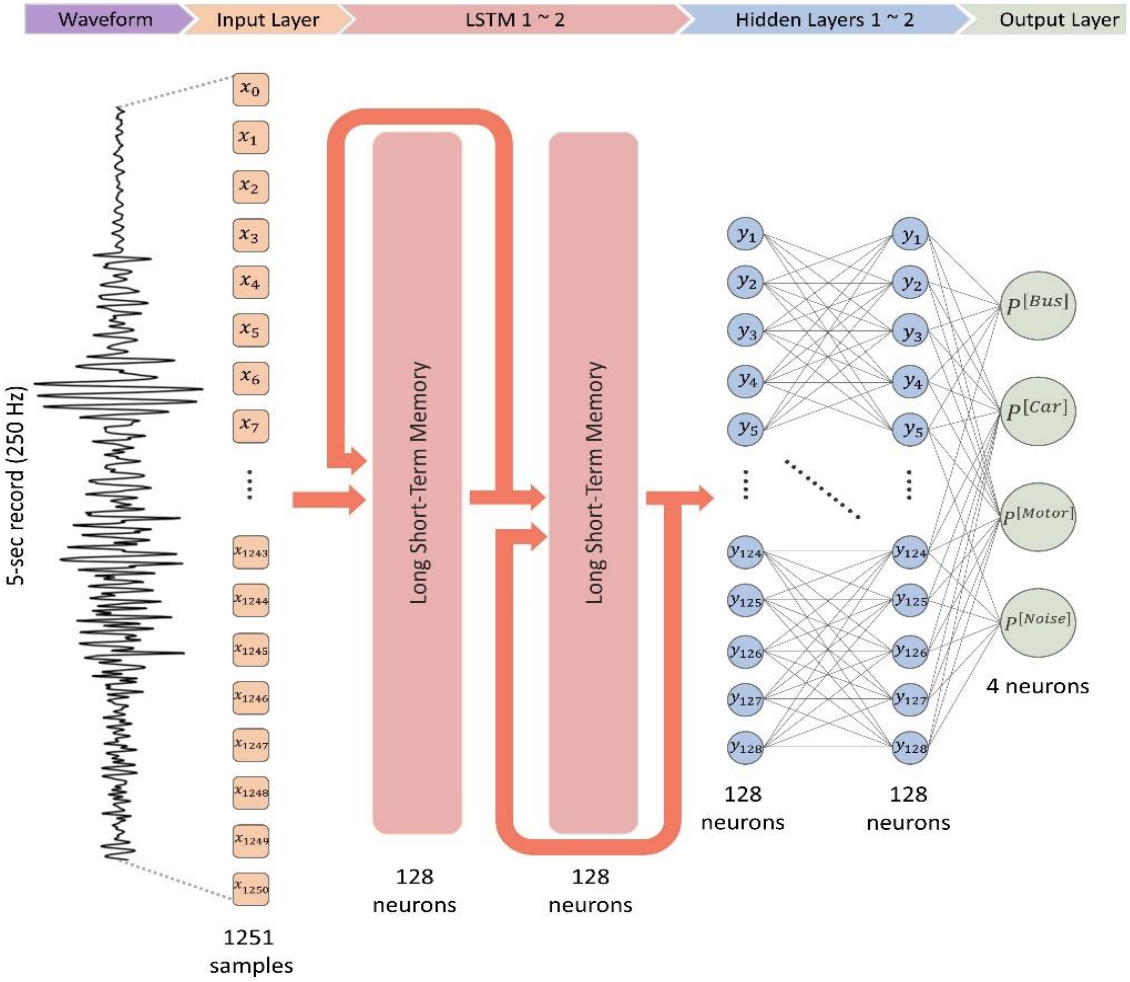

Figure 5.4 The RNN architecture was used in this study. The model contains two LSTM layers and two hidden layers. The model produces four values, indicating the probability of each vehicle class (Ahmad and Tsuji, 2021b).

Table 5. 4 The components of RNN's architecture, the output of each layer, and the parameters.

Layer (type)	Output Shape	Param #
LSTM_1	(None, 1, 128)	706560
LSTM_2	(None, 128)	131584
Hidden_Layer_1 (Dense)	(128)	16512
Hidden_Layer_2 (Dense)	(128)	16512
Output Layer (Dense)	(4)	516

Total params: 871,684
Trainable params: 871,684
Non-trainable params: 0

5.2.4. Logistic Regression (LR) for ML

The probability of a target variable is predicted using the supervised learning classification technique known as logistic regression. Since the dependent variable's nature is dichotomous, only two viable classes exist. In LR, I take the output of the linear function and compress the value to the range of (0,1) using the sigmoid function (logistic function). Any real-valued integer may be mapped to a value between 0 and 1 using the sigmoid function, which is an S-shaped curve but never precisely at those values (Rymarczyk et al., 2019). To build my classifier model, I used generalized linear models with LR (Figure 5.5).

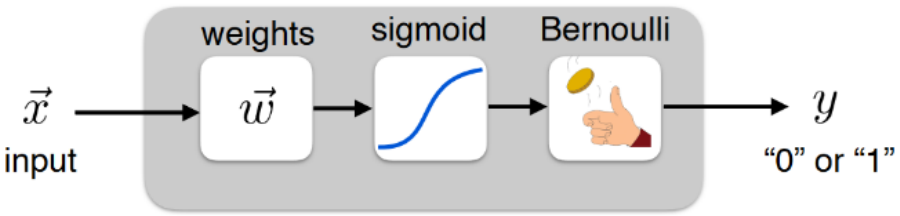

Figure 5.5 Two-class classification using generalized linear models with LR (Ahmad et al., 2021).

A logistic regression model makes mathematical predictions about P(Y=1) as a function of X. Several category problems, including spam detection and diabetes prediction, may be solved using one of the most fundamental machine learning methods.

5.2.5. Support Vector Machine (SVM)

The SVM algorithm was implemented in Matlab to train SVM classifiers for model-building and then use the optimal classifier for new data classification. I used SVM with a non-linear kernel, e.g., a radial basis function. The traditional C-SVM model was used as a classification model and can be described as follows:

$$\frac{1}{2}\ \|w\|^2 + C\sum_{i=1}^{l}\zeta_i \tag{5.4}$$

$$y_i[w \cdot x_i + b] \geq 1 - \zeta_i, (\zeta_i \geq 0), \quad i = 1,2,3 \ldots\ l \tag{5.5}$$

where w is the average vector, C is the penalty factor, and ζ_i is the margin of error. x_i is the input, y_i is the class label, b is the bias to the separation hyperplane, and l is the number of samples of the input x_i.

Additionally, the radial basis kernel function, which was applied to address the non-linear characteristics of the geophysical data, can be described as:

$$K(x_i, x_j) = exp(-g\|x_i - x_j\|^2), \quad g > 0 \tag{5.6}$$

where g is the kernel parameter that denotes the transformed data's gamma distribution, and the kernel parameter g and penalty factor C are adjusted to search for optimal separation hyperplane. I used ten-fold cross-validation for training classifiers to avoid overfitting.

In contrast, the SVM approach involves adopting a non-linear kernel function to transform the input data into a higher-dimensional feature space, making it easier to separate the data. The iterative learning process in SVM identifies the optimal hyperplanes with the maximum margin between each class in a higher-dimensional feature space.

5.2.6. Naïve Bayes (NB)

NB is a probabilistic classifier that applies Bayes' theorem with strong (naïve) independence assumptions between the features. The following was used to calculate a posterior probability of A happening given that B happened:

$$P(A \mid B) = P(A \cap B)/P(B) = P(A) \times P(B \mid A)/P(B) \qquad (5.7)$$

Where *A* and *B* are events or classes, *P(A)* and *P(B)* are the probabilities of *A* occurring and *B* occurring independently. *P(B)* should be greater than zero, and *P(B/A)* is the probability of *B* occurring, given that *A* is true. Bayes' Rule was applied to my two-class classification problem; I classified my data into the population that maximizes the posterior probability for the decision rule.

5.2.7. Optimization of Weights and Biases

Before using the networks, I optimized the weights and bias values using a back-propagation process. Back-propagation occurs during model training, where the data flows from the end of the network to the first layer for another iteration. I repeatedly cycled through a known dataset, calculating the error and optimizing the parameters by minimizing the loss function. To ensure a fair comparison, I adopted cross-entropy for all networks, which expresses the average discrepancy between the predicted class and class as follows:

$$\mathrm{E} = -\sum y'_k \log (y_k) \qquad (5.8)$$

where *y* is the outcome of *SoftMax* for the k class, and *y'k* is 1 for a true prediction and 0 for a false one. I used the Adam optimizer (Kingma and Ba, 2015) for the loss function with a learning rate of 0.001 and for monitoring the accuracy and mean square error.

This study used a work frame consisting of the TensorFlow 2.3.0 machine learning platform with graphics processing unit (GPU) support and the ObsPy, NumPy, and sci-kit-learn libraries. I used a hardware platform containing dual GeForce RTX 2080 ti GPUs with 64 GB RAM to run all algorithms.

5.3. Data

5.3.1. Data Set

In this study, I used geophones to obtain seismic data for different vehicles at Kyushu University in July 2020. I placed the geophones in three stations 15 m apart, located 0.5 m from the road, as illustrated in Figure 5.6. The vertical motions (vibration) were recorded at a rate of 250 Hz. I tagged vehicles by size as large (e.g., buses and trucks), medium (e.g., private passenger cars), and small (e.g., motorcycles and scooters).

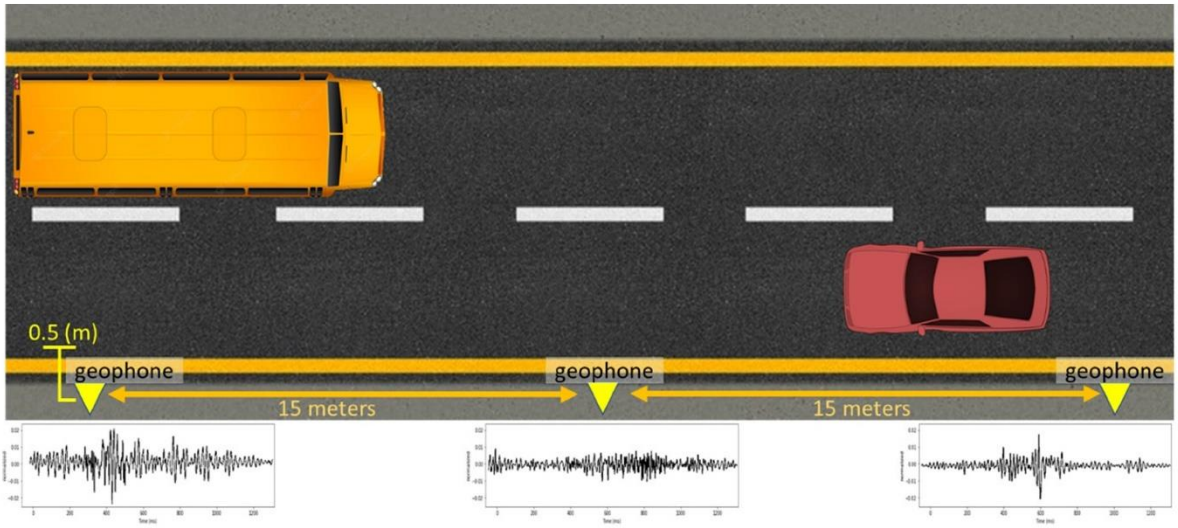

Figure 5.6 A schematic illustration for the survey performed at Kyushu University to collect seismic data using three geophones (sensors) at a 15 m spacing and a 0.5 m distance from the road (Ahmad et al., 2022).

During the experiment, a video camera was used to provide a visual guide for the manual preparation of the training data. Each event (the passage of a vehicle) lasted 2–3 s when the vehicle was close to the geophone. Based on signals at three stations, I estimated the speeds of the vehicles. The speeds of most vehicles used in this experiment were 25~35 km/h, and the maximum speed was 45 km/h. In the training process, I chose clear vehicle signals, eliminating all signals that contained surrounding noise or that overlapped with other vehicles to avoid overfitting the models, as appears in Figure 5.7.

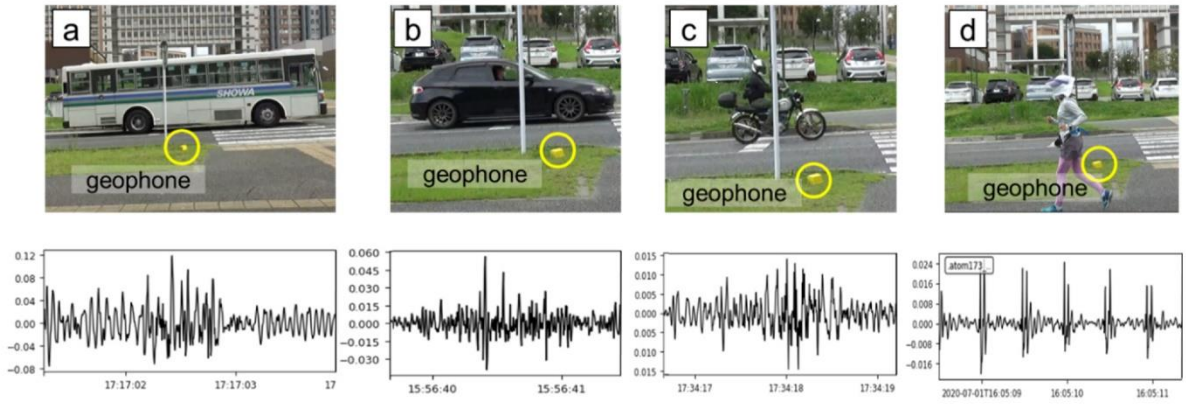

Figure 5.7 Example of signal plots for (a) a large vehicle (bus), (b) a medium-sized vehicle (light car), (c) a small vehicle (motorcycle), and (d) other noise (pedestrian). A yellow circle in each image indicates the seismic sensor (Ahmad et al., 2021, 2022).

The selected events were extracted from the record in the form of Windows 5 s long, containing 1251 data points (5 × 250 Hz = 1250 samples). This duration was selected to guarantee the inclusion of the whole seismic waveform. I extracted, on average, 68 waveform windows per geophone station for each of the three vehicle classes for a total of 612 windows. I also selected 318 waveform windows to represent the noise in my data as the fourth class. These include noise produced by strong winds, bicyclists, walkers, pedestrians pushing a trolley, road maintenance, and ambient noise. These 930 windows constituted the entire input to the three neural networks; examples of each class in the dataset are shown in Figure 5.8.

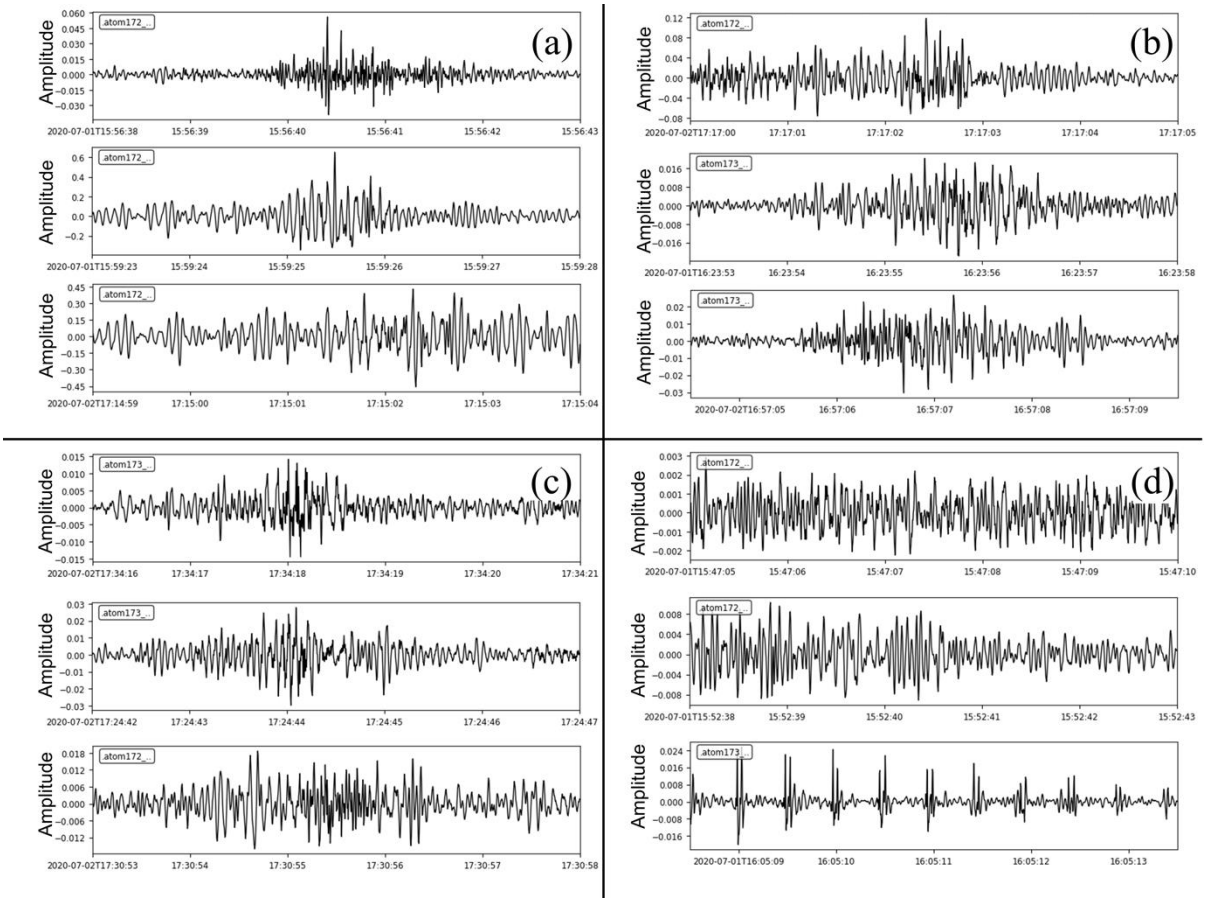

Figure 5.8 Examples of the waveforms used in the training process. (a) Examples of large vehicles like buses and trucks, (b) examples of medium vehicles like cars, (c) examples of small vehicles like motorcycles, and (d) examples of noise like people walking, winds, and side street maintenance (Ahmad and Tsuji, 2021b).

5.3.2. Training Data Augmentation

Large networks are trained using large amounts of training data to avoid overfitting (Waldeland et al., 2018). my dataset of 930 samples was inadequate for this purpose; therefore, I generated synthetic data from my initial dataset for training purposes. I added random noise to waveforms to change their signal-to-noise ratio (SNR), as shown in Figure 5.9. I varied the SNR (Tyagi et al., 2012) from 1 to 5 as determined by the following:

$$SNR = \frac{P_{signal}}{P_{noise}} = \left(\frac{A_{signal}}{A_{noise}}\right)^2, \qquad (5.9)$$

where *P* is the average power and *A* is the root mean square amplitude. The resulting augmented dataset used for training contained 4650 synthetic samples (5 × 930).

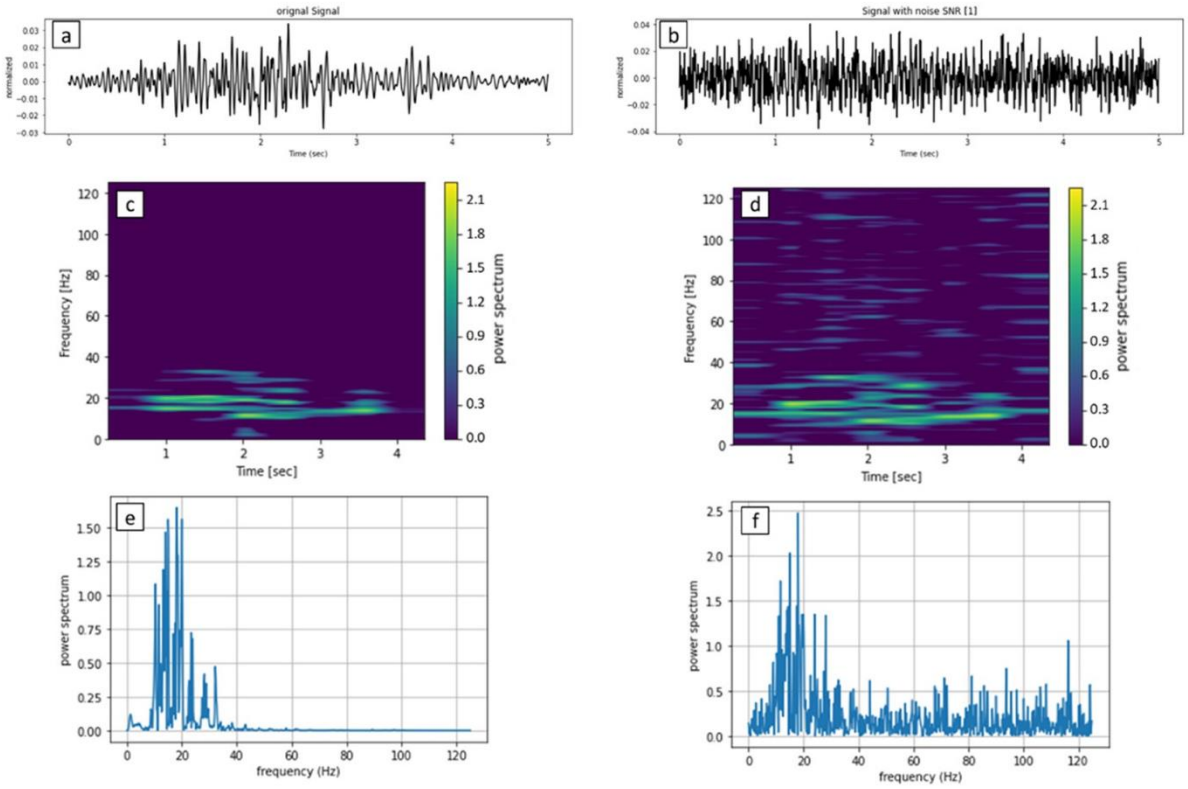

Figure 5.9 (a) Seismic bus signal before adding noise. (b) Seismic signal after adding noise with SNR = 1. Panels (c,d) show the original and noisy signal spectrograms, respectively. Panels (e,f) show the power spectra calculated in the original and noisy signals, respectively (Ahmad et al., 2022).

5.4. Results

5.4.1. Training and Validation for the Nural Networks

I split the augmented dataset randomly into three portions, using the sci-kit-learn splitting function, dedicating 60% for training, 20% for validation, and 20% for testing. I used the same training set for each of the three networks, trained them over 150 iterations, and then selected the model with the best validation accuracy. I also improved the training experience and prevented overfitting in two ways.

First, I applied early stopping in which the networks monitored the validation accuracy and terminated the training when accuracy did not increase for 20 iterations. Second, I set a 30% dropout chance for all weights and biases. So, in each iteration, all weights and biases have a 30% chance of being ignored in the training process.

The dropout technique improves the independence of the individual weights (Srivastava et al., 2014b). Training took a short computation time: DNN took 87 s, CNN took 112 s, and RNN took 56 s. Because of early stopping, DNN and RNN trained for less than 150 iterations. All models showed a great improvement during training, reaching accuracies close to 99% (Figure 5.10).

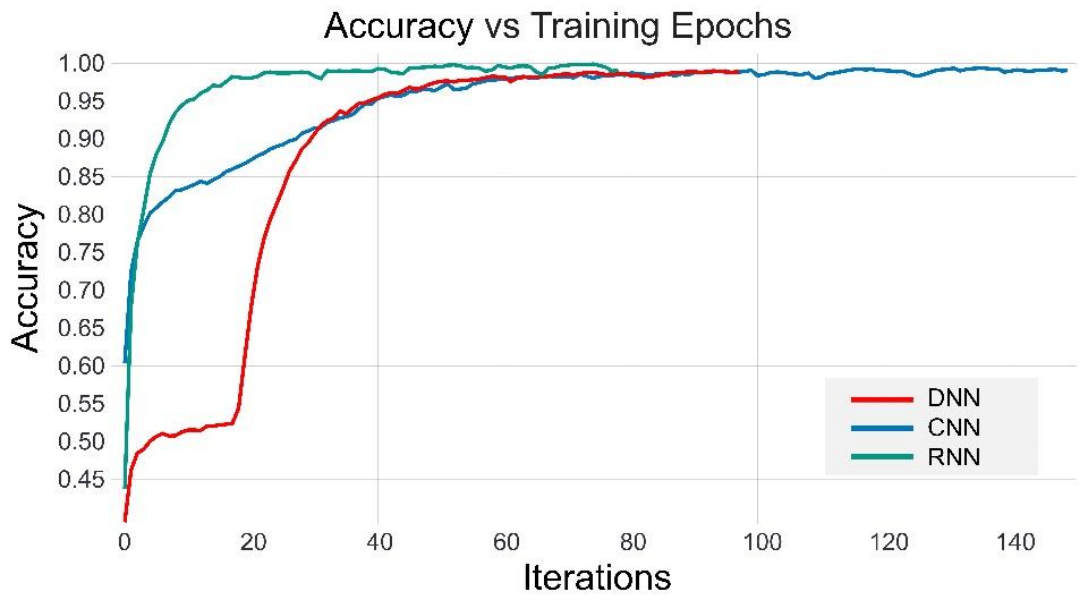

Figure 5.10 The plot shows the improvement in accuracy with increasing iterations during the training process for DNN (red), CNN (blue), and RNN (green). RNN was stopped early at 79 iterations, and DNN was stopped at 97 iterations (Ahmad and Tsuji, 2021b).

In the validation process, I checked the models' performance with new data or data that were not used in the training process. The models did not display any overfitting, thanks to the early stopping that curtailed training before any degradation of the validation accuracy. The resulting validation curve represents the generality of the model. Both DNN and CNN reached accuracies of approximately 97%, whereas RNN validation accuracy was approximately 85% (Figure 5.11). I also evaluate other metrics, as illustrated in Figure 5.12.

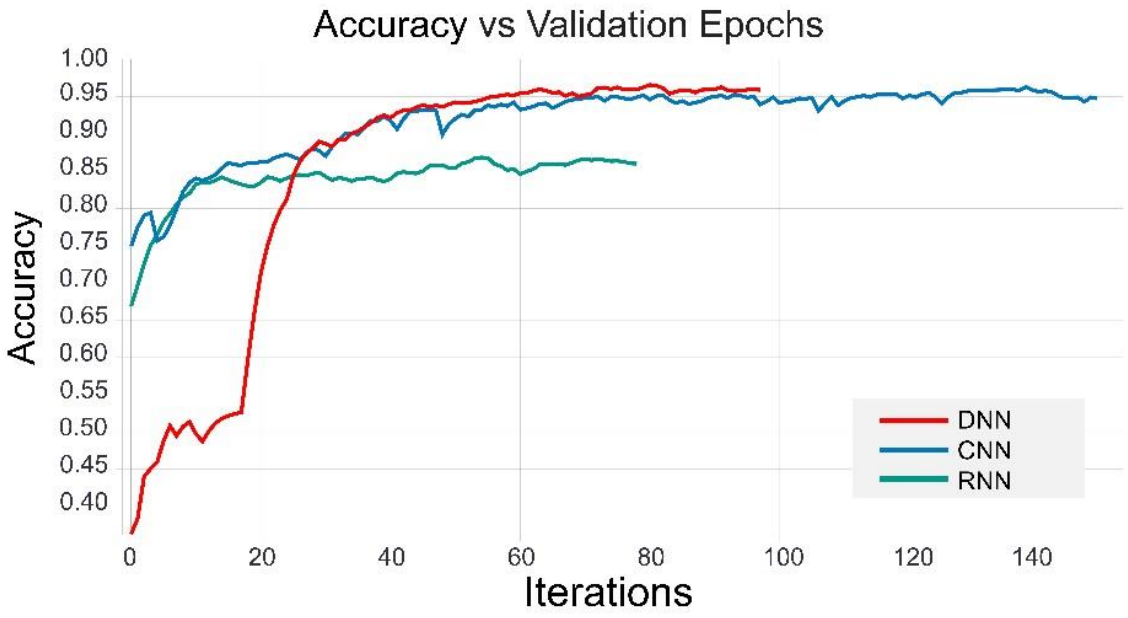

Figure 5.11 The plot shows the improvement in accuracy during the validation process for DNN (red), CNN (blue), and RNN (green) (Ahmad and Tsuji, 2021b).

I also monitored the improvements in loss function and mean square error in Figure 5.12. Table 5.5 summarizes the performance of the three models during training and validation.

Table 5. 5 Performances of networks for training (3420 waveforms) and validation (1140 waveforms).

	DNN	**CNN**	**RNN**
Time (s): Total training	87	112	56
(Average per epoch [1])	(0.89)	(0.74)	(0.69)
Accuracy (%): Training	98.6	99.1	99.2
(Validation)	(95.6)	(94.7)	(86.1)
Loss: Training	7.80×10^{-2}	2.77×10^{-2}	3.52×10^{-2}
(Validation)	(0.293)	(0.240)	(1.070)
Mean square error: Training	6.02×10^{-3}	3.58×10^{-3}	2.98×10^{-3}
(Validation)	(0.019)	(0.023)	(0.065)

[1] Each epoch includes 4560 waveforms of 5 s each.

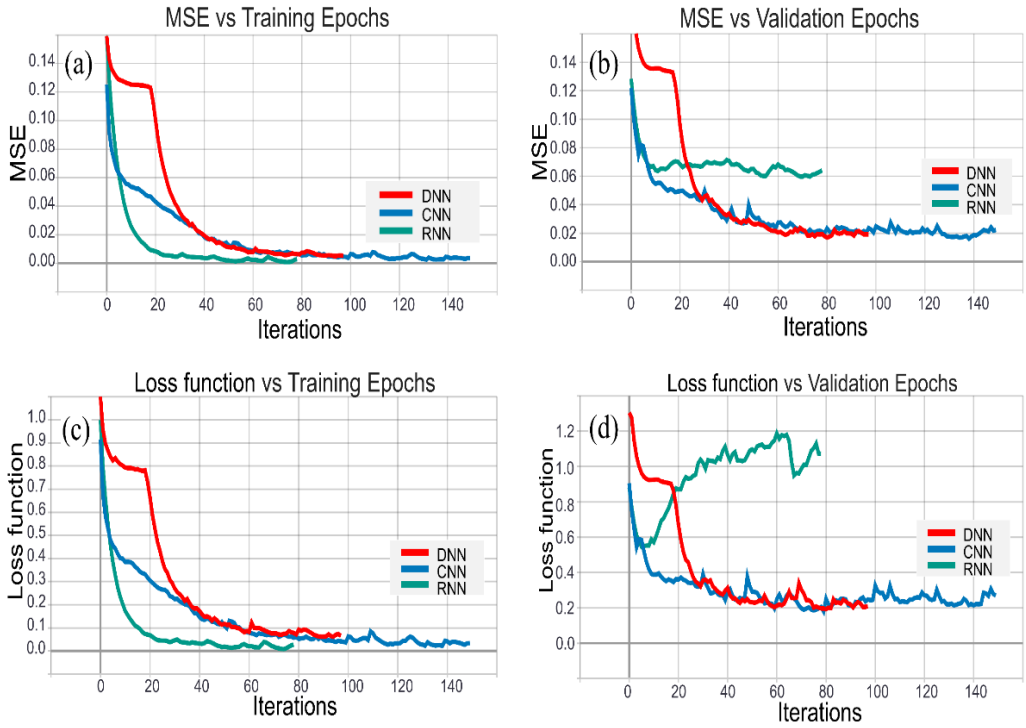

Figure 5.12 Other factors were monitored during the training and validation process for DNN(red), CNN(blue), and RNN (green). (a) The curve of Mean Square Error (MSE) improves while training, (b) the MSE curve while validating the methods, (c) the decreasing of the loss function while training, and (d) the loss function curve while validating each method (Ahmad and Tsuji, 2021b).

5.4.2. Classification Accuracy

I tested the classification accuracy of the three networks using 20% of the dataset (1116 samples). I compared the results with those of a similar method for seismic event detection called template matching (Skoumal et al., 2014). I randomly selected 50 waveforms for each vehicle class from the training data to be used as templates. I also recorded 15 min of new data for this experiment. I took into consideration factors that might affect the data, including the time of recording, location of stations, and types of geophones. The networks were not retrained before this exercise, and the templates also were not changed.

The resulting detection accuracies are listed in Table 5.6. DNN achieved the best accuracy, with 97.8% correct detections, followed by CNN with 96.6% and RNN with 85.3%. Template matching had much lower classification accuracy and took an order of magnitude longer to process the testing data.

Table 5. 6 Performances and running time (1140 waveforms) of networks and template matching.

Matrics	Template Matching	DNN	CNN	RNN
Time (ms)	560	74	67	55
Accuracy (%)	77.3	97.8	96.6	85.3
Mean square error	N/A	0.009	0.014	0.063

5.4.3. Vehicle Detection in Continuous Records

Because practical applications involve records longer than 5 seconds, I tested the framework for detecting vehicles using the 15-minute continuous waveform dataset described in the previous section. The single-channel waveforms were cut into 5 s long windows, with a gap between consecutive windows of 1 s to reduce the potential.

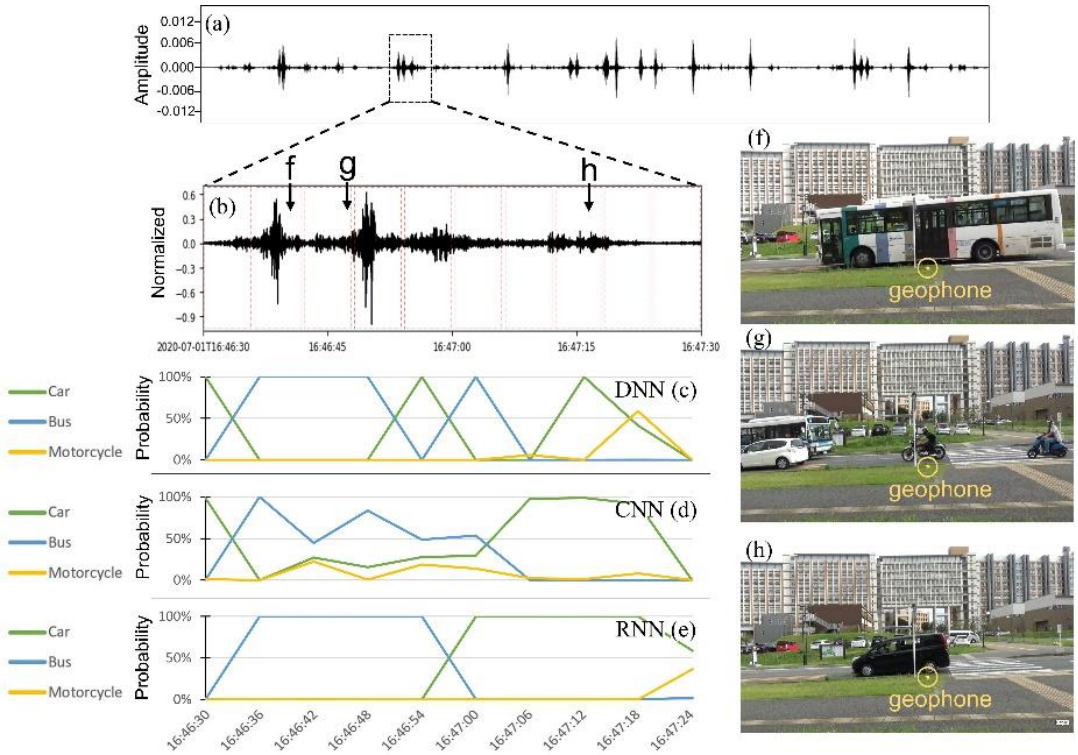

*Figure 5.13 (**a**) A continuous seismic record 20 min long. (**b**) Detail of (**a**) showing a data window 1 min long divided into 5 s waveforms (red boxes) with gaps of 1 s between them. (**c**) The probability of vehicle types during the window in (**c**) is estimated using DNN, (**d**) CNN, and (**e**) RNN. Events during the window include the passage of (**f**) a bus, (**g**) a motorcycle, and (**h**) a car in mixed traffic. The vibrations recorded at times of pictures (**f**), (**g**,**h**) are displayed on panel (**b**) (Ahmad and Tsuji, 2021b).*

Thanks to the feature extraction implemented in the convolutional layer, CNN was able to detect vehicles of different classes with overlapping seismic records. In the example of Figure 5.14, a truck, a lightweight car, and a motorcycle passed the geophone in quick succession.

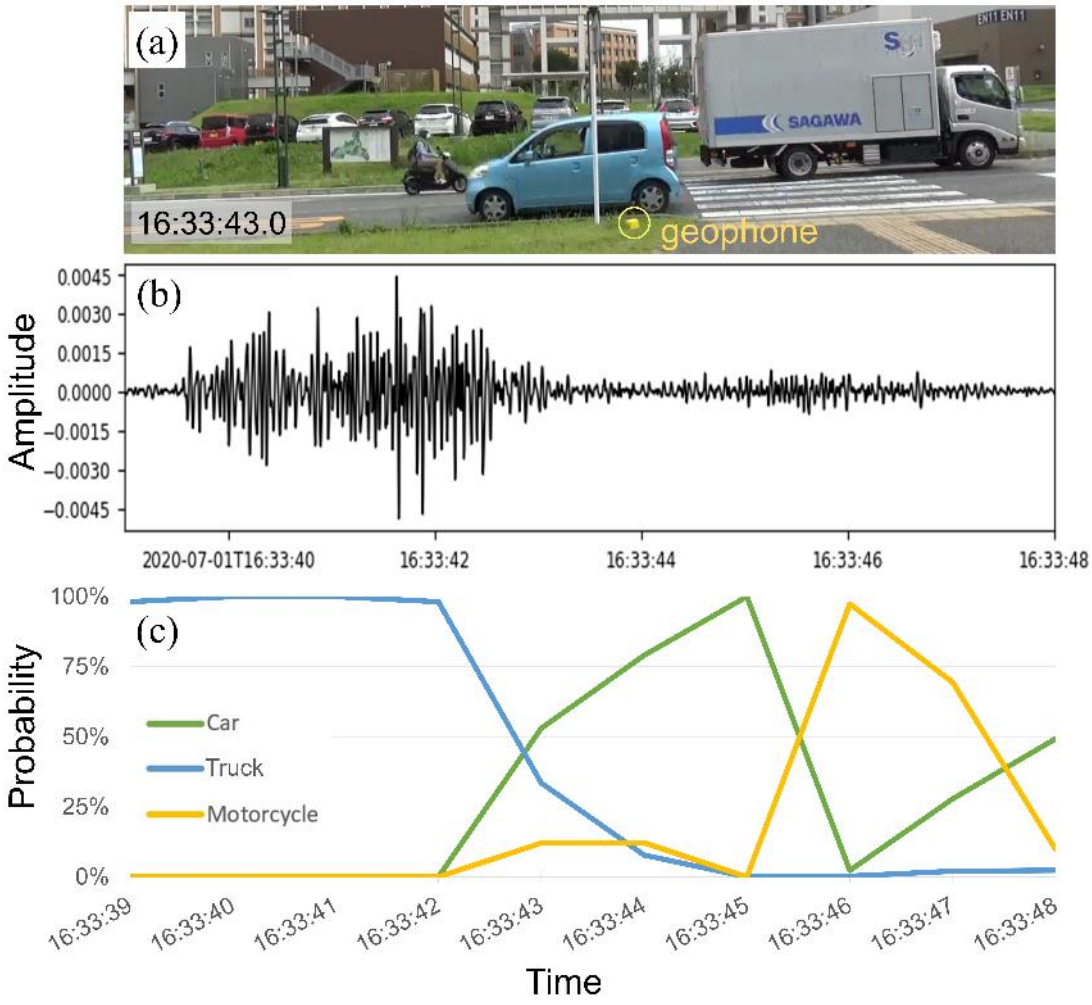

*Figure 5.14 (**a**) A video frame documenting several vehicles passing the receiver at time 16:33:43. (**b**) The seismic noise generated a 10 s window. (**c**) Vehicle type probabilities estimated by CNN at intervals of 1 s during the window in (**b**) contain 10 interpretation points with 80% overlapping (Ahmad and Tsuji, 2021b).*

I used a 90% probability threshold to determine the predicted vehicle class. The 15-minute record included 93 different vehicles. Table 5.7 shows the performance of the three models in terms of precision and recall per vehicle class.

Precision represents the percentage of correct declarations among all declarations made by the model, and recall represents the percentage of correct declarations among all declarations:

$$\text{Precision}_{Class} = \frac{TP_{Class}}{TP_{Class} + FP_{Class}} \quad (5.10)$$

$$\text{Recall}_{Class} = \frac{TP_{Class}}{TP_{Class} + FN_{Class}} \quad (5.11)$$

where *TP* stands for true positive, *FP* stands for false positive, and *FN* stands for false negative (Davis and Goadrich, 2006). I used visual data, as shown in Figures 13f–h and 14a, to determine the true positive/true negative and ensure I calculated the real accuracy for my method. By clear margins, CNN had the best precision, and RNN had the best recall.

Table 5. 7 Precision and recall of networks on a 15-minute data record, including 16 large, 49 medium, and 28 small Vehicles.

	Class	DNN	CNN	RNN
Precision (%)	Big (bus, trucks)	100	100	88.8
	Medium (light car)	75.8	97.9	81.3
	Small (motorcycle)	90.4	90.9	80
Recall (%)	Big (bus, trucks)	93.8	100	100
	Medium (light car)	95.9	95.2	97.9
	Small (motorcycle)	67.8	72.2	85.7
Average Precision (Recall) (%)		88.7 (85.8)	96.2 (89.1)	83.3 (94.5)

5.4.4. Scalability to Long Records

One desirable feature of a seismic-based system for traffic monitoring is its ability to operate continuously with minimal supervision, which means the system needs to deal with long records (e.g., several weeks or months). For that reason, I evaluated the computational cost of the three models, ignoring their accuracy and focusing on the scalability of networks to handle large records. I chose one hour of data to measure running time and memory usage, then repeated the measurements after successively doubling the size of the dataset to a maximum of 1024 hr (nearly 43 days) (Figure 5.15). CNN interpreted a month-long (720 h) record in 70 min, a computation time 10% faster than DNN.

CNN also had the lowest memory usage, requiring 40% less memory than RNN. Regarding computational cost for long records, CNN was more efficient than DNN and RNN.

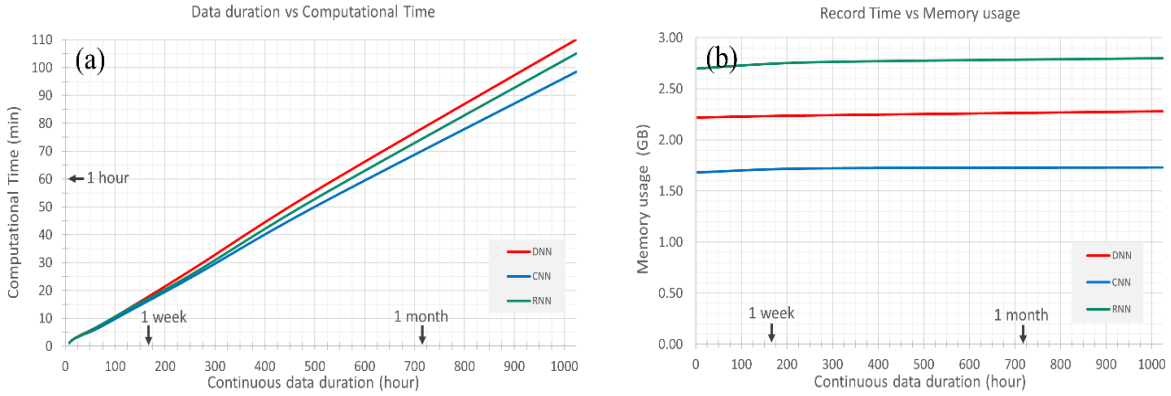

*Figure 5.15 (**a**) The run time required by DNN (red), CNN (blue), and RNN (green) to process a seismic record is 1024 h long (2.35 GB). (**b**) The memory usage required by the three networks to process the long seismic record, including the RAM usage and TensorFlow in the backend (Ahmad and Tsuji, 2021b).*

5.4.5. CNN VS other ML methods

I calculated precision, recall, f1-score, and accuracy using the same training and test data to evaluate the three proposed methods. The formula for each evaluation technique is described as the following equation:

$$f1 - score = \frac{2 \times Precision \times Recall}{Precision + Recall}, \quad (5.12)$$

$$Accuracy = \frac{True\ Positive + True\ Negative}{all\ predictions}, \quad (5.13)$$

I randomly split the dataset into training and testing data sets in a 75–25 ratio. The testing data set includes (259 buses, 439 cars, 228 motorcycles, and 469 noise) data samples, including actual and synthetic data.

I used a confusion matrix heat map to visualize the performance of LR, SVM, and NB, as shown in Figure 5.16. Apart from the decision accuracy evaluation, I measured the computational time for the three methods and compared those results with the state-of-the-art CNN architecture.

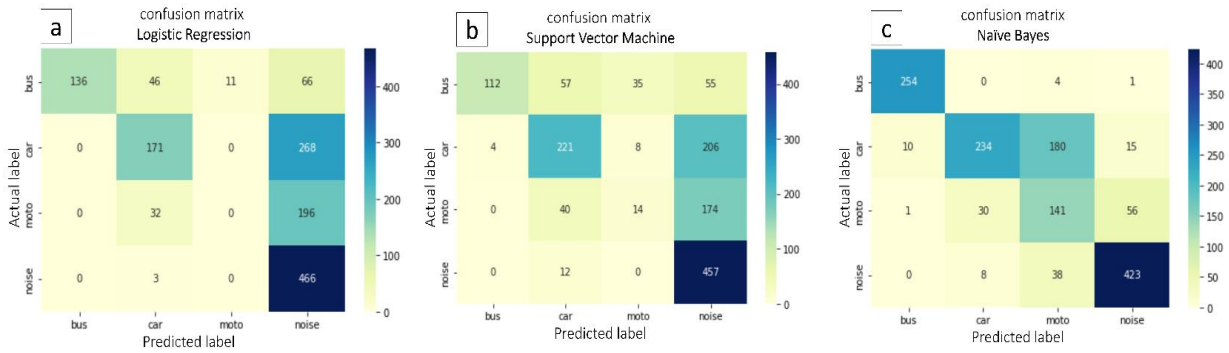

Figure 5.16 A confusion matrix for prediction decisions for (a) LR model, (b) SVM model, and (c) NB model. The vertical axis shows the actual class, and the horizontal axis shows the predicted class by each model (Ahmad et al., 2022).

The confusion matrix of LR detection is presented in Figure 5.16a. Table 5.8 shows the precision, recall, and the f1-score for each class of LR calculated based on the result of Figure 5.16a. Based on Figure 5.16a, LR has failed to detect any motorcycle singles, overpredicting the noise, especially for car and motorcycle classes (Ahmad et al., 2022).

Table 5. 8 Shows the evaluation parameters for LR model prediction for 1395 data samples, including precision, recall, and f1-score, which were calculated per class, averaged, and weighted based on the number of samples for each class.

	Precision	**Recall**	**F1-score**	**Number of predictions**
Bus/Truck	0.53	1.00	0.69	136
Passenger car	0.39	0.68	0.49	252
Motorcycle	0.00	0.00	0.00	11
Noise	0.99	0.47	0.64	966
Average	0.48	0.54	0.45	1395
Weighted average	0.83	0.55	0.61	1395

LR has made 11 predictions for a motorcycle, but all were false positive predictions toward the bus class, as shown in Figure 5.16a. Table 5.8. LR scores 99% precision for the noise class and 47% recall only for the same class. On the other hand, LR scores 100% recall and 53% precision for the bus class.

These scores indicate that the LR classifier is unsuitable for the proposed task and will probably miss or incorrectly detect the right vehicle's class. Figure 5.16b shows the decisions made by the SVM model. I can see a slight improvement compared to LR model predictions. Based on Figures 3.16b and Table 5.9, SVM has 14 true positive motorcycle predictions. However, the SVM's scores are relatively too low to be a reliable method for the given task.

Table 5. 9 shows the evaluation parameters for SVM model prediction for 1395 data samples, including precision, recall, and f1-score, which were calculated per class, averaged, and weighted based on the number of samples for each class.

	Precision	**Recall**	**F1-score**	**Number of predictions**
Bus/Truck	0.43	0.97	0.60	116
Passenger car	0.50	0.67	0.57	330
Motorcycle	0.06	0.25	0.10	57
Noise	0.97	0.51	0.67	892
Average	0.49	0.60	0.49	1395
Weighted average	0.78	0.58	0.62	1395

The third algorithm I tested in this study (NB) has shown significant improvement in the prediction. NB could successfully predict most of the Motorcycle data samples, which LR and SVM failed to do. NB has also sourced 98% precision and 97% f1-score for the bus class, as shown in Table 5.10. NB scored a 47% f1-score for the motorcycle class, considered the highest among the three methods. NB has scored relatively high precision, recall, and f1-scores, which might make it an excellent competitor for the CNN algorithm in this task.

Table 5. 10 Shows the evaluation parameters for NB model prediction for 1395 data samples, including precision, recall, and f1-score, which were calculated per class, averaged, and weighted average on the number of samples for each class.

	Precision	Recall	F1-score	Number of predictions
Bus/Truck	0.98	0.96	0.97	265
Passenger car	0.53	0.86	0.66	272
Motorcycle	0.62	0.39	0.48	363
Noise	0.90	0.85	0.88	495
Average	0.76	0.77	0.75	1395
Weighted average	0.77	0.75	0.75	1395

In addition to the previous evaluation parameters, I have calculated the accuracy using equation 10, measured the running time for all three methods, and compared it with the accuracy and running time for CNN, as shown in Table 5.11. For this task, I used a work frame consisting of Python code based on ObsPy, NumPy, and sci-kit-learn libraries. I used a cloud computing platform containing dual Tesla K80 GPUs with 12 GB RAM to run all algorithms. While CNN still scores the highest accuracy along all proposed methods, NB has a 1000 times faster computation time. While CNN required 112 seconds to finalize the training and test, NB needed 0.15 seconds to do the same task using an identical data set.

Table 5. 11 Accuracy and running time of LR, SVM, NB, and CNN. The running time includes the training and testing on a data set of 5,580 samples.

	LR	SVM	NB	CNN
Accuracy	55%	58%	75%	94%
Running time (Seconds)	1.664	12.49	0.150	112.3*

*CNN has trained for 100 iterations

5.5. Discussion

This study achieved good performance in probabilistic vehicle detection, and it confirmed the effectiveness of long-term monitoring. The neural networks outperformed template matching in computational cost, accuracy, and generalization. CNN, in particular, achieved state-of-the-art performance in analyzing new data compared to all other methods.

CNN detected and identified these vehicles by their frequency components, even when their signals overlapped. For example, at 16:33:43 in Figure 5.14, CNN determined a 40% probability for a truck and a 60% probability for a car, even though the truck's signal was stronger than the car's. I attribute this ability to the convolutional filters in CNN, which, unlike RNN and DNN, input extracted features to the dense layers. Although RNN had the highest recall, CNN had the highest precision. Because CNN detected the overlapped vehicles with a probability of less than 90% (Figures 13d and 14), these identifications were not counted as detections, but the recall score could be enhanced by decreasing the threshold probability to below 90%. However, CNN and other networks have failed to recognize the existence of overlapped vehicles within the same type. The current network's architectures were not designed to count multiple vehicles. This problem could be overcome by using more than one receiver.

The relatively poor performance of RNN may stem from the intrinsic conflict between the independence of vehicle events and the inclusion of the LSTM layer in RNN that detects sequences of events. The RNN tries to create a long memory for the sequence of vehicle classes, but the succession of vehicle events is random.

All networks were similar in their computational cost. However, CNN had the shortest running time for very long records. On average, CNN needed 5 min to interpret a 1-day record and 70 min to interpret a 1-month record. DNN had the lowest memory demand of the three models, using a maximum of 1.72 GB of the system RAM; however, memory usage was tolerable for the other two models (Figure 5.15). Theoretically, memory usage costs are constant at all traffic levels because the neural network only needs to store the weights and biases (Perol et al., 2018).

Ultimately, the proposed system based on seismic signals has been proved as an alternative solution for vehicle classification with an accuracy of up to 97%, close to the previously adopted systems based on automatic visual classification (90~99%) and the loop detector systems (99% accuracy). The systems I tested did not have high power requirements or high computational costs and were physically unobtrusive. More importantly, the traffic monitoring system based on seismic data could detect and classify vehicles reliably without violating the public's privacy.

I have tested three ML algorithms, Logistic Regression, Support Vector Machine, and Naïve Bayes, using the same data set to investigate which is suitable for traffic monitoring based on the ground motion generated by vehicles. I observed four factors in training and testing to evaluate the efficiency of the methods and compared them to the state-of-the-art CNN using 5,580 data samples. After testing and observation, I find that neither Logistic Regression nor Support Vector Machine suits the mentioned task. Logistic Regression and Support Vector Machine scored low in all evaluations. LR and SVM failed to recognize any motorcycle seismic signals, and both of them have low precision for vehicles and high precision for noise, indicating that these methods frequently mispredicted vehicles as noise. SVM was computationally expensive relative to the other ML algorithm. Therefore, I recommend not considering Logistic Regression or Support Vector Machine for the given task.

On the other hand, Naïve Bayes has shown promising results. NB has average F-1 scores of 75%, up to 97% in some cases. NB did not have difficulty correctly predicting motorcycles and scored 62% precision. Although CNN is the superior method in accuracy and precision, Naïve Bayes has shown modest computational cost. NB was 750 times faster than CNN under the same conditions. I recommend developing and enhancing models for traffic monitoring using NB with frequency domain data. I will consider this factor in future research. Therefore, I recommend NB for vehicle classification applications that have real-time processing. Otherwise, CNN can be adopted for offline applications based on the significant compromise on accuracy.

5.6. Conclusions

Machine learning proved an effective and low-cost technique to enable real-time traffic monitoring based on seismic data. In this study, I evaluated three neural network systems for this purpose and demonstrated that CNN provided the best performance in terms of accuracy and speed. CNN also surpassed the others in its ability to detect overlapping signals. RNN did not perform as well as the others for traffic monitoring because its intrinsic reliance on temporal sequences conflicts with the random nature of traffic data. Although seismic data can be used for traffic monitoring, all neural networks have a shortcoming in counting vehicles because they cannot identify multiple vehicles of the same class within a waveform frame. The main limitation of neural networks is the human effort in acquiring and compiling a suitable amount of training data. I augmented my dataset by adding random noise. Although the models can be deployed without extra training, I recommend retraining the model as much as possible to guarantee the best performance in the generalization. Neural networks that process seismic data offer compelling advantages over current approaches to traffic monitoring.

The seismic record has small file sizes compared to videos and other types of monitoring data. Because the system is simple and passive, consisting of a few geophones, it can be implemented for months at a time without supervision. The recorded data can be analyzed at a low computational cost to give clear statistical information for vehicles during implementation. This makes the proposed system suitable for use on hard-to-access roads. The favored method, based on CNN, is suitable for continuous records of a month or longer; CNN was able to process a month’s worth of data in approximately an hour. However, this approach faces some challenges as the current approach is limited to a single-vehicle pass; this problem may be overcome by installing two or more geophones within a known distance near the roadway. I plan to study real-time traffic monitoring in the future, as current research only uses recorded seismic data. My method could be improved to predict traffic features like speed, direction, and safe driving. I also aim to apply this method to different types of transportation, including ships, bicycles, pedestrians, and airplanes. We're exploring how to accurately estimate vehicle speeds and consider expanding this technique to estimate more traffic data and apply it to various modes of transportation.

Chapter 6

General conclusion and future direction

6.1. Overview

In the third chapter, the focus is on the development of innovative borehole seismic survey techniques, particularly the B-PASS and HE-PASS systems. These systems, deriving from the original PASS design, are tailored for surface and borehole usage and effectively handle challenges such as surface noise interference. The B-PASS system is notable for its ability to generate stable, low-energy seismic signals and its effectiveness in monitoring large areas and detecting deep subsurface waves. Field tests have demonstrated its efficacy in reaching up to 425 meters horizontally from the borehole, and the repeatability test showed a stable source with no changes for 19 continuous hours of operation. The HE-PASS system further extends this capability, achieving significant signal propagation over 1 kilometer with just an hour of operation, and I could achieve reflected waves at a depth of 1.2 seconds using DAS. These systems have diverse applications in environmental and geological monitoring, including CCS projects, landslide detection, and earthquake fault monitoring.

Chapter four delves into the efficiency of Convolutional Neural Networks (CNNs) in interpreting slump and fault systems in plate subduction zones. The chapter includes a qualitative comparison between CNN results and conventional ant-track and coherency-attribute methods for detecting fault systems, indicating that CNN provides more natural and human-like interpretations. The CNN effectively processed large 3D seismic volumes, precisely identifying a slump unit in the Kumano forearc basin in the Nankai Trough. It also detected previously 3 unknown complex slump units. The study details the CNN training from the Nankai Trough for 10,000 iterations, achieving a 95% classification accuracy for slumping units. When applied to seismic data from Sanriku-Oki, northeast Japan, the CNN matched 85% of human interpretations for the slump units in that region. Additionally, CNN accurately mapped gas chimneys in the West Delta Deep Marine field in Egypt. The chapter suggests

potential improvements in CNN-based methods, including exploring more advanced deep learning architectures for better classification accuracy and broader geological applications.

Chapter five discusses and explores the use of machine learning, specifically neural networks, for real-time traffic monitoring using seismic data. The study evaluates different neural network systems and finds that CNN provides the best performance in terms of accuracy and speed, especially for processing overlapping signals. Despite the limitations in vehicle counting within a waveform frame, the method offers advantages over traditional traffic monitoring approaches due to the small file size of seismic records and the low computational cost of data analysis. The study highlights that the Convolutional Neural Network (CNN) outperformed other methods in analyzing new data. The proposed CNN architecture not only achieved a 96% classification accuracy for vehicle size but also processed month-long (720 hours) records in just 70 minutes using minimal computational resources. Furthermore, it was capable of distinguishing different types of vehicles simultaneously. Additionally, a method to expand the training data size by 500% through the integration of synthetic random noise was proposed.

Overall, the chapters highlighted here emphasize the significant role of modern technologies and machine learning in advancing seismic monitoring and interpretation. They illustrate the wide-ranging applications of these technologies, from geological research to environmental monitoring and traffic management. Central to these chapters is the theme of utilizing big data for monitoring and detection objectives, where artificial intelligence (AI) emerges as a crucial tool in interpreting and enhancing the processing of unconventional data sources. This overview demonstrates the increasing importance and transformative potential of AI and related technologies in various sectors, particularly in handling and interpreting complex seismic data.

6.2. Future Direction

Based on the summary of the dissertation, the future direction of seismic monitoring and interpretation indeed seems to be moving towards a deeper integration of advanced technology and machine learning. Key areas of focus for future research and development may include:

Enhanced Deep Learning Techniques: Continual improvement and customization of neural network architectures like CNN, RCNN, U-net, and SegNet are essential. This would involve not just refining their accuracy but also tailoring them for specific geological and environmental conditions, leading to more precise and context-specific interpretations.

CCS Monitoring with CNN: The thesis highlights innovative methodologies for continuous data monitoring in Carbon Capture and Storage (CCS) systems using CNNs. This approach, particularly in detecting minor CO2 leakages, signifies a substantial advancement in environmental monitoring and sustainability efforts.

Expanding Applications in Environmental Monitoring: Broadening the scope of seismic monitoring systems for diverse environmental applications, such as monitoring CO2 storage sites, detecting landslides, analyzing volcanic activities, and predicting earthquakes, can significantly contribute to disaster prevention and environmental conservation.

Real-Time Data Processing in Traffic Monitoring: Implementing real-time processing of seismic data for traffic monitoring could revolutionize urban planning and traffic management. This could lead to more effective management of traffic flows, congestion reduction, and overall urban infrastructure development.

Diverse Transportation Mode Analysis: Extending seismic monitoring to various transportation modes, including maritime, aviation, and pedestrian traffic, can provide a holistic view of transportation dynamics. This comprehensive data can be instrumental in designing more efficient and interconnected transport systems.

Automated Interpretation in Geophysical Exploration: Utilizing machine learning to automate data interpretation in the oil, gas, and renewable energy sectors could significantly enhance exploration efficiency. This automation could lead to faster, more accurate identification of potential energy resources, reducing costs and environmental impacts.

Integration with Other Technologies: The convergence of seismic monitoring with cutting-edge technologies like drones for inaccessible area data collection, augmented reality for enhanced data visualization, and IoT for seamless data transmission and analysis can open new frontiers in seismic research and application.

Cross-Disciplinary Collaboration and Standardization: Fostering cooperation among geoscientists, engineers, data scientists, and environmentalists is crucial for developing standardized protocols. This multidisciplinary approach can ensure the effective and ethical deployment of seismic technologies across various regions and fields.

Addressing Environmental and Safety Concerns: Prioritizing the development of eco-friendly seismic monitoring techniques is key. These methods should minimize ecological impacts while maximizing data collection efficiency and accuracy.

The dissertation's insights and proposed directions have the potential not only to advance scientific knowledge but also to enhance environmental and public safety and drive innovation in numerous sectors. The intersection of machine learning with seismic technology is poised to transform our understanding and management of Earth's geophysical processes, marking a new era in environmental and geological sciences.

Reference List

Abiodun, O. I., A. Jantan, A. E. Omolara, K. V. Dada, N. A. E. Mohamed, and H. Arshad, 2018, State-of-the-art in artificial neural network applications: A survey: Heliyon, **4**, 938.

Adeoti, L., K. Ishola, U. Olodu, M. Bello, and O. Adeogun, 2013, Application of Uphole Seismic Refraction Survey for Subsurface Investigation: A Case Study of Liso Field, Niger Delta, Nigeria: World Applied Sciences Journal, **26**.

Ahmad, A. B., and T. Tsuji, 2021a, Machine learning for automatic slump identification from 3D seismic data at convergent plate margins: Marine and Petroleum Geology, **133**, 105290.

Ahmad, A. B., and T. Tsuji, 2021b, Traffic Monitoring System Based on Deep Learning and Seismometer Data: Applied Sciences, **11**.

Ahmad, A. B., T. Tsuji, H. Saibi, and A. N. Belkacem, 2021, Vehicles detection based on their seismic surface waves using classification techniques, *in* Sixth International Conference on Engineering Geophysics, Virtual, 25–28 October 2021, , 244–247.

Ahmad, A. B., H. Saibi, A. N. Belkacem, and T. Tsuji, 2022, Vehicle Auto-Classification Using Machine Learning Algorithms Based on Seismic Fingerprinting: Computers, **11**.

Ahmad B. Ahmad, Takeshi Tsuji, Takuya Miura, Takao Nibe, Kimiaki Ochi, and Takeya Nagata, 2023, Subsurface imaging with Portable Active Seismic Source through amplified vertical vibration: Subsurface Imaging with Portable Active Seismic Source through Amplified Vertical Vibration, 4.

Ahmed, S. H., S. H. Bouk, M. A. Yaqub, D. Kim, H. Song, and J. Lloret, 2016, CODIE: Controlled Data and Interest Evaluation in Vehicular Named Data Networks: IEEE Transactions on Vehicular Technology, **65**, 3954–3963.

Aki, K., and P. Richards, 2002, Quantitative Seismology, 2nd Ed: .

Alam, M., M. D. Samad, L. Vidyaratne, A. Glandon, and K. M. Iftekharuddin, 2020, Survey on deep neural networks in speech and vision systems: Neurocomputing, **417**, 302–321.

Alavi, A. H., and A. H. Gandomi, 2012, Energy-based numerical models for assessment of soil liquefaction: Geoscience Frontiers, **3**, 541–555.

Arrowsmith, S. J., D. T. Trugman, J. MacCarthy, K. J. Bergen, D. Lumley, and M. B. Magnani, 2022, Big data seismology: Reviews of Geophysics, **60**, e2021RG000769.

Artman, B., 2006, Imaging passive seismic data: Geophysics, **71**, SI177–SI187.

Azamathulla, H. M., 2013, A review on application of soft computing methods in water resources engineering: Metaheuristics in Water, Geotechnical and Transport Engineering, 27.

Balid, W., and H. H. Refai, 2018, Real-time magnetic length-based vehicle classification: Case study for inductive loops andwireless magnetometer sensors in Oklahoma state: Transportation Research Record, **2672**, 102–111.

Binley, A., S. S. Hubbard, J. A. Huisman, A. Revil, D. A. Robinson, K. Singha, and L. D. Slater, 2015, The emergence of hydrogeophysics for improved understanding of subsurface processes over multiple scales: Water Resources Research, **51**, 3837–3866.

Biondi, B. L., 2006, 3D Seismic Imaging: Society of Exploration Geophysicists.

Bohnhoff, M., G. Dresen, W. L. Ellsworth, and H. Ito, 2010, Passive seismic monitoring of natural and induced earthquakes: case studies, future directions and socio-economic relevance: New Frontiers in Integrated Solid Earth Sciences, 261–285.

Boot-Handford, M. E., J. C. Abanades, E. J. Anthony, M. J. Blunt, S. Brandani, N. Mac Dowell, J. R. Fernández, M.-C. Ferrari, R. Gross, and J. P. Hallett, 2014, Carbon capture and storage update: Energy & Environmental Science, **7**, 130–189.

Bormann, P., and E. Wielandt, 2013, Seismic signals and noise, *in* New manual of seismological observatory practice 2 (NMSOP2), Deutsches GeoForschungsZentrum GFZ, 1–62.

Bouska, J., 2010, Distance separated simultaneous sweeping, for fast, clean, vibroseis acquisition: Geophysical Prospecting, **58**, 123–153.

Budinis, S., S. Krevor, N. Mac Dowell, N. Brandon, and A. Hawkes, 2018, An assessment of CCS costs, barriers and potential: Energy Strategy Reviews, **22**, 61–81.

Bugge, A. J., J. E. Lie, and S. Clark, 2018, Automatic facies classification and horizon tracking in 3D seismic data: 1st EAGE/PESGB Workshop on Machine Learning, **2018**, 1–3.

Caesary, D., S. Y. Song, H. Yu, B. Kim, and M. J. Nam, 2020, A review on CO2 leakage detection in shallow subsurface using geophysical surveys: International Journal of Greenhouse Gas Control, **102**, 103165.

Carli, R., M. Dotoli, and N. Epicoco, 2018, Monitoring traffic congestion in urban areas through probe vehicles: A case study analysis: Internet Technology Letters, **1**, e5.

Carli, R., M. Dotoli, N. Epicoco, B. Angelico, and A. Vinciullo, 2015, Automated evaluation of urban traffic congestion using bus as a probe: 2015 IEEE International Conference on Automation Science and Engineering (CASE), 967–972.

CHANGE, O. N. C., 2007, Intergovernmental panel on climate change: World Meteorological Organization, **52**.

Cheng, F., J. Xia, Y. Xu, Z. Xu, and Y. Pan, 2015, A new passive seismic method based on seismic interferometry and multichannel analysis of surface waves: Journal of Applied Geophysics, **117**, 126–135.

Chhun, C., and T. Tsuji, 2020, Pore pressure analysis for distinguishing earthquakes induced by CO2 injection from natural earthquakes: Sustainability, **12**, 9723.

Chhun, C., A. Kioka, J. Jia, and T. Tsuji, 2018, Characterization of hydrate and gas reservoirs in plate convergent margin by applying rock physics to high-resolution seismic velocity model: Marine and Petroleum Geology, **92**, 719–732.

Coifman, B., and S. Neelisetty, 2014, Improved speed estimation from single-loop detectors with high truck flow: Journal of Intelligent Transportation Systems: Technology, Planning, and Operations, **18**, 138–148.

Cordes, E. E., D. O. B. Jones, T. A. Schlacher, D. J. Amon, A. F. Bernardino, S. Brooke, R. Carney, D. M. DeLeo, K. M. Dunlop, and E. G. Escobar-Briones, 2016, Environmental impacts of the deep-water oil and gas industry: a review to guide management strategies: Frontiers in Environmental Science, **4**, 58.

Council, N. R., 2001, Basic research opportunities in earth science: .

Crane, J. M., J. M. Lorenzo, and J. B. Harris, 2013, A new electrical and mechanically detonatable shear wave source for near surface (0–30m) seismic acquisition: Journal of Applied Geophysics, **91**, 1–8.

Cutler, R. P., 1998, Development of a Hydraulic Borehole Seismic Source:

Daley, T. M., B. M. Freifeld, J. Ajo-Franklin, S. Dou, R. Pevzner, V. Shulakova, S. Kashikar, D. E. Miller, J. Goetz, and J. Henninges, 2013, Field testing of fiber-optic distributed acoustic sensing (DAS) for subsurface seismic monitoring: The Leading Edge, **32**, 699–706.

Daniel, W. W., 1990, Applied Nonparametric Statistics: PWS-KENT Pub.

Davis, J., and M. Goadrich, 2006, The relationship between precision-recall and ROC curves: ACM International Conference Proceeding Series, **148**, 233–240.

Dong, H., X. Wang, C. Zhang, R. He, L. Jia, and Y. Qin, 2018, Improved Robust Vehicle Detection and Identification Based on Single Magnetic Sensor: IEEE Access, **6**, 5247–5255.

Dugda, M. T., A. B. Kassa, L. Pouchard, H. Saylor, and E. Dires, 2022, Development of Big Seismic Data Processing Tools: AGU Fall Meeting Abstracts, **2022**, S32D-0281.

Dziewonski, A. M., and D. L. Anderson, 1984, Seismic Tomography of the Earth's Interior: The first three-dimenstional models of the earth's structure promise to answer some basic questions of geodynamics and signify a revolution in earth science: American Scientist, **72**, 483–494.

Evans, N., 2010, Automated Vehicle Detection and Classification using Acoustic and Seismic Signals.University of Yorkp.

Fleming, J. R., 1998, Historical Perspectives on Climate Change: Oxford University Press.

Freed, D., 2008, Cable-free nodes: The next generation land seismic system: The Leading Edge, **27**, 878–881.

Furre, A.-K., O. Eiken, H. Alnes, J. N. Vevatne, and A. F. Kiær, 2017, 20 Years of Monitoring CO2-injection at Sleipner: Energy Procedia, **114**, 3916–3926.

Gadallah, M. R., and R. Fisher, 2008, Exploration Geophysics: Springer Science & Business Media.

Gao, D., 2011, Latest developments in seismic texture analysis for subsurface structure, facies, and reservoir characterization: A review: Geophysics, **76**, W1–W13.

Al Ghafri, S. Z. S., C. Revell, M. Di Lorenzo, G. Xiao, C. E. Buckley, E. F. May, and M. Johns, 2023, Techno-economic and environmental assessment of LNG export for hydrogen production: International Journal of Hydrogen Energy, **48**, 8343–8369.

Girty, G. H., 2009, Understanding Processes Behind Natural Disasters - Chapter 8 Landslides:

Grandi, S., M. Dean, and O. Tucker, 2017, Efficient containment monitoring with distributed acoustic sensing: feasibility studies for the former Peterhead CCS Project: Energy Procedia, **114**, 3889–3904.

Groenenberg, H., and H. de Coninck, 2008, Effective EU and Member State policies for stimulating CCS: International Journal of Greenhouse Gas Control, **2**, 653–664.

Grossberg, S., and M. E. Rudd, 1989, A neural architecture for visual motion perception: Group and element apparent motion: Neural Networks, **2**, 421–450.

Hammond, J. O. S., R. England, N. Rawlinson, A. Curtis, K. Sigloch, N. Harmon, and B. Baptie, 2019, The future of passive seismic acquisition: Astronomy & Geophysics, **60**, 2–37.

Haszeldine, R. S., 2009, Carbon capture and storage: how green can black be? Science, **325**, 1647–1652.

Hibino, G., S. Ashina, D. Silva Herran, T. Masui, Y. Motoki, T. Hirayama, and T. Ota, 2022, Japan's quantitative emission scenario of GHG net zero and its implications for Asian countries: Glob Environ Res, **26**, 11–21.

IEA, R., 2020, Energy technology perspectives 2020: Special Report on Carbon Capture, Utilisation and Storage.

Ioffe, S., and C. Szegedy, 2015, Batch Normalization: Accelerating Deep Network Training by Reducing Internal Covariate Shift: 32nd International Conference on Machine Learning, ICML

2015, **1**, 448–456.

Ismail, A., H. Ewida, S. Nazeri, M. Al-Ibiary, and A. Zollo, 2021, Gas channels and chimneys prediction using artificial neural networks and multi-seismic attributes, offshore West Nile Delta, Egypt: Journal of Petroleum Science and Engineering, **208**.

Jeng, S. T., and L. Chu, 2014, A high-definition traffic performance monitoring system with the Inductive Loop Detector signature technology: 2014 17th IEEE International Conference on Intelligent Transportation Systems, ITSC 2014, 1820–1825.

Jenkins, C., A. Chadwick, and S. D. Hovorka, 2015, The state of the art in monitoring and verification—Ten years on: International Journal of Greenhouse Gas Control, **40**, 312–349.

Jie*, B., P. Deli, W. Aiqi, C. Kai, H. Xianguo, and Y. Boya, 2014, Minimizing the seismic acquisition footprint in a nature reserve, *in* SEG Technical Program Expanded Abstracts 2014, Society of Exploration Geophysicists, 259–263.

Jin, G., B. Ye, Y. Wu, and F. Qu, 2019, Vehicle Classification Based on Seismic Signatures Using Convolutional Neural Network: IEEE Geoscience and Remote Sensing Letters, **16**, 628–632.

Karbasi, M., and H. M. Azamathulla, 2017, Prediction of scour caused by 2D horizontal jets using soft computing techniques: Ain Shams Engineering Journal, **8**, 559–570.

Ketcham, S. A., M. L. Moran, J. Lacombe, R. J. Greenfield, and T. S. Anderson, 2005, Seismic source model for moving vehicles: IEEE Transactions on Geoscience and Remote Sensing, **43**, 248–256.

Kim, D., E.-S. Bang, W. Kim, E.-S. Bang, and W.-C. Kim, 2004, Evaluation of Various Downhole Data Reduction Methods for Obtaining Reliable VS Profiles: Geotechnical Testing Journal - GEOTECH TESTING J, **27**.

Kingma, D. P., and J. L. Ba, 2015, Adam: A method for stochastic optimization: 3rd International Conference on Learning Representations, ICLR 2015 - Conference Track Proceedings.

Kret, K., T. Tsuji, C. Chhun, and O. Takano, 2020, Distributions of gas hydrate and free gas accumulations associated with upward fluid flow in the Sanriku-Oki forearc basin, northeast

Japan: Marine and Petroleum Geology, **116**, 104305.

Krischer, L., J. Smith, W. Lei, M. Lefebvre, Y. Ruan, E. S. de Andrade, N. Podhorszki, E. Bozdağ, and J. Tromp, 2016, An adaptable seismic data format: Geophysical Supplements to the Monthly Notices of the Royal Astronomical Society, **207**, 1003–1011.

Lackey, J., G. Moore, and M. Strasser, 2018, Three-dimensional mapping and kinematic characterization of mass transport deposits along the outer Kumano Basin and Nankai accretionary wedge, southwest Japan: Progress in Earth and Planetary Science, **5**, 65.

Lamas-Seco, J. J., P. M. Castro, A. Dapena, and F. J. Vazquez-Araujo, 2015, Vehicle classification using the discrete fourier transform with traffic inductive sensors: Sensors (Switzerland), **15**, 27201–27214.

Lee, H., and B. Coifman, 2015, Using LIDAR to Validate the Performance of Vehicle Classification Stations: Journal of Intelligent Transportation Systems: Technology, Planning, and Operations, **19**, 355–369.

Li, F., and Z. Lv, 2017, Reliable vehicle type recognition based on information fusion in multiple sensor networks: Computer Networks, **117**, 76–84.

Li, S., C. Yang, H. Sun, and H. Zhang, 2019a, Seismic fault detection using an encoder–decoder convolutional neural network with a small training set: Journal of Geophysics and Engineering, **16**, 175–189.

Li, Y., A. Y. C. Tok, and S. G. Ritchie, 2019b, Individual Truck Speed Estimation from Advanced Single Inductive Loops: Transportation Research Record, **2673**, 272–284.

Li, Z., M. Meier, E. Hauksson, Z. Zhan, and J. Andrews, 2018, Machine learning seismic wave discrimination: Application to earthquake early warning: Geophysical Research Letters, **45**, 4773–4779.

Ligorría, J. P., and C. J. Ammon, 1999, Iterative deconvolution and receiver-function estimation: Bulletin of the Seismological Society of America, **89**, 1395–1400.

Liner, C. L., T. A. McGilvery, C. L. Liner, and T. A. McGilvery, 2019, Historical Overview of Petroleum and Seismology: The Art and Science of Seismic Interpretation, 41–56.

Litman, T., 2007, Developing indicators for comprehensive and sustainable transport planning: Transportation Research Record, 10–15.

Liu, N., T. He, Y. Tian, B. Wu, J. Gao, and Z. Xu, 2020, Common-azimuth seismic data fault analysis using residual UNet: Interpretation, **8**, SM25–SM37.

Lumley, D., 2010, 4D seismic monitoring of CO 2 sequestration: The Leading Edge, **29**, 150–155.

Lumley, D. E., 2001, Time-lapse seismic reservoir monitoring: GEOPHYSICS, **66**, 50–53.

Ma, J., L. Li, H. Wang, Y. Du, J. Ma, X. Zhang, and Z. Wang, 2022, Carbon capture and storage: history and the road ahead: Engineering, **14**, 33–43.

Malehmir, A., R. Durrheim, G. Bellefleur, M. Urosevic, C. Juhlin, D. J. White, B. Milkereit, and G. Campbell, 2012, Seismic methods in mineral exploration and mine planning: A general overview of past and present case histories and a look into the future: Geophysics, **77**, WC173–WC190.

Martin, P. T., Y. Feng, and X. Wang, 2003, Detector Technology Evaluation: Mountain-Plains Consortium Fargo, ND.

Martinez, J. F., J. Cartwright, and B. Hall, 2005, 3D seismic interpretation of slump complexes: Examples from the continental margin of Israel: Basin Research, **17**, 83–108.

Meinshausen, M., J. Lewis, C. McGlade, J. Gütschow, Z. Nicholls, R. Burdon, L. Cozzi, and B. Hackmann, 2022, Realization of Paris Agreement pledges may limit warming just below 2 C: Nature, **604**, 304–309.

Miyamoto, M., and K. Takeuchi, 2019, Climate agreement and technology diffusion: Impact of the Kyoto Protocol on international patent applications for renewable energy technologies: Energy Policy, **129**, 1331–1338.

Mocholi Belenguer, F., A. Martinez-Millana, A. Mocholi Salcedo, and J. H. Arroyo Nunez, 2019, Vehicle Identification by Means of Radio-Frequency-Identification Cards and Magnetic Loops: IEEE Transactions on Intelligent Transportation Systems, 1–9.

Mok, Y. J., C. S. Park, and B. H. Nam, 2016, A borehole seismic source and its application to measure in-situ seismic wave velocities of geo-materials: Soil Dynamics and Earthquake Engineering, **80**, 127–137.

Mondol, N. H., 2010, Seismic exploration: Petroleum Geoscience, **1**, 375–402.

Moore, G. F., and M. Strasser, 2016, Large mass transport deposits in Kumano basin, Nankai Trough, Japan, *in* G. Lamarche, J. Mountjoy, S. Bull, T. Hubble, S. Krastel, E. Lane, A. Micallef, L. Moscardelli, C. Mueller, I. Pecher, and S. Woelz, eds., Advances in Natural and Technological Hazards Research, Vol. 41. Springer International Publishing, 371–379.

Moore, G. F., B. B. Boston, M. Strasser, M. B. Underwood, and R. A. Ratliff, 2015, Evolution of tectono-sedimentary systems in the Kumano Basin, Nankai Trough forearc: Marine and Petroleum Geology, **67**, 604–616.

Moran, M. L., and R. J. Greenfield, 2008, Estimation of the acoustic-to-seismic coupling ratio using a moving vehicle source: IEEE Transactions on Geoscience and Remote Sensing, **46**, 2038–2043.

Naghizadeh, M., P. Vermeulen, A. Crook, A. Birce, S. Ross, A. Stanton, M. Rodriguez, and W. Cookson, 2023, EcoSeis: A novel acquisition method for optimizing seismic resolution while minimizing environmental footprint: The Leading Edge, **42**, 61–68.

Nair, V., and G. E. Hinton, 2010, Rectified linear units improve Restricted Boltzmann machines: ICML 2010 - Proceedings, 27th International Conference on Machine Learning, 807–814.

Nair, V., and G. E. Hinton, ForthcomingRectified Linear Units Improve Restricted Boltzmann Machines:

Nakajima, T., and Z. Xue, 2017, Trapping Mechanisms in Field Scale: Results from Nagaoka Geologic CO2 Storage Site: Energy Procedia, **114**, 5015–5022.

Nakata, N., R. Snieder, T. Tsuji, K. Larner, and T. Matsuoka, 2011, Shear wave imaging from traffic noise using seismic interferometry by cross-coherence: GEOPHYSICS, **76**, SA97–SA106.

Nimiya, H., T. Ikeda, and T. Tsuji, 2021, Temporal changes in anthropogenic seismic noise

levels associated with economic and leisure activities during the COVID-19 pandemic: Scientific Reports, **11**, 20439.

Odat, E., J. S. Shamma, and C. Claudel, 2018, Vehicle Classification and Speed Estimation Using Combined Passive Infrared/Ultrasonic Sensors: IEEE Transactions on Intelligent Transportation Systems, **19**, 1593–1606.

Orfanidis, S. J., 1996, Introduction to Signal Processing: Prentice Hall.

Ozawa, A., T. Tsani, and Y. Kudoh, 2022, Japan's pathways to achieve carbon neutrality by 2050–Scenario analysis using an energy modeling methodology: Renewable and Sustainable Energy Reviews, **169**, 112943.

Page, B., G. Turan, A. Zapantis, J. Burrows, C. Consoli, J. Erikson, I. Havercroft, D. Kearns, H. Liu, and D. Rassool, 2020, The global status of CCS 2020: vital to achieve net zero: .

Parkes, G. E., and L. Hatton, 1986, The Marine Seismic Source: Springer Science & Business Media.

Perol, T., M. Gharbi, and M. Denolle, 2018, Convolutional neural network for earthquake detection and location: Science Advances, **4**, e1700578.

Puzyrev, V., and C. Elders, 2020, Unsupervised seismic facies classification using deep convolutional autoencoder: .

Qin, B., T. Allemand, and G. Lambaré, 2015, Full waveform inversion using preserved amplitude reverse time migration: SEG International Exposition and Annual Meeting, SEG-2015.

Robinson, E. A., and S. Treitel, 2012, 10. Predictive Deconvolution of Seismic Traces, *in* Geophysical Signal Analysis, , 238–250.

Rock, L., S. O'Brien, S. Tessarolo, J. Duer, V. O. Bacci, B. Hirst, D. Randell, M. Helmy, J. Blackmore, C. Duong, A. Halladay, N. Smith, T. Dixit, S. Kassam, and M. Yaychuk, 2017, The Quest CCS Project: 1st Year Review Post Start of Injection: Energy Procedia, **114**, 5320–5328.

Rymarczyk, T., E. Kozłowski, G. Kłosowski, and K. Niderla, 2019, Logistic Regression for

Machine Learning in Process Tomography: Sensors, **19**.

Shearer, P. M., 2019, Introduction to Seismology, 3rd ed.: Cambridge University Press.

Shim, K., M. Lee, I. Choi, Y. Boo, and W. Sung, 2017, SVD-Softmax: Fast Softmax Approximation on Large Vocabulary Neural Networks: Advances in Neural Information Processing Systems, **30**, 5463–5473.

Shimshoni, Y., and N. Intrator, 1998, Classification of seismic signals by integrating ensembles of neural networks: IEEE Transactions on Signal Processing, **46**, 1194–1201.

Skoumal, R. J., M. R. Brudzinski, B. S. Currie, and J. Levy, 2014, Optimizing multi-station earthquake template matching through re-examination of the Youngstown, Ohio, sequence: Earth and Planetary Science Letters, **405**, 274–280.

Srivastava, N., G. Hinton, A. Krizhevsky, and R. Salakhutdinov, 2014a, Dropout: A Simple Way to Prevent Neural Networks from Overfitting:

Srivastava, N., G. Hinton, A. Krizhevsky, I. Sutskever, and R. Salakhutdinov, 2014b, Dropout: A Simple Way to Prevent Neural Networks from Overfitting: J. Mach. Learn. Res., **15**, 1929–1958.

Steeper, T., 2013, CO2CRC Otway Project Social Research: Assessing CCS Community Consultation: Energy Procedia, **37**, 7454–7461.

Suzuki, R., K. Yamaoka, S. Tsuji, and T. Watanabe, 2021, Ground water-induced changes in velocities of P and S waves (Vp and Vs) measured using an accurately controlled seismic source: Earth, Planets and Space, **73**, 152.

Sweatman, R., S. Marsic, and G. McColpin, 2010, New approach and technology for CO2 flow monitoring and remediation: Abu Dhabi International Petroleum Exhibition and Conference.

Tanaka, Y., Y. Sawada, D. Tanase, J. Tanaka, S. Shiomi, and T. Kasukawa, 2017, Tomakomai CCS demonstration project of Japan, CO2 injection in process: Energy Procedia, **114**, 5836–5846.

Tarbuck, E. J., and F. K. Lutgens, 1984, The Earth: An Introduction to Physical Geology.:

C.E.Merrill.

Thierry, M., and C. Pierre, 1996, Classification of Offshore Mass Movements: SEPM Journal of Sedimentary Research, **Vol. 66**, 43–57.

Titos, M., A. Bueno, L. Garcia, and C. Benitez, 2018, A Deep Neural Networks Approach to Automatic Recognition Systems for Volcano-Seismic Events: IEEE Journal of Selected Topics in Applied Earth Observations and Remote Sensing, **11**, 1533–1544.

Tsuji*, T., T. Ikeda, and K. Yamaoka, 2020, Permanent monitoring system using continuous and controlled seismic source: Monitoring of dynamic behaviors from smaller reservoir to larger crust, *in* Fifth International Conference on Engineering Geophysics, Al Ain, UAE, 21?24 October 2019, , . SEG Global Meeting AbstractsSociety of Exploration Geophysicists, 211–215.

Tsuji, T., H. Yamaguchi, T. Ishii, and T. Matsuoka, 2009, Mineral classification from quantitative X-ray maps using neural network: Application to volcanic rocksi ar_682 105..119: .

Tsuji, T., S. Tsuji, J. Kinoshita, T. Ikeda, and A. B. Ahmad, 2022, 4 cm Portable Active Seismic Source (PASS) for Meter- to Kilometer-Scale Imaging and Monitoring of Subsurface Structures: Seismological Research Letters, **94**, 149–158.

Tsuji, T., K. Kawamura, T. Kanamatsu, T. Kasaya, K. Fujikura, Y. Ito, T. Tsuru, and M. Kinoshita, 2013, Extension of continental crust by anelastic deformation during the 2011 Tohoku-oki earthquake: The role of extensional faulting in the generation of a great tsunami: Earth and Planetary Science Letters, **364**, 44–58.

Tsuji, T., T. Ikeda, R. Matsuura, K. Mukumoto, F. L. Hutapea, T. Kimura, K. Yamaoka, and M. Shinohara, 2021, Continuous monitoring system for safe managements of CO2 storage and geothermal reservoirs: Scientific Reports, **11**, 19120.

Tyagi, V., S. Kalyanaraman, and R. Krishnapuram, 2012, Vehicular Traffic Density State Estimation Based on Cumulative Road Acoustics: IEEE Transactions on Intelligent Transportation Systems, **13**, 1156–1166.

de Vasconcelos Lopes, A. E., and L. C. Nunes, 2010, Pitfalls of tremor-like signals for

hydrocarbon exploration in producing oil fields in Potiguar Basin, northeast Brazil: The Leading Edge, **29**, 826–830.

Vergniault, C., and J.-L. Mari, 2020, 1 Shear velocity measurement in boreholes, *in* Well seismic surveying and acoustic logging, EDP Sciences, 15–48.

Waldeland, A. U., A. C. Jensen, L.-J. Gelius, and A. H. S. Solberg, 2018, Convolutional neural networks for automated seismic interpretation: The Leading Edge, **37**, 529–537.

Wang, L., Q. Zhao, J. Gao, Z. Xu, M. Fehler, and X. Jiang, 2016, Seismic sparse-spike deconvolution via Toeplitz-sparse matrix factorization: GEOPHYSICS, **81**, V169–V182.

Wang, S., X. Zhang, J. Cao, L. He, L. Stenneth, P. S. Yu, Z. Li, and Z. Huang, 2017, Computing urban traffic congestions by incorporating sparse GPS probe data and social media data: ACM Transactions on Information Systems, **35**.

White, D., 2013, Seismic characterization and time-lapse imaging during seven years of CO2 flood in the Weyburn field, Saskatchewan, Canada: International Journal of Greenhouse Gas Control, **16**, S78–S94.

Whittaker, S., B. Rostron, C. Hawkes, C. Gardner, D. White, J. Johnson, R. Chalaturnyk, and D. Seeburger, 2011, A decade of CO2 injection into depleting oil fields: Monitoring and research activities of the IEA GHG Weyburn-Midale CO2 Monitoring and Storage Project: Energy Procedia, **4**, 6069–6076.

William, P. E., and M. W. Hoffman, 2011, Classification of military ground vehicles using time domain harmonics'amplitudes: IEEE Transactions on Instrumentation and Measurement, **60**, 3720–3731.

Won, M., 2019, Intelligent Traffic Monitoring Systems for Vehicle Classification: A Survey: .

Wong, J., P. Hurley, and G. F. West, 1983, Crosshole seismology and seismic imaging in crystalline rocks: Geophysical Research Letters, **10**, 686–689.

Wu, L., and B. Coifman, 2014a, Improved vehicle classification from dual-loop detectors in congested traffic: Transportation Research Part C: Emerging Technologies, **46**, 222–234.

Wu, L., and B. Coifman, 2014b, Vehicle length measurement and length-based vehicle classification in congested freeway traffic: Transportation Research Record, **2443**, 1–11.

Wu, X., L. Liang, Y. Shi, and S. Fomel, 2019, FaultSeg3D: Using synthetic data sets to train an end-to-end convolutional neural network for 3D seismic fault segmentation: .

Wu, X., S. Yan, J. Qi, and H. Zeng, 2020, Deep Learning for Characterizing Paleokarst Collapse Features in 3-D Seismic Images: Journal of Geophysical Research: Solid Earth, **125**, e2020JB019685.

Yamaoka, K., T. Kunitomo, K. Miyakawa, K. Kobayashi, and M. Kumazawa, 2001, A trial for monitoring temporal variation of seismic velocity using an ACROSS system: Island Arc, **10**, 336–347.

Yamaoka, K., H. Miyamachi, T. Watanabe, T. Kunitomo, T. Michishita, R. Ikuta, and M. Iguchi, 2014, Active monitoring at an active volcano: amplitude-distance dependence of ACROSS at Sakurajima Volcano, Japan: Earth, Planets and Space, **66**, 1–17.

Yanagi, K., and A. Nakamura, 2020, Towards a low/zero carbon society for the Asia-Pacific Region: Policy and legal development for carbon capture and storage (CCS) in Japan: Sustainability and Law: General and Specific Aspects, 585–605.

Yang, D., Y. Cai, G. Hu, X. Yao, and W. Zou, 2020, Seismic fault detection based on 3D Unet++ model: SEG Technical Program Expanded Abstracts, 1631–1635.

Yang, Q., W. Zhao, T. H. Dixon, F. Amelung, W. S. Han, and P. Li, 2015, InSAR monitoring of ground deformation due to CO2 injection at an enhanced oil recovery site, West Texas: International Journal of Greenhouse Gas Control, **41**, 20–28.

Yilmaz, Ö., 2001a, Seismic Data Analysis: Society of exploration geophysicists Tulsa.

Yilmaz, Ö., 2001b, Seismic Data Analysis: Processing, Inversion, and Interpretation of Seismic Data: .

Yuan, S., J. Liu, S. Wang, T. Wang, and P. Shi, 2018, Seismic Waveform Classification and First-Break Picking Using Convolution Neural Networks: IEEE Geoscience and Remote Sensing Letters, **15**, 272–276.

Zhang, H., T. Chen, Y. Liu, Y. Zhang, and J. Liu, 2021, Automatic seismic facies interpretation using supervised deep learning: Geophysics, **86**, IM15–IM33.

Zhang, T., G. V Lowry, N. L. Capiro, J. Chen, W. Chen, Y. Chen, D. D. Dionysiou, D. W. Elliott, S. Ghoshal, and T. Hofmann, 2019, In situ remediation of subsurface contamination: opportunities and challenges for nanotechnology and advanced materials: Environmental Science: Nano, **6**, 1283–1302.

Zhang, Y., Y. Liu, H. Zhang, and H. Xue, 2020, Seismic Facies Analysis Based on Deep Learning: IEEE Geoscience and Remote Sensing Letters, **17**, 1119–1123.

Zhao, T., 2018, Seismic facies classification using different deep convolutional neural networks: 2018 SEG International Exposition and Annual Meeting, SEG 2018, 2046–2050.

2016, Traffic Monitoring Guide - Updated October 2016 (U. S. F. H. Administration, ed.,): FHWA-PL-17-003.

Appendix A

Supplementary materials for Chapter 3

Depth 50 cm test

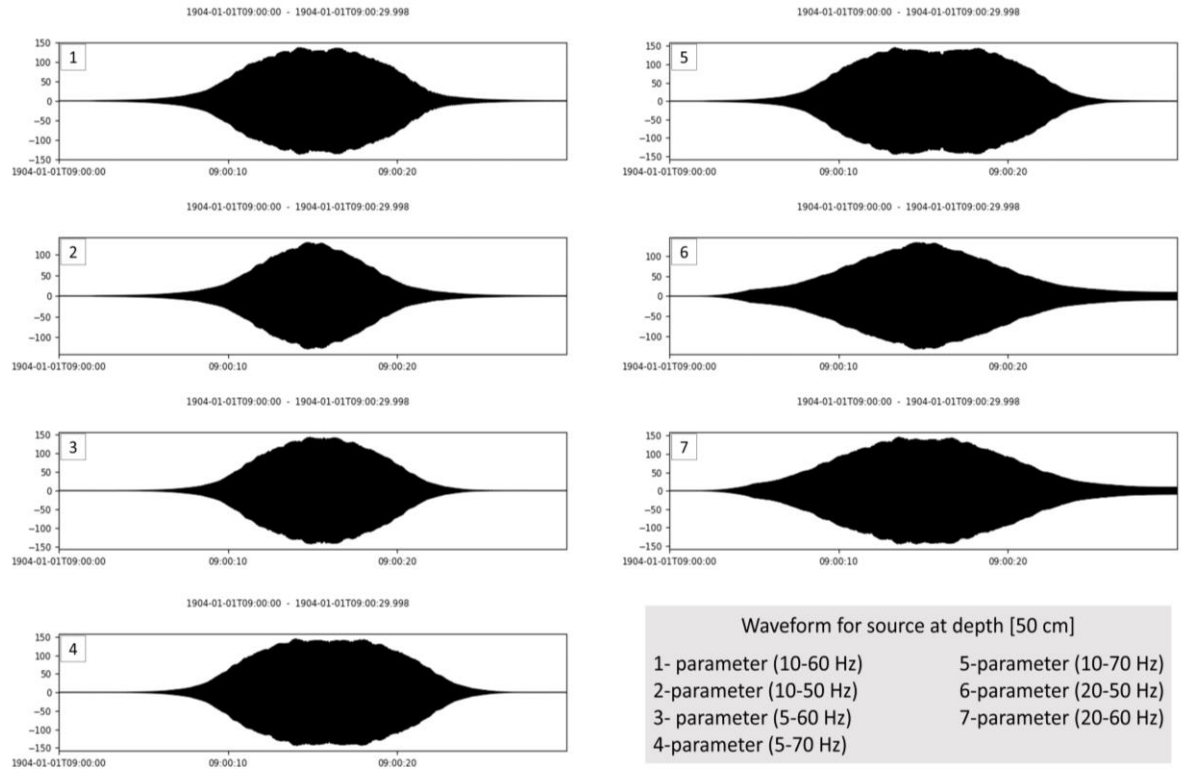

Figure 1S. The waveform of the source function at a 50-cm depth.

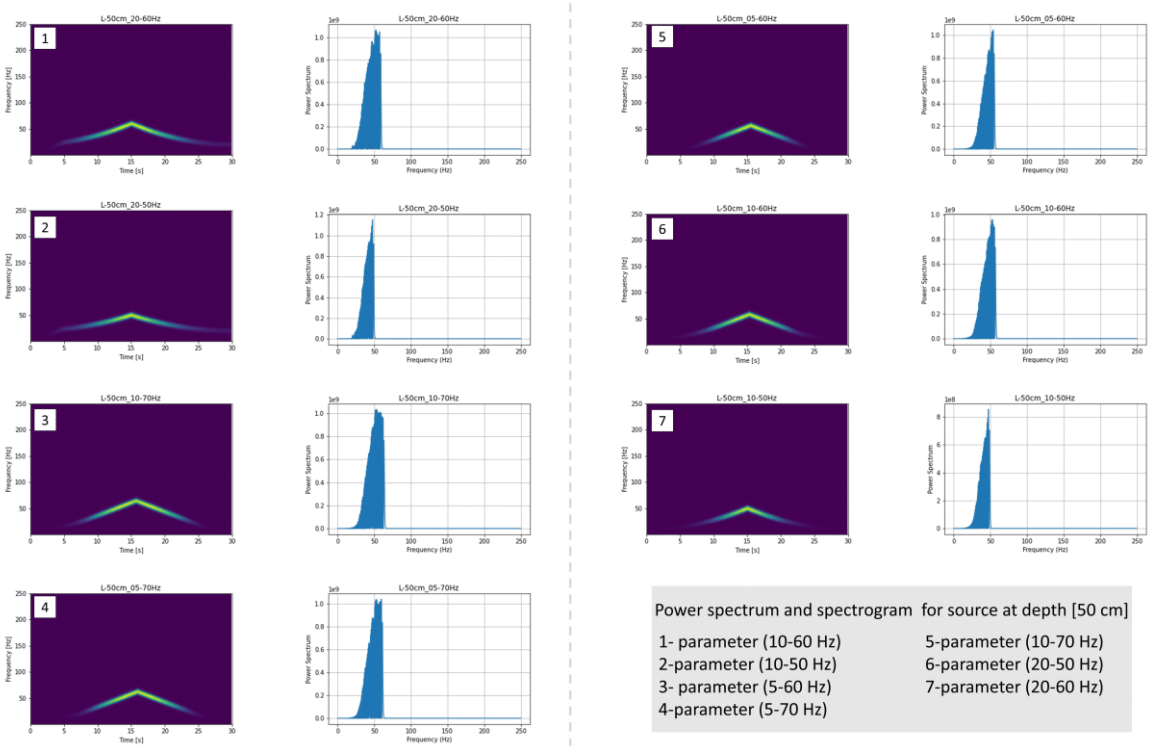

FIGURE 2S. The power spectrum and spectrogram for the source function at 50 cm depth.

Depth 25 m test

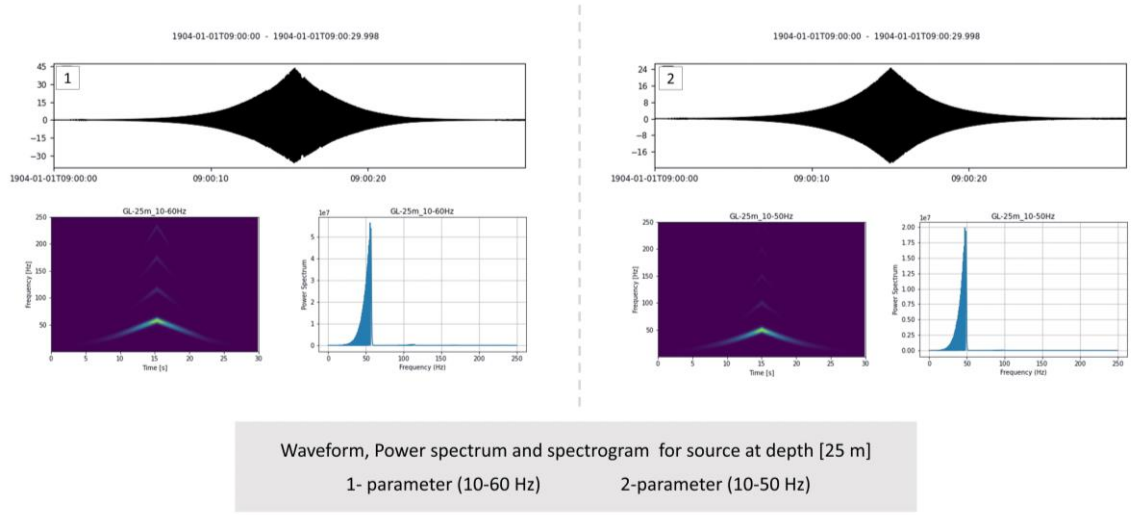

Figure 3S. The waveform, power spectrum, and spectrogram for the source function at 25-meter depth.

Depth 50 m test

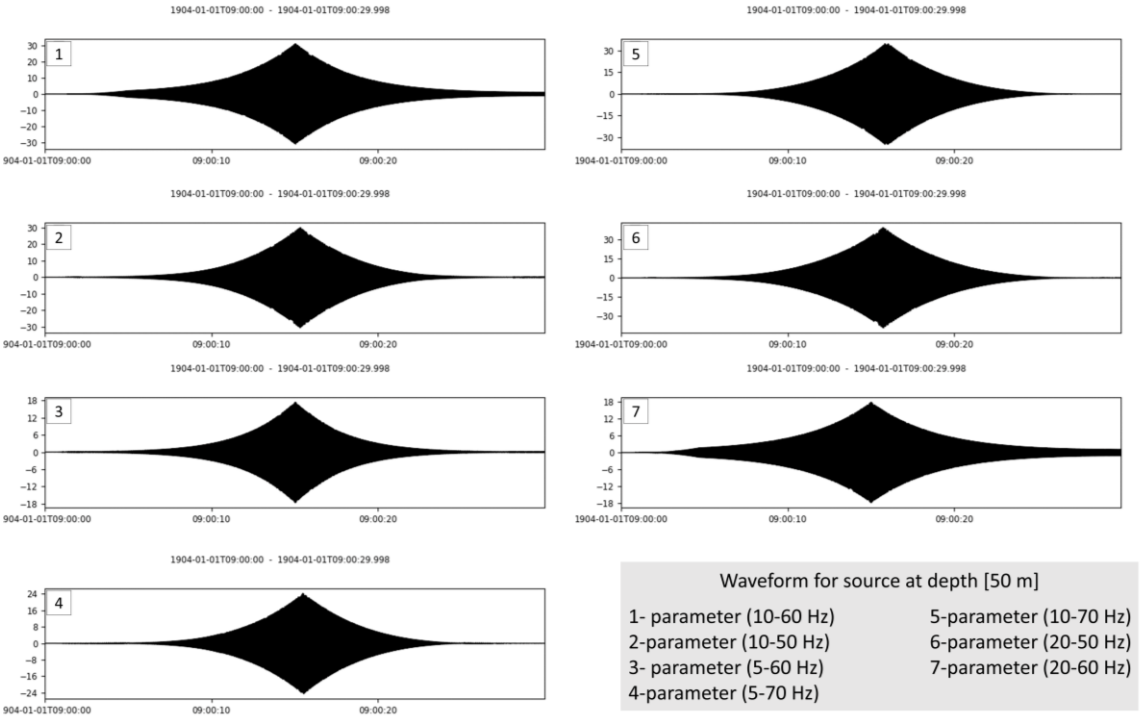

Figure 4S. The waveform of the source function at a 50-meter depth.

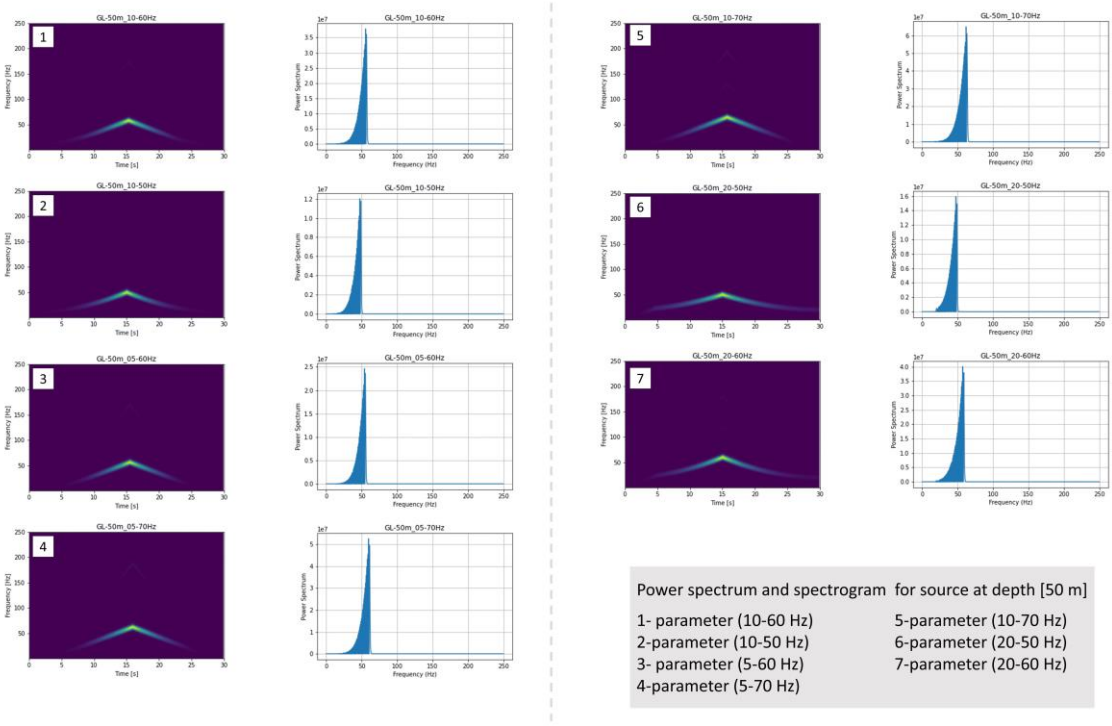

Figure 5S. The power spectrum and spectrogram for the source function at a 50-meter depth.

Different frequencies results

This section visualizes the result of using horizontal B-PASS in different frequencies as follows:

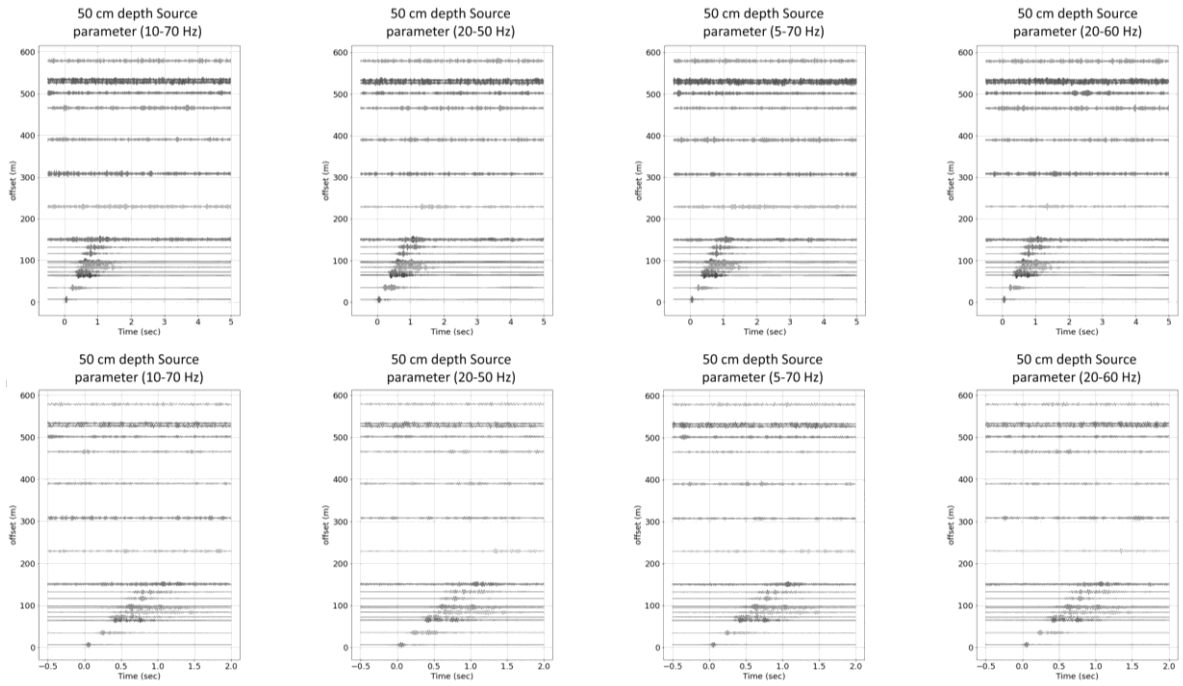

Figure 6S. The results of using B-PASS at a depth of 50 cm for frequencies [10-70, 20-50, 5-70, 20-60] Hz using horizontal motion B-PASS zoomed in at the left side.

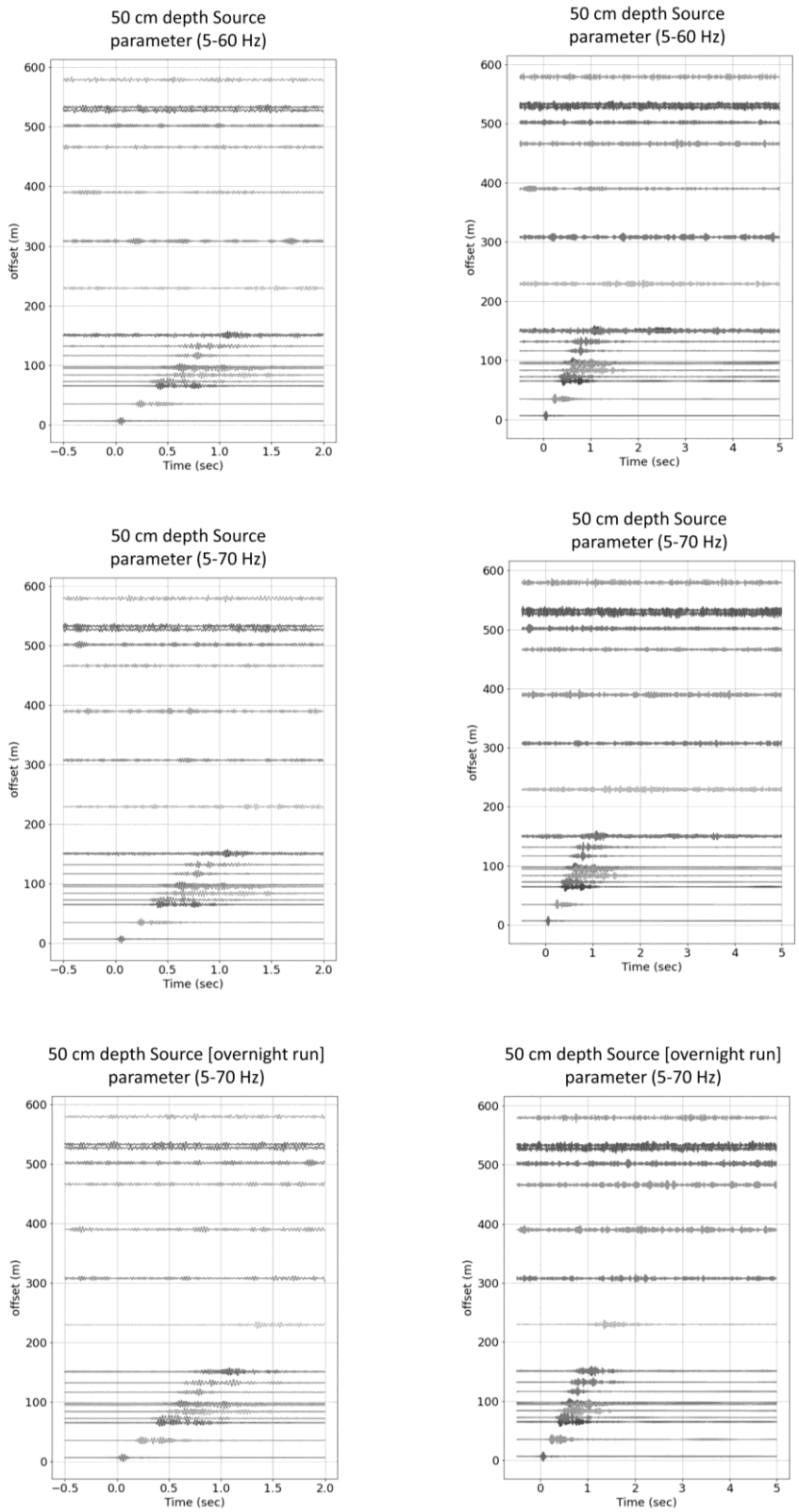

Figure 7S. The results of using B-PASS at a depth of 50 cm for frequencies [5-60, 5-70, 5-70 (overnight)] Hz using horizontal motion B-PASS zoomed in at the left side.

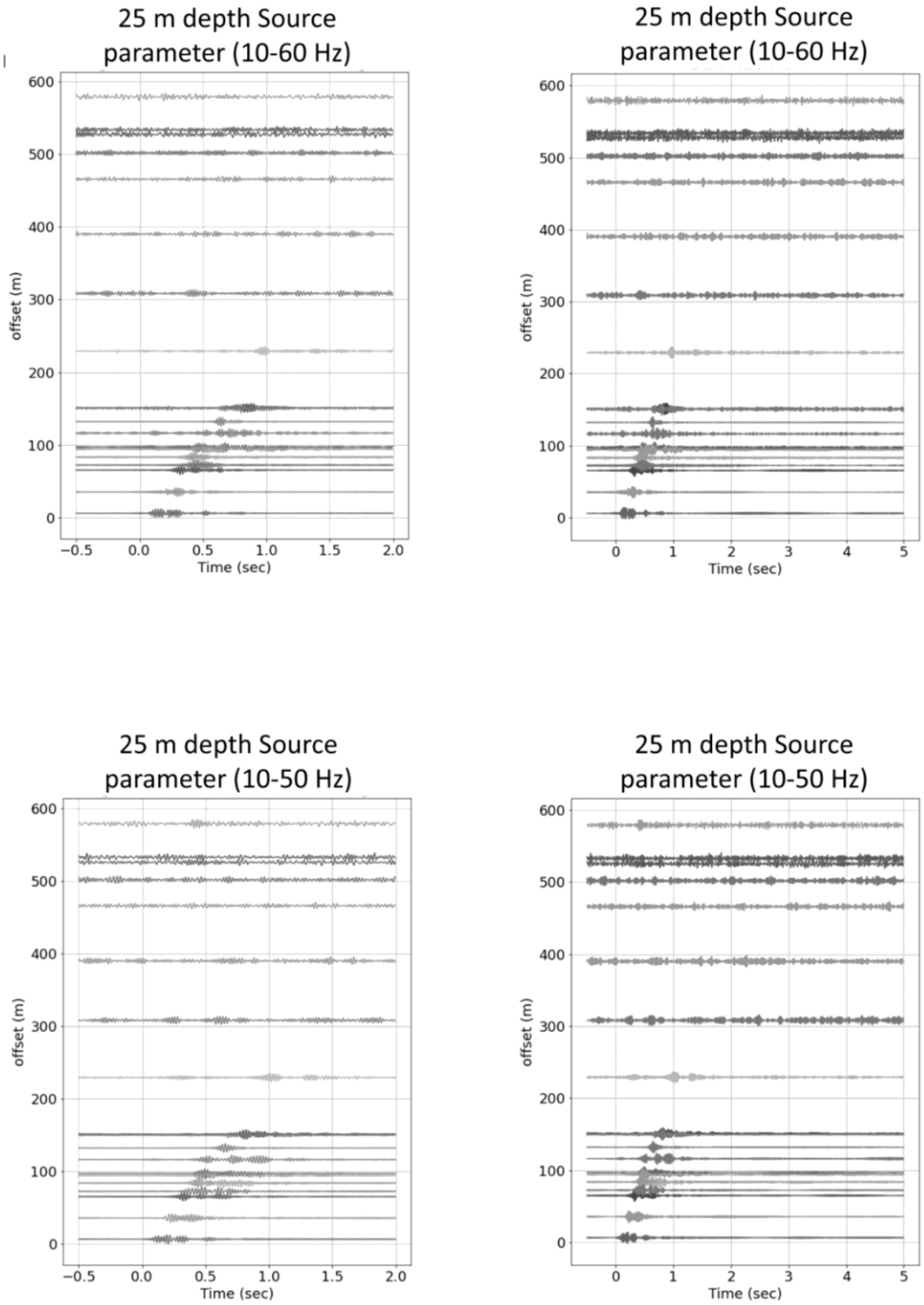

Figure 8S. The results of using B-PASS at a depth of 25 meters for frequencies [10-50, 10-60] Hz using horizontal motion B-PASS zoomed in at the left side.

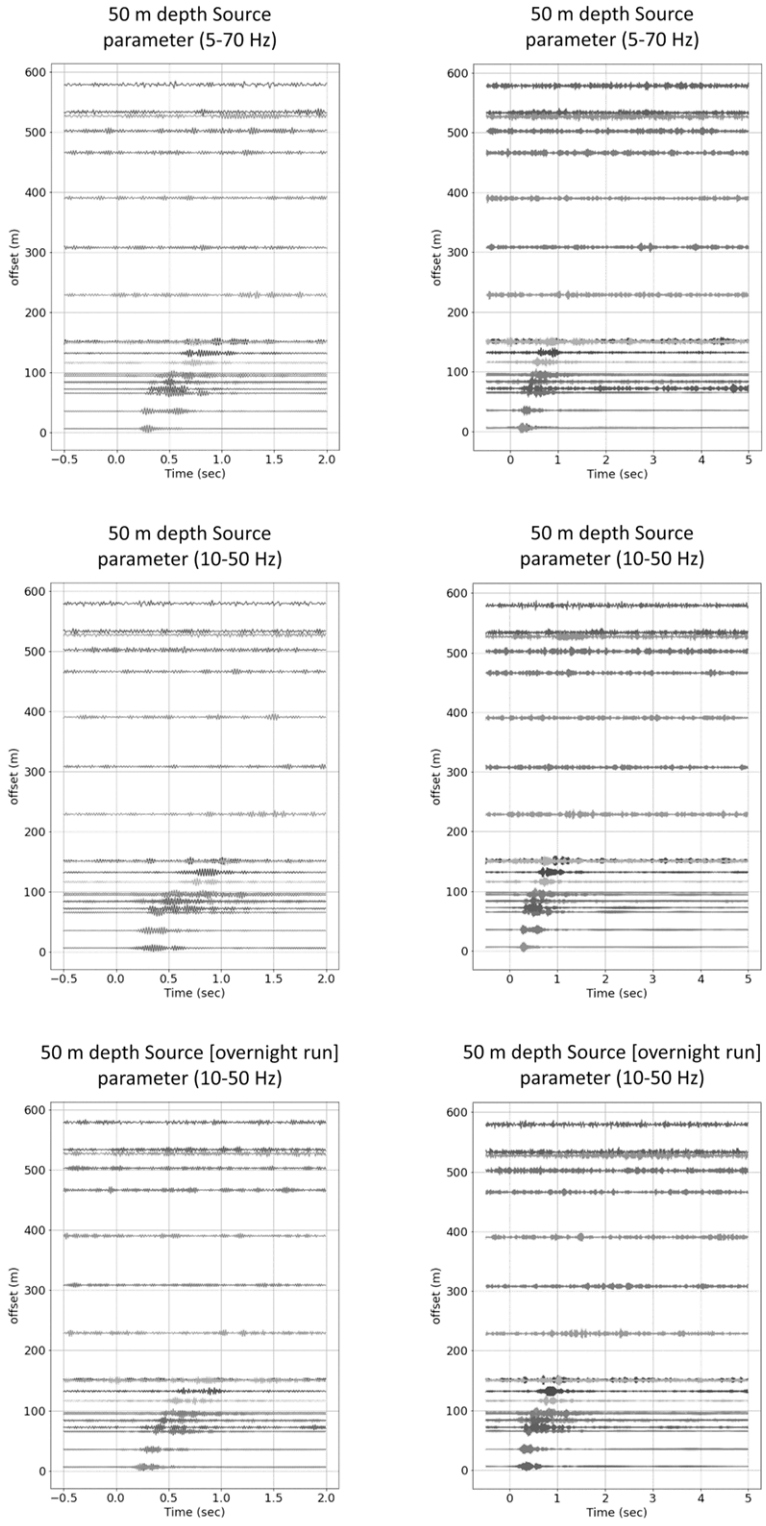

Figure 9S. The results of using B-PASS at a depth of 50 meters for frequencies [10-50, 5-70, 10-50 (overnight)] Hz using horizontal motion B-PASS zoomed in at the left side.

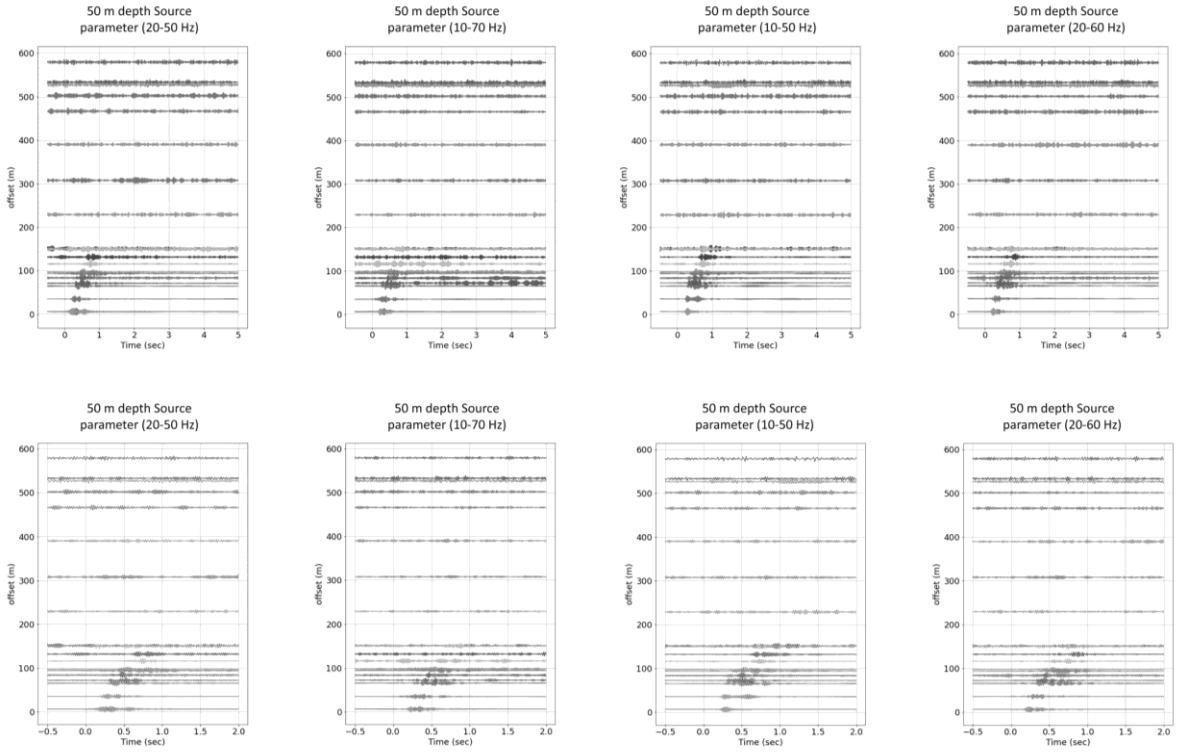

Figure 10S. The results of using B-PASS at a depth of 50 meters for frequencies [20-50, 10-70, 10-50, 20-60] Hz using horizontal motion B-PASS zoomed in at the left side.

Results of the Second Field Experiment

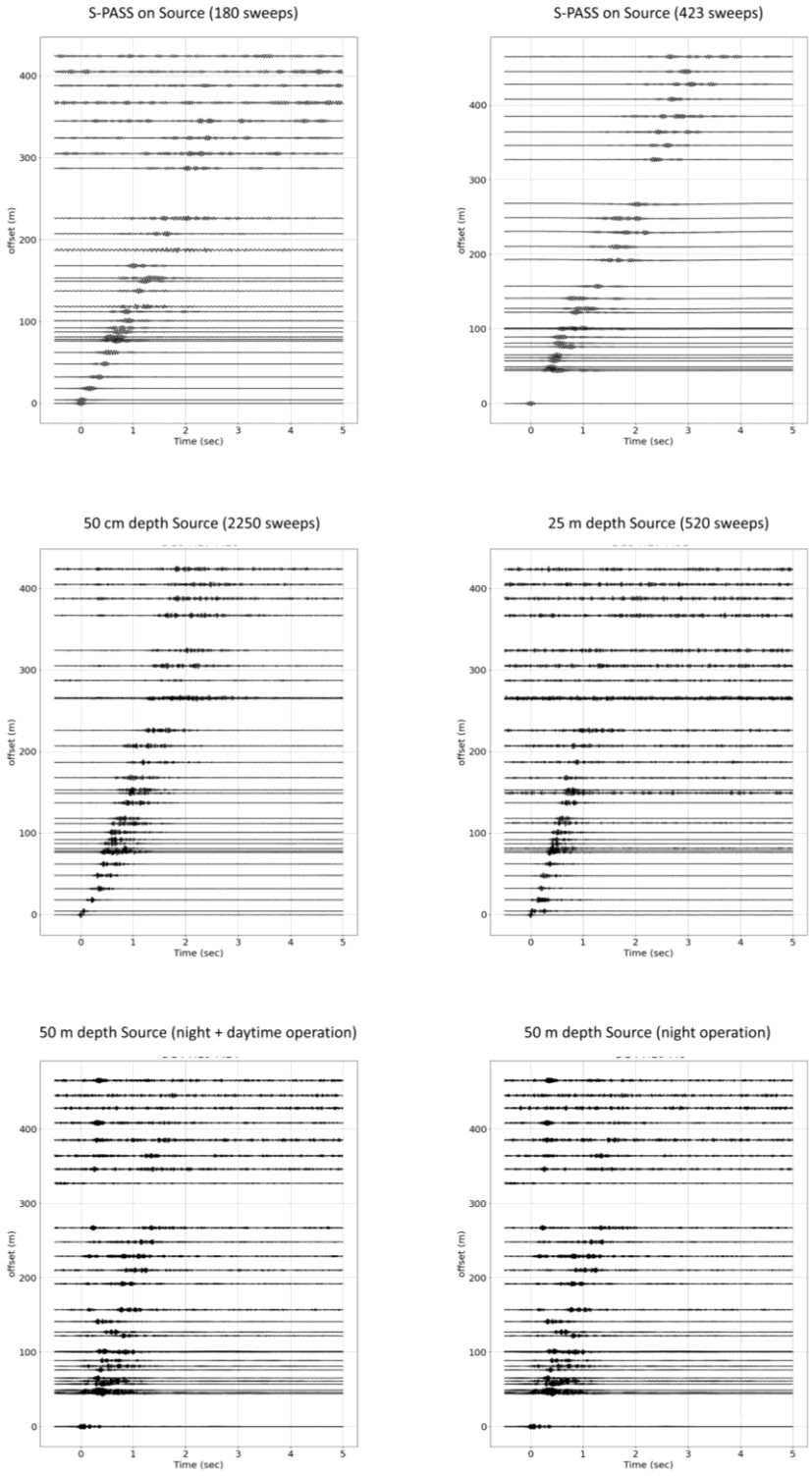

Figure 11S. Results from vertical motion B-PASS in 3 depth and compared with S-PASS in the top